

---

Ph.D. thesis  
December 2014

**Corso di Dottorato in Fisica e Astronomia  
Ciclo XXVII**

Dipartimento di Fisica “G. Occhialini”  
Università degli Studi di Milano-Bicocca

**Evolution of the CMS ECAL Performance  
and R&D Studies for Calorimetry Options  
at High Luminosity LHC**



Doctoral Student  
**Marco Toliman Lucchini**

Tutor  
**Prof. Marco Paganoni**  
Università degli Studi di Milano-Bicocca  
Dipartimento di Fisica G. Occhialini

External Supervisor  
**Dr. Etienne Auffray**  
CERN – PH-CMX

---



*A via Aldo Moro  
e tutto ciò che, lì,  
rimane.*

*To Rue du Commerce  
and its restaurant, AGG.*

*À Rue Lafayette,  
le tournesol.*



# Riassunto

---

Negli anni ultimi il Large Hadron Collider (LHC) del CERN ha operato con una massima energia nel centro di massa pari a  $\sqrt{s} = 8$  TeV e una luminosità istantanea di circa  $7 \times 10^{33} \text{ cm}^{-2}\text{s}^{-1}$ . L'analisi dei dati raccolti (luminosità integrata di  $23 \text{ fb}^{-1}$ ) ha permesso la scoperta di un bosone di Higgs, avvenuta il 4 Luglio 2012. Per studiare con maggior precisione le proprietà del bosone di Higgs appena scoperto, è stata recentemente approvata la decisione di estendere il programma di ricerca di LHC fino al 2035. In questo contesto, intorno al 2022, verrà effettuato un importante rinnovamento dell'ottica del fascio nel punto di interazione che permetterà di raggiungere una luminosità istantanea pari a  $\mathcal{L} = 5 \times 10^{34} \text{ cm}^{-2}\text{s}^{-1}$ , condizione nominale alla quale LHC ad alta luminosità (HL-LHC) dovrà operare.

Durante questa fase di HL-LHC, i livelli di radiazione diverranno significativamente più alti rispetto ai valori nominali per i quali il rivelatore di CMS era stato progettato. Risulta quindi di cruciale importanza identificare e quantificare gli effetti del danno da radiazione, sull'attuale rivelatore, al fine di preparare un adeguato rinnovamento dei sotto-rivelatori di CMS e mantenere un buon funzionamento durante HL-LHC.

In questa tesi è discusso uno studio dettagliato sugli effetti che il danno da radiazione comporterà sulla prestazione del calorimetro elettromagnetico (ECAL) di CMS. Una campagna di irraggiamento con protoni di 24 GeV è stata portata a termine grazie all'utilizzo del Protosincrotron (PS) del CERN durante il 2011 e il 2012. Diversi cristalli di tungstato di piombo ( $\text{PbWO}_4$ ), identici a quelli utilizzati in ECAL, sono stati irraggiati con fluenze di protoni fino a  $14 \times 10^{13} \text{ cm}^{-2}$ . Simili livelli di radiazione sono previsti al termine della fase di HL-LHC nella regione in avanti del rivelatore. Il degradarsi delle proprietà dei cristalli, tra cui la resa di luce, la linearità e la risoluzione energetica, è stato studiato attraverso misure in laboratorio e test su fascio. Un confronto dei risultati ottenuti con un modello di simulazione ha permesso di valutare l'evoluzione della prestazione di ECAL durante l'intero periodo di HL-LHC.

---

Nella regione in avanti del rivelatore, in cui i livelli di radiazione sono più alti, il termine costante della risoluzione energetica crescerà fino al  $\sim 10\%$  (a  $|\eta| = 2.2$ ) dopo una luminosità integrata di  $3000 \text{ fb}^{-1}$ , prevista per la fine di HL-LHC. Una perdita di risoluzione energetica di tale entità non permetterà un adeguato funzionamento del rivelatore. Siccome anche il calorimetro adronico in avanti verrà sensibilmente danneggiato dalla radiazione, sarà necessario sostituire l'intero calorimetro in avanti con un nuovo dispositivo più resistente alla radiazione prima dell'inizio della fase di HL-LHC.

A questo proposito, diversi progetti e tecnologie in grado di soddisfare i requisiti per un nuovo calorimetro resistente alla radiazione di HL-LHC sono in corso di studio. Tra le varie opzioni, molte richiedono la ricerca e lo sviluppo di scintillatori e *wavelength-shifter* (WLS) in grado di resistere alle alte dosi e fluenze di radiazione previste per HL-LHC. In questo lavoro sono presentati i risultati raggiunti nello studio e nell'ottimizzazione di alcuni scintillatori candidati per applicazioni di calorimetria a HL-LHC. In particolare, sono stati studiati cristalli inorganici (LuAG, YAG, LSO, YSO), quarzo ( $\text{SiO}_2:\text{Ce}$ ) e vetro pesante (DSB:Ce) dopati con ioni di elementi rari ( $\text{Ce}^{3+}$ ,  $\text{Pr}^{3+}$ ). Le proprietà ottiche e di scintillazione dei diversi campioni sono state caratterizzate in laboratorio. Successivamente, i campioni sono stati irraggiati con sorgenti  $\gamma$  e fasci di protoni per studiarne il danno da radiazione. Tale studio ha permesso di identificare i campioni di ciascun materiale più resistenti alla radiazione e di definire i parametri ottimali per la loro produzione.

Uno studio approfondito è stato svolto su cristalli di LuAG cresciuti in forma di fibra attraverso la tecnica di *micro-pulling-down*. La possibilità di usare cristalli pesanti con geometrie particolari (fino a 1 m di lunghezza e con diametro variabile tra 0.2 e 3 mm) rappresenta un strumento particolarmente versatile per adattarsi al meglio ai requisiti geometrici di svariati calorimetri. Simili fibre sono un possibile candidato per la sostituzione dello scintillatore plastico attualmente utilizzato nel calorimetro adronico. Possono al tempo stesso essere utilizzate come wavelength-shifter per la raccolta di luce in un calorimetro à la Shashlik o come scintillatore in un calorimetro à la SpaCal.

I risultati ottenuti durante test su fascio svolti al CERN e a FNAL sono presentati in questa tesi. Diversi prototipi di calorimetro a campionamento, costituiti da un assorbitore di ottone e fibre di LuAG, sono stati testati con fasci di elettroni e pioni. I dati sperimentali ottenuti hanno confermato il potenziale di questa tecnologia per applicazioni calorimetriche e fornito la base per la progettazione di futuri prototipi di calorimetro di maggiori dimensioni.

# Abstract

---

During the past years the Large Hadron Collider (LHC) at CERN operated with a maximum center-of-mass energy of  $\sqrt{s} = 8$  TeV, a peak luminosity of around  $7 \times 10^{33}$  cm $^{-2}$ s $^{-1}$  and collected about  $23$  fb $^{-1}$  of data which lead to the discovery of a Higgs Boson in July 2012. To further constrain the properties of the newly discovered Higgs boson, the decision to extend the LHC program has recently been made. In this framework, a major upgrade of the beam optics in the interaction region will take place around 2022 to achieve a leveled peak luminosity of  $\mathcal{L} = 5 \times 10^{34}$  cm $^{-2}$ s $^{-1}$ . These will be the operating conditions during the High Luminosity LHC (HL-LHC) which is expected to deliver an integrated luminosity of  $3000$  fb $^{-1}$  by 2035.

During HL-LHC phase the radiation levels will become much higher with respect to the nominal values for which the CMS detector was designed. Therefore it is of crucial importance to identify and quantify the effects of radiation damage on the current detector in order to prepare an adequate upgrade of its components and maintain a good performance throughout its whole operation.

In this thesis, a detailed study of the radiation damage effects on the performance of the CMS Electromagnetic Calorimeter (ECAL) is presented. A dedicated campaign of irradiation with 24 GeV protons has been performed at CERN Proton Synchrotron during 2011 and 2012. Lead tungstate (PbWO<sub>4</sub>) crystals have been irradiated to different proton fluences up to  $14 \times 10^{13}$  cm $^{-2}$  which is close to the integrated fluences expected at the end of HL-LHC in the ECAL endcaps (EE). Degradation of crystal properties such as light output, energy linearity and energy resolution has been studied combining laboratory measurements and test beam results, obtained with 10-150 GeV electrons provided by the CERN H4 facility. Results have been compared with a simulation model which properly reproduce the experimental data and allows to extrapolate the performance of the CMS ECAL throughout the whole HL-LHC phase.

---

Especially in the forward region of the detector, where radiation levels are higher, the constant term of the energy resolution will increase up to  $\sim 10\%$  (at  $|\eta| = 2.2$ ) after  $3000 \text{ fb}^{-1}$  of data, foreseen for the end of HL-LHC. A similar degradation of the calorimeter resolution will not allow a proper operation.

Since also the Hadronic Calorimeter endcap (HE) will be strongly damaged by radiation, a general upgrade of the whole endcap calorimeter (EE+HE) will be required during the long shutdown foreseen around 2022. In this framework, a set of more radiation hard calorimeter designs and technologies which are able to operate under HL-LHC conditions are currently being investigated for the upgrade of the calorimetric system. Among the different options, several of them require the developments of radiation hard scintillators and wavelength shifters. In this work, R&D studies on several scintillators candidates for calorimetry applications are presented. Attention is focused on inorganic crystals (LuAG, YAG, LSO, YSO) doped with rare earth ions ( $\text{Ce}^{3+}$ ,  $\text{Pr}^{3+}$ ) and cerium doped quartz ( $\text{SiO}_2:\text{Ce}$ ) and barium disilicate (DSB:Ce). In addition to a full characterization of optical and scintillation properties, a dedicated study of radiation hardness was performed on a set of samples. Irradiation with  $\gamma$  and proton sources were performed in different facilities leading to the identification of the most radiation tolerant samples and the best production parameters.

Particular efforts were made on the study of LuAG crystals directly grown in a fiber shape by micro-pulling-down technique. The possibility to use heavy crystals in fiber geometry represents a flexible and powerful tool for many calorimeter options. Such fibers are good candidates for the replacement of the current HE plastic scintillator. In addition, doped crystal fibers can provide a radiation hard wavelength shifter to read out the signal from Shashlik-based detectors or can be used as scintillator in a SpaCal calorimeter design.

Results obtained from several test beams performed at CERN and FNAL facilities are presented. Different configuration of sampling calorimeter modules made of brass and LuAG fibers have been tested with electrons and pions beams. The potential of crystal fibers for calorimetry applications has been demonstrated and further tests on larger calorimeter prototypes are foreseen for the early future.

# Acknowledgments

---

This thesis is the result of my path as a doctoral student. Therefore, I want to thank my supervisors *Marco Paganoni* and *Etienne Auffray* for the exciting opportunity I had to work in an international and challenging environment such as CERN.

I had the chance to work with experts who definitely helped me while learning how to work on data analysis to draw coherent scientific conclusions. For their guidance and counselling I acknowledge *Tommaso Tabarelli de Fatis* and *Alessio Ghezzi*.

A grateful acknowledgment goes to *Jean-Louis Faure* and *Sasha Singovsky* for their collaboration in the test beam studies with proton irradiated PbWO<sub>4</sub> crystals which lead to the successful evaluation of the future aging of CMS ECAL.

The test beam results obtained on crystal fiber calorimetry presented in this thesis were possible because of the fruitful and enjoyable collaboration with *Chris Tully* and *Tatiana Medvedeva* from Princeton University and *Arjan Heering* from Notre Dame University. I also acknowledge the ILM of Lyon University and Fibercryst company who spent several efforts to provide in time all the crystal fibers used for the calorimetric modules.

I want to acknowledge *Mikhail Korjik* for the productive collaboration in the study of crystals radiation hardness and for common efforts on the development of new scintillators.

While moving on with my PhD studies, I discovered how scientific work can not, nowadays, be carried out without large collaborations with world wide communities of scientists. In particular I would like to thank all the colleagues from the *CMS Collaboration* and the *Crystal Clear Collaboration* with whom I have been working.

---

Nevertheless, I spent the most of my time with the Lab27 group conducted under the wise advices of *Paul Lecoq* and *Etienne Auffray*. None of the measurements on crystal transmission would have been possible without the precious work of *Dominique Deyrail* and *Alain Machard* who always provided precious assistance in preparing crystals and setting up laboratory measurements.

A special thank goes to my office mates: *Pawel* the hologram expert and *Kristof* who always provided good answers to my novelline questions about laboratory measurements and initiated me to crystal fiber calorimetry.

Moving to the next-door office, I want to acknowledge *Andrea* whose programming skills and smart comments on data analysis were fundamental for obtaining many of the results presented in this thesis.

On the same floor, I give special credits to the “schnitzel group” of *Arno* and *Stefan* as well as to our science communication expert *Rita*. Descending down the stairs I want to mention the ever-smiling *Rosana* and the mysterious *Zheng*, then passing by the “three-ladies” office of *Giulia*, *Katayoun* and *Farah* to finally reach the “coffee break room”.

A special thanks is dedicated to *Nicolas*, *Pizzi* and *Mythra* who always guaranteed a good way to break interminable afternoons with random-topic chats.

Beyond working hours, I want to acknowledge all the other numerous people I have met, loved and lived with during the past three years. These being a good reason to write an enjoyable novel instead of a Ph.D. thesis.

# Contents

---

<b>Introduction</b>	<b>1</b>
<b>1 Theoretical Background</b>	<b>3</b>
1.1 Calorimetry . . . . .	3
1.1.1 Electromagnetic Shower Development . . . . .	4
1.1.2 Hadronic Shower Development . . . . .	8
1.1.3 Energy Resolution of Calorimeters . . . . .	10
1.1.4 Considerations on Hadronic Calorimeters . . . . .	16
1.2 The Scintillation Mechanism . . . . .	19
1.2.1 Scintillation Mechanism in Inorganic Scintillators . . . . .	19
1.2.2 General Characteristics of Inorganic Scintillators . . . . .	21
1.3 The Cherenkov Effect . . . . .	26
<b>2 The CMS Experiment at the Large Hadron Collider</b>	<b>29</b>
2.1 The Large Hadron Collider (LHC) . . . . .	30
2.2 The CMS detector . . . . .	32
2.2.1 The coordinate system . . . . .	33

2.2.2	Inner Tracking System . . . . .	35
2.2.3	The Electromagnetic Calorimeter . . . . .	36
2.2.4	The Hadronic Calorimeter . . . . .	38
2.2.5	The Magnet . . . . .	41
2.2.6	The Muon System . . . . .	41
2.2.7	The Forward Detectors . . . . .	43
2.2.8	Trigger and Data Acquisition System . . . . .	45
<b>3</b>	<b>Test Beam Study with Proton-Irradiated ECAL Endcap Crystals</b>	<b>47</b>
3.1	Radiation Damage in Lead Tungstate . . . . .	48
3.1.1	Electromagnetic Damage . . . . .	48
3.1.2	Hadronic Damage . . . . .	49
3.1.3	Recovery Studies . . . . .	50
3.2	Radiation Environment at HL-LHC . . . . .	52
3.3	Proton Irradiation of PbWO <sub>4</sub> Crystals . . . . .	55
3.3.1	PS Irradiation Setup . . . . .	55
3.3.2	Light Transmission Measurements . . . . .	55
3.4	Test Beam Setup . . . . .	59
3.4.1	Test Matrix . . . . .	59
3.4.2	Crystal Matrix Configurations . . . . .	60
3.4.3	Beam Counters . . . . .	60
3.4.4	Readout . . . . .	61
3.4.5	Data Acquisition System . . . . .	62
3.4.6	Data Taking Procedure . . . . .	63
3.5	Test Beam Analysis . . . . .	64
3.5.1	Average Induced Absorption for a 3×3 Matrix . . . . .	64
3.5.2	LED Monitoring System . . . . .	64

3.5.3	System Stability . . . . .	64
3.5.4	Pedestal Subtraction . . . . .	65
3.5.5	Beam Spot Selection . . . . .	67
3.5.6	Energy Calibration . . . . .	70
3.5.7	Energy Linearity . . . . .	71
3.5.8	Energy Resolution . . . . .	72
3.6	Test Beam Results . . . . .	74
3.6.1	Scintillation Pulse Shapes . . . . .	74
3.6.2	Single Crystal Light Output . . . . .	75
3.6.3	Non-irradiated Matrix Performance . . . . .	77
3.6.4	Irradiated Matrices Performance . . . . .	77
3.7	Conclusions . . . . .	82
<b>4</b>	<b>Extrapolation of EE Crystals Performance Until the End of HL-LHC</b>	<b>83</b>
4.1	Comparison of Test Beam Data with Simulation . . . . .	83
4.1.1	Simulation Setup . . . . .	84
4.1.2	“Fast” and “Full” Simulations . . . . .	85
4.1.3	Effect of a Non-Uniform $\mu_{ind}$ inside the Crystal . . . . .	89
4.2	Extrapolation of Future ECAL Performance . . . . .	93
4.2.1	Extrapolation of Crystal Ageing Effects on ECAL Performance . . . . .	93
4.2.2	Conclusions . . . . .	96
<b>5</b>	<b>Study of Radiation Hardness on Scintillator Candidates for Calorimetry at HL-LHC</b>	<b>99</b>
5.1	Options for the CMS Endcap Calorimeters Upgrade . . . . .	100
5.2	Requirements for Scintillator Candidates . . . . .	102
5.3	$\text{Lu}_2\text{SiO}_5$ and $\text{Y}_2\text{SiO}_5$ Crystals . . . . .	103
5.3.1	Samples and Experimental Procedure . . . . .	104

5.3.2	Induced Absorption . . . . .	105
5.3.3	Induced Phosphorescence . . . . .	108
5.4	$\text{Lu}_3\text{Al}_5\text{O}_{12}$ and $\text{Y}_3\text{Al}_5\text{O}_{12}$ Crystals . . . . .	111
5.4.1	Induced Absorption . . . . .	111
5.5	DSB:Ce Glass . . . . .	114
5.6	$\text{SiO}_2:\text{Ce}$ Doped Quartz . . . . .	116
5.7	Conclusions . . . . .	116
<b>6</b>	<b>Test Beam Results on Crystal Fibers for Calorimetry Applications</b>	<b>119</b>
6.1	Crystal LuAG Fibers Grown with Micro-Pulling-Down Technique . . . . .	120
6.2	Motivations for Crystal Fibers Calorimetry . . . . .	121
6.3	Preliminary Test Beam in Pointing Configuration . . . . .	123
6.3.1	LuAG Fibers and Calorimetric Module . . . . .	123
6.3.2	H <sub>2</sub> Beam Line and Test Beam Setup . . . . .	124
6.3.3	Test Beam Results . . . . .	126
6.3.4	Discussion . . . . .	133
6.4	FNAL Test Beam in Transverse Configuration . . . . .	136
6.4.1	Experimental Setup . . . . .	136
6.4.2	Analysis Procedure . . . . .	139
6.4.3	Results . . . . .	144
6.5	Discussion and Conclusions . . . . .	157
<b>Conclusions and Outlook</b>		<b>158</b>
<b>Appendix</b>		<b>161</b>
<b>A Double Readout Option to Mitigate ECAL Endcaps Aging</b>		<b>161</b>
A.1	Implications on Light Collection Efficiency . . . . .	162

A.2	Improvements of Energy Resolution . . . . .	163
A.3	Practical Considerations . . . . .	166
<b>Bibliography</b>		<b>169</b>



# Introduction

---

One of the major discovery of the last decade in Particle Physics has been the observation of a Higgs boson which fits the Standard Model expectations. This new particle was observed at the Large Hadron Collider (LHC) by the two multi-purpose experiments, CMS (Compact Muon Solenoid) and the ATLAS (A Toroidal LHC ApparatuS) on the 4<sup>th</sup> July, 2012. Such challenging discovery was made possible because of the huge work of a wide community of physicists and engineers.

A sophisticated data analysis is required to select rare events over a large background and to compare the experimental data with theoretical expectations. The quality of experimental data collected by the experiments strongly relies on the performance of its particle detectors. As a consequence, limitations to the exploitation of the full LHC potential arise from the finite resolution of current detectors. In particular, the precision on the energy resolution of hadronic particles and jets present non-trivial challenges as discussed in Chap. 1.

An appropriate choice of tecnhologies and design is required for all the subdetectors to measure as precisely as possible all the particles produced during collisions. The design of the current CMS calorimeter, resulted from more than 10 years of R&D on a wide range of technologies, is presented in Chap. 2.

In the next years, the LHC will operate increasing its center of mass energy from 8 to 14 TeV and succesively, around 2022, it will be upgraded to achieve higher collision rate. During this High Luminosity LHC (HL-LHC) Phase the detectors will collect a huge amount of data improving the potential for the discovery of new physics. The future operating conditions of the LHC (and HL-LHC) will represent a challenging environment for particle detectors which will have to upgrade several components in order to maintain

---

a good performance. The levels of radiation, both electromagnetic and hadronic, to which detectors will be exposed will be much higher than their initial design conditions.

The study of radiation damage effects on the performance of the Electromagnetic Calorimeter (ECAL) of the CMS detector is presented in Chap. 3. Dedicated irradiation studies on lead tungstate crystals ( $\text{PbWO}_4$ ), which is the active component of the ECAL detector, have been performed at the CERN Proton Synchrotron to reproduce future radiation levels expected in the next phases of LHC and HL-LHC. Combining test beam studies, laboratory measurements and data from the real detector a coherent model of ECAL aging describing the evolution of its performance has been defined as presented in Chap. 4.

It has been demonstrated that the forward region of the current ECAL, being more exposed to radiation, will not be able to operate properly until the end of the HL-LHC phase. Several R&D studies have started to identify new technologies and calorimeter designs which are able to withstand radiation levels foreseen for HL-LHC. Recently developed inorganic crystals doped with rare earth ions and other quartz based scintillators, namely DSB:Ce and  $\text{SiO}_2:\text{Ce}$ , are potential radiation tolerant candidates as presented in Chap. 5.

Among several options, particular attention is focused on crystal fiber technology which can provide a powerful tool for innovative calorimeter designs. Growing heavy inorganic crystals directly into fiber shape, allows to save time and costs with respect to standard crystal growth which would require further cutting and polishing to achieve similar high aspect ratio. Fiber geometry is particularly suitable to design homogenous and extremely granular calorimeters: the former being a fundamental requirement for good energy resolution; the latter representing a potential tool to improve particle identification capabilities and pile up mitigation.

A set of test beam studies have been performed both at CERN and Fermilab test beam facilities. The performance of sampling calorimeter prototypes, made of brass and crystal fibers, is presented in Chap. 6. The calorimetric modules have been tested with electrons and pions beam, confirming the potential of this technology for calorimetry applications.

# Theoretical Background

---

In this chapter the main theoretical aspects required for the understanding of this thesis will be reviewed. The basic concepts of calorimetry and two of the most important physical processes involved in the operation of light-based calorimeters, namely the scintillation mechanism and the Cherenkov effect, will be introduced.

## 1.1 Calorimetry

Calorimetry comprises all the experimental methods which aim to measure the energy of particles. A calorimeter is essentially a block of matter which is able to entirely absorb a particle and to produce a measurable signal proportional to the particle energy [1]. Historically, calorimeters were first used for the study of cosmic rays [2]. Later on, during the 1960's and the early 1970's, the raising interest in accelerator experiments provided a boost for the development of new types of dedicated calorimeters. One of the feature which made calorimeters particularly attractive for the collider experiments is their capability to measure the energy of both charged and neutral particles. Depending on their particular design, calorimeters may be able to provide also measurements of position and particle identification, for instance making use of a proper transverse and longitudinal segmentation respectively.

The signal resulting from the absorption of a particle in a calorimeter can be of different nature: electrical, optical, thermal or acoustical [3, 4]. The majority of calorimeters, es-

pecially those used in collider experiments, are based on the  $dE/dx$  technique, i.e. the signal depends on the energy deposited by the shower particles in the sensitive material. The signal generated by the deposition of energy can be light, for calorimeters with scintillators, or ionization charge, for those with gaseous or semiconductive sensitive material. A different principle of operation is exploited by calorimeters composed of lead glass or quartz fibers [5, 6, 7] make use of the light produced via Cherenkov effect.

Calorimeters can be divided in two categories: *homogeneous*, if the whole detector volume is active (i.e. producing signal), or *sampling*, if the detector comprises a purely passive absorber and only a fraction of it consists of active volume. In the latter case, only a fraction of the deposited energy is transformed into signal.

Because of the very different ways in which photons, electrons and hadrons interact with matter, the geometrical design and material choice of a particular calorimeter is often optimized for the detection of either electromagnetic or hadronic particles. However, the use of a same calorimeter for detection of both types of particles can provide significant advantages as argumented in [8].

### 1.1.1 Electromagnetic Shower Development

An electromagnetic shower is the process through which energetic ( $\gtrsim$  GeV) electromagnetic particles interact with matter generating a cascade process consisting of a large production of secondary particles (photons, electrons and positrons).

This occurs because electrons and positrons with energy higher than 1 GeV lose energy mostly through bremsstrahlung and photons through pair production [1, 9]. The secondary particles produced by the primary one interact through the same processes leading to the development of a particle shower inside the calorimeter. Electrons and positrons with energies  $E \leq 10$  MeV interact with matter and lose energy mainly through ionization of the atoms of the detector. The shower development ceases when secondary particles are slowed down to energies at which energy losses from ionization processes are higher than from bremsstrahlung.

Additional processes such as Moller scattering, Bhabha scattering and positron annihilation do not contribute significantly to energy loss, as shown in Fig. 1.1. The energy loss per unit length from ionization is practically constant, since it depends logarithmically on electron/positron energy,  $|dE/dx|_{ion} \propto \ln E$ , in contrast to energy loss from bremsstrahlung which shows linear dependence on energy,  $|dE/dx|_{brem} \propto E$  (see Fig. 1.1).

To describe the development of an electromagnetic shower, it is useful to define the *critical energy*,  $E_c$ , as the energy at which the loss rates from ionization and from bremsstrahlung become equal. The critical energy is a crucial parameter which characterizes the material

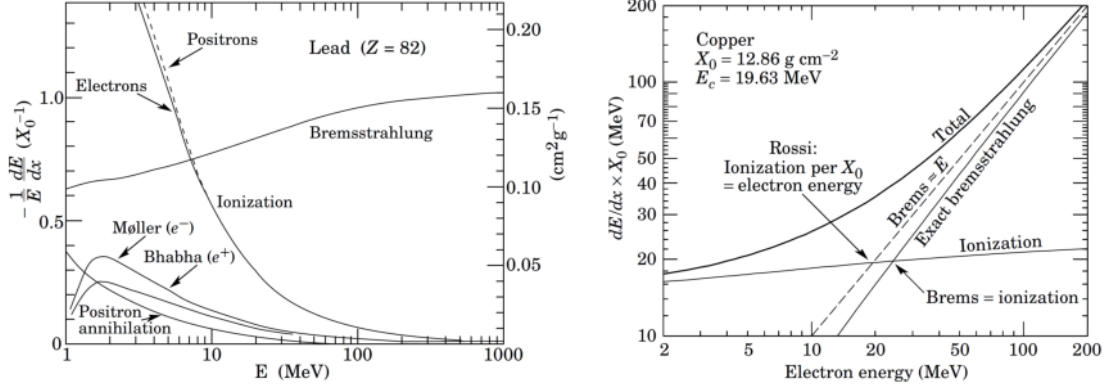


**Figure 1.1:** Left: relative energy loss per unit length ( $\frac{1}{E} \frac{dE}{dx}$ ) in lead for different processes as a function of electron or positron energy. Right: energy loss per unit length from ionization and bremsstrahlung as a function of electron energy (in copper). Both forms of defining  $E_c$  are shown, according to  $(\frac{dE}{dx})_{ion} = (\frac{dE}{dx})_{brem}$  or  $(\frac{dE}{dx})_{ion} = \frac{E_c}{X_0}$ . Pictures are taken from [10].

of a calorimeter. A reasonable parameterization of  $E_c$  obtained from experimental results [10] is given by

$$E_c = \frac{610}{Z + 1.24} \text{ MeV}, \quad \text{for liquids or solids} \quad (1.1)$$

$$E_c = \frac{710}{Z + 0.92} \text{ MeV}, \quad \text{for gases} \quad (1.2)$$

The shower development inside a material strongly depends on the value of  $E_c$ . Other parameters which are used to define the longitudinal and transverse sizes of a shower are respectively the radiation length and the Molière radius. The *radiation length*,  $X_0$ , is defined as the mean distance that an electron traverses to lose  $(1 - 1/e)$  of its energy by bremsstrahlung. It can be parameterized as

$$X_0 = \frac{716.4 \cdot A}{Z(Z + 1) \cdot \ln(287/\sqrt{Z})} \text{ gr/cm}^2 \quad (1.3)$$

where  $A$ ,  $Z$  are respectively the mass and the atomic numbers of material. Eq. 1.3 can be approximated to  $X_0 \approx 180 \cdot A/Z^2$  (in gr/cm). The mean distance traveled by a photon before converting to a  $e^-e^+$  pair with probability  $(1 - 1/e)$  is equal to  $\frac{9}{7}X_0$ . This means that if the incident primary particle is a photon, the shower will start to develop slightly later with respect to electrons. Nevertheless, in both cases, the mean longitudinal profile of the energy deposited by an electromagnetic shower can be described by a  $\Gamma$ -distribution function [9, 10] according to

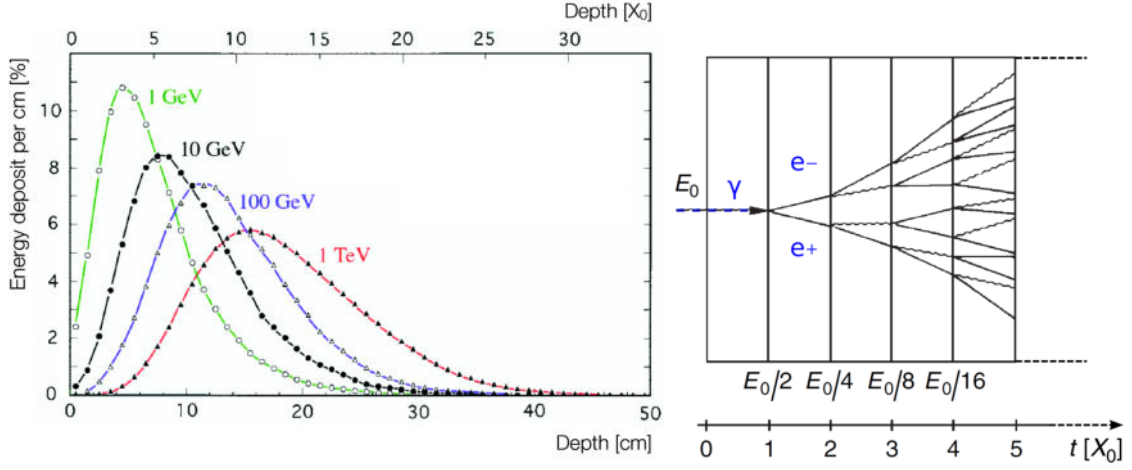


**Figure 1.2:** Left: Energy deposit for electrons of 1, 10, 100 and 1000 GeV as a function of depth in a block of copper; integrals are normalized to same value. Depth of shower maximum increases logarithmically with energy, according to Eq. 1.5. Picture is taken from [8]. Right: schematization of a shower development model.

$$\frac{dE}{dt} = E \cdot b \cdot \frac{(bt)^{\alpha-1} e^{-bt}}{\Gamma(\alpha)} \quad (1.4)$$

where  $t = x/X_0$ ,  $b \approx 0.5$ ,  $\alpha = bt_{max} + 1$  and  $t_{max}$  is the point where the distribution has its maximum.

The maximum of the energy deposited by the shower corresponds the position where the number of secondaries starts to decrease. The depth of this *shower maximum* moves logarithmically with the energy of incident particle as shown in Fig. 1.2, according to

$$t_{max} = \ln \left( \frac{E}{E_c} \right) \quad (1.5)$$

The energy of the electromagnetic shower is contained at 95% level within a distance  $L_{EM}(95\%)$  approximated by

$$L_{EM}(95\%) = X_0 \cdot (t_{max} + 0.08 \cdot Z + 9.6) \quad (1.6)$$

The shower develops also in the transverse direction, due to multiple scattering of electrons by nuclei's field (multiple Coulomb scattering). The transverse size of an electromagnetic shower is governed by the so called Molière radius,  $R_M$ , defined as

$$R_M = E_s \cdot \frac{X_0}{E_c} \quad (1.7)$$

where  $E_s = \sqrt{4\pi/\alpha} m_e c^2 = 21.2$  MeV. A simpler approximate expression for Eq. 1.7 is  $R_M \approx 7 \cdot A/Z$  (in gr/cm<sup>2</sup>). On average, 90% of shower energy is contained within a cylinder of radius  $R_M$ , 95% (99%) in a radius of  $2R_M$  ( $3.5R_M$ ) respectively. The Molière radius is an important parameter to be considered to define the transverse granularity of the calorimeter readout channels.

In case the absorber of the calorimeter is made of a mixture of materials with different  $X_0^i$  and  $R_M^i$  the effective radiation length  $X_0^{eff}$  and Molière radius  $R_M^{eff}$  can be calculated with

$$\frac{1}{X_0^{eff}} = \sum_i^N \frac{w^i}{X_0^i} \quad (1.8)$$

$$\frac{1}{R_M^{eff}} = \frac{1}{E_s} \sum_i^N \frac{w^i E_c^i}{X_0^i} \quad (1.9)$$

where  $w_i$  is the composition by weight and  $X_0^i$ ,  $E_c^i$ , the radiation length and the critical energy of the corresponding element respectively.

In most calorimeters, the total amount of energy,  $E_{visible}$ , responsible for signal production (scintillation light or charge) is proportional to the total energy loss of shower particles through ionization. Practically  $|dE/dx|_{ion}$  is constant with energy. Thus, the signal produced in a calorimeter is proportional to the total track length,  $T$ , traveled by the charged particles of the shower

$$E_{visible} \propto E_{ionization} = T \cdot \left| \frac{dE}{dx} \right|_{ion} \propto T \quad (1.10)$$

To estimate the track length and better understand the meaning of Eq. 1.4, we can assume that on average, electrons and positrons interact through bremsstrahlung after a distance  $X_0$ , and that a photon converts to a  $e^-e^+$  pair every  $X_0$ . This means that after traveling a distance  $t = x/X_0$  inside the calorimeter, the shower will consist of  $N = 2^t$  particles, with  $E/N$  energy per particle. Since the production of new secondaries stops typically when almost every particle in the shower has energy around  $E_c$ , the total particle multiplicity is roughly equal to  $E/E_c$ , and every particle has traversed on average a distance  $X_0$ . According to this modeling of the shower, represented in Fig. 1.2, the total track length inside the calorimeter is

$$T = X_0 \cdot \frac{E}{E_c} \quad (1.11)$$

Equations 1.10 and 1.11 clearly manifest the fundamental operation principle of a calorimeter: the produced signal is proportional to the energy of incident particles. From

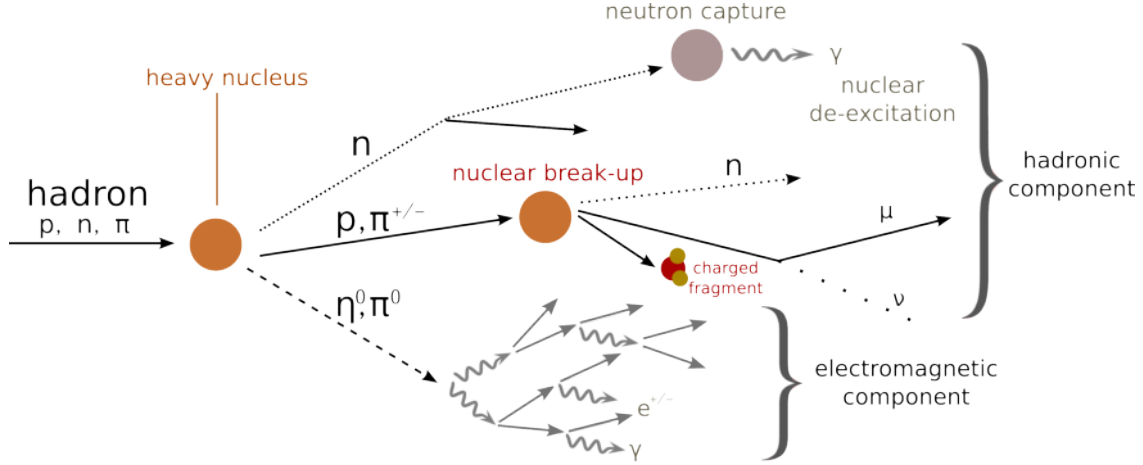


**Figure 1.3:** Schematic model of hadronic shower development. Incident hadron can interact through several processes leading to a largely different response of the calorimeter.

Eq. 1.5 and 1.6 it is also evident the reason why the size of an electromagnetic calorimeter has to scale logarithmically with the energy of incident particles it aims to measure, in order to avoid shower leakage and maintain its linear response.

### 1.1.2 Hadronic Shower Development

Due to their different nature, hadrons interaction with matter presents a significantly different behavior with respect to electrons and photons. As shown in Fig. 1.3, the incidence of a high energy hadron in a calorimeter produces a shower of particles due to inelastic collisions with nucleons of the absorber's nuclei [9, 11, 12]. The secondary particles which are produced via *strong interaction* are mainly pions ( $\approx 90\%$ ) and nucleons with a multiplicity which increases logarithmically with energy. On average  $\approx 30\%$  of produced pions are  $\pi^0$ 's, that subsequently decay into photons generating electromagnetic showers as described in Sec. 1.1.1. Charged hadrons ( $p, \pi^\pm, \mu$ ) also dissipate energy via elastic scattering and ionization. On the other hand, a large fraction of the hadron energy does not dissipate in particle production but is lost to break the nuclear binding energy and thus it does not contribute to detectable signal. Also neutrinos produced from secondary interactions do not deposit energy in the detector and represent an intrinsic source of non-detectable energy.

An important part of the shower is also made of neutrons which slow down via elastic scattering and once thermalized are subject to neutron capture by the nuclei. De-excitation of nuclei via emission of photons can yield a delayed detectable signal. An example of the average intensity of different components in a hadronic shower generated by 5 GeV protons in lead is reported in Table 1.1.

Physical process	Amount of Energy	Contribution
Ionization energy of charged particles ( $p$ , $\pi$ , $\mu$ )	1980 MeV	40 %
Electromagnetic shower ( $\pi^0$ , $\eta^0$ , $e$ )	760 MeV	15 %
Neutrons	520 MeV	10 %
Photons from nuclear de-excitation	310 MeV	6 %
Non-detectable energy (nuclear binding, neutrinos)	1430 MeV	29 %
Total	5000 MeV	100 %

**Table 1.1:** Example of contribution of different components to a hadronic shower generated by 5 GeV protons in lead. Results are obtained with Geant4 simulation tool.

For each incident hadron the shower development can differ significantly from each other due to the large fluctuations on the (small) number of  $\pi^0$ 's produced and their position along the shower development. This consequently yields large fluctuations of the energy deposition profile. However, similarly to electromagnetic showers a quantity describing the average longitudinal development of showers can be introduced. The so called *interaction length*,  $\lambda_I$ , is defined as the mean distance that a hadron traverses to lose  $(1 - 1/e)$  of its energy in inelastic collisions. It is given by the equation

$$\lambda_I = \frac{A}{N_{Av} \cdot \rho \sigma_{inel}} \text{ cm} \approx 35 \cdot A^{1/3} \text{ gr/cm}^2 \quad (1.12)$$

where  $A$  is the mass number of the material,  $\rho$  the density,  $N_{Av}$  the Avogadro number and  $\sigma_{inel}$  is the cross section of inelastic interaction for protons which scales as  $\propto A^{2/3}$ . The longitudinal profile of the energy deposition of a hadronic shower can be parameterized by a sum of functions with the form of Eq. 1.4 convoluted with a descending exponential, representing the purely electromagnetic and the purely hadronic component of the shower respectively. From experimental data the maximum of hadronic showers occurs at depth  $t_{max}^{had}$ , which is approximately:

$$t_{max}^{had} \sim 0.2 \cdot \ln E + 0.7 \quad (1.13)$$

and the total depth that is necessary to contain 95% of the shower energy is

$$L_{had}(95\%) \sim t_{max}^{had} + 2.5 \cdot \lambda_I \cdot E^{0.13} \quad (1.14)$$

with  $t_{max}^{had}$  in units of  $\lambda_I$  and  $E$  in GeV. The transverse development of a hadronic shower is determined by the mean transverse momentum of the produced particles, which is roughly  $\langle p_T \rangle \sim 0.35$  GeV. The transverse development does not scale with  $\lambda_I$ , however 95% of the shower energy is contained in a cylinder of radius  $R_{had} \simeq \lambda_I$ .

The signal generated by a hadronic shower is lower than that produced by an electro-

magnetic shower originated by an identical incident particle energy. This is due to the significant fraction ( $\approx 30\%$ ) of the total energy which is lost in nuclear break-up and excitation processes. This intrinsic difference, between the signal generated by hadrons and the signal generated by electrons of the same incident energy, represents an important property of a calorimeter and it is usually referred to as *degree of compensation* or *e/h ratio*. Such a quantity can change depending on the construction parameters like the choice of materials, the signal generation mechanisms and geometrical design. The *e/h* ratio is intrinsic to the nature of a particular calorimeter and does not depend on particle energy. It can be derived indirectly by the measurement of the  $e/\pi$  ratio defined as the ratio of the signal generated by electrons to the signal produced by charged pions of same energy. The relation between the two ratios, being energy dependent, is given by

$$\frac{e}{\pi}(E) = \frac{e/h}{1 + (e/h - 1) \cdot f_{em}(E)} \quad (1.15)$$

where  $f_{em}(E)$  is the average fraction of energy contributing to the electromagnetic component of a hadronic shower, mainly through  $\pi^0$ 's and  $\eta^0$ 's production. The  $f_{em}$  function evolves with energy as shown in Fig. 1.4. Energy dependence of  $f_{em}$  has been studied both experimentally and theoretically and can be approximated by the expression [7]

$$f_{em}(E) = 1 - \left( \frac{E}{E_0} \right)^{m-1} \quad (1.16)$$

in which  $E_0$  is in the range 0.7–1 GeV and  $m$  can vary between 0.8 and 0.9 depending on the material properties.

The higher complexity of hadronic showers development, as discussed in this section, is the reason why the achievement of good energy resolution in hadronic calorimeters is far more difficult with respect to electromagnetic ones.

### 1.1.3 Energy Resolution of Calorimeters

There are two major properties which define the response of a calorimeter: its proportionality to the energy of incident particle (*linearity*) and the precision of this measurement (*energy resolution*). The response of all calorimeters should have a linear behavior in the energy range of the particles it has to measure. In some cases, this is not a trivial task, especially for hadronic particles which are characterized by an energy-dependent  $f_{em}$ . Strategies to solve this problem, known as *compensation* techniques, will be discussed in Sec. 1.1.4.

The energy resolution of a calorimeter is affected by stochastic fluctuations which arise from different sources along the chain of probabilistic processes from energy deposition

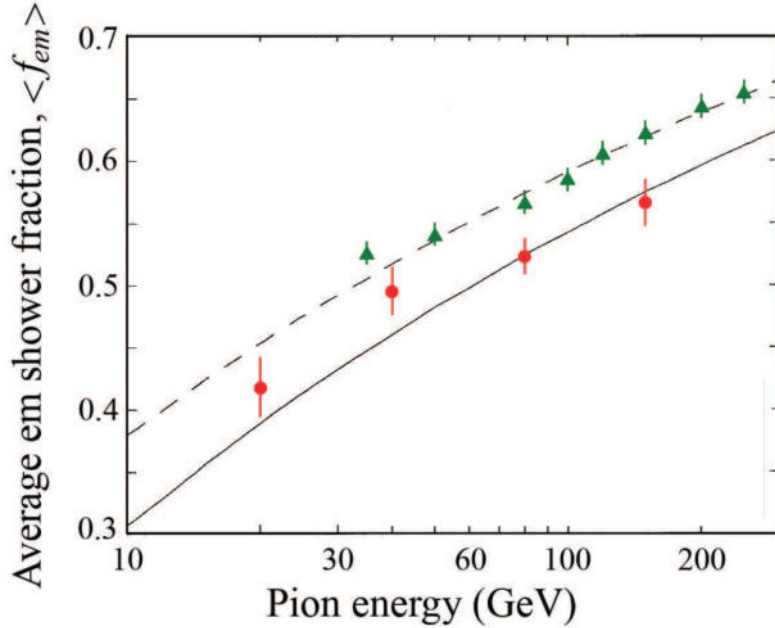


**Figure 1.4:** Evolution of electromagnetic component  $f_{em}$  of hadronic shower for lead (red dots) and copper (green triangles) as measured in [13, 14] superimposed with Eq. 1.16 with parameters  $m = 0.82$ ,  $E_0^{lead} = 1.3$  GeV,  $E_0^{copper} = 0.7$  GeV.

to signal generation and detection. The fluctuations of calorimeter response are related to particle energy and can be grouped into three main components, depending on their origin: a stochastic term  $A$  which scales as  $1/\sqrt{E}$ , a noise term  $B$  which scales as  $1/E$  and a constant term  $C$  which does not depend on energy. The energy resolution of a calorimeter can then be written as

$$\left(\frac{\sigma_E}{E}\right)^2 = \left(\frac{A}{\sqrt{E}}\right)^2 + \left(\frac{B}{E}\right)^2 + C^2 \quad (1.17)$$

where the three components can be affected by several sources, thus  $A^2 = \sum_i a_i^2$ ,  $B^2 = \sum_i b_i^2$  and  $C^2 = \sum_i c_i^2$ . Eq. 1.17 is a simplified way to parameterize the resolution as a function of energy. It is worth to notice that often, especially for non-compensating hadronic calorimeters (see Sec. 1.1.4), the measured distributions are non-gaussian and their behavior can differ from Eq. 1.17. A summary of common sources of fluctuations affecting the energy resolution of most calorimeters is presented in the following. In the design of a calorimeter, it is of fundamental importance to identify and to study these contributions in order to minimize them as much as possible.

## Stochastic Term

A list of common contributions to the stochastic term are:

- Shower fluctuations
- Photostatistics
- Sampling fluctuations
- Landau fluctuations
- Track length fluctuations
- Fluctuations of  $f_{em}$

In an ideal homogeneous calorimeter, the whole shower generated by incident particles is contained and perfectly converted into signal as shown in Fig. 1.5. In this case, the resolution is limited only by *shower fluctuations* which are intrinsic to fundamental probabilistic processes of the shower development, i.e. the stochastic fluctuations on the number of particles  $N$  which are generated

$$\frac{\sigma_E}{E} \propto \frac{\sigma_N}{N} \approx \frac{\sqrt{N}}{N} = \frac{1}{\sqrt{N}} \quad (1.18)$$

For electromagnetic showers the average number of particles produced scales with energy according to  $N \approx E/E_c$ , thus

$$\frac{\sigma_E}{E} = \frac{1}{\sqrt{N}} \propto \frac{1}{\sqrt{E}} \quad (1.19)$$

For common electromagnetic calorimeters the contribution of these fluctuations is around  $1\%/\sqrt{E}$ . This is not the case of hadronic calorimeters for which the intrinsic fluctuations are much larger ( $\approx 40\%/\sqrt{E}$ ) due to the small number of  $\pi^0$ 's produced in the early part of hadronic showers which is subject to large statistical fluctuations.

For detectors which convert deposited energy into light, the uncertainty on the number of photons  $N_{pe}$  converted into detected signal is responsible for additional fluctuations, usually referred to as *photostatistic fluctuations*. These are related to the processes of:

- photon production (e.g. scintillation or cherenkov);
- light collection (e.g. absorption, diffusion, wavelength shifting, light extraction);
- conversion of photons into electrical signal (e.g. efficiencies of photodetectors).

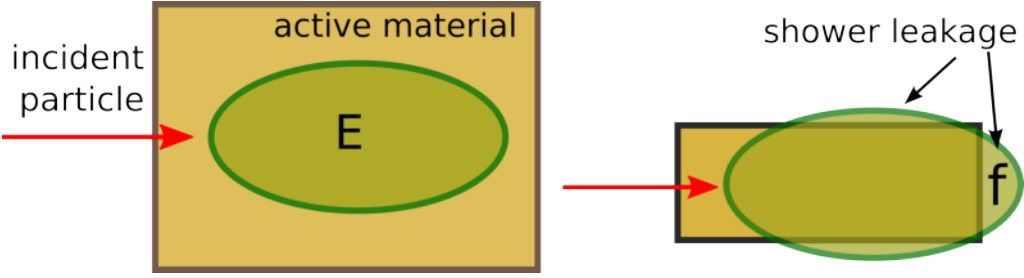


**Figure 1.5:** Left: schematic representation of a homogenous calorimeter in which the whole energy  $E$  deposited in the active medium is converted into detectable signal. Right: example of shower leakage  $f$  in a calorimeter of limited dimensions.

Photostatistic fluctuations decrease with the number of photons as

$$\frac{\sigma_e}{E} \propto \frac{\sigma_{N_{pe}}}{N_{pe}} \approx \frac{1}{\sqrt{N_{pe}}} \quad (1.20)$$

Since the number of photons produced is usually proportional to the energy deposited, these contributions decrease with energy according to  $\sigma_E/E \propto 1/\sqrt{E}$ . Photostatistic fluctuations are negligible for processes which generate a large number of photons (e.g. scintillators with high light yield) whereas they become a dominant contribution in Cherenkov based calorimeters in which the amount of light produced is rather low.

In case of non-homogenous calorimeters, in which only a fraction of the energy deposited by the shower is measured (see Fig. 1.6), additional *sampling fluctuations* arise. The number of secondary particles  $N_{sec}$  crossing the active layers of the detector is

$$N_{sec} = N_{max} \cdot (1 - t_{abs}) = \frac{E}{E_c} \cdot (1 - t_{abs}) \quad (1.21)$$

where the maximum number of particles produced is  $N_{max} = E/E_c$  and  $t_{abs}$  is the fraction of absorber thickness in unit of  $X_0$  wrt the total detector width. This introduces fluctuations on the measured energy which scale according to

$$\frac{\sigma_E}{E} \propto \frac{\sigma_{N_{sec}}}{N_{sec}} = \sqrt{\frac{E_c}{E(1 - t_{abs})}} \quad (1.22)$$

Eq. 1.22 suggests that this contribution can be reduced using materials with high  $Z$  (i.e. small  $E_c$ ) and increasing the sampling fraction (i.e. reducing  $t_{abs}$ ).

Due to multiple scattering, particles in the shower traverse the calorimeter volume at different angles and “see” a different effective absorber thickness

$$t_{abs}^{eff} = \frac{t_{abs}}{\cos \theta} \quad (1.23)$$

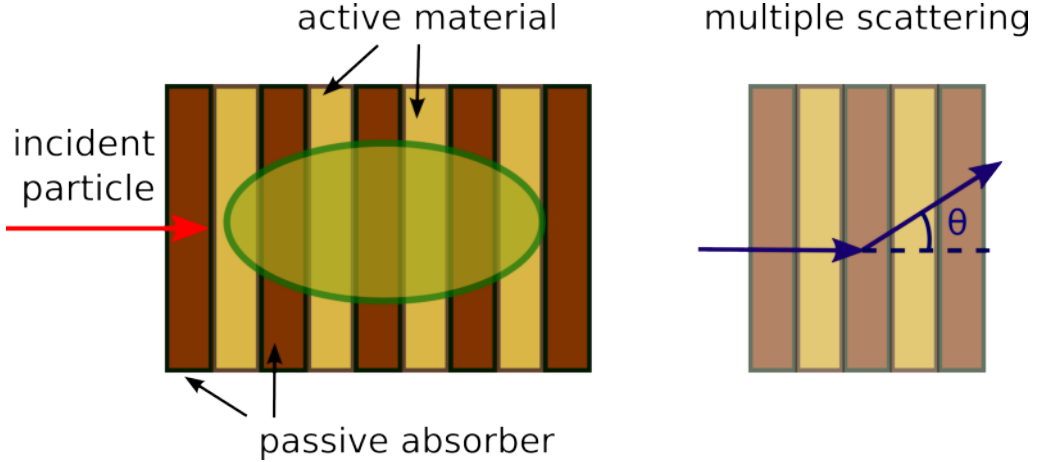


**Figure 1.6:** Left: schematic representation of a sampling calorimeter in which only a fraction of the energy is deposited in the active medium (yellow layers) and converted into detectable signal. Right: example fluctuations in the effective absorber thickness  $t_{abs}^{eff}$  due to the angle  $\theta$  of shower particles after multiple scattering.

where  $\langle \cos \theta \rangle \simeq \cos [E/(\pi E_c)]$ . For this reason, event-by-event fluctuations around the mean value of  $\theta$  result in *track length fluctuations*. Furthermore, asymmetric distributions of energy deposits in thin active layers (Landau instead of Gaussian distribution) is the cause for *Landau fluctuations*

$$\frac{\sigma_E}{E} = \frac{1}{\sqrt{N_{sec}}} \cdot \frac{3}{\ln(k \cdot \delta)} \quad (1.24)$$

where  $k = 1.3 \cdot 10^4 \text{ MeV}^{-1}$  and  $\delta$  is the average energy loss in active layers in MeV. These fluctuations are discussed in detail in [15] and are negligible for calorimeters made of liquid or solid sensitive material, whereas for gaseous calorimeters they could contribute up to 5% to 10% per  $\sqrt{E}$ .

In addition to the sources of fluctuations mentioned so far, hadronic showers present further complications. As previously discussed, they are composed by a purely electromagnetic part and a purely hadronic one, with a relative ratio approximated by the function  $f_{em}(E)$  which increases with energy as shown in Fig. 1.4. The intrinsic difference in the response of a calorimeter to these different components of hadronic showers is expressed by the  $e/h$  ratio. Deviations of  $e/h$  from 1 represent different efficiency to convert deposited energy into visible signal, depending on the type of particles in the shower. Large and non Poissonian *fluctuations in the electromagnetic fraction*  $f_{em}$  affects the energy resolution in a way which depends on  $e/h$ . As a result, in typical calorimeters the hadronic response function is non-Gaussian, the hadronic signals are non-linear, and the hadronic energy resolution exhibits substantial deviations from  $1/\sqrt{E}$  scaling [16].

### Noise Term

The electronics devices used for the generation of electrical signal are usually characterized by intrinsic noise fluctuations which can arise for different reasons. An unavoidable source of electronic noise at room temperature is the *thermal noise* which is due to thermal agitation of the charge carriers (usually the electrons) inside an electrical conductor at equilibrium, which happens regardless of any applied voltage. This fluctuation adds up to the signal in a way which does not depend on particle energy ( $\sigma_E^{noise} = B$ ). Its contribution to the total resolution thus decreases when the intensity of the signal  $S$  gets higher, improving the  $S/N$  ratio.

### Constant Term

Typical sources of constant term can arise from shower leakage and spatial non uniformity of response. In the majority of calorimeters, due to their limited size, the showers are not fully contained. A fraction of the shower can escape from the sides or from the back of the detector leading to *transverse* and *longitudinal shower leakage* respectively. This fraction fluctuates event by event and slightly depends on energy due to the change in the position of the shower maximum. In a first approximation, its contribution to the energy resolution can be parameterized as

$$\frac{\sigma_E}{E} \simeq \left( \frac{\sigma_E}{E} \right)_{f=0} \cdot [1 + 4f] \quad (1.25)$$

where  $f$  is the average fraction of shower leaking out of the calorimeter [5].

Another source of constant term affecting common calorimeters is the *spatial non uniformity of the response*, i.e. the fact that signal generated by an incident particle can vary depending on the position where the particle hits the calorimeter. For example, in sampling calorimeters, this is often related to variations of sampling fraction within the detector volume. It can also be related to a non-uniformity of light or charge collection efficiency across the active material volume.

More in general, all non statistical fluctuations contribute to the constant term of the resolution of a calorimeter. Construction defects, material inhomogeneity, calibration errors, non linear response of electronics etc., cause resolution degradation which is difficult to estimate in advance and which usually scales with energy as  $\sigma_E^{noise} = C \cdot E$ .

### 1.1.4 Considerations on Hadronic Calorimeters

Although in principle, a unique calorimeter can be designed to detect both electromagnetic and hadronic particles often, for practical reasons, it results more convenient to split the detection of particles into separate electromagnetic and hadronic sections.

Because of the relatively compact volumes required to contain an electromagnetic shower and its smaller intrinsic fluctuations, it is easier to achieve a better energy resolution for electromagnetic particles than for hadrons. For instance, homogeneous calorimeters, as the one discussed in Sec. 2.2.3, can provide a very precise measurement of energy for electrons, positrons and photons. On the other hand, the large volumes required to contain hadronic showers, for cost reasons, set stringent requirements on the technology that can be used to instrument them. This requires the development of cheaper and more sophisticated techniques to achieve very precise measurements of hadrons energy. The performance of sampling calorimeters, which represent the simplest way to instrument big volumes (by means of a cheap absorber interleaved with active layers), is strongly limited by the large intrinsic fluctuations of hadronic showers described earlier.

In addition to the measurements of single hadrons, hadronic calorimeters are also supposed to measure *jets* with a good precision. Jets are complex objects made of a mixture of particles (hadrons, neutrons, electrons, photons, muons) originating from the interaction of partons during the hadron-hadron collisions. A good precision of their energy scale and transverse momentum resolution is of crucial importance for many physics analyses [17] and represent a big challenge for hadronic calorimeters. Further considerations on the performance of hadronic calorimeters are discussed below and possible strategies to improve their performance are presented.

## Compensation

As previously stated (Sec. 1.1.2), a peculiarity of hadronic calorimeters is that their response differs for electromagnetic and hadronic particles due to the intrinsic properties of the detector which define the *e/h ratio*. The  $e/h$  value cannot be directly measured but can be derived from the  $e/\pi$  signal ratios, measured at various energies. In practice, since invisible-energy losses in the non-em component are naturally leading to  $e/h$  values larger than 1, most calorimeters have typical  $e/h$  ratios between 1.5 and 2.0 and they are called *undercompensating*. If particular conditions are satisfied, however, calorimeters can have  $e/h < 1$  and are referred to as *overcompensating*. Since  $f_{em}$  increases with energy, according to Eq. 1.15, both type of calorimeters will show non-linear response to hadrons. Since linearity is a fundamental requirement for calorimetric measurements it is important to understand how it can be restored.

The basic idea of *compensation* is to design a sampling calorimeter whose  $e/h$  ratio is forced to be equal to 1 by means of an appropriate choice of geometry and active materials. To properly tune the  $e/h$  ratio, it is important to take into account the contribution of different particles to the calorimetric signal. The calorimeter response to hadrons,  $h$ , arises from different components

$$h = f_{ion} \cdot I + f_n \cdot N + f_\gamma \cdot \Gamma + f_B \cdot B \quad (1.26)$$

where  $f_{ion}$ ,  $f_n$ ,  $f_\gamma$ ,  $f_B$  are respectively the fraction of ionizing particles, neutrons, photons from nuclear reactions and nuclear binding energy inside a certain hadronic shower and  $I$ ,  $N$ ,  $\Gamma$ ,  $B$  are the responses of the calorimeter to that type of particle. By a proper choice of active materials and sampling fraction, the relative response of the calorimeter to different particles can be tuned to correct for invisible energy losses.

One of the easiest way, used in most of the compensating calorimeters, is based on the amplification of the neutron signal  $N$ . In hadronic showers an important role is played by neutrons which typically carry not more than  $\approx 10\%$  of the non-em shower energy (i.e.  $f_n < 0.1$ ). However, their contribution to the calorimeter signal may be much larger than that. This can be achieved because at the relatively low energies of neutrons in hadronic showers, the main process involved in the energy loss of neutrons is elastic scattering. In this process, the transferred energy fraction is on average

$$f_{elastic} = \frac{2A}{(A+1)^2} \quad (1.27)$$

where  $A$  is the atomic number of the target nucleus. In hydrogen, this  $f_{elastic}$  is 50%, in lead it is 100 times smaller. Therefore, in a sampling calorimeter made of 50% lead and 50% hydrogen, neutrons with energy in the MeV-range, will transfer 98% of their kinetic energy to hydrogen nuclei, and only 2% to lead. This example shows how it is possible to amplify the response to neutrons  $N$  (with respect to charged shower particles depositing the same amount of energy), to compensate for the invisible-energy losses.

## Dual Readout

Hardware compensation techniques allow to restore the linearity of response to hadrons. However, other approaches exist consisting in an event-by-event software compensation of  $f_{em}$  fluctuations. A possible strategy which has been explored in detail by the DREAM collaboration is the *dual readout technique* [16]. This method exploits the fact that production of Cherenkov light in hadronic showers is mostly due to the electromagnetic component (see Sec. 1.3). This occurs because electrons and positrons produced in the em showers are relativistic down to  $\approx 0.2$  MeV, while the spallation protons dominating the non-em

calorimeter signals are typically non-relativistic.

By simultaneously measuring the scintillation signal,  $S$ , proportional to the total energy deposited by ionizing particles, with the Cherenkov light,  $C$ , emitted in a hadronic shower, it is possible to determine the  $f_{em}$  event by event. For a given hadronic shower, generated by a particle of energy  $E$ , having an electromagnetic fraction  $f_{em}$ , the signals originated by the two different mechanisms can be written as

$$S \propto E \cdot (f_{em} + (1 - f_{em}) \cdot h/e|_s) \quad (1.28)$$

$$C \propto E \cdot (f_{em} + (1 - f_{em}) \cdot h/e|_c) \quad (1.29)$$

where  $h/e|_s$  and  $h/e|_c$  represent the  $h/e$  ratios of the scintillator and cherenkov calorimeter structures, respectively. Calculating the ratio of Eq. 1.28 and 1.29 we obtain

$$\frac{C}{S} = \frac{f_{em} + h/e|_c(1 - f_{em})}{f_{em} + h/e|_s(1 - f_{em})} \quad (1.30)$$

Once the values of  $h/e|_s$  and  $h/e|_c$  are experimentally determined via Eq. 1.15, it is possible to calculate the  $f_{em}$  of the shower event-by-event and to correct for it. If this correction is applied, the energy distributions become much more Gaussian, the linearity of response is restored and the energy resolution improves.

## Particle Flow

Another option to improve resolution to jets, is the *particle flow approach* which aims to identify and reconstruct the energy of all the particles originated in hadron collisions [18]. A key requirement for detectors, in order to efficiently apply this technique, is the combined use of a precision tracker and a highly-granular calorimeter. In this way, charged jet fragments can be precisely measured with the tracker, while the energy of the neutral particles (photons, neutrons) would be measured with the calorimeter. High granularity would then allow to separate energy deposits originating from different particles, improving particle identification. However, a limitation of this approach is the risk of *double counting* the energy of charged hadrons. This can occur because their energy is usually measured with the tracker but they also deposit energy in the calorimeters. Separation of their contribution from the total calorimetric signal (which includes also photons and neutrons) it is not a trivial task.

Particle flow algorithms have been successfully used to improve the resolution of jets at LEP [19] and at the LHC, for instance by the CMS Collaboration [20]. Important developments on future calorimeters which are designed to optimize this approach are

being carried on by the CALICE Collaboration [21]. It is worth to notice that dual readout and particle flow approaches do not exclude each other. In principle, it is possible to design a highly granular calorimeter with dual readout capabilities and which makes use of particle flow algorithms to improve the overall performance.

## 1.2 The Scintillation Mechanism

The *scintillation mechanism* is usually referred to as a general process converting energy deposited by ionizing radiation into a light signal (i.e. optical photons). This can occur in different ways depending on the particular nature of the material involved. A wide variety of scintillators are currently used for different applications. Scintillators can be in solid, liquid or gaseous physical state and are commonly divided into two main categories based on their composition: organic and inorganic scintillators.

The *organic scintillators* are made of aromatic hydrocarbon compounds which contain benzene ring structures bounded in various ways (anthracene, stilbene, naphthalene). In these materials the light is emitted as a consequence of transitions made by the free valence electrons of the molecules which occupy the molecular orbitals. This process, being very fast, leads to a luminescence which typically decays within few nanoseconds. For this reason they are mostly used for applications which require a fast response such as time tagging or time of flight measurements. Organic plastic scintillators (in which the primary fluorescent emitter is suspended in a solid polymer matrix) are largely used also because of their ability to be easily shaped and their relatively low cost.

*Inorganic scintillators* are usually crystals grown in high temperature furnaces, for example alkali metal halides, often with a small amount of activator impurity. In this case, the scintillation process is due to the electronic band structure which characterizes crystals and it is not molecular in nature as in the case of organic scintillators. One particular advantage of this type of scintillators is their high density which provides a good stopping power for incident radiation. This allows to contain and convert the whole particle energy into light signal providing a very precise measurement of their energy.

### 1.2.1 Scintillation Mechanism in Inorganic Scintillators

Five steps can be identified in the scintillation mechanism of inorganic crystals as summarized in Fig. 1.7. The first step is the *absorption of ionizing radiation* with the creation of electronic excitations. For very high incident particle energy, the excitations are essentially deep holes  $h$  created in inner-core bands and hot electrons  $e$  in the conduction band.

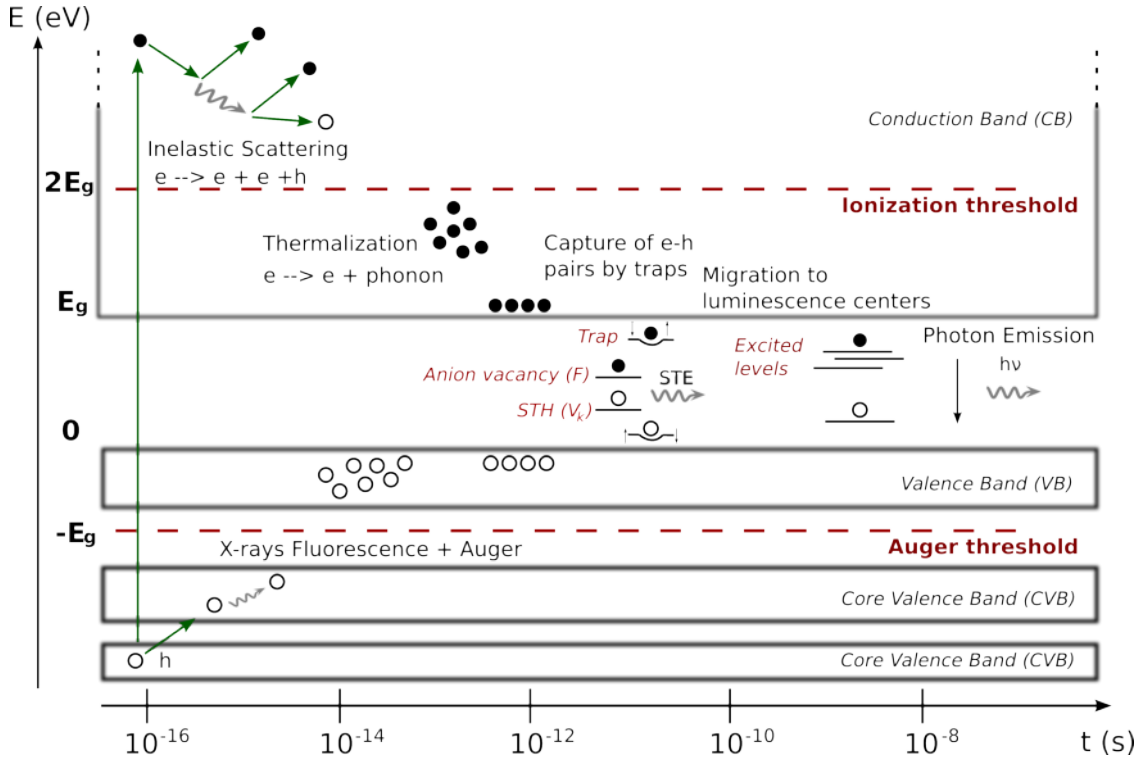


**Figure 1.7:** Schematic representation of the scintillation mechanism in an inorganic scintillator with core valence band (CVB), valence band (VB) and conduction band (CB). The process is shown as a function of time and show the evolution of particle energy during the several processes ( $e$  for electrons,  $h$  for holes,  $ph$  for phonons,  $h\nu$  for photons,  $V_k$  for self-trapped holes,  $F$  for anion vacancies).

In a very short time scale ( $10^{-16}$ - $10^{-14}$  s), a large number of secondary electronic excitations are produced through inelastic electron-electron scattering and Auger processes with creation of electrons in the conduction band and holes in core and valence bands. The energy of secondaries decreases during this *relaxation* process until it falls below the *ionization threshold* ( $2E_g$ ) and the avalanche process stops. At this point, all electrons in the conduction band have an energy smaller than  $2E_g$  and all holes occupy the valence band if there is no core band lying above the Auger process threshold (general case).

Secondaries are unable to produce further ionization and they can lose their energy only through interaction with the vibrations of the lattice, producing phonons. This process, called *thermalization*, ends when electrons have reached the bottom of the conduction band and holes have reached the top of the valence band. All the energy dissipated non-radiatively and converted into phonons during this process is lost since it cannot contribute to the scintillation signal.

The next stage is characterized by the *migration* of the excitations through their interaction with stable defects (anion vacancies  $F$ ) and impurities of the material. In case of shallow traps, close to the conduction (or valence) band, charge carriers can get trapped and

subsequently be released because of thermal agitation. Though, this process involves a delay in the scintillation process, these carriers can still take part to the recombination process. Due to charge carriers interaction with the phonons of the lattice, many ionic crystals show a phenomenon of localization of the valence holes in a regular lattice which yields to the creation of  $V_K$  centers where a hole can be trapped (self-trapped hole STH). It can then occur that self-trapped excitons (STEs) are formed through the capture of free electrons by  $V_K$  centers and subsequently decay emitting a photon.

The last step of the scintillation process is the *recombination* of electron-hole pairs and the consequent emission of photons (radiative recombination) or phonons (non-radiative recombination). Radiative recombination can be *direct* if it occurs between the direct bandgap of a semi-conductor. In this case, when the electron-hole pair with energy close to  $E_g$  binds together to form an exciton it then recombines emitting a photon with energy  $E = h\nu$ . Most scintillators are so called extrinsic since their matrix does not have sufficient scintillating properties. To enhance the probability of radiative recombination, in this case, a dopant element which acts as a luminescent center is inserted into the matrix. These activators are usually rare earth ions (like  $\text{Ce}^{3+}$ ) because of the parity and spin-allowed transition  $4f^{n-1}5d \rightarrow 4f^n$ . Since for most of the host matrices the ground state ( $4f$ ) and the lowest excited level ( $5d$ ) lies in the band gap, the radiative recombination is probabilistically favoured due to smaller energy gap. Recombination through this doping centers are therefore favored from the energetic point of view. Electrons and holes can also recombine non-radiatively by interacting with the lattice of the crystal, emitting phonons. In this case the energy is dissipated thermically and does not contribute to the optical signal. The probability of non-radiative recombination increases with temperature due to larger vibrations of the lattice whereas at  $T = 0$  K only radiative recombinations can occur.

### 1.2.2 General Characteristics of Inorganic Scintillators

From the scintillation process described above, it is clear that each crystal will have a different behavior depending on its physical properties (band structure, defects concentration, etc.). For a given application, it is important to choose a scintillator with optimal scintillation properties. The most important characteristics which are often used to compare inorganic scintillators are briefly discussed in the following.

#### Light Yield

Of crucial importance, is the capability of a scintillator to convert the energy deposited by ionizing radiation into optical signal. It is therefore fundamental that the amount of light generated is as large as possible in order to be efficiently detected and converted into

an electrical signal, usually by means of a photodetector. This property, called *light yield*, is defined as the number of photons produced per MeV of deposited energy  $E_{dep}$

$$LY = \frac{n_{photons}}{E_{dep}} = \frac{E_{dep} \cdot \eta}{\langle h\nu \rangle \cdot E_{dep}} = \frac{\eta}{\langle h\nu \rangle} \quad (1.31)$$

where  $\langle h\nu \rangle$  is the average energy of emitted optical photons and  $\eta$  the overall conversion efficiency. This number depends on the efficiency of energy conversion during the various processes of scintillation, from pair production to light emission. The number of electron-hole pairs generated depends on the energy  $\xi_{eh}$  required to create them via the equation

$$N_{eh} = E_{dep}/\xi_{eh} \quad (1.32)$$

where  $\xi_{eh}$  is related to the band-gap  $E_g$  of the scintillator

$$\xi_{eh} = \beta \cdot E_g \quad (1.33)$$

and the numerical coefficient  $\beta$  is around 1.5–2 for ionic crystals. Considering inefficiencies in the process of charge carriers migration to the luminescences centers and the quantum efficiency of photon emission, an additional factor  $\alpha$  will contribute to the total efficiency. Thus, the overall conversion efficiency from energy to light can be written as

$$\eta = \frac{\alpha}{\beta} \cdot \frac{\langle h\nu \rangle}{E_g} \quad (1.34)$$

From Eq. 1.34 it can be observed that crystals with larger  $\langle h\nu \rangle/E_g$  ratio can have, in principle, a higher scintillation efficiency.

## Time Response

The time distribution of emitted photons is also relevant for most applications. It is usually important to have a fast signal, especially for calorimetry applications, in order to allow operation at high rates without being affected by signal pileup effects. The intensity of emission  $I(t)$  rises exponentially with a *rise time constant* which is very fast ( $\approx 10^{-11}$  s) due to the short duration of the first steps of the scintillation process (i.e. e-h pairs creation and migration to the luminescence centers). Once all the luminescence centers are filled, the emission is close to its maximum and starts to decrease with an exponential behavior which depends on the number of luminiscence centers  $N$ , their relative intensity  $P_i$  and their decay (rise) time constants  $\tau_{d,i}$  ( $\tau_{r,i}$ ). The general formula [22] describing the probability density function of scintillation photons to be emitted at a time  $t$  after the beginning of the scintillation process at time  $\Theta$  is

$$P(t|\Theta) = \sum_i^N P_i \frac{1}{\tau_{d,i} - \tau_{r,i}} \times \left[ e^{-\frac{t-\Theta}{\tau_{d,i}}} - e^{-\frac{t-\Theta}{\tau_{r,i}}} \right] \quad (1.35)$$

where for most of the crystals  $\tau_{r,i} \ll \tau_{d,i}$  and the maximum of emission occurs at  $t \approx \Theta$ . In case several luminescence centers ( $> 3$ ) with similar  $\tau_{d,i}$  are involved, the time distribution loses its exponential behavior and estimation of the different components becomes crucial. A more practical quantity  $\tau^{eff}$ , can be defined as the time interval containing a fraction  $(1 - 1/e)$  of the scintillation light

$$\frac{\int_0^{\tau^{eff}} I(t)dt}{\int_0^{\infty} I(t)dt} = \left(1 - \frac{1}{e}\right) \approx 63\% \quad (1.36)$$

Such quantity, regardless of the specific kinetic of the color centers, gives an indication of the time response and allows to compare the time response of different scintillators.

## Optical Properties

In order to be detected the light emitted has to reach the photodetector and to produce an electrical signal. For this reason it is very important to understand the processes occurring from the point of emission of a photon to its detection. These processes are mainly *absorption*, Fresnel reflections and Rayleigh scattering. Their relative probability depends on the bandgap width, the refractive index  $n$  of the material and the amount of impurities in the lattice which can result in the creation of absorption and scattering centers. A way to quantify these two effects is to measure the *transmission* of a crystal, i.e. the fraction of direct light which is transmitted inside the crystal. Since these effects show a dependence on the wavelength,  $\lambda$ , the transmission is usually measured by mean of spectrophotometers which provide a light beam of variable wavelengths. By comparing the intensity of the light before and after it traversed a certain thickness inside the crystal, it is possible to estimate the fraction of photons which has been absorbed or diffused. Transmission measured using spectrophotometers has to take into account Fresnel reflection which set an upper limit to the maximum transmission given by

$$T_{th}(\lambda) = \frac{(1-r)^2}{1-r^2} \quad (1.37)$$

where  $r$  is the reflection coefficient related to the refractive index  $n(\lambda)$  according to

$$r(\lambda) = \left| \frac{n(\lambda) - 1}{n(\lambda) + 1} \right|^2 \quad (1.38)$$

By comparing the measured transmission  $T_{meas}$  with Eq. 1.37 the intrinsic absorption coefficient of a crystal can be defined as

$$\mu_0(\lambda) = \frac{1}{L} \ln \left( \frac{T_{th}}{T_{meas}} \right) \quad (1.39)$$

where  $L$  is the length of the crystal which is traversed by the light beam.

### Emission Spectrum

The bandgap of the host matrix as well as the band structure of activators in extrinsic scintillators, will define the wavelength distribution of emitted photons, usually referred to as *emission spectrum*. This property of scintillators has to be taken into account when the signal has to be detected by mean of photosensors whose efficiency of converting light into electrical signal is  $\lambda$ -dependent. In particular to optimize the detection of photons, it is important that the quantum efficiency of the photosensors is sufficiently high in the range of wavelengths close to the maximum of emission. Inorganic scintillators usually display wide luminescence bands because the photon assisted transitions are broadened due to the strong interaction of carriers with phonons of the lattice.

### Phosphorescence

A feature which characterizes some scintillators is a long-time luminescence with decay constants of several microseconds and more which is usually called *phosphorescence* or *afterglow*. This effect is due to the thermal release of electrons and holes from traps, i.e. defects and impurities in the crystal lattice as well as defects induced by irradiation. The intensity of phosphorescence  $J(t)$  usually decreases exponentially with a time constant  $\tau_s$  which represents the probability of a charge carrier to be released. Considering a charge carrier trapped in a potential well of energy  $E$ , the probability to escape from the well at a temperature  $T$  is

$$\propto e^{-E/k_b T} \quad (1.40)$$

with  $k_b$  is the Boltzmann constant equal to  $8.617 \times 10^{-5}$  eVK $^{-1}$  [23]. The intensity of afterglow (valid for  $\tau_s \gg \tau_{d,i}$ ) can be described by the equation

$$J(t) = \frac{k_b N}{\tau_s} e^{-\frac{t}{\tau_s}} \quad (1.41)$$

in which  $k_b N$  is the number of photons emitted by luminescence centers which are excited by electrons released from traps.

Depending on the particular band structure (relative position of traps and color centers energetic levels), trapped carriers can also migrate to neighbouring luminescence center due to tunnelling effect. The tunnelling effect has a temperature-independent probability to occur which yield the following equation for the concentration of trapped electrons at time  $t$  [24]

$$N(t) = \frac{N(0)}{1 + N(0) \frac{\pi a^3}{6} \ln^3(vt)} \quad (1.42)$$

where  $N(t)$  and  $N(0)$  are the concentration of electron defects at time  $t$  and 0 respectively and  $a = h/2\pi[2m(U_{max} - E)]^{1/2}$  with  $m$  the mass of the electron and  $(U_{max} - E)$  the difference between the potential barrier and the center energy.

### Radiation Hardness

Even if scintillators are designed to measure ionizing radiation, the interaction of this radiation with crystals invariably creates new traps and defects. As shown in Fig. 1.8, defects can be of different nature. As a consequence, the properties of the scintillator can degrade in the following ways:

1. An increase in the number of shallow traps enhances the phosphorescence.
2. The formation of new traps acting as color centers can result in new absorption bands which absorb the photons emitted in the scintillation process, lowering the detectable light.
3. New defects in the crystal structure can decrease mobility of charge carriers and the efficiency of e-h pair to recombine in luminescence centers, reducing the light yield.
4. Direct interaction of radiation with luminescence centers can modify the characteristics of emitted light such as emission peak and decay time.
5. High energy hadrons (protons, neutrons, etc.) can activate the scintillator material leading to induced radioactivity which results in additional background phosphorescence.

Radiation hardness can be considered as the capability of a material to maintain its scintillating properties unchanged after irradiation. Hence it is not a well defined quantity but requires to be studied in details under several aspects. In the majority of inorganic scintillators, the main effect of radiation damage consists in loss of transmission. For calorimetry applications also the increase of phosphorescence can represent a crucial problem to deal with, as discussed in detail in Chap. 4.

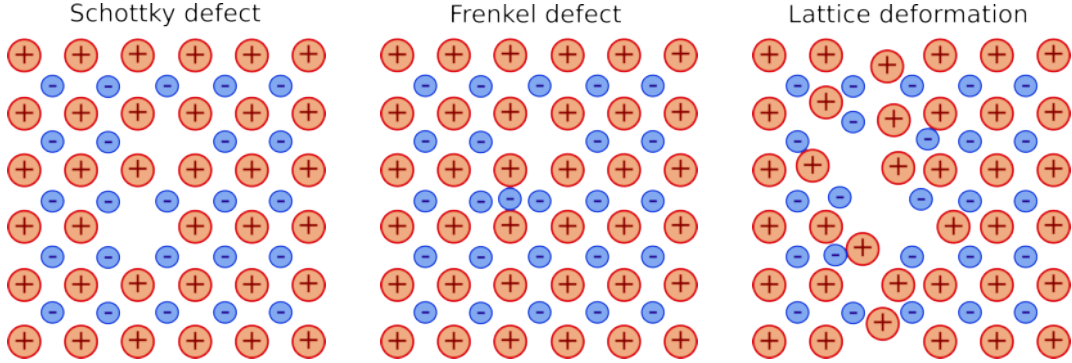


**Figure 1.8:** Schematic representation of most common lattice defects. Schottky defects (left) are formed when oppositely charged ions leave their lattice site, creating vacancies. Frenkel defects (center) occur when an atom or cation leaves its place in the lattice, creating a vacancy, and becomes an interstitial by lodging in a nearby which is not usually occupied by an atom. These defects can create additional absorption bands in the crystal [23]. Interaction of energetic hadrons with the crystalline structure can also create cluster of defects and distortion of the lattice (right) which in addition to absorption centers, introduce scattering centers which diffuse the light through Rayleigh scattering [25].

### 1.3 The Cherenkov Effect

As introduced at the beginning of this section, a technique used in calorimetry to produce an optical signal proportional to the particle energy is based on the *Cherenkov effect*. This phenomenon was detected for the first time in the 1934 by the scientist Pavel Alekseyevich Cherenkov, who formulated a first explanation of it.

The Cherenkov radiation is generated when a charged particle travels in a medium with velocity higher than the light velocity in that medium. In this case a polarization of the atoms along the particle trajectory occurs. If  $\beta = v/c$  is the velocity of the particle and  $n$  the refractive index of the medium, Cherenkov photons are emitted if

$$\beta > \frac{1}{n} \equiv \beta_{threshold} \quad (1.43)$$

with angle of emission  $\theta_c$ , relatively to the axis of motion of the particle, defined by

$$\cos \theta_c = \frac{1}{n\beta} \quad (1.44)$$

as shown in Fig. 1.9. As an example, for quartz, having  $n = 1.45 - 1.55$  in the range of  $\lambda = 600 - 200$  nm, the threshold velocity is  $\beta_{threshold} = 0.65 - 0.69$  and the angle of emission is  $\theta_c = 46^\circ - 50^\circ$ .

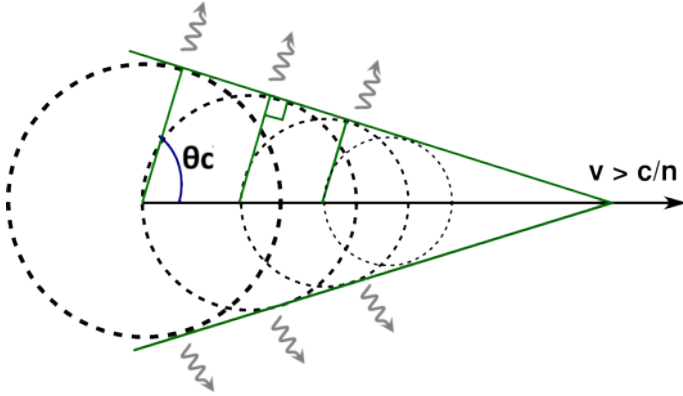


**Figure 1.9:** Schematic representation of Cherenkov light production for a charged particle with velocity  $v$  moving in a medium having refractive index  $n$ . Light is emitted at an angle  $\theta_c$  according to Eq. 1.44.

The number of photons that are emitted per unit wavelength and per unit path length in the medium is given by the following equation

$$\frac{d^2N_{ph}}{dLd\lambda} = 2\pi\alpha z^2 \frac{\sin^2\theta_c}{\lambda^2} = 2\pi\alpha z^2 \frac{1}{\lambda^2} \cdot \left(1 - \frac{1}{n^2\beta^2}\right) \quad (1.45)$$

where  $\alpha = 1/137$ ,  $z$  is the charge of the particle in units of  $e$ ,  $\lambda$  the wavelength of the photon and  $dL$  the path length in the medium. From Eq. 1.45 it can be noticed that light is emitted mostly in the UV region due to the  $1/\lambda^2$  production dependence. It is worth to notice that number of Cherenkov photons emitted is much lower with respect to number of photons produced in typical scintillation processes for the same amount of deposited energy. Another important feature of Cherenkov light is the non-isotropic nature of the process. The emitted photons are produced along a cone with opening angle  $\theta_c$  with respect to the trajectory of the particle. This represent an important difference with respect to scintillation light and has consequences on the choice of the geometry of Cherenkov-based calorimeters [5]. One of the advantage of Cherenkov light, which makes it of particular interest for application at high rates like those required by collider experiments, is its very fast emission. The Cherenkov effect occurs practically simultaneously with the passage of particles and the width of the produced signal is much shorter than time constants involved in most scintillation processes [5, 6, 7]. In addition, the Cherenkov effect has a production threshold which is given by Eq. 1.43. This threshold can be expressed in term of energy using the relativistic equation

$$E = mc^2 = \frac{m_0c^2}{\sqrt{1 - \frac{v^2}{c^2}}} = \frac{E_{rest}}{\sqrt{1 - \beta^2}} \quad (1.46)$$

where  $m_0$  and  $E_{rest}$  are respectively mass and the energy of the particle at rest. Using Eq. 1.43 and Eq. 1.46 we can obtain the kinetic energy corresponding to the Cherenkov

threshold as

$$(KE)_{rest} = (E - E_{rest}) = E_{rest} \left[ \frac{1}{\sqrt{1 - \beta_{threshold}^2}} - 1 \right] \quad (1.47)$$

It is worth to remark a characteristic feature of quartz fiber calorimeters. From Eq. 1.45, we see that the particles of higher velocities produce more light and so their contribution to the total signal will be larger. In other words this means that a calorimeter which is based on quartz fibers is sensitive mainly to the core of the shower [5, 6, 7] since this part consists of charged particles with relatively larger energies and velocities. On the other hand the calorimeters that are based on  $dE/dx$  technique are mainly sensitive to the charged particles of the shower with lower energies. Consequently the visible transverse size of electromagnetic and hadronic showers in quartz fiber calorimeters appears narrower if compared to the size of showers visible by  $dE/dx$  calorimeters.

# The CMS Experiment at the Large Hadron Collider

---

The Large Hadron Collider (LHC), built near Geneva (Switzerland), represents the more recent part in the long history of particle physics research carried out at CERN (Conseil Européen pour la Recherche Nucléaire). CERN was founded in 1954 with 12 member states [26]. Two years later in 1959 the Proton-Synchrotron (PS), being the first proton accelerator with the ability to accelerate protons up to an energy of 28 GeV, was built. At the beginning of the 70's the CERN success story moves forward, starting with the discovery of neutral currents in the Gargamelle-bubble chamber in 1973 [27, 28]. In the following years, new more energetic machines were built leading to the discovery of the W and Z boson (1983) [29, 30]. The Super Proton Synchroton (SPS) accelerating protons up to 300 GeV was built in 1976 and the Large Electron Positron (LEP) with a circumference of 27 km was finalized in 1989. LEP ends its operation in November of 2000 clearing the way for the construction of the LHC which started its operation in 2009.

In July 4th, 2012 the missing particle predicted by the Standard Model, the Higgs boson with a mass of 125 GeV was observed at LHC by the ATLAS and CMS experiments [31, 32, 33]. This result, being one of the main motivations for the construction of LHC, represents one of the most important discovery in particle physics of the last decade. In this chapter the LHC accelerator complex and its experiments will be described with particular emphasis on the Compact Muon Solenoid detector.

## 2.1 The Large Hadron Collider (LHC)

The LHC [34] is currently the world largest particle accelerator with a circumference of 26.7 km situated in average around 100 m beneath the surface in the tunnel of the former LEP experiment. With a present center of mass energy of  $\sqrt{s} = 8$  TeV in proton-proton collisions it represents the world most energetic collider as well. The physics program at the LHC began in 2010 with proton-proton collision at an initial energy of  $\sqrt{s} = 7$  TeV, increased to 8 TeV in 2012. During this period a maximum instantaneous luminosity of  $\mathcal{L} = 7.67 \cdot 10^{33} \text{ cm}^{-2}\text{s}^{-1}$  has been reached and an integrated luminosity of  $\approx 23 \text{ fb}^{-1}$  was delivered. Additional, dedicated periods with heavy ion runs have been performed with an energy of 2.76 TeV per nucleon and  $\mathcal{L} = 10^{27} \text{ cm}^{-2}\text{s}^{-1}$  until February 2013. A long shutdown (LS1) is now ongoing in order to upgrade the machine to the design parameters of  $\sqrt{s} = 14$  TeV with an instantaneous luminosity of  $\mathcal{L} = 1 \cdot 10^{34} \text{ cm}^{-2}\text{s}^{-1}$  and 25 ns bunch spacing.

Four experiments are installed at the collision points: ALICE<sup>1</sup> [35], ATLAS<sup>2</sup> [36], CMS<sup>3</sup> [37] and LHCb<sup>4</sup> [38]. LHCb and ALICE are experiments designed to study predefined physics, where LHCb is optimized for precision measurements of CP violation and decays of B mesons and ALICE focuses on physics of strongly interacting particles and the so called quark-gluon plasma, which is expected at extreme values of energy density and temperature. CMS and ATLAS are general purpose detectors. Their primary aim, which was the discovery of the Higgs boson, has been achieved in 2012 and during the next phase of LHC they will be dedicated to the search of new physics beyond the Standard Model [39].

A schematic layout of the CERN accelerator complex is presented in Fig. 2.1. The LHC is a particle-particle collider consisting of two rings with counter-rotating proton beams. Protons are pre-accelerated in the PS and SPS facilities up to an energy of 400 GeV and injected afterwards in the LHC ring. The beams are further accelerated via 16 high frequency cavity resonators and are crossed at four interactions points, where the main experiments are arranged. In order to bend both proton beams circulating in the LHC tunnel, 1232 dipole magnets able to generate 8.3 T magnetic fields are installed across the ring. Quadrupole and sextupole magnets are used in order to focus and squeeze the beam. The advantage of using protons, compared to electrons/positrons as used in the former LEP experiment is the highly reduced beam energy loss due to synchrotron radiation. Hence higher energies can be achieved only constrained by the magnetic fields available to bend the beams. A “drawback” of proton-proton collisions is the composite nature of protons and hence the a priori unknown center-of-mass energy of the involved

---

<sup>1</sup>ALICE: A Large Ion Collider Experiment

<sup>2</sup>ATLAS: A Toroidal LHC ApparatuS

<sup>3</sup>CMS: Compact Muon Solenoid

<sup>4</sup>LHCb: Large Hadron Collider beauty experiment

### 2.1. The Large Hadron Collider (LHC)

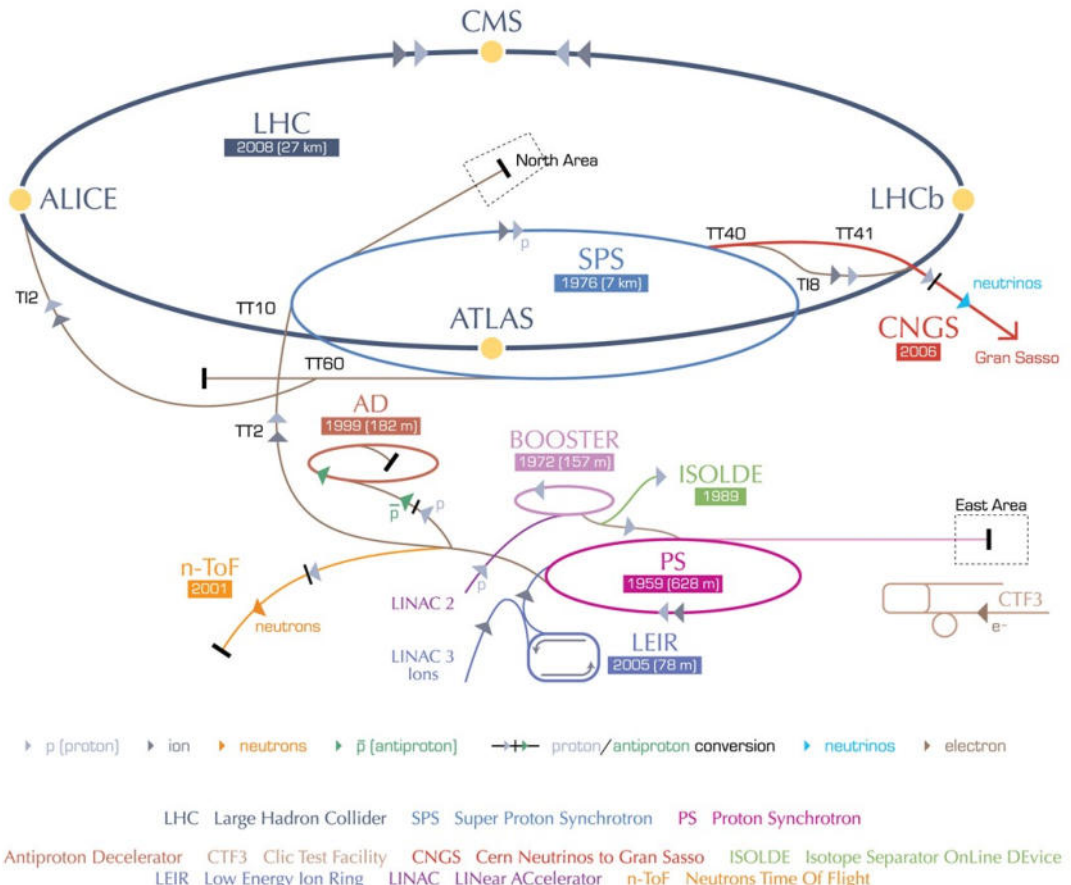


**Figure 2.1:** The CERN accelerator facility with the large LHC ring and the four main experiments. Protons getting pre-accelerated in the Proton-Synchrotron (PS) and Super-Proton-Synchrotron (SPS) up to 400 GeV before the injection into the main ring. Other experiments like the CERN-Neutrino to Gran Sasso (CNGS) beam, which was used by the OPERA (Oscillation Project with EmulsionRacking Apparatus) [40] collaboration for the exciting neutrino time of flight measurement [41], are shown as well.

partons, except the transverse energy which is known to be zero. As a consequence, mostly transverse components of particle observables are used in the analysis of hadron collisions. Beside the importance of the beam energy another quantity, earlier mentioned, is the *instantaneous luminosity*, defined as

$$\mathcal{L} = \frac{f K_b N_p^2}{4\pi\epsilon_n\beta^*} \cdot F \quad (2.1)$$

where  $\gamma$  is the Lorentz factor,  $f$  the revolution frequency,  $k_B$  the number of bunches,  $N_P$  the number of protons per bunch,  $n$  the normalized transverse emittance,  $\beta^*$  the betatron function of the interaction point and  $F$  is a reduction factor induced by the crossing angle of the beams. In order to accumulate a large amount of events in a given time period, a high luminosity is required since it is directly related with the production rate

$$R = \sigma_{prod} \cdot \mathcal{L} \quad (2.2)$$

with  $\sigma_{prod}$  the production cross section for a specific process.

At the nominal intensity each beam will consist of 2808 bunches with about  $10^{11}$  protons in a single bunch colliding with a frequency of 40 MHz. A “drawback” of this high luminosity is the high average number of collision per bunch crossing, which is on the order of about 20 collisions. The *integrated luminosity* is defined as the integration of the luminosity over time and is mostly quoted as the amount of accumulated events

$$N = \int \sigma \cdot \mathcal{L} dt = \sigma \cdot L_{int} \quad (2.3)$$

In Fig. 2.2 the instantaneous and integrated luminosity are shown for the 2012 data taking up to the technical stop in November. In total, a data sample corresponding to an integrated luminosity of  $L_{int} = 21.79 \text{ fb}^{-1}$  was recorded.

## 2.2 The CMS detector

In this section the Compact Muon Solenoid (CMS) detector and its components will be reviewed with particular emphasis on the calorimeters. A more detailed description can be found elsewhere [37]. The CMS detector is a general purpose detector designed and constructed by one of the largest worldwide operating collaboration of physicists, engineers and technicians up to now. As a result of this collaboration an excellent and compact detector with a length of 21.6 m, a diameter of 14.6 m with a total weight of 12500 tons is operational since the start of the LHC program in 2009. A schematic overview of the detector can be seen in Fig. 2.3.

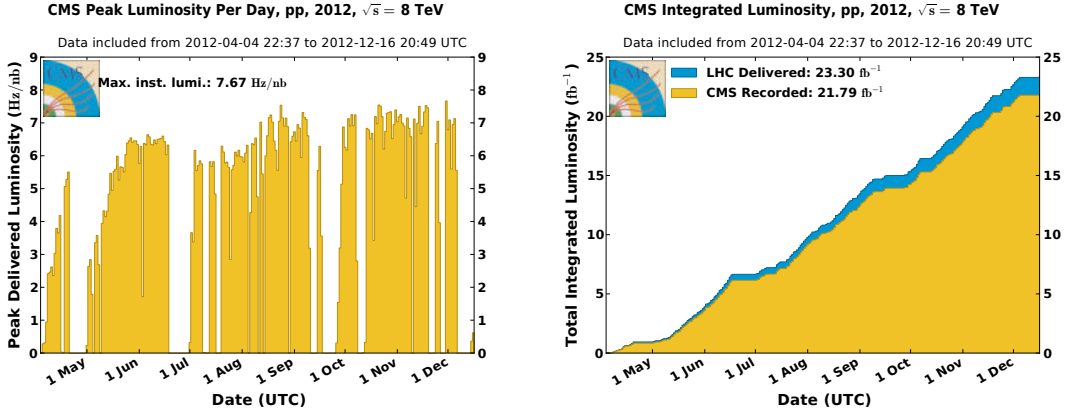


**Figure 2.2:** The daily peak instantaneous (left) and integrated (right) luminosity delivered by the LHC (blue) and recorded by CMS (orange) during stable beams and for p-p collisions at 8 TeV centre-of-mass energy in 2012. In total a data sample corresponding to an integrated luminosity of  $L_{int} = 21.79 \text{ fb}^{-1}$  was recorded with a maximum peak luminosity of  $\mathcal{L} = 7.67 \text{ nbs}^{-1}$  reached at the end of the year.

The detector is built approximately symmetric around the beam axis with a central barrel and two endcaps on both sides. A 13 m long, 5.9 m inner diameter and 3.8 T superconducting solenoid was chosen to design a compact detector with a good momentum resolution of charged particles. Within the solenoid, an inner tracking system and the calorimeters are installed. The still strong return field outside the solenoid, including a fully saturated 1.5 m thick iron yoke, harbors four layers of muon chambers inside this yoke. A more detailed review of the several subsystems will be discussed in the next sections by following the trajectory of particles emerging from the collision point as shown in Fig. 2.3.

### 2.2.1 The coordinate system

The nominal collision point is the origin of the coordinate system used within the CMS collaboration. The  $z$ -axis is defined by the beam line and the perpendicular  $y$  and  $x$  axis are forming a right-handed coordinate system, where the  $y$ -axis is pointing vertically upwards and the azimuthal angle  $\phi$  with respect to the positive  $x$ -axis is measured in the  $x - y$  plane. Similar the polar angle  $\theta$  is defined with respect to the positive  $z$ -axis. The *pseudorapidity*  $\eta$  defined as

$$\eta = -\ln \left[ \tan \left( \frac{\theta}{2} \right) \right] \quad (2.4)$$

is commonly used in collider experiments to indicate the angle of a particle relative to the beam axis. The pseudorapidity depends only on the polar angle  $\theta$  and is zero for any vector in the  $x - y$  plane approaching infinity for the limit  $\theta \rightarrow 0$ . The sign of  $\eta$  indicates the hemisphere.

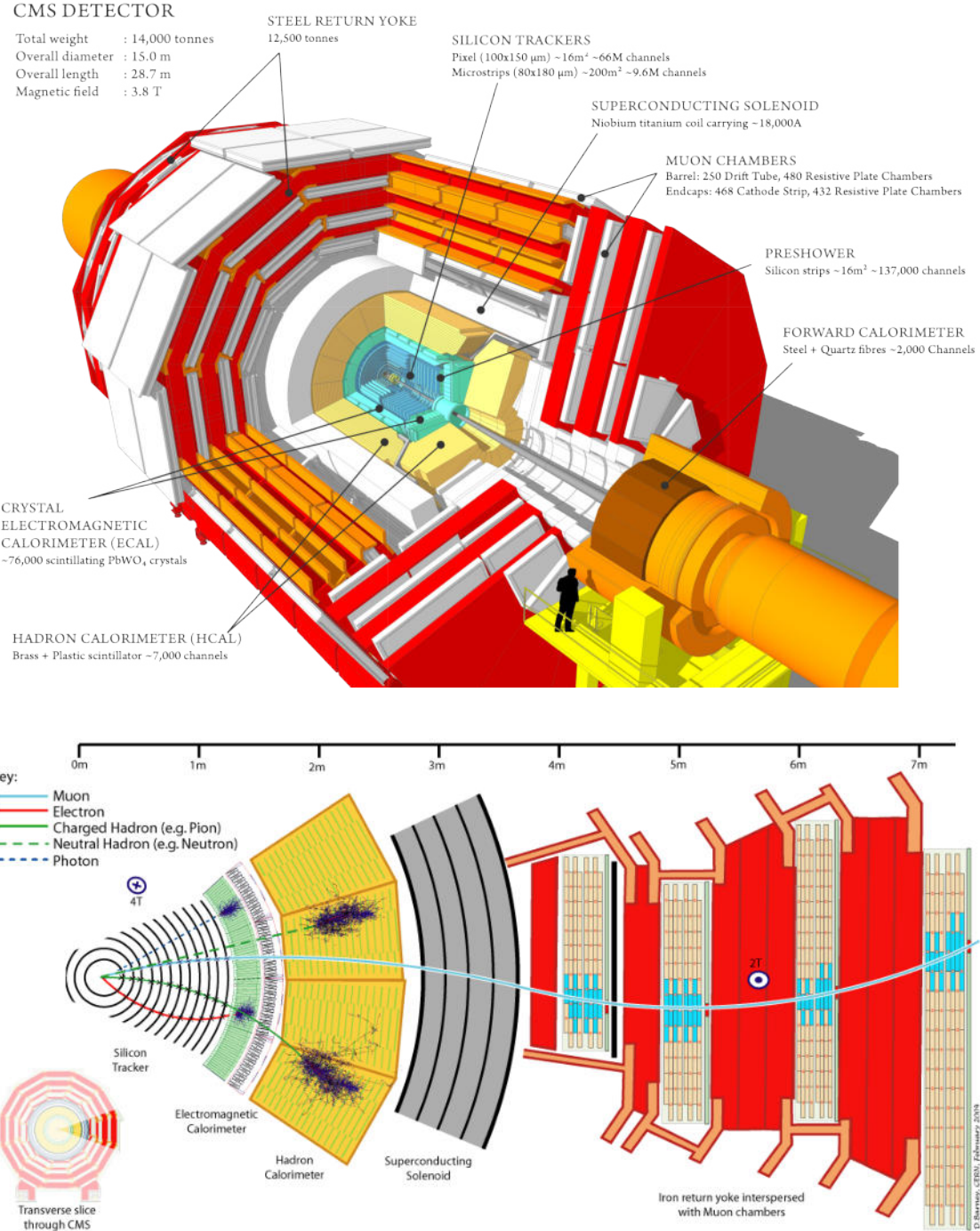


**Figure 2.3:** Top: Three dimensional view of the CMS detector compared with human size. The cylindrical geometry consisting in a barrel region with two endcaps is clearly visible. Bottom: Transverse slice of the CMS detector. Trajectories of different particles from the interaction point to the outer layers are shown. Charged particles are tracked in the inner region, photons and electrons/positrons are measured in the electromagnetic calorimeter whereas hadrons are stopped in the hadronic calorimeter. Muons are measured in the outer rings by the muon system. Trajectory of particles is bended by the magnet which is positioned between the hadronic calorimeter and the muon chambers.

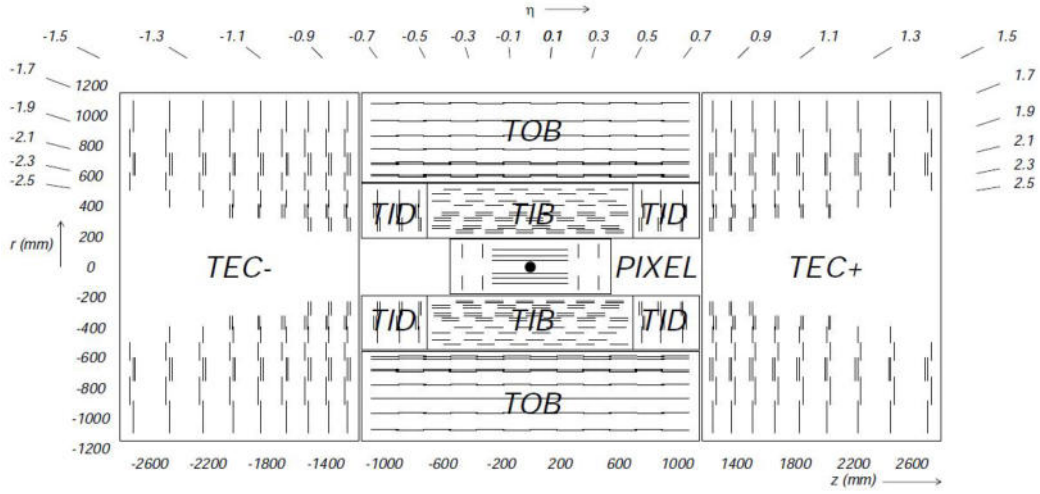


**Figure 2.4:** Schematic overview of the CMS inner tracking system [43]. Each line indicates a detector and double lines back-to-back elements. The inner tracking system consists of three layers pixel detectors in the barrel and two disks attached on each endcap. They are surrounded by ten layers of silicon strip detectors and twelve disks at each endcap. The picture is taken from [37].

### 2.2.2 Inner Tracking System

The inner tracking system [37, 42, 43] is designed to measure with high precision and efficiency the trajectories of charged particles traversing it and allows to reconstruct primary and secondary vertices. It is a 5.8 m long with and 2.5 m diameter cylindrical structure built around the beam pipe. A schematic overview of the inner tracking systems can be seen in Fig. 2.4.

If the LHC is running at the design luminosity of  $\mathcal{L} = 10^{34} \text{ cm}^{-2}\text{s}^{-1}$ , there will be around 20 overlapping events per proton-proton collision leading to an average of 1000 particles to detect each 25 ns. High granularity and fast response are required to ensure a proper trajectory identification and a long lifetime of the detector modules is necessary to withstand the high radiation levels. Another important point is the material budget used in order to minimize multiple scattering, bremsstrahlung, photon conversions and nuclear interactions. A tracker design using a combination of silicon pixel and strip detectors was chosen to meet the discussed requirements. Closest to the beam pipe, where the occupancy of the detector modules is highest, the silicon pixel elements are used. At higher radii lower occupancy allows to use silicon strip detectors. In total the inner tracking systems is composed of 1440 silicon pixel and 15148 strip detector elements covering pseudo rapidities up to  $|\eta| < 2.5$  with a total of  $200 \text{ m}^2$  active material.

## Silicon Pixel Detector

The silicon pixel modules are the part of the tracker system closest to the beam pipe [42]. A precise tracking in  $r - \phi$  and  $r - z$  is crucial for a small impact parameter resolution and identification of secondary vertices. Three layers of pixel detectors are used in the barrel region (BPix) at radii 4.4 cm, 7.3 cm and 10.2 cm and two disks on each endcap (FPix) at  $z = \pm 34.5$  cm and  $z = \pm 46.5$  cm. This involves a total amount of 66 million pixels (48 million BPix + 18 million FPix) corresponding to  $1 \text{ m}^2$  of active pixel material covering pseudo rapidities up to  $|\eta| < 2.5$ , where the size of a single cell is  $100 \times 150 \mu\text{m}^2$ .

Charged particles passing a silicon pixel detector induce electron-hole pairs perceiving a Lorentz drift in the crossed electric and magnetic fields in the barrel region. The angle between the Lorentz drift and the electric field is the so called Lorentz angle, which leads to a charge spreading over more than one pixel. This charge sharing of multiple pixels improves the spatial resolution. This design of three layers in the barrel region and two disks on the endcaps yields three tracking points for each charged particle over almost the full  $\eta$ -range of the pixel detector with a spatial resolution of about  $10 \mu\text{m}$  for the  $r - \phi$  and  $20 \mu\text{m}$  for the z-measurement.

## Silicon Strip Detector

At higher radii the occupancy and the radiation fluences are getting lower and silicon strip detectors with a larger surface can be used. Ten layers of silicon strips are surrounding the pixel-detectors in the barrel region between the radii 20 cm and 116 cm. The silicon strip detectors can be classified into three subsystems: the Tracker Inner Barrel and Disks (TIB, TID) consist of four layers in the barrel (radii 20–55 cm) and three disks in both endcap regions, followed by six layers of Tracker Outer Barrel (TOB) up to a radii of 116 cm and nine disks mounted with Tracker EndCap (TEC) elements. All silicon strip detector elements with 9.6 million strips have an active material area of  $198 \text{ m}^2$ . The single point resolution varies from  $230 - 530 \mu\text{m}$  in z and  $23 - 52 \mu\text{m}$  in the  $r - \phi$  measurement and ensures at least nine tracking points in the  $\eta$ -range of  $|\eta| < 2.4$ .

### 2.2.3 The Electromagnetic Calorimeter

The Electromagnetic Calorimeter (ECAL) [44] provides precise energy measurement of photons, electrons and positrons. Beside the common criteria like fine granularity, fast response and radiation hardness, the ECAL was designed to provide an excellent diphoton resolution in order to identify the Higgs decay into two photons.

The ECAL is a hermetic homogeneous calorimeter built of lead tungstate ( $\text{PbWO}_4$ ) crystals. These crystals are optimal candidates for such application because of their high density,  $\rho = 8.28 \text{ g/cm}^3$ , short radiation length,  $X_0 = 0.89 \text{ cm}$  and small Molière radius,  $R_M = 2.2 \text{ cm}$ . These properties allow to design a compact ECAL with fine granularity. Another advantage of  $\text{PbWO}_4$  crystals is the fast scintillation decay time, namely about 80% of the total light emission occurs within 25 ns, which is in the same order of the LHC bunch crossing rate. Similar to the inner tracking system, the ECAL is divided into a barrel region (EB) and two endcaps (EE) as shown in Fig. 2.5.

The EB crystal volume is in total  $8.14 \text{ m}^3$  with an inner radius of 129 cm and a weight of 67.4 t. It covers pseudo rapidities up to  $|\eta| < 1.479$  and the granularity is 360-fold in  $\phi$  and 2  $\times$  85-fold in  $\eta$  leading to a total amount of 61200 crystals mounted in a quasi-projective geometry to avoid cracks aligned with particle trajectories. The crystals have a tapered geometry with a front face cross section of  $22 \times 22 \text{ mm}^2$  and  $26 \times 26 \text{ mm}^2$  at the rear face, corresponding to a granularity in  $\eta - \phi$  of  $0.0174 \times 0.0174$ . The length of the crystals is 230 mm, which corresponds to  $25.8 X_0$ .

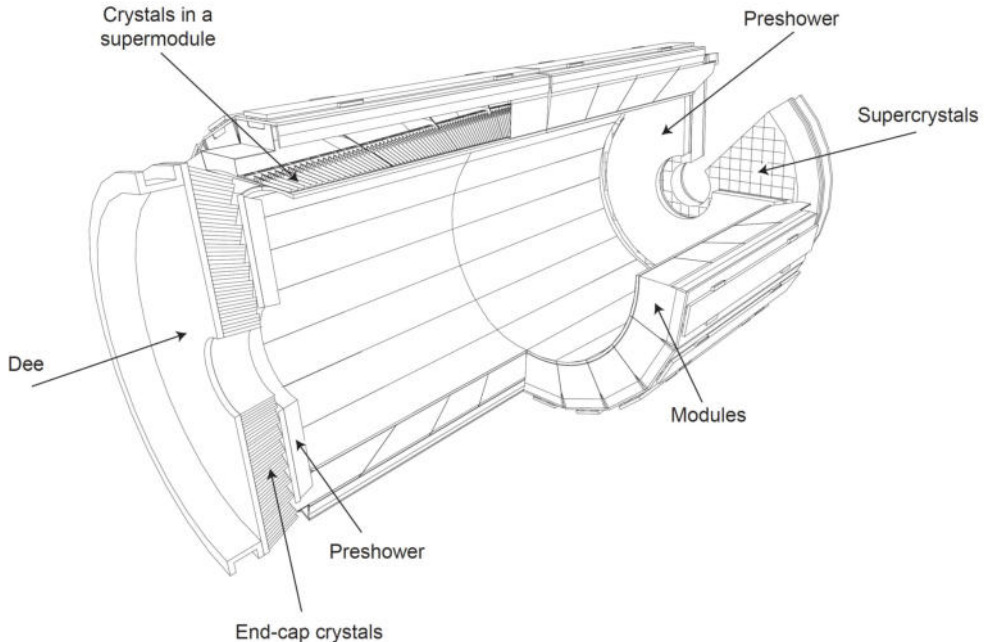


**Figure 2.5:** Layout of the CMS ECAL, showing the barrel supermodules, the two endcaps and the preshower detectors. The ECAL barrel coverage is up to  $|\eta| = 1.48$ ; the endcaps extend the coverage to  $|\eta| = 3.0$ ; the preshower detector fiducial area is approximately  $1.65 < |\eta| < 2.6$ .

The EE are extending the pseudorapidity coverage of the ECAL in the range  $1.479 < |\eta| < 3.0$  and are placed at  $z = \pm 315.4 \text{ cm}$ . The endcaps consist of additional 14648 identically shaped crystals arranged in  $5 \times 5$  array modules called *Supercrystals* and mounted in a rectangular x-y grid, where each crystal is pointing slightly off the interaction point. The front face cross section is  $28.62 \times 28.62 \text{ mm}^2$  and the rear face  $30 \times 30 \text{ mm}^2$  by a crystal

length of 220 mm corresponding to  $24.7 X_0$ . The low light yield of PbWO<sub>4</sub> crystals, the high longitudinal magnetic field and high radiation levels, especially in the endcap region of the ECAL, lead to the choice of two types of photodetectors: avalanche photodiodes (APD) [45] in the EB and vacuum phototriodes (VPT) [46] in the endcaps. APDs are insensitive to high magnetic fields and the high particle flux in the endcaps favored VPTs with lower quantum efficiency and internal gain, but larger surface coverage.

An additional part of the ECAL is the preshower detector (ES) which is installed in front of the endcaps in order to identify pions, covering a range of  $1.653 < |\eta| < 2.6$ . The ES is a sampling detector with two layers of lead radiators with silicon strip sensors attached and aligned orthogonal in the two planes. While the radiators work as initiators for electromagnetic showering, the silicon strip detectors measure the deposited energy and the transverse shower shape. The thickness of the first radiator layer corresponds to a material budget of  $2X_0$  and the second to  $1X_0$ , hence 95% of single photons starts showering before the second sensor plane. In 2004 the energy resolution of the ECAL was measured with electron beams of energy between 20 and 250 GeV to be

$$\left(\frac{\sigma_E}{E}\right)^2 = \left(\frac{2.8\%}{\sqrt{E}}\right)^2 + \left(\frac{12\%}{E}\right)^2 + (0.3\%)^2 \quad (2.5)$$

as reported in [47]. The energy resolution consists of three parts: the stochastic term, mostly affected by photostatistics, a noise term including electronic, digitization and pileup noise and a constant term mostly related to non-uniformity of longitudinal light collection, shower leakage and crystal-to-crystal response intercalibration. For unconverted high energy photons,  $E \approx 100$  GeV, the dominant contribution to the resolution arises from the constant part hence a very precise calibration of ECAL is mandatory for a good performance.

The absolute energy calibration and the intercalibration have been performed using electron test beams and in situ physics events as accurately described in [48]. The intercalibration is a channel-to-channel relative component, which originates from crystal-to-crystal variations of the scintillation light yield and crystal transparency. A fundamental role in the monitoring of this variations is played by the laser monitoring system [49] which allows to correct for time-dependent change of individual crystal response.

#### 2.2.4 The Hadronic Calorimeter

A cross section view of the Hadronic Calorimeter (HCAL) [50] is shown in Fig. 2.6. The HCAL is important for the measurements of hadronic jets and missing transverse energy, due to undetected neutrinos or new exotic weakly interacting particles. The calorimeter structure is splitted into four subsystems. The HCAL barrel (HB) and endcaps (HE) are

installed behind the ECAL system and the size is constrained to  $R = 1.77$  m for the inner radius and  $R = 2.95$  m for the outer in order to be placed within the magnet coil. Due to this constrained size the amount of absorber material is limited and an additional outer component (HO) of the HCAL, outside the solenoid, used as a so called tail catcher is needed. The HB and HE have a coverage in pseudo rapidity up to  $|\eta| < 3.0$ , which is extended up to  $|\eta| < 5.2$  by a forward calorimeter (HF) placed at  $z = 11.2$  m, with respect to the nominal interaction point.

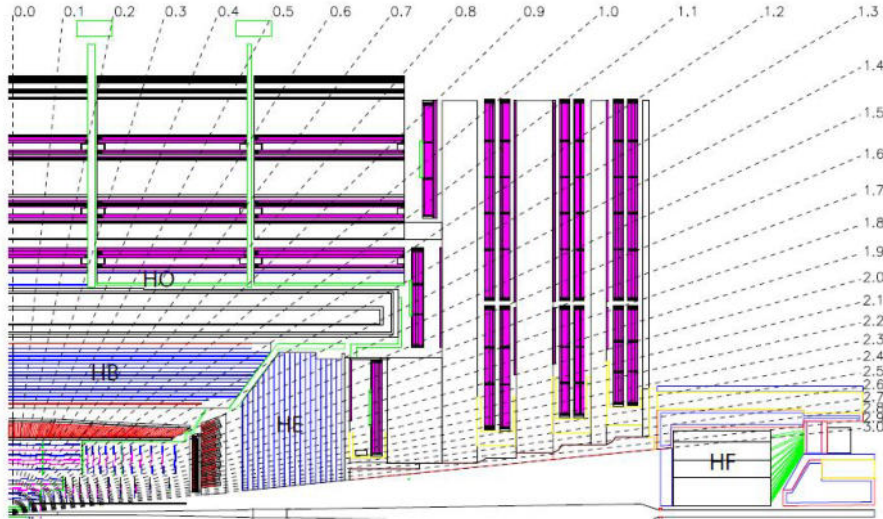


**Figure 2.6:** Schematic overview of the CMS hadronic calorimeter [37] embedded within the superconducting solenoid. The HCAL is divided into four parts: the barrel hadronic calorimeter (HB), the endcap calorimeter (HE) and an outer calorimeter (HO) outside the solenoid needed for the limited absorber material in the central region. An additional calorimeter is placed in the most forward region (HF). For comparison also the location of the inner tracking system, the ECAL and the muon system as well are shown. The picture is taken from [51].

The HB is a sampling calorimeter based on steel and brass as absorber materials and plastic scintillators tiles as active material whose geometry corresponds to a granularity of  $\Delta\eta \times \Delta\phi = 0.087 \times 0.087$ . The inner and outer most absorber plates are stainless steel absorber for structural strength and the rest are brass plates. Brass has a density of  $\rho = 8.53 \text{ g/cm}^3$  with a radiation length of  $X_0 = 1.46 \text{ cm}$  and an interaction length of  $5.82\lambda_I = 16.42 \text{ cm}$ . At  $\eta = 0$  the total absorber thickness corresponds to  $\lambda_I$  whereas, at  $|\eta| = 1.3$ , it is  $10.6\lambda_I$  due to geometry reasons. The ECAL in front of the HCAL adds around  $1.1\lambda_I$  of absorber material. Wavelength-shifting and clear fibers are employed to collect and transport optical signals emitted in the active material to hybrid photodiodes (HPD), that can operate in high axial magnetic fields.

Brass as absorber material was also used for the HE whose design was defined to minimize the amount of cracks between HB and HE, rather than optimizing the resolution of hadronic jets in the endcap region. In total the HE has a thickness of about  $10\lambda_I$  including

ECAL material and a granularity of the scintillator tiles of  $\Delta\eta \times \Delta\phi = 0.087 \times 0.087$  for  $1.3 < |\eta| < 1.6$  and  $\Delta\eta \times \Delta\phi = 0.17 \times 0.17$  for  $1.6 < |\eta| < 3.0$ .

Very forward ranges  $3.0 < |\eta| < 5.0$  are covered by the HF calorimeter. The design of the HF calorimeter was first and foremost guided by the necessity to withstand the extremely high radiation environment ( $\approx 10$  MGy after 10 years of operation). This was the principal reason which lead to the choice of quartz fibers (fused-silica core and polymer hard-cladding) as active medium. The signal is generated when charged shower particles above the Cherenkov threshold ( $E > 190$  keV for electrons) generate Cherenkov light, thereby making the calorimeter mostly sensitive to the electromagnetic component of showers (Sec. 1.3). The forward calorimeter is essentially a cylindrical steel structure with an outer radius of 130.0 cm. The front face of the calorimeter is located at  $\pm 11.2$  m from the interaction point. The hole for the beam pipe is cylindrical, with radius 12.5 cm from the center of the beam line. The fibers run parallel to the beam line. A large plug structure in the back of the detector provides additional shielding (see Fig. 2.7).

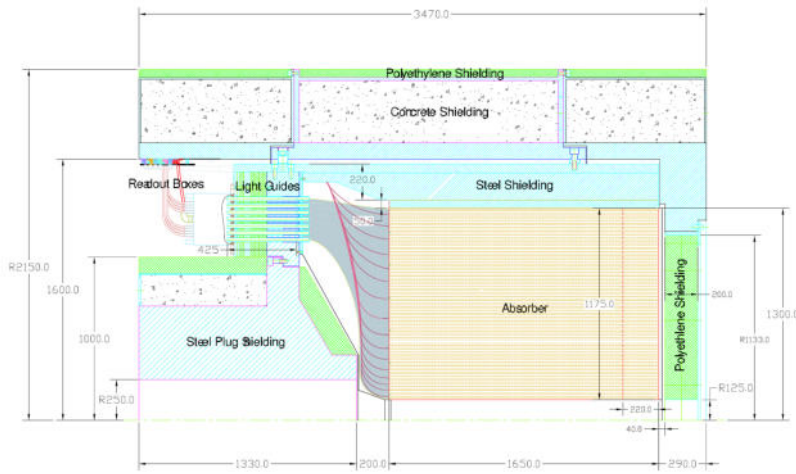


**Figure 2.7:** Cross section view of the CMS HF calorimeter [37]. Concrete, polyethylene and steel shieldings are used to protect light guide fibers and readout electronics from the harsh radiation environment. Quartz fibers are embedded in the absorber structure parallel to the beam axis.

Bundled fibers are held in ferrules which illuminate one end of the air-core light guides that penetrate through 42.5 cm of the shielding matrix (steel, lead, and polyethylene). This shielding is necessary to protect the photomultipliers and the front-end electronics housed in the readout boxes. The air-core light guide consists of a empty tube lined on the inside with highly reflective sheets. These metal-coated reflectors are designed to be very efficient ( $> 90\%$ ) in the visible spectrum at the relevant angles ( $\sim 70^\circ$  from normal). Light on average makes five bounces before reaching the photocathode and nearly half the photons are lost in this transport. Each light guide is coupled to a standard bialkaline, 8-

stage photomultiplier tube with a borosilicate glass window. A readout box (RBX) houses 24 PMTs and services half of a wedge ( $10^\circ$  in  $\phi$ ).

The HCAL energy resolution has been measured in test beams with electrons, pions, protons and muons and complementary in cosmic muon data as well [52]. For the barrel and endcap calorimeters (HB, HO, HE) the energy resolution to pions between 2 and 350 GeV was measured to be [53]

$$\left(\frac{\sigma_E}{E}\right)^2 = \left(\frac{84.7\%}{\sqrt{E}}\right)^2 + (7.4\%)^2 \quad (2.6)$$

and for the forward calorimeter (HF) [54]

$$\left(\frac{\sigma_E}{E}\right)^2 = \left(\frac{198\%}{\sqrt{E}}\right)^2 + (9.0\%)^2 \quad (2.7)$$

where  $E$  is the energy in GeV. The two terms on the right side of the equation represent respectively the stochastic and the constant term. As anticipated in Sec. 1.1.4, the stochastic term of hadronic energy resolution is largely determined by fluctuations in the neutral pions production in showers.

### 2.2.5 The Magnet

A large superconducting solenoid [55] is installed inside the CMS detector and encloses the inner tracker system, the ECAL and HCAL except the outer hadronic calorimeter. It has a length of 12.9 m and inner diameter of 5.9 m. A high magnetic field of 3.8 T inside the magnet is required to achieve a momentum resolution of  $\sigma_p/p \approx 10\%$  for energetic muons ( $E \approx 1$  TeV). The magnetic flux generated by the solenoid coil is returned via a 1.5 m thick saturated iron yoke, which also hosts several layers of the muon system.

### 2.2.6 The Muon System

The outermost part of the CMS detector [56] consists of the Muon System shown in Fig. 2.8. Muons are involved in many interesting physics processes, like Higgs decays and SUSY processes. In addition they are utilized for many SM precision measurements involving B physics and electroweak processes. The identification, reconstruction and momentum resolution of muons as well as the capability of triggering on muons is therefore of prior importance.

The muons system is splitted into two parts including three types of gaseous detectors to identify muon candidates and measure their momentum: the central part muon barrel

(MB) up to  $|\eta| < 1.2$  and the forward parts with two muon endcaps (ME) extending the coverage up to  $|\eta| < 2.4$ . In the barrel region drift tube chambers (DT) are used. Although slow because of the drift time and sensitive to the magnetic field because of the Lorentz force on the drifting electrons, they can be used in the barrel region because of the small neutron background, low muon rate and low residual magnetic field. In contrast, the endcap region have larger neutron background, higher muon rate and stronger magnetic field. Hence the so called cathode strip chambers (CSC) are used. In both muon subsystems also resistive plate chambers (RPC) are added, having a fast response and good time resolution, in order to assign correct bunch crossings. The spatial resolution of the RPCs is worse compared to the resolution of the DTs and CSCs and therefore a combination in both subsystem was chosen.

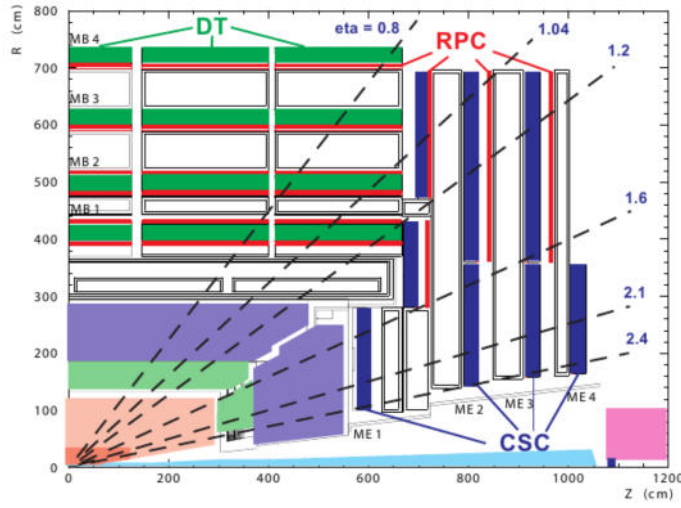


**Figure 2.8:** The muon system is the largest part of the CMS detector embedded in the iron return yoke of the solenoid. In the barrel region four stations including several layers of DTs and RPCs are installed, whereas in the endcap region four disks mounted with CSCs and RPCs are in usage. The picture is taken from [51].

The DT are 1.2 mm thick and 9.6 mm long aluminium cathodes with stainless steel anodes wires at their center. A mixture of Argon and CO<sub>2</sub> is used as gas. The DTs have a maximal drift length of 2 cm and spatial resolution around 200  $\mu\text{m}$ . The precision along  $\phi$  is 100  $\mu\text{m}$  and 1 mrad in the direction of the muon vector with a time resolution of 5 ns. In comparison, the CSCs are  $1 \times 2 \text{ m}^2$  trapezoidal chambers consisting of six gas gaps with each having a plane of radial cathodes and a plane of anode wires oriented perpendicular. A mixture of Ar-CO<sub>2</sub>-CF<sub>4</sub> gas is used to fill them. The spatial resolution is typically on the order of 200  $\mu\text{m}$  with an angular resolution of about 10 mrad in  $\phi$  with a time resolution of 6 ns, which is a little bit higher compared to DTs. The last detector type used in the muon system are the RPCs. They consist of a double-gap chamber operating in avalanche mode with a gap width of 2 mm. The spatial resolution of the RPC is defined by the cell size.

### 2.2.7 The Forward Detectors

The pseudorapidity range  $|\eta| > 5.2$  in CMS is covered by additional dedicated detectors: a quartz-tungsten sampling calorimeter (CASTOR) for  $5.2 < |\eta| < 6.6$  and the Zero Degree Calorimeter (ZDC) for  $|\eta|$  up to 8.3.

CASTOR

The CASTOR (Centauro And Strange Object Research) [57] detector is located at 14.38 m from the interaction point. Its physics motivation is to complement the nucleus-nucleus physics programme, developed essentially in the baryon-free mid-rapidity region, and also the diffractive and low- $x$  physics in p-p collisions.

The CASTOR detector is a Cherenkov-based calorimeter, similar in concept to the HF. It is constructed from layers of tungsten (W) plates (alloy density  $\rho = 18.5 \text{ g/cm}^3$ ) as absorber and fused silica quartz (Q) plates as active medium. For the electromagnetic (EM) section, the W plates have a thickness of 5.0 mm and the Q plates of 2.0 mm. For the hadronic (HAD) section, the W and Q plates have thicknesses of 10.0 mm and 4.0 mm, respectively. The W/Q plates are inclined 45° with respect to the direction of the impinging particles, in order to maximize the Cherenkov light output in the quartz. The Cherenkov light, produced by the passage of relativistic charged particles through the quartz medium, is collected in sections along the length of the calorimeters and focused by air-core light guides onto the photomultiplier (PMT), as shown in Fig. 2.9.

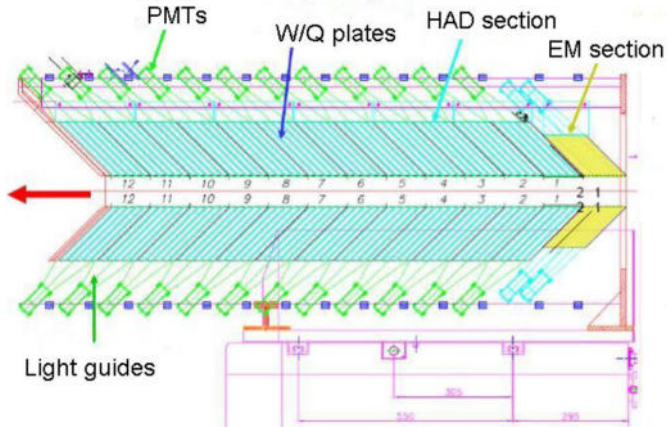


**Figure 2.9:** Details of the components and geometry of the CASTOR calorimeter.

The energy linearity and resolution as well as the spatial resolution of CASTOR prototypes have been studied at CERN/SPS [58]. The response of the calorimeter to electromagnetic and hadronic showers has been analysed with  $E = 20 - 200$  GeV electrons,  $E = 20 - 350$  GeV pions, and  $E = 50, 150$  GeV muons. Good energy linearity for electrons and

pions in the full range tested is observed. For the EM section, the constant term of the energy resolution, that limits performance at high energies, is less than 1%, whereas the stochastic term is  $\approx 50\%$ . As common quartz calorimeters, CASTOR presents a good radiation hardness, a fast response and compact detector dimensions. All these properties, are unavoidable requirements to withstand experimental conditions encountered in the very forward region at the LHC.

## ZDC

A set of two zero degree calorimeters [59], extending the pseudorapidity coverage up to  $|\eta| \leq 8.3$  for neutral particles, are designed to complement the CMS very forward region. Each ZDC has two independent parts: the electromagnetic (EM) and hadronic (HAD) sections.

Sampling calorimeters using tungsten and quartz fibers have been chosen for the detection of the energy in the ZDCs with a design similar to HF and CASTOR. The quartz-quartz fibers can withstand up to 30 GRad with only a few percent loss in transparency in the wavelength range 300-425 nm. The HAD section consists of 24 layers of 15.5 mm thick tungsten plates and 24 layers of 0.7 mm diameter quartz fibers ( $6.5\lambda_I$ ). The tungsten plates are tilted by  $45^\circ$  to optimize Cherenkov light collection. The EM section is made of 33 layers of 2-mm-thick tungsten plates and 33 layers of 0.7-mm-diameter quartz fibers ( $19X_0$ ). The tungsten plates are oriented vertically and the fibers are laid as strips. An optical air-core light guide will carry the light extracted from quartz fibers through radiation shielding to the photomultiplier tube.

The response of the ZDC has been studied in beam tests [60]. The calorimeter was measured to be linear within 2% in the range from 20 GeV to 100 GeV. The energy resolution obtained for the different positron energies can be parametrized as

$$\left(\frac{\sigma_E}{E}\right)^2 = \left(\frac{70\%}{\sqrt{E}}\right)^2 + (8\%)^2 \quad (2.8)$$

where  $E$  is in GeV. Positive pions with energies of 150 GeV and 300 GeV were used to measure the response of the combined EM+HAD system. The pion energy resolution, obtained by a Landau fit, can be parametrized as

$$\left(\frac{\sigma_E}{E}\right)^2 = \left(\frac{138\%}{\sqrt{E}}\right)^2 + (13\%)^2 \quad (2.9)$$

where  $E$ , again, is in GeV.

### 2.2.8 Trigger and Data Acquisition System

At the design luminosity of the LHC with a bunch crossing rate of 40 MHz there will be around 109 collisions per second in the detector. Assuming an event size of 1.5 MB leads to tens of TB/s to record. A similar rate is impossible to handle with the limited computing resources available. For this reason a two level trigger and data acquisition system were designed in order to reduce the amount of recorded collisions by six orders of magnitude (see Fig. 2.10). The trigger selects interesting events out of millions of uninteresting ones, so the trigger is of exceptional importance and needs a very careful consideration.

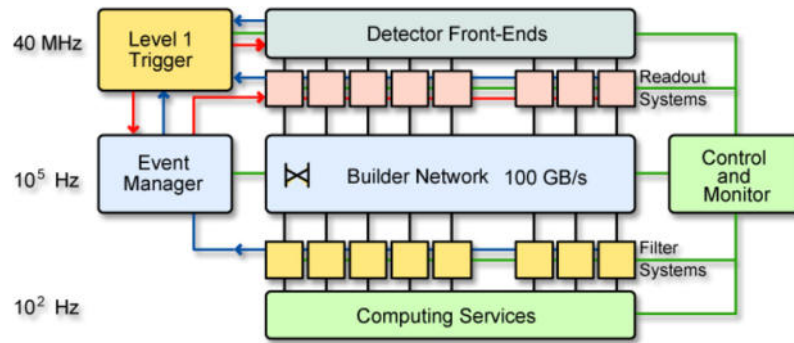


**Figure 2.10:** The data acquisition and trigger systems consists of the front-end readout electronics, a L1 trigger system and a software based HLT system running on a computer farm. This system allows to reduce the event rate of about 40 MHz at the design luminosity of the LHC to a manageable level of about 100 Hz. The picture is taken from [51]

#### L1 Trigger

The Level-1 (L1) trigger system [61] is built of hardware processors and reduces the event rate from 40 MHz to 100 kHz. In total  $3.2 \mu\text{s}$  are allocated for the transition from the front-end electronics to the L1 trigger system including the decision making time. The detector informations are stored meanwhile in memory buffers of the front-end electronics. The L1 decision is based on informations of the calorimeters and muon systems with a reduced granularity and resolution of the detector. Also correlations of both detector subsystems are taken into account by so called global L1 triggers.

#### HLT trigger

If an event is accepted by the L1 trigger the high resolution detector data is passed to the high level trigger software running on a CPU farm. The High-Level trigger (HLT) system [61] is a software based routine which reduces the event rate from 100 kHz to

about 150 Hz. A more sophisticated event reconstruction is used to provide all needed objects and topologies in order to select events according to the physics goals. Since the HLTs are software triggers, the operation is very flexible and due to changing environments or physics goals the individual trigger rates can easily be adjusted in terms of selection algorithm and object thresholds. The final event rate of about 150 Hz corresponds to the data stream of 225 MB/s (with event size  $\approx$  1.5 MB) which is then transferred to a central storage system based at CERN.

# Test Beam Study with Proton-Irradiated ECAL Endcap Crystals

---

The CMS Electromagnetic Calorimeter presented in Sec. 2.2.3 had a big role in the discovery of the Higgs Boson, on the 4<sup>th</sup> July 2012. The choice of a homogeneous calorimeter, indeed, was driven by the requirement of an excellent energy resolution for electrons, positron but especially photons in order to discriminate the  $H \rightarrow \gamma\gamma$  peak from background events. Although theoretically a homogenous calorimeter represents the best way to achieve optimal energy resolutions (Sec. 1.1.3), many practical factors affecting the constant term has to be taken into account in order to control and limit their contribution to the calorimeter performance.

As introduced in Sec. 1.2, interaction of radiation with inorganic scintillators can produce defects causing a loss of crystal transparency leading to a severe degradation of the ECAL energy resolution and trigger capabilities. Although during the design and construction of the calorimeter, several studies were made to evaluate the radiation hardness of lead tungstate, the extreme hadron fluences predicted for the High Luminosity LHC (HL-LHC) require further investigations.

For this reason, a dedicated campaign of irradiation with 24 GeV protons was performed at CERN PS during 2011-2012. Degradation of crystal properties was measured in laboratory and allowed to define a useful correlation between proton fluence and induced absorption. The proton-irradiated crystals were then used to build a set of ECAL endcap supercrystals which were tested with electrons in the 10-150 GeV energy range at the H4 test beam facility in the CERN North Area. In this chapter, after a brief introduction on radiation damage effects in lead tungstate and radiation environment inside CMS is given. Recent test beam results are then combined with laboratory measurements providing a coherent and complete picture of hadron-damage effects in  $\text{PbWO}_4$ .

### 3.1 Radiation Damage in Lead Tungstate

Effects of radiation damage on lead tungstate crystals have been extensively studied in [62, 63, 64, 65] during the process of optimization of this scintillator for the CMS ECAL. The occurrence of radiation-induced defects mostly related to  $O^-V_cO^-$  centers and  $(WO_3)^{2-}$  point defects due to oxygen vacancies, has been observed. These defects are responsible for the creation of absorption bands (*color centers*) around 620 and 370 nm respectively. Previous studies also demonstrated that radiation does not change the scintillation properties of the crystal (emission spectrum and decay kinetics), but only affects the light transmission enhancing the probability of absorption and diffusion processes. Nevertheless, the amount of defects depends on the type of radiation ( $\gamma$ , neutrons, protons). Due to their nature, hadrons create more concentrated clusters of defects which affect differently the recovery kinetic and the transmission spectrum. As discussed in the following, radiation damage can be divided in two main categories: *electromagnetic* and *hadronic* radiation damage.

#### 3.1.1 Electromagnetic Damage

A particular feature of color centers induced by electromagnetic radiation (i.e. ionizing particles) is their spontaneous recovery at room temperature. This effect has been understood and explained in [66, 67]. A phenomenological model to describe observed effects has also been proposed in [68]. Since during irradiations both annihilation and creation processes coexist, this yield to a dose rate dependent transmission loss. The damage, indeed, saturates when the rate of defect (trap) filling by radiation-created carriers becomes equal to their release rate. Assuming the annihilation speed of the color center is proportional to a constant  $a_i$  and its creation speed is proportional to a constant  $b_i$ , at a given dose rate,  $R$ , the density of the color centers in the crystal at time  $t$  can be written as

$$D(t) = \sum_{i=1}^n \left\{ \frac{b_i R D_i^{all}}{a_i + b_i R} [1 - e^{-(a_i + b_i R)t}] + D_i^0 e^{-(a_i + b_i R)t} \right\} \quad (3.1)$$

where  $D_i^{all}$  is the total density of traps related to the center  $i$  and  $D_i^0$  is the initial density. When the equilibrium is achieved the density of color centers, which depends on the dose rate is then

$$D_{eq} = \sum_{i=1}^n \frac{b_i R D_i^{all}}{a_i + b_i R} \quad (3.2)$$

If irradiation stops then color centers start to recover according to Eq. 3.1 with  $R = 0$ . Spontaneous recovery of transmission has been observed and studied both in laboratory

### 3.1. Radiation Damage in Lead Tungstate

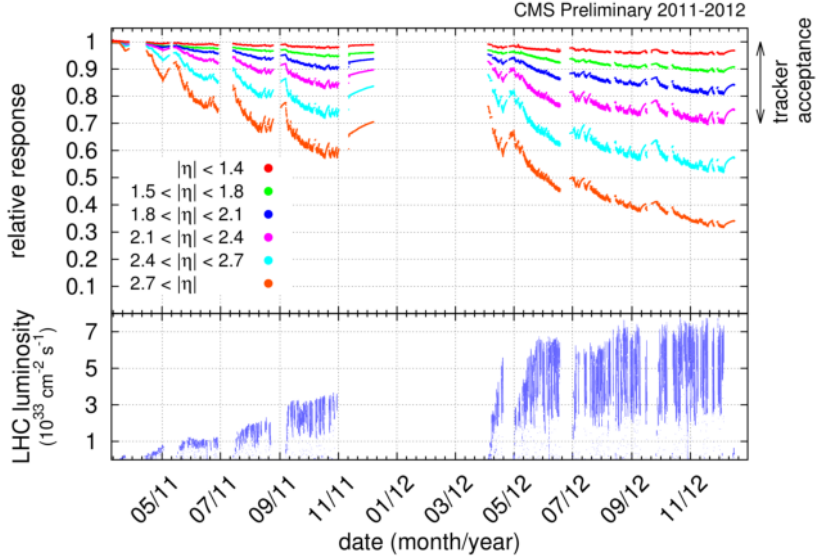


**Figure 3.1:** Top: CMS ECAL relative response to laser light (440 nm) versus time, averaged over all crystals in a given pseudorapidity bin, for 2011 and 2012 data taking. Bottom: LHC instantaneous luminosity versus time.

and during the operation of the real calorimeter. As mentioned in Sec. 2.2.3, the transparency of ECAL crystals is monitored *in situ* during LHC running using a dedicated light injection system [49]. The cycles of loss and recovery observed during 2011-2012 LHC data taking are shown in Fig. 3.1. In the most forward EE regions used for electron and photon reconstruction (tracker acceptance  $|\eta| \leq 2.1$ ), the maximum response loss is around 30% whereas it increases up to 70% in the channels closest to the beam pipe, where the ionizing dose rate is higher. In the operation of ECAL so far, the ionizing radiation is responsible for the most of signal loss since hadron fluences are very small.

#### 3.1.2 Hadronic Damage

Interaction of hadrons with crystals occurs mainly through inelastic nuclear interactions which break up target nuclei creating impurities and distortions in the crystal lattice. In addition, the heavy nuclear fragments created in this process produce a very dense ionization along their path which displace a large number of lattice atoms and ionize much more densely than minimum ionizing particles. The overall result is that, with respect to electromagnetic particles, hadrons induce a significantly different type of damage involving the creation of *clusters* of colour centers with peculiar features [69, 70, 71].

First, there is almost no defect recovery at room temperature, hence the damage effect is cumulative. Second, the band edge of the transmission curve is shifted by several tens of nanometers to higher values leading to an overlap with the  $\text{PbWO}_4$  emission peak as shown

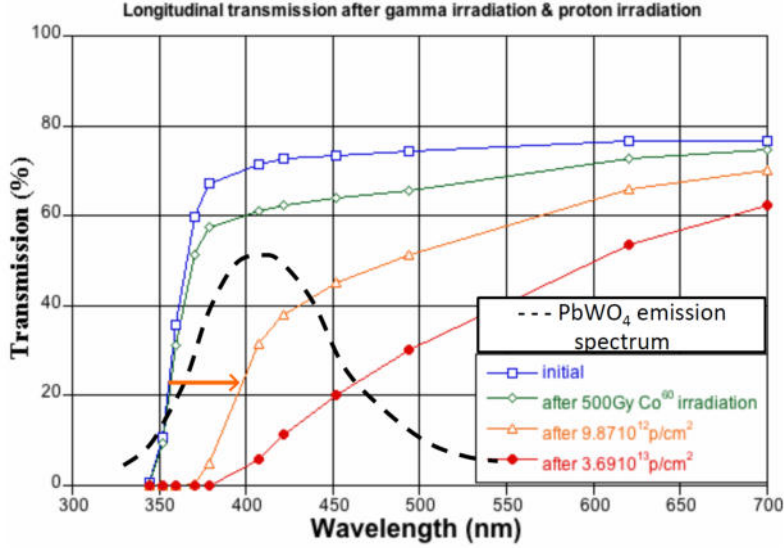


**Figure 3.2:** Transmission curves of PWO crystals after 500 Gy  $\gamma$ -irradiation (green curve) and different fluences of proton-irradiation (orange-red curves). A shift of the band edge in the transmission spectrum is observed for hadron damage. Transmission curve of a non-irradiated PWO crystal and its emission spectrum are also shown (green and black curve respectively).

in Fig. 3.2. Because of these peculiar properties, the hadron damage represents a more dramatic limitation to the PbWO<sub>4</sub> crystal performance in high radiation environments.

### 3.1.3 Recovery Studies

In order to minimize the effect of radiation damage, two techniques which enhance the recovery rate of color centers were investigated: *thermal annealing* and *optical bleaching*. The former consists in heating the crystal to temperatures which are able to destroy color centers by thermal activation. The probability for a charge carrier in trap of energy  $E$  to be released increases with temperature according to  $P \propto e^{-\frac{E}{kT}}$  as anticipated in Sec. 1.2. Hence, by slowly increasing the temperature and monitoring the recovery of transmission in time it is possible to study the depth of different traps [72].

The second possibility to improve recovery rate of defects is optical bleaching. By illuminating a crystal with optical light of a specific wavelength it is possible to transfer enough energy to the trapped electrons to release them from the potential well of the trap. Light intensity has to be high enough to ionize traps but not too high to avoid damaging of the crystal. Optical bleaching with  $\lambda = 540$  and 740 nm has been studied demonstrating the feasibility of this approach [73].

Thermal and optical bleaching techniques can also be combined together to improve the overall effect. Although these methods allow to restore completely the crystal trans-

### 3.1. Radiation Damage in Lead Tungstate

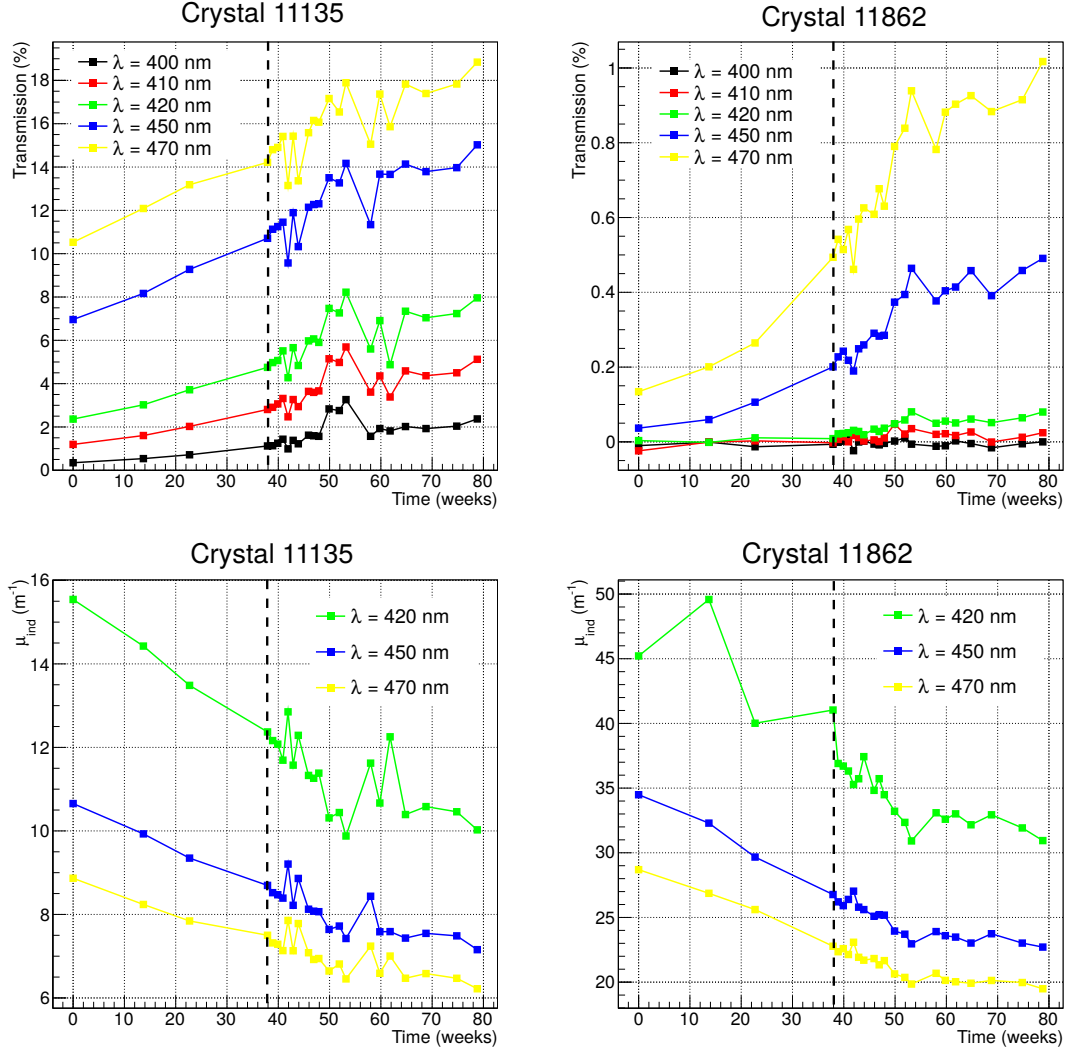


**Figure 3.3:** Transmission and  $\mu_{ind}$  values measured at different wavelengths for two proton-irradiated  $\text{PbWO}_4$  crystals (labelled as 11135 and 11862) over a period of about two years. Dotted vertical lines represent the transition between room temperature recovery and oven recovery at 50°C. Large systematic fluctuations in the data are due to systematics intrinsic to the transmission measurement.

parency, their implementation in a real detector like CMS ECAL presents practical limitations. First, increasing the temperature of the crystals during the detector operation would modify the performance of the crystals themselves (e.g. lowering the light yield because of higher probability of non-radiative recombination) as well as the performance of the electronics. Second, the maximum temperature to which the ECAL can be exposed is around 50-70°C which imposes constraints on the energy depth of defects which can be annealed. Also the injection of optical light into the crystals presents some difficulties since it could affect the stability of the crystal and photodetector response during operation.

A recovery study was made on two proton-irradiated crystals used for test beam studies, discussed later on in Sec. 3.3. After irradiation with protons and beam testing, the crystals were kept at room temperature for a period of about 30 weeks. After this period a recovery study was started.

Crystals were put in a oven at 50°C and transparency was measured periodically every 2-4 weeks for a period of about one year. A small recovery was observed both at room temperature and at 50°C as reported in Fig. 3.3. The first part of the recovery can be attributed to small defects induced by the electromagnetic part of proton interaction with crystals, (i.e. low density defect clusters). A slow but clear recovery is still present after 35 weeks when the oven recovery started, indicating that some hadron-induced defects can anneal also at 50°C. After about 2 years the induced absorption coefficient decreased from 16 to 10 m<sup>-1</sup> at 420 nm, for crystal 11135 and from 45 to 30 m<sup>-1</sup> for the strongly irradiated crystal 11862. Fig. 3.3 show the recovery dynamics for different wavelengths around the PbWO<sub>4</sub> emission peak. Each time the crystals were removed from the oven, cleaned and measured with a spectrophotometer. Transmission measurement is affected by 1-2% systematic uncertainties which is responsible for the fluctuations observed in the data. Especially because of the poor crystal transparency and strong non uniformity of the damage inside the crystal (see Sec. 3.3) this measurement is particularly sensitive to the crystal alignment, residual dust on the crystal surfaces and spectrophotometer precision.

It is very difficult to extrapolate the recovery dynamic of the crystal on a longer time scale. It could be that hadron damage could create defects which will never recover at 50°C and thus the recovery will saturate at a certain point. However, these results shows that a very slow recovery of a certain component of the hadron damage can recover and should be further investigated.

## 3.2 Radiation Environment at HL-LHC

In order to quantify the consequences of radiation damage on the performance of the real calorimeter, the nature and the intensity of the radiation environment in CMS have to be understood. Intensity of radiation will depend on the operating conditions of LHC as summarized in Table 3.1.

In 2012 the Large Hadron Collider (LHC) reached a center-of-mass energy of  $\sqrt{s} = 8$  TeV, an instantaneous peak luminosity of  $\mathcal{L} = 7.67 \times 10^{33}$  cm<sup>-2</sup>s<sup>-1</sup> and an integrated luminosity of  $\int \mathcal{L} dt = 23$  fb<sup>-1</sup>. The first long shutdown (LS1) started in early 2013 in order to increase the LHC center-of-mass energy up to 13 TeV by 2015. The instantaneous peak luminosity will be increased to  $\mathcal{L} = 2 \times 10^{34}$  cm<sup>-2</sup>s<sup>-1</sup> following an injection upgrade in 2018 (LS2 shutdown). A major upgrade of the interaction region will be performed around 2022 (LS3 shutdown) in order to achieve a peak luminosity of  $\mathcal{L} = 10^{35}$  cm<sup>-2</sup>s<sup>-1</sup> and a levelled

	2012 Running	LHC Design	HL-LHC
Center of Mass Energy $\sqrt{s}$ [TeV]	8	14	13
Instantaneous Luminosity [ $\text{cm}^{-2}\text{s}^{-1}$ ]	$1\text{-}7 \times 10^{33}$	$1 \times 10^{34}$	$5 \times 10^{34}$
Integrated Luminosity [ $\text{fb}^{-1}$ ]	23	500	3000
$\gamma$ dose rate [Gy/h] (EB $ \eta  = 1.0$ )	0.14	0.2	1.0
$\gamma$ dose rate [Gy/h] (EE $ \eta  = 2.6$ )	4.2	6	30
Hadron fluence [ $\text{cm}^{-2}$ ] (EB $ \eta  = 1.0$ )	$5.8 \times 10^{10}$	$12 \times 10^{11}$	$7.6 \times 10^{12}$
Hadron fluence [ $\text{cm}^{-2}$ ] (EE $ \eta  = 2.6$ )	$1.5 \times 10^{12}$	$3 \times 10^{13}$	$2.0 \times 10^{14}$

**Table 3.1:** Operating beam conditions and radiation levels during 2012 compared with LHC design parameters and predictions for HL-LHC phase.

value of  $\mathcal{L} = 5 \times 10^{34} \text{ cm}^{-2}\text{s}^{-1}$  during the High Luminosity LHC Phase (HL-LHC) which is expected to deliver an integrated luminosity of  $3000 \text{ fb}^{-1}$  by 2035.

The CMS detector was designed to withstand the radiation levels expected by the end of the nominal LHC running [37], before LS3, when  $500 \text{ fb}^{-1}$  of data are planned to be collected [34]. The expected ionizing radiation levels correspond to 0.2 Gy/h in EB and 6 Gy/h in EE (at  $|\eta| = 2.6$ ). The hadron fluence after  $500 \text{ fb}^{-1}$  is expected to be  $1.2 \times 10^{11} \text{ cm}^{-2}$  for EB and  $3 \times 10^{13} \text{ cm}^{-2}$  for EE (at  $|\eta| = 2.6$ ) [74].

According to dedicated FLUKA simulations [75, 76] (which make use of the current detector geometry), during HL-LHC the ionizing dose rate inside CMS have been predicted to be around 5 times higher (1 Gy/h in EB and 30 Gy/h in EE) and the integrated particle fluences to be around 6 times higher ( $7.6 \times 10^{12} \text{ cm}^{-2}$  in EB and  $2 \times 10^{14} \text{ cm}^{-2}$  in EE). Detailed maps of the radiation levels in different positions inside the detector have been calculated and are reported in Fig. 3.4. The intensity of radiation shows a strong  $|\eta|$  dependence, due to the higher fluence of particles close to the beam pipe.

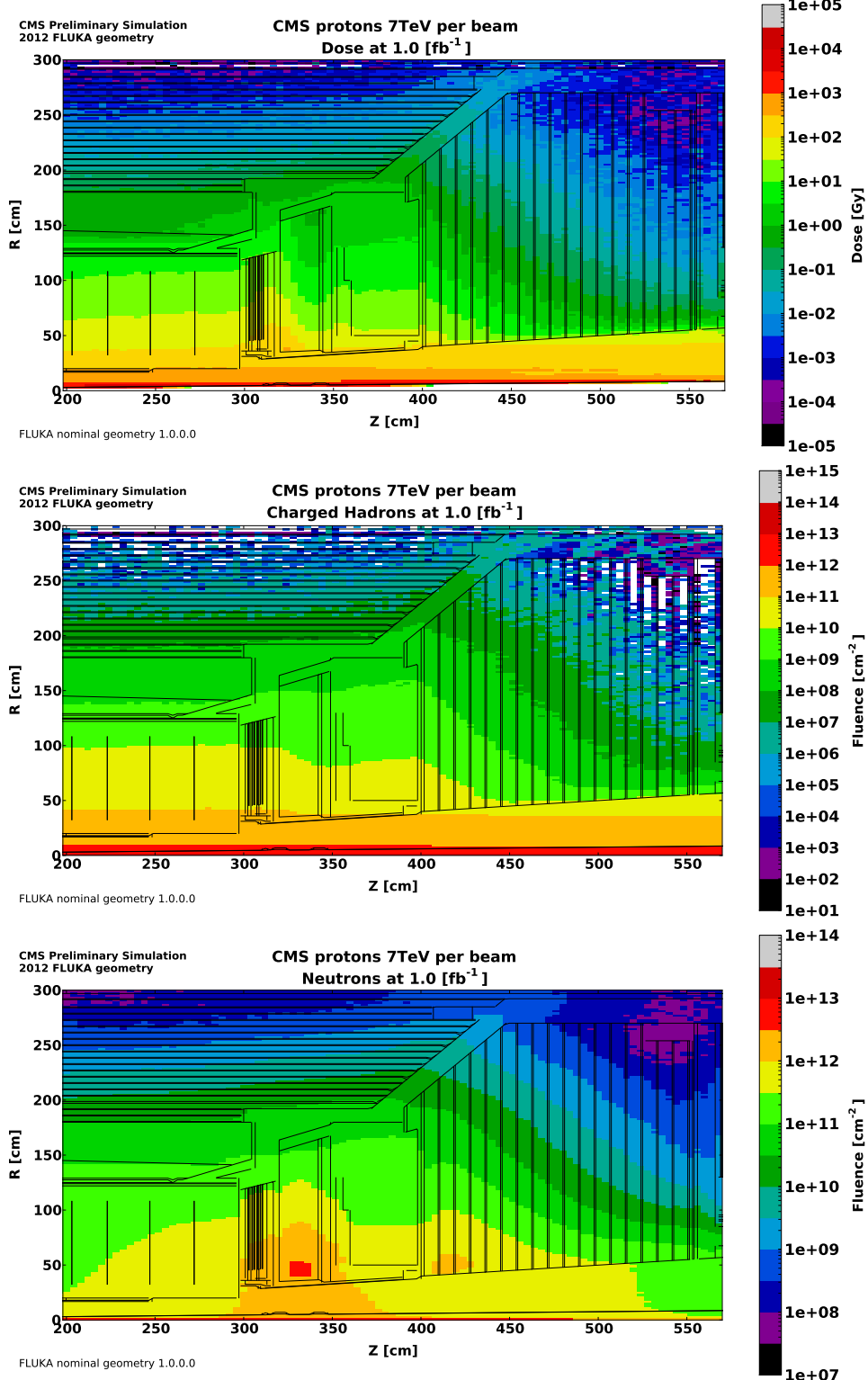


**Figure 3.4:** Monte Carlo prediction for the absorbed dose (top), the charged hadron fluence (middle) and the neutron fluence (bottom), at CMS for primary proton-proton collisions with an energy of 7 TeV. Values are obtained using FLUKA and correspond to an integrated luminosity of  $1 \text{ fb}^{-1}$ . The tracker geometry corresponds to the current detector (2012) which consists of  $500 \mu\text{m}$  thick layers of silicon surrounded by an average material density of  $0.047 \text{ g/cm}^3$ .

### 3.3 Proton Irradiation of PbWO<sub>4</sub> Crystals

#### 3.3.1 PS Irradiation Setup

A set of PbWO<sub>4</sub> crystals with dimensions identical to the ones used in the EE (rear face,  $30 \times 30 \times 220 \text{ mm}^3$ ) have been irradiated with 24 GeV protons at the Proton Synchrotron (PS) IRRAD3 facility at CERN [77] in 2011 and 2012. A picture of some of the irradiated crystals is shown in Fig. 3.5. Crystals have been irradiated to different proton fluences up to  $\approx 14 \times 10^{13} \text{ cm}^{-2}$  which almost cover the full range of fluences expected up to  $|\eta| = 2.6$  until the end of HL-LHC (see Table 3.1). During the irradiation at PS, the average proton flux through the crystal front face was around  $10^9 \text{ cm}^{-2}\text{s}^{-1}$ . The integrated fluence traversing the crystal face was measured to a precision of 10% using the activation of aluminium foils technique [78].

The beam profile was monitored using the standard instrumentation of the irradiation facility and was tuned before each irradiation to be uniform across a  $35 \times 35 \text{ mm}^2$  area. The beam monitoring was not operational during irradiation due to the very high radiation background in the experimental area caused by the beam-crystal interactions. The stability of the irradiation profile therefore relied on the stability of the beam line equipment. At the beginning of the 2012 irradiation campaign a new beam detector with higher sensitivity and finer granularity was installed for better beam profile monitoring. The beam profile for the 2012 irradiation is presented in Fig. 3.6.

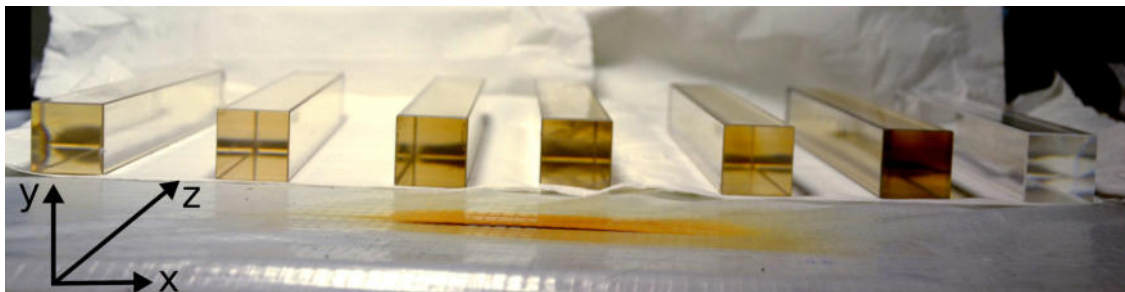


**Figure 3.5:** Picture of PbWO<sub>4</sub> crystals irradiated at different fluences. Top right crystal is non-irradiated and show the best transparency. The other crystals, having different  $\mu_{ind}$ , show different level of brownish color due to the creation of radiation induced defects.

#### 3.3.2 Light Transmission Measurements

The transparency loss was calculated for each crystal by measuring the light transmission curve in the 300-700 nm range, before and after irradiation, using the ACCOS spectrophotometer developed for quality control of the CMS ECAL crystals [79]. The induced

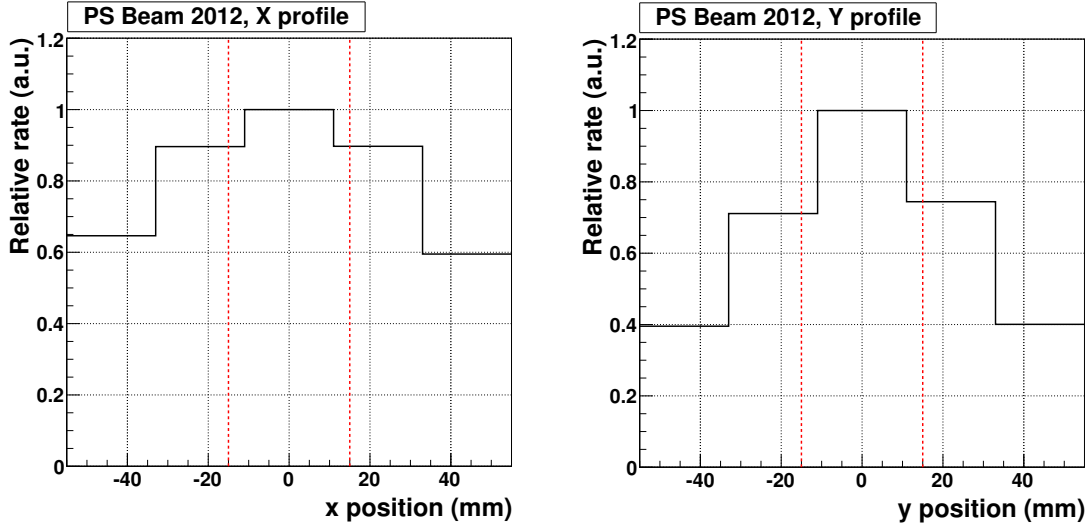


**Figure 3.6:** PS beam profile during the 2012 irradiation along X (left) and Y (right) axis of the crystal rear face. Red dotted line represents the crystal face dimensions.

absorption coefficient  $\mu_{ind}$  at 420 nm (maximum of the PbWO<sub>4</sub> emission spectrum) was obtained

$$\mu_{ind} = \frac{1}{L} \ln \frac{T_{before}}{T_{after}} \quad (3.3)$$

where  $L$  is the crystal length equal to 0.22 m,  $T_{before}$  and  $T_{after}$  are the crystal longitudinal light transmission at 420 nm before and after irradiation.

Since non-uniformities of the proton beam would lead to non-uniform damage in the crystal, the light transmission has been measured across the  $x$  and  $y$  axis of the crystal face using a dedicated spectrophotometer with an optical beam spot of 2 mm diameter. The transmission profiles were measured for all the crystals in the 300-700 nm range and the corresponding  $\mu_{ind}$  were calculated. Results obtained for one of the crystals irradiated in 2012 are shown in Fig. 3.7. Comparing the light transmission at 420 nm for different  $x$  and  $y$  coordinates across the crystal face, we observed a strong non-uniformity as shown in Fig. 3.7. Light transmission along the crystal length ( $z$  axis) was also measured and provided the longitudinal profile of 24 GeV protons damage inside the crystal (see Fig. 3.8).

To take into account the transverse non-uniformity of the damage, the value of  $\mu_{ind}$  used in this study represents the average  $\mu_{ind}$  over the whole crystal face. The average value is obtained using the damage profiles shown in Fig. 3.7, measured for each irradiation period. For 2012 crystals, the average  $\mu_{ind}$  corresponds to  $\sim 48\%$  of the  $\mu_{ind}$  measured by ACCOS in the centre of the crystal. For the crystals irradiated in 2011, the profiles are more uniform and the correction is close to 1. We estimate a 10% relative error on

### 3.3. Proton Irradiation of PbWO<sub>4</sub> Crystals

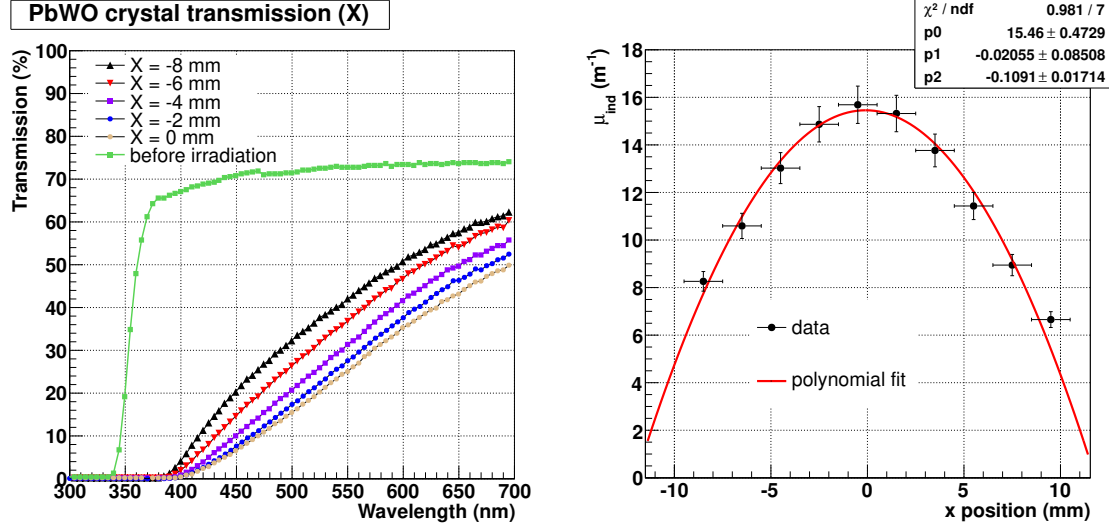


**Figure 3.7:** Left: Transmission curves for crystal 11135 (irradiated to a fluence of  $5.36 \times 10^{13} \text{ p/cm}^2$  in 2012) at different positions on the  $x$  axis of the crystal front face compared with a non-irradiated crystal (green line). Right: Transverse profile of the  $\mu_{ind}$  calculated from transmission curves at 420 nm. Spectrophotometer beam spot is 2 mm. Data points are fitted using a 2<sup>nd</sup> order polynomial function. Similar profile is obtained across the  $y$  axis.

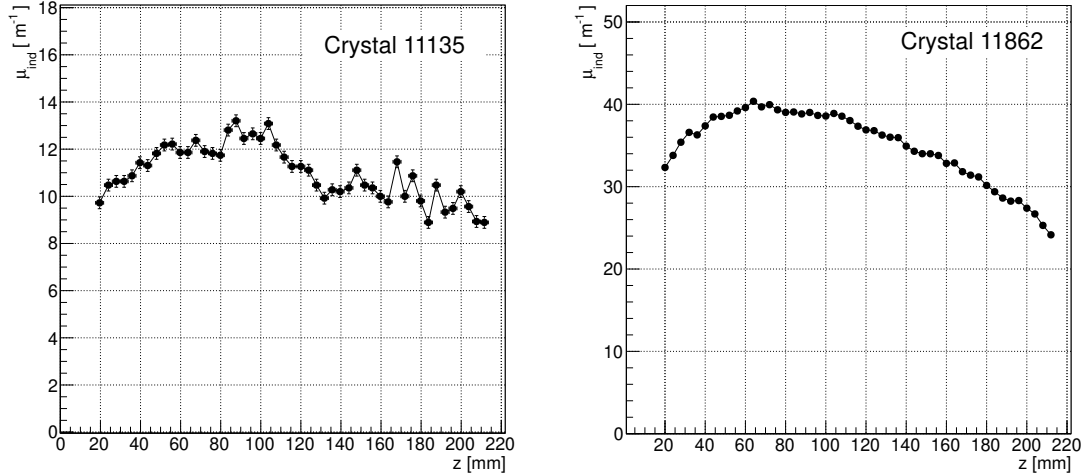


**Figure 3.8:** Longitudinal profile of the  $\mu_{ind}$  for crystal 11135 (left) and crystal 11862 (right) calculated from transmission curves at 420 nm. The spectrophotometer beam spot was 2 mm diameter. The front face of the crystal corresponds to  $z = 0$ .

the estimation of  $\mu_{ind}$  due to a  $\sim 2\%$  systematic error in the transmission measurement which propagates to  $\sigma_{\mu_{ind}}$  via Eq. 3.3. An additional uncertainty of 20% related to the transverse spread of  $\mu_{ind}$  is added in quadrature.

The correlation between the accumulated hadron fluence  $\Phi$  and the  $\mu_{ind}$  for crystals irradiated in 2011 and 2012 is shown in Fig. 3.9. A linear fit is performed, with the physical

constraint of  $\mu_{ind} = 0$  for  $\Phi = 0$ , yielding the relation

$$\mu_{ind} = 1.492 \times 10^{-13} \cdot \Phi \quad (3.4)$$

A similar correlation was obtained in previous studies [69] using ECAL barrel crystals irradiated up to  $\mu_{ind} \approx 10 \text{ m}^{-1}$ . This result is obtained on ECAL endcap crystals and extends the range of the study up to  $\mu_{ind} \approx 20 \text{ m}^{-1}$  yielding a more optimistic relation between hadron fluence and induced absorption. It is worth to notice that experimental uncertainties (mostly the irradiation beam specifics) are large. In addition, non linear mechanisms in the production of defects could occur for high fluences quenching the damage effects.

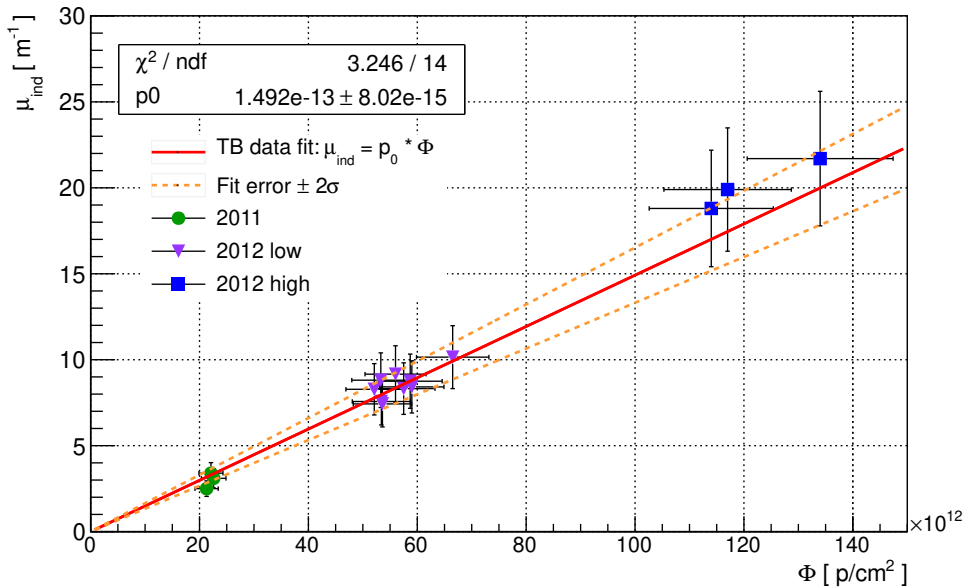


**Figure 3.9:** Correlation between the accumulated proton fluence and the  $\mu_{ind}$  for crystals irradiated in 2011 and two sets of crystals irradiated in 2012 at different fluences (low and high). The error bars take into account both systematic uncertainties in the light transmission and fluence measurements as well as the spread in the  $\mu_{ind}$  value across the crystal face. A linear fit (red line) is performed to obtain a correlation between proton fluence and induced absorption. The  $2\sigma$  uncertainties on the linear coefficient are shown as the orange dotted lines.

## 3.4 Test Beam Setup

To evaluate the calorimetric performance (energy resolution and linearity) of the irradiated crystals to high energy electrons (10-150 GeV), a beam test was set up at the H4 CERN facility. Details of the experimental setup are illustrated in the following.

### 3.4.1 Test Matrix

The calorimeter module components that were tested are essentially the spare parts of the real EE detector described in [44]. Twenty-five production EE-type crystals were placed in the standard supercrystal alveolar structure. The plastic inserts in front of the crystals were the same as those used in EE, while the aluminium inserts at the photodetector side were modified to house Hamamatsu Photonics photomultipliers (PMTs) [80]. Some additional mechanics were added to allow individual mounting of PMTs providing a small pressure of PMT against the crystal. The crystals were coupled to the PMT with an optical couplant with refractive index 1.45. The alveolar structure was surrounded by 1 cm thick Cu plates with pipes for the water circulation used for thermal stabilisation of the crystals. Two thermal sensors were installed on both sides of the crystal assembly. The precision of the temperature monitoring was better than 0.1°C and the temperature variation was found to be lower than 0.2°C with negligible effects on the system stability.

The scintillation light extracted from the crystals was read out using Hamamatsu Photonics PMTs instead of the standard Vacuum Photo Triodes (VPT) used in EE. This choice was made to allow the possibility of tuning the gain and guarantee a reasonable signal also for highly irradiated crystals with very low light output. Although, this configuration does not reproduce the real electronic noise of the current ECAL detector, it allows to precisely measure the evolution of its stochastic and constant terms without being dominated by the noise term contribution to the energy resolution.

During the 2011 runs 6-stage R5380 PMTs were used for the central  $3 \times 3$  crystals and 10-stage R8619 PMTs [81] for the others. During the 2012 runs all crystals were readout with 6-stage R5380 PMTs [82]. Both types of PMT have bialkali photocathodes and borosilicate glass windows of the same dimensions as in the VPTs used in EE [44]. This means that the  $\text{PbWO}_4$  scintillation light collection of the test module is similar to the light collection in the EE. The radiation damage effects on the crystal light collection uniformity should therefore be well reproduced.

A LED-based light monitoring system, similar to the one used in EE, was set up. It consisted of a blue LED light source (455 nm emission peak) and a bundle of quartz optical fibres used to deliver the light to the back end of each crystal. The module, including the cooling and light monitoring system, was mounted inside the sealed aluminium box which

provided the optical and thermal isolation. The box was installed on a remotely controlled table with a displacement range in  $x$  and  $y$  of  $\pm 30$  cm and positioning precision of  $\approx 1$  mm. A picture of the experimental box containing the test module is shown in Fig. 3.10.

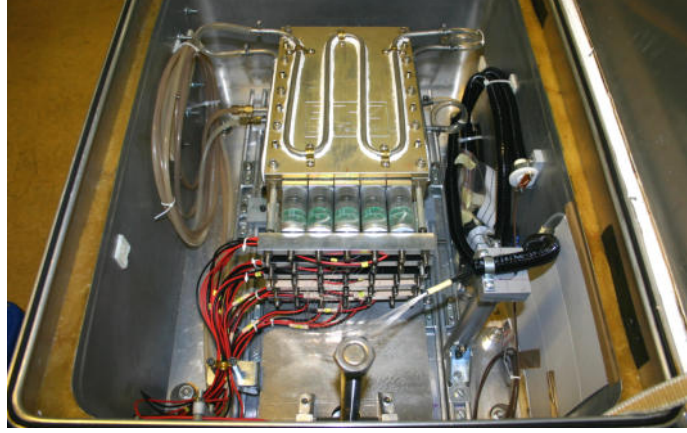


**Figure 3.10:** Test beam setup. The test beam crystals are in a carbon fibre alveolar structure inside cooling plates (yellow). PMTs with HV dividers (green) and cables are behind the crystals. The LED light source and fibres for light monitoring are attached to the right wall of the box.

### 3.4.2 Crystal Matrix Configurations

The crystals inside the test module were arranged in  $5 \times 5$  matrices configured to have the irradiated crystals placed within the central  $3 \times 3$  array and non-irradiated or slightly irradiated crystals in the outer part. The specific matrix configurations used for the test beam are shown in Fig. 3.11. The values of  $\mu_{ind}$  quoted on top of each crystal represent the average  $\mu_{ind}$  measured just before the beam tests.

### 3.4.3 Beam Counters

A sketch of the H4 beam line (located at the CERS SPS North Area) is presented in Fig. 3.12. The incoming beam particles were detected by a set of four 2 mm-thick scintillation counters: S1 ( $60 \times 60$  mm $^2$ ), S3 ( $40 \times 40$  mm $^2$ ), S4 ( $10 \times 10$  mm $^2$ ) and S6 ( $60 \times 60$  mm $^2$ ), installed at 5525 mm, 5340 mm, 5210 mm and 2820 mm from the front face of the crystal matrix, respectively. Two beam settings were used during the data acquisition: “Wide beam” – coincidence of S1&S6, and “Narrow beam” – coincidence of S1&S3&S4&S6. The impact point of beam particles on the crystal matrix was measured using two sets of hodoscopes. Each set was composed of two planes of 64 scintillating fibres of  $0.5 \times 0.5$  mm $^2$  cross-section, read out by a multi-anode PMT. The planes FH1 and FH3 measured the horizontal coordinate, and FH2 and FH4 the vertical one. These planes were installed at

### 3.4. Test Beam Setup

2012, Matrix 1 - $\mu = 0 \text{ m}^{-1}$					2011, Cluster 12 - $\mu = 3.5 \text{ m}^{-1}$					2011, Cluster 11 - $\mu = 10.1 \text{ m}^{-1}$				
0	1	2	3	4	0	1	2	3	4	0	1	2	3	4
11980	11820	11821	11932	11974	11141	11128	11992	11147	11950	11141	11128	11992	11147	11950
5	6	7	8	9	5	6	7	8	9	5	6	7	8	9
11177	0	0	0	0	9.8	5.1	3.1	3.6	9	9.8	5.1	3.1	3.6	9
10	11	12	13	14	11962	12014	11845	11121	11964	11962	12014	11845	11121	11964
11999	0	0	0	0	10.9	10.9	3.4	0.8	14	10.9	10.9	3.4	0.8	14
15	16	17	18	19	11118	11133	11856	11935	11928	11118	11133	11856	11935	11928
11981	0	0	0	0	11.4	2.5	0	2.6	19	11.4	2.5	0	2.6	19
20	21	22	23	24	7022	11830	11832	11952	11929	7022	11830	11832	11952	11929
11931	12000	12008	11819	12011	S4571	S4455	S4664	11819	12011	S4571	S4455	S4664	11819	12011

2012, Matrix 2 - $\mu = 10.9 \text{ m}^{-1}$					2012, Matrix 3 - $\mu = 7.7 \text{ m}^{-1}$					2012, Matrix 4 - $\mu = 20.3 \text{ m}^{-1}$				
0	1	2	3	4	0	1	2	3	4	0	1	2	3	4
11980	11820	11821	11932	11974	11980	11820	11821	11932	11974	11980	11820	11821	11932	11974
5	6	7	8	9	5	6	7	8	9	5	6	7	8	9
11177	4.0	10.9	3.6	0.8	11177	9.2	8.8	8.3	9	11177	9.2	8.3	7.6	9
10	11	12	13	14	10	11	12	13	14	10	11	12	13	14
11999	5.1	11.4	9.8	2.6	11999	10.2	7.4	8.8	14	11999	19.9	21.7	18.8	14
15	16	17	18	19	15	16	17	18	19	15	16	17	18	19
11981	3.4	10.9	3.1	2.5	11981	7.6	8.4	8.3	19	11981	10.2	8.4	8.8	19
20	21	22	23	24	20	21	22	23	24	20	21	22	23	24
11931	12000	12008	11911	11186	11931	12000	12008	11911	11186	11931	12000	12008	11911	11186

**Figure 3.11:** Top (from left to right): 5×5 matrix of non-irradiated crystals (“2012 matrix 1”); 3×4 matrix of proton-irradiated crystals tested in 2011, two 3×3 clusters centered around crystal 12 (“2011 cluster 12”) and 11 (“2011 cluster 11”) have been selected. Bottom (from left to right): 3×4 matrix of hadron-irradiated (“2012 matrix 2”); 3×3 matrices of hadron-irradiated crystals (“2012 matrices 3 and 4”). The 3×3 cluster of crystals used for the analysis is surrounded by a coloured line. The average value of  $\mu_{ind}$  for the selected cluster is also shown and is defined in Sec. 3.5.1.

6015 mm, 3490 mm, 5650 mm, and 3125 mm from the matrix respectively and provided the trigger signal to the front-end electronics and data-acquisition system.

#### 3.4.4 Readout

The signals from the PMTs, beam counters and hodoscopes were delivered to the counting room, located about 60 m from the beam zone, by coaxial cables. The signals from the PMTs were digitized by a VME LeCroy 1182 12 bit Charge Analog-to-Digital Converter (ADC) [83]. The integration time was set to 300 ns to accommodate the PMT pulse length and channel-to-channel transition time variation in the long coaxial cable connecting PMT output and ADC input. The signals from the beam hodoscopes were first connected to a custom shaping amplifier and then to 48-input LeCroy 4448 coincidence registers, read out via CAMAC bus. The signals from the beam counters were first connected to a NIM shaper and then processed by NIM-based logical units, generating the coincidence signal.

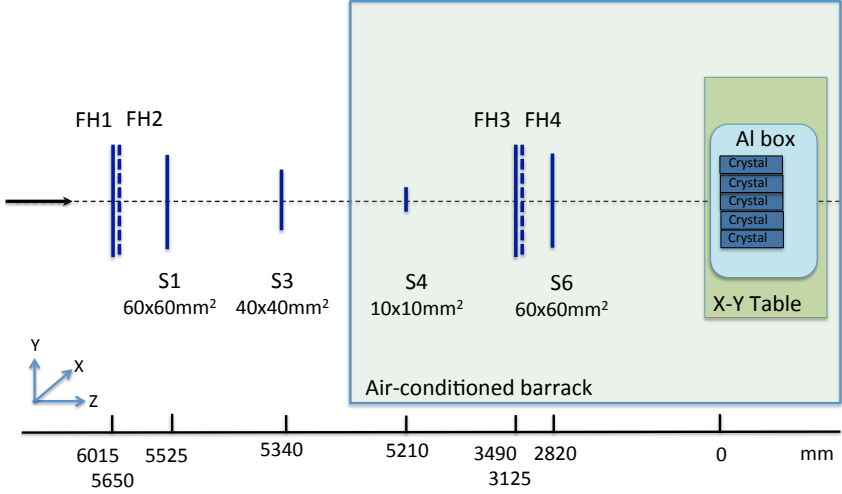


**Figure 3.12:** Sketch of the H4 test beam zone showing the position of the fibre hodoscopes (FH1, FH2, FH3, FH4) and the scintillation counters (S1, S3, S4, S6) with respect to the box containing the crystals. The black arrow indicates the beam direction.

### 3.4.5 Data Acquisition System

The data were read out via a CAEN VME-PCI bridge to a dedicated DAQ PC, running a LabView application [84]. Three types of event were recorded: “electron” – coincidence of the beam counter signals, “LED” – generated by the LED pulser, running at about 30 Hz, and “PED” – generated by a random gate generation at about 10 Hz rate and used for ADC pedestal measurement. All the triggers were mixed at the logical OR unit. Simple dead-time logic blocked the trigger input after arrival of any of the triggers for a period sufficient for the event readout.

All trigger signals together with the “spill” signal from the Super Proton Synchrotron (SPS), indicating the start and stop of particle spills in the beam line, were connected to a pattern unit to allow recognition of the type of trigger for each event. The SPS spill structure was slightly different for each run and even varied during the run, depending on the LHC operation. The overall cycle was 38-45 seconds and consisted of a slow extraction to the fixed target ( $\sim 10$  s) and several fast extractions for the CNGS neutrino beam and LHC injection. The beam data were collected during the slow extraction, recorded to disk and analysed during the remaining 25-30 seconds of the SPS cycle. A typical spill accumulated about 10k beam triggers and about 3k LED/PED events. The data taking rate was about 3000 events per spill.

### 3.4.6 Data Taking Procedure

#### PMT Stabilisation and HV Tuning

The high voltage (HV) of the PMTs was turned on about one week before the start of the beam test. The DAQ was also running before the test beam, acquiring LED and PED triggers. PMT gain stabilisation at a  $< 1\%$  level was observed with LED monitoring signals. After the beam start-up, the HV of each PMT was tuned such that the signal from 50 GeV electrons corresponded to a peak around 1500 ADC counts. This setting allowed the use of the same PMT gain for the whole energy scan in the 10-150 GeV range. For strongly damaged crystals in 2012 matrix 4 ( $\mu_{ind} \approx 20 \text{ m}^{-1}$ ) the required gain could not be achieved due to the maximum HV limit of the PMTs. In this case, the resulting peak position for 50 GeV electrons was around 1000 ADC counts.

#### Calibration Runs

Calibration of the crystal matrix readout chain was performed by positioning each crystal, one-by-one, into the 50 GeV electron beam by moving the table which supported the matrix. The table movement was controlled by the DAQ PC and the calibration procedure was fully automatic. The reproducibility of the table positioning was measured to be better than 1 mm. The beam trigger was set to the “Narrow beam” configuration and the particle rate was around 1 kHz. All three types of event: “electron”, “LED”, and “PED” were recorded. For standard beam conditions, the full matrix calibration required about 60 minutes.

#### Energy Scan

The energy scans were performed with the beam incident on the central crystal of each matrix. The electron momentum was defined by the magnet elements located along the beam-line. The current configuration of the H4 beam line provides an adequate quality of the electron beam in the 10 GeV/c to 150 GeV/c range with hadron and muon contamination below 0.2%, sufficient rate and small angular divergency. Beam momenta of 10, 20, 50, 100, 120 and 150 GeV/c were used. The momentum resolution of the beam line, defined by the collimators, was set to the optimal value for H4 of about  $\delta(p)/p = 0.3\%$ , where  $\delta(p)$  is the FWHM of the momentum distribution.

## 3.5 Test Beam Analysis

In this section, the method used to monitor the stability of the acquisition system and the quality of the data are presented. The procedure used to calibrate  $3 \times 3$  matrices of crystals in order to reconstruct electron energy is also discussed.

### 3.5.1 Average Induced Absorption for a $3 \times 3$ Matrix

The crystals inside the  $3 \times 3$  matrices used for this test are characterized by different values of  $\mu_{ind}$  according to Fig. 3.11. For this reason, it is useful to define an average  $\mu_{ind}^{3 \times 3}$  for each matrix as the sum of the  $\mu_{ind}$  of the corresponding crystals weighted for their relative contribution to the reconstruction of an electromagnetic shower centered on the  $3 \times 3$  matrix

$$\mu_{ind}^{3 \times 3} = \sum_{i=1}^9 \mu_{ind}^i \cdot w^i, \quad \sum_{i=1}^9 w^i = 1 \quad (3.5)$$

where for the central crystal,  $w^5$  is equal to 0.84, for the crystals adjacent to the central one  $w^2 = w^4 = w^6 = w^8 = 0.032$ , and for the crystals in the corners of the matrix  $w^1 = w^3 = w^7 = w^9 = 0.008$ . The weights have been determined by measuring the average fraction of energy deposited in each crystal of the  $3 \times 3$  non-irradiated matrix using 50 GeV electrons within  $10 \times 10 \text{ mm}^2$  beam spot.

### 3.5.2 LED Monitoring System

Light from the LED was injected into all 25 crystals of the supercrystal to monitor the gain stability of the PMTs which can vary with anode current. The purpose of this system was to verify that the gain of the PMTs was constant during and between spills. We define “LED stability” as the stability of the crystal+PMT+ADC readout chain monitored using the LED light injection as described above. The LED signal was monitored during a long acquisition run of about 26 hours and found to be stable within 0.5% as shown in Fig. 3.13. In some cases, on a time scale of several hours, a difference of a few percent in the recorded LED signal has been observed. To take these variations into account we monitored the global system response as described in Sec. 3.5.3.

### 3.5.3 System Stability

Approximately every 25 hours, the matrix was calibrated using a 50 GeV electron beam to monitor the effective response of the crystal+PMT+ADC chain for all 25 channels. On

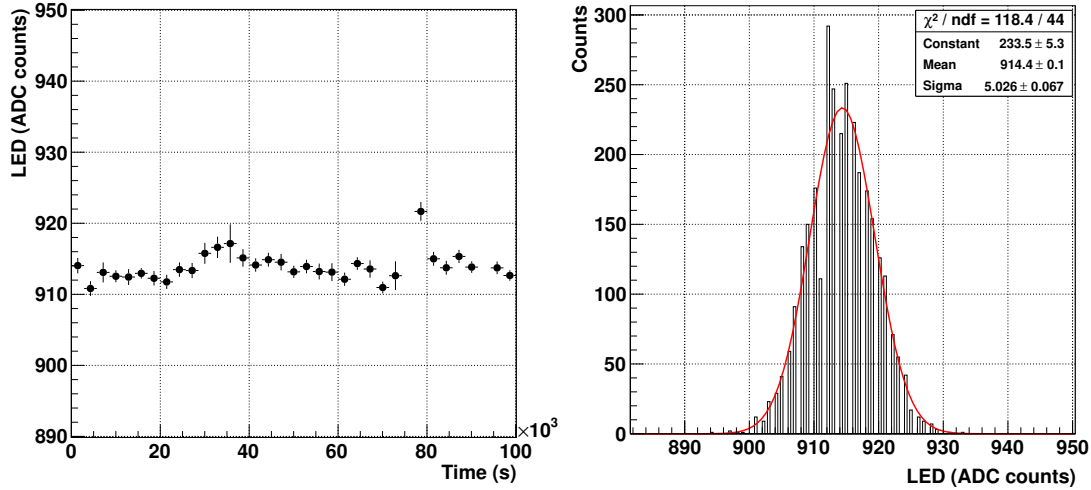


**Figure 3.13:** Left: The average LED signal versus time is shown during a long acquisition run of about 26 hours in May 2012 test beam, for the central crystal. Right: the LED amplitude distribution is fitted with a Gaussian function.

a time scale of several hours, a change in the PMT gain can occur, affecting the intercalibration coefficients and thus introducing a bias in the energy reconstruction. During some of the test beam running periods a drift in the response, up to 2%, was observed. Fig. 3.14 shows the system response evolution during several days of beam tests. To maintain the effect of these fluctuations below 1%, the intercalibration procedure was performed at least once per day during data taking.

### 3.5.4 Pedestal Subtraction

The value of the pedestal for each channel was continuously monitored. Both the mean pedestal value and its fluctuation,  $\sigma_{ped}$ , were estimated by fitting the pedestal peak. The mean has been subtracted from the signal channel-by-channel to obtain the correct signal amplitude. The  $\sigma_{ped}$  has been used to estimate the contribution of the PMT+ADC electronic noise to the energy resolution.

The noise contribution,  $B$ , to the reconstructed energy resolution using a  $3 \times 3$  cluster of crystals has been calculated by adding in quadrature the  $\sigma_{ped}^i$  of each channel  $i$  involved in the reconstruction

$$B = \sqrt{\sum_{i=1}^9 (\sigma_{ped}^i \cdot C_{calib}^i)^2} \quad (3.6)$$

where  $C_{calib}^i$  is the ADC to GeV conversion coefficient for a specific channel which allows the different gain of each PMT to be taken into account (see Sec. 3.5.6).

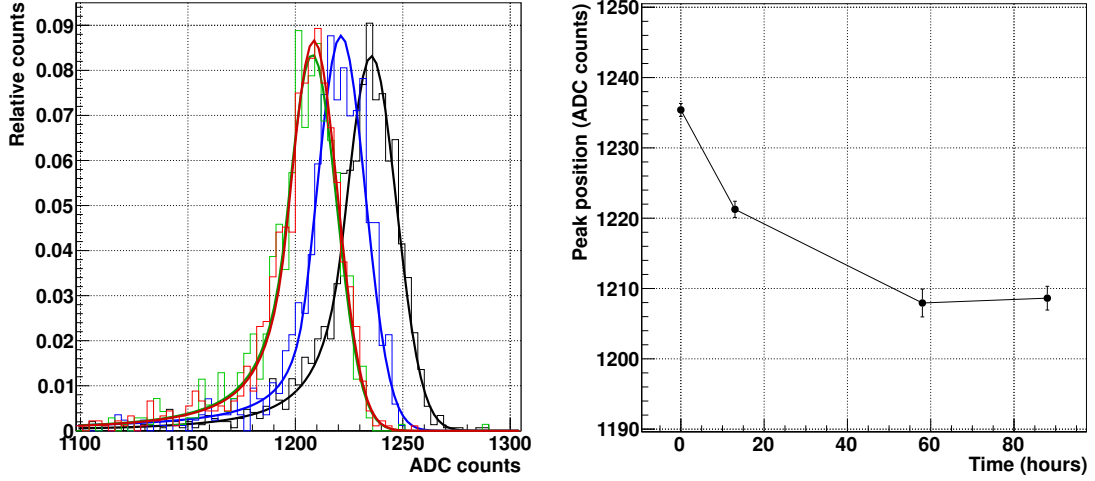


**Figure 3.14:** Left: ADC signal from a single crystal, corresponding to a 50 GeV electron beam striking the central crystal for different calibration runs. Right: Black points show the shift of the peak position obtained from fits of the distributions shown on the left plot. The error bar represents the error on the estimation of the peak position. The variation of the crystal + PMT system response as a function of time is due to unstable PMT gain.

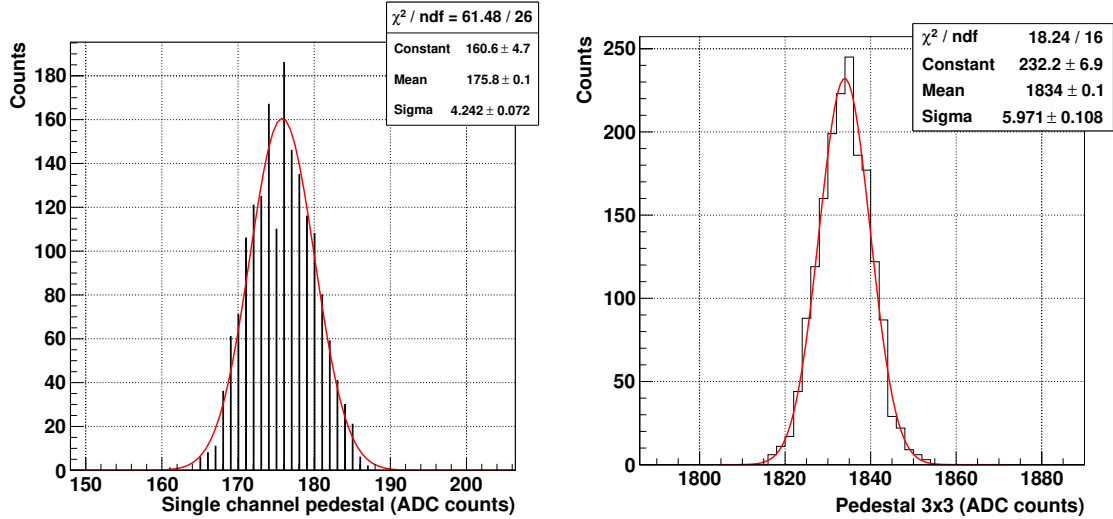


**Figure 3.15:** Left: distribution of pedestal signal corresponding to the central channel of 2012 matrix 1. Right: sum of the pedestals of the nine channels in 2012 matrix 1, with a Gaussian fit superimposed.

The pedestal of a single channel was around 200 ADC counts with a noise equivalent  $\sigma$  varying between 40 and 150 MeV depending on the specific channel. The pedestal of the central channel in the 2012 matrix 1 is shown in the left plot of Fig. 3.15. For the central  $3 \times 3$  cluster of the non-irradiated 2012 matrix, the sum of pedestals in ADC counts was

around 1800 with a noise equivalent  $\sigma_{ped}^{3 \times 3} = B \approx 220$  MeV. These values can change from matrix to matrix depending on the specific set of crystals and high voltages used for the PMTs but remain constant for a given configuration. Table 3.2 shows the values of  $B$  obtained for several matrix configurations. The specific noise of each matrix depends on the intrinsic noise of the PMTs which varies significantly from PMT to PMT. This will be an additional contribution to the systematic uncertainty of energy measurements.

Year	Matrix #	B [GeV]
2011	cluster 12	0.17
	cluster 11	0.17
2012	1	0.22
2012	2	0.34
2012	3	0.19
2012	4	0.25

**Table 3.2:** Contribution of the noise term to the energy resolution for each configuration of the matrices used during test beam running.

Eq. 3.6 is valid only if there is no correlated noise between the channels. This was verified looking for correlations between the pedestals of each pair of channels. No correlation was found. To verify this conclusion we also compared the results obtained from Eq. 3.6 with the spread of the distribution given by the sum of the pedestals from the nine central channels. The results obtained from the non-irradiated matrix are shown in the right plot of Fig. 3.15. The estimated contribution of the noise obtained with the two methods is consistent since the spread  $\sigma_{ped}^{3 \times 3}$  of the right spectrum in Fig. 3.15 is equal to the value obtained by summing in quadrature the individual contributions.

### 3.5.5 Beam Spot Selection

The beam hodoscopes,  $FH_{1,2}$  and  $FH_{3,4}$ , were positioned before the crystal matrix along the beam line at  $z_{FH_{1,2}}$  and  $z_{FH_{3,4}}$  respectively. They were used to reconstruct the hit position of the electron on the matrix  $(x_m, y_m)$  by extrapolating the particle trajectory

$$x_m = x_{FH_1} + (x_{FH_3} - x_{FH_1}) \cdot \frac{z_{FH_1}}{z_{FH_1} - z_{FH_3}} \quad (3.7)$$

The information on the electron position permits to study the crystal response as a function of impact point. These profiles enable the crystal center to be determined with respect to the matrix coordinate system  $(x_m, y_m)$ . The coordinates  $(x_c^i, y_c^i)$  of the center are obtained for each crystal  $i$  by fitting these distributions with a 2<sup>nd</sup> order polynomial function in the range of  $\pm 10$  mm (see Fig. 3.16).

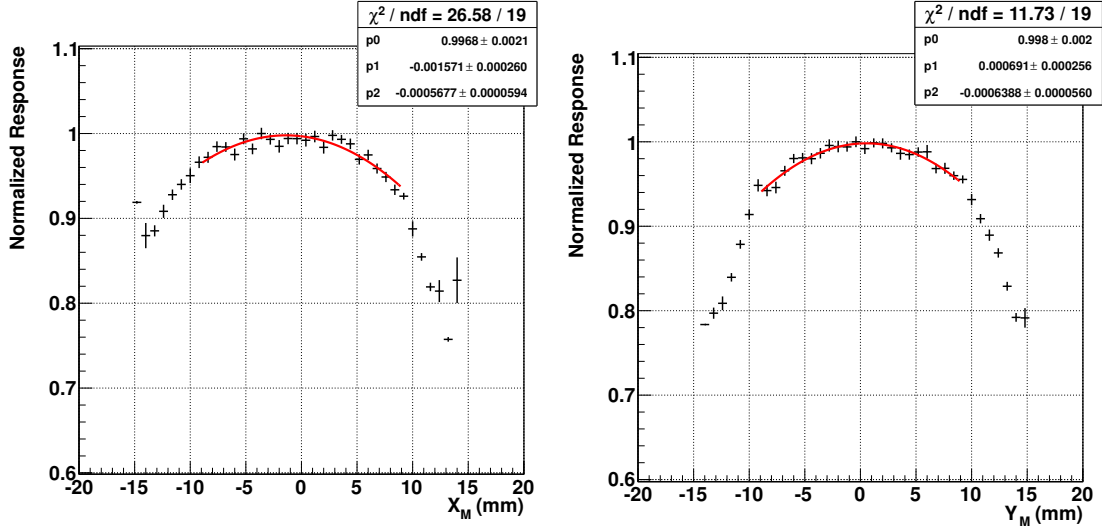


**Figure 3.16:** The profiles of the crystal response with respect to the impact point normalized at the maximum, shown separately for  $x$  and  $y$  axes in the matrix coordinate system. A 2<sup>nd</sup> order polynomial fit is performed in the range  $\pm 10$  mm to find the maximum which is assumed to be the center of the crystal. The plots correspond to the central crystal of the non-irradiated matrix.

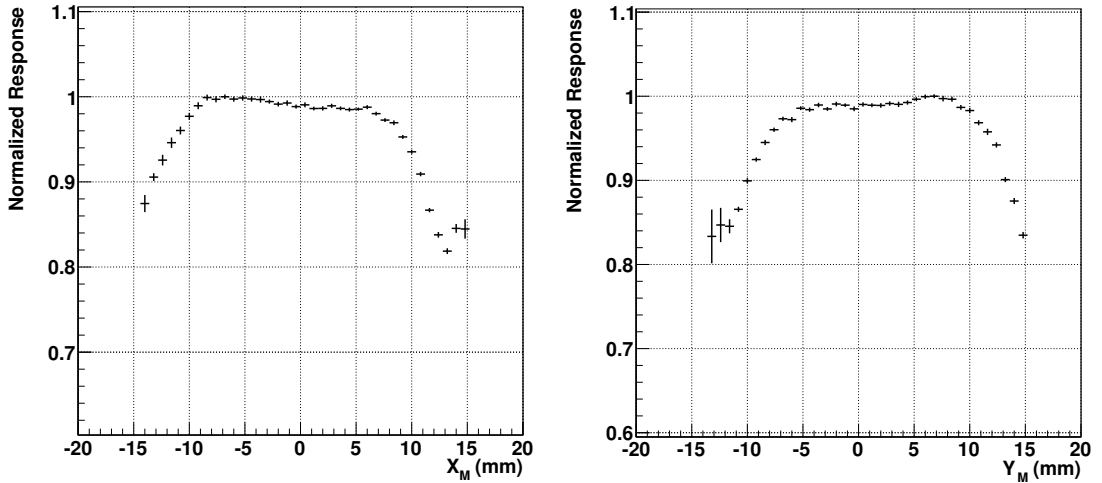


**Figure 3.17:** The profiles of the crystal response with respect to the impact point normalized at the maximum, shown separately for  $x$  and  $y$  axes in the matrix coordinate system. These distributions, obtained from central crystal of the irradiated matrix 3 in 2012, are not symmetric and their maximum does not correspond to the center of the crystal.

The fit has been performed both on  $x$  and  $y$  separately and the maximum response obtained is assumed to be the center of the corresponding crystal. This procedure allows to estimate the position of the center for each crystal in the matrix with a precision of  $\sim 1$  mm. For

### 3.5. Test Beam Analysis

---

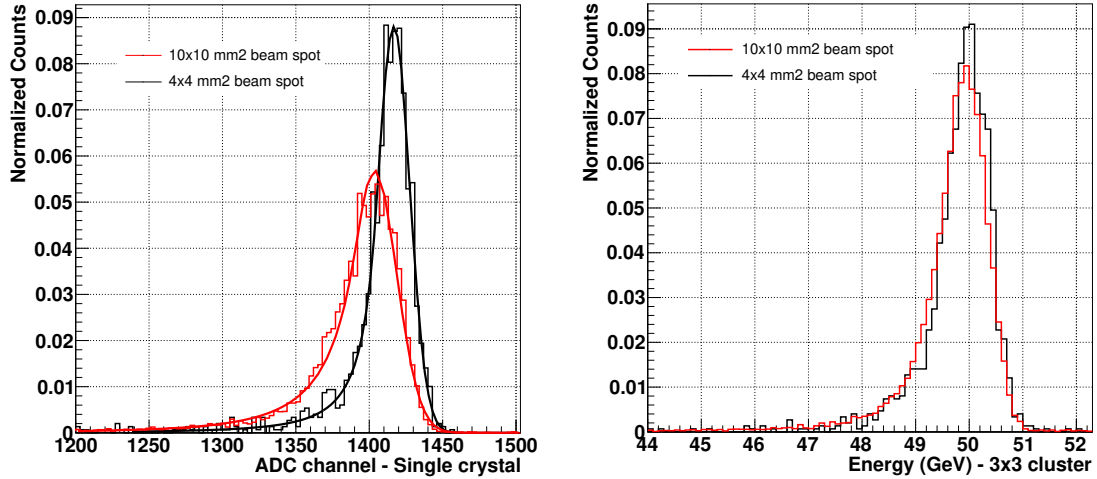


**Figure 3.18:** Left: Amplitude distributions of a single non-irradiated crystal with a 50 GeV electron beam and a beam spot selection of  $4 \times 4 \text{ mm}^2$  (black) and  $10 \times 10 \text{ mm}^2$  (red). A fit with a Crystal Ball function [85] is performed on both distributions to estimate the resolution and the peak position. Right: Amplitude distributions reconstructed using a  $3 \times 3$  cluster with a 50 GeV electron beam, with a beam spot selection of  $4 \times 4 \text{ mm}^2$  (black) and  $10 \times 10 \text{ mm}^2$  (red) for the non-irradiated matrix.

the irradiated matrices of 2012 we observed irregular containment distributions, as shown in Fig. 3.17, due to non-uniformities of the damage inside the crystals. Since this non-uniformity leads to a biased estimation of the crystal center, for the three irradiated matrices of 2012, the same coordinates of the centers as those extracted from the non-irradiated matrix were used, since the position of the box was maintained with 1 mm precision.

To calculate the intercalibration coefficients between crystals, a fit of the amplitude distribution of individual channels was used. A narrow beam spot of  $4 \times 4 \text{ mm}^2$  around the crystal center was selected in order to reduce fluctuations in amplitude due to partial shower containment. This selection improved the resolution of the peak and consequently the precision of the intercalibration coefficients as shown in Fig. 3.18. The relative differences in the peak positions and in the resolutions of amplitude distributions have been calculated with and without beam spot selection for all 25 crystals of the non-irradiated matrix. The resolution of the single crystal distributions improves from  $\sim 11\%$  (large beam spot) to  $\sim 9\%$  (narrow beam spot) and the peak position is shifted on average by  $\sim 1.4\%$ .

Such a beam spot selection reduces the statistics in proportion to the beam spot area. Furthermore, the efficiency of the beam hodoscopes ( $\sim 70\text{-}90\%$  per plane) used to record both x and y coordinates is an additional limiting factor. A beam spot selection of  $4 \times 4 \text{ mm}^2$

reduces statistics almost by a factor 10.

The energy spectra reconstructed using a  $3 \times 3$  cluster both with large ( $10 \times 10 \text{ mm}^2$ ) and small ( $4 \times 4 \text{ mm}^2$ ) beam spots are shown in Fig. 3.19 for three matrices from 2012. The improvement due to a smaller beamspot is lower than that obtained with the single crystal distribution because of the better containment of the shower in a  $3 \times 3$  cluster and it is partially compensated by the statistical error which increases. The improvement in resolution has been estimated to be around  $2 \pm 1\%$ . In the following analysis a beam spot of  $10 \times 10 \text{ mm}^2$  around the center of the crystal has been used to estimate the performance of the matrices.

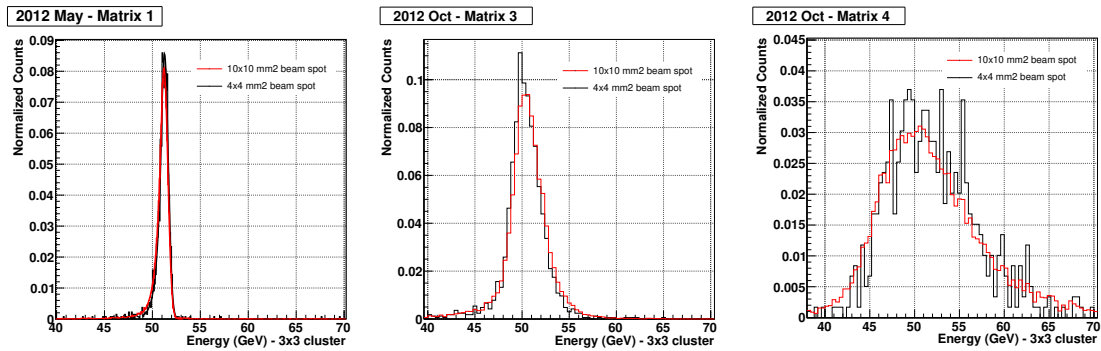


**Figure 3.19:** Amplitude distributions reconstructed using a  $3 \times 3$  cluster with a 50 GeV electron beam, with a beam spot selection of  $4 \times 4 \text{ mm}^2$  (black) and  $10 \times 10 \text{ mm}^2$  (red). From left to right the distributions corresponding to clusters centered around the central crystal for matrices of 2012 are shown, matrix 1 ( $\mu_{ind} = 0 \text{ m}^{-1}$ ), matrix 3 ( $\mu_{ind}^{3 \times 3} = 7.7 \text{ m}^{-1}$ ) and matrix 4 ( $\mu_{ind}^{3 \times 3} = 20.3 \text{ m}^{-1}$ )

### 3.5.6 Energy Calibration

The ADC-to-GeV conversion was performed using the relationship

$$E_i = G \cdot c_i \cdot S_i \cdot A_i \quad (3.8)$$

where  $A_i$  is the ADC signal from crystal  $i$ ,  $c_i$  the coefficient accounting for different PMT gain,  $S_i$  the coefficient which takes into account the crystal average transparency and crystal light yield and  $G$  is a calibration factor to convert ADC counts to GeV for a  $3 \times 3$  cluster. The values of  $c_i \cdot S_i$  have been obtained for all the crystals during calibration runs and vary between 1 and 2.5.

### Intercalibration Coefficients

The response of each crystal to 50 GeV electrons has been recorded through several calibration runs (Sec. 3.4.6). The amplitude distribution (in ADC channel) obtained for each crystal after the beam spot selection described in Sec. 3.5.5 has been fitted using a Crystal Ball function [85] which takes into account the asymmetric tails of the distributions. The inverse of the peak position obtained from the fit, normalized to a reference value, was used as the *intercalibration coefficient* for the corresponding crystal. These coefficients combine the  $c_i$  and  $S_i$  corrections.

To estimate the error that the beam spot selection and position dependent energy spectra can induce on the intercalibration coefficients, we varied the beam spot size in the range from  $2 \times 2 \text{ mm}^2$  to  $8 \times 8 \text{ mm}^2$  and compared the intercalibration coefficients obtained in the two cases. Assuming a precision on the beam spot size of  $\pm 1 \text{ mm}$ , the effect on the coefficients would be at the level of 0.2%. The center position was varied from  $x_{center} = y_{center} = -1 \text{ mm}$  to  $x_{center} = y_{center} = 1 \text{ mm}$ , which corresponds to the level of precision for the procedure used to calculate the centers in Sec. 3.5.5. We observed a variation of the estimated coefficients at the level of 0.2%.

### Energy Calibration Coefficient $G$

Once the individual crystals have been intercalibrated, the energy deposited by the shower within a  $3 \times 3$  cluster of crystals can be estimated by summing up all the contributions from the 9 crystals

$$E_{3 \times 3} = G \cdot \sum_{i=1}^9 c_i \cdot S_i \cdot A_i \quad (3.9)$$

The obtained distribution is then fitted using a Crystal Ball function to find the peak position in ADC counts which corresponds to a 50 GeV electron beam. We define the energy calibration coefficient  $G$  of Eq. 3.9 by setting the peak of the energy reconstructed using the  $3 \times 3$  matrix to be equal to the beam energy.

#### 3.5.7 Energy Linearity

The linearity of the readout chain, PMT+ADC, was not measured for this particular setup. The contribution of the PMT was estimated based on the producer specification [80] which is less than 1% for the peak output current of 10 mA, estimated as a maximum PMT current for the 150 GeV electron signal. The ADC contribution, according to the producer specifications [83], is ( $\pm 0.25\% + 2 \text{ ADC counts}$ ) within the full measurement range. A maximum readout chain non-linearity of 1% was then taken into account as a

systematic error.

The matrices have been exposed to the electron beam at several energies in the range between 10 and 150 GeV. The *energy linearity* has been defined as the ratio between the reconstructed energy and the nominal beam energy

$$\text{Linearity } (E_{beam}) = \frac{E_{3\times 3}}{E_{beam}} \quad (3.10)$$

By definition the linearity is equal to unity at 50 GeV, which is the energy used to calibrate the reconstructed response.

### 3.5.8 Energy Resolution

The standard parameterization of the energy resolution (see Sec. 2.2.3) has been used in this analysis

$$\left(\frac{\sigma_E}{E}\right)^2 = \left(\frac{A}{\sqrt{E}}\right)^2 + \left(\frac{B}{E}\right)^2 + C^2 \quad (3.11)$$

The value of the noise term  $B$  was fixed for each matrix configuration using the corresponding values in Table 3.2. To disentangle the noise contribution from the resolution of a given matrix, the noise term was subtracted in quadrature from the  $\sigma(E)/E$  for each matrix yielding the simplified formula

$$\left(\frac{\sigma_E}{E}\right)^2 = \left(\frac{A}{\sqrt{E}}\right)^2 + C^2 \quad (3.12)$$

The energy distributions of both irradiated and non-irradiated crystals show asymmetric tails which are persistent also when the  $4 \times 4 \text{ mm}^2$  beam spot selection is applied. This effect is shown in Fig. 3.20 for crystal 11135 before and after irradiation equivalent to  $\mu_{ind} = 7.4 \text{ m}^{-1}$ . In particular, a low energy tail is observed for non-irradiated matrices while a high energy tail appears for highly irradiated ones. This effect can be observed both in the energy distribution of the single crystal as well as in the  $3 \times 3$  energy distribution. In the single crystal distributions, the effect of partial containment of the shower is more relevant and leads to a more pronounced tail at low amplitudes.

Due to this change in the energy distributions a simple gaussian fit is not the best method to estimate the energy resolution. Two different methods for the estimation of the energy resolution were investigated. The first method performs a fit of the energy distributions using a Crystal Ball function. This method underestimates the peak width  $\sigma_{CB}$  by not appropriately taking into account the tails of the distributions.

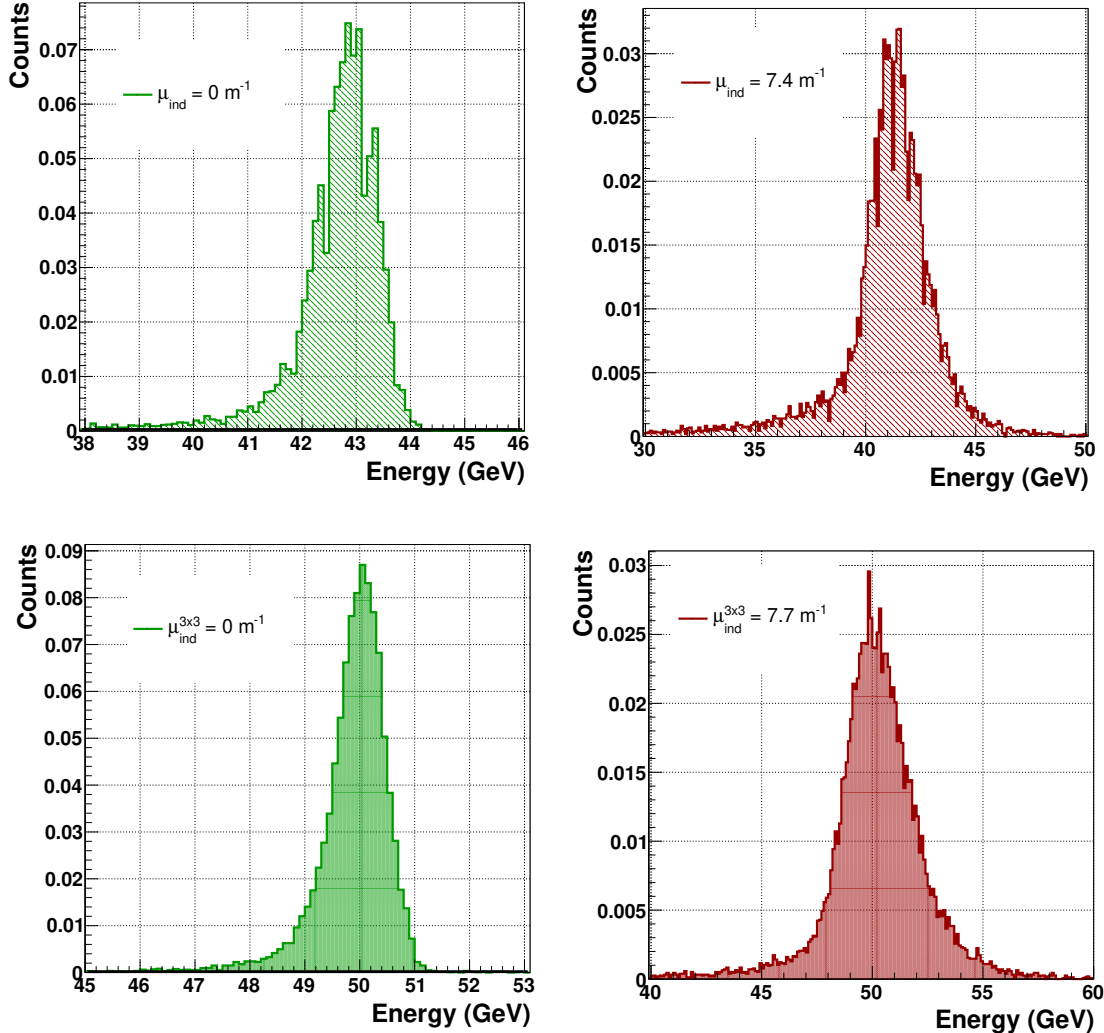


**Figure 3.20:** Single crystal 50 GeV electron energy spectra. Top: crystal 11135 before (left) and after (right) irradiation to a  $\mu_{ind} = 7.4 \text{ m}^{-1}$ . Bottom: 3×3 cluster of non-irradiated crystals in the 2012 matrix 1 ( $\mu_{ind}^{3\times 3} = 0 \text{ m}^{-1}$ ) centered on crystal 11135 (left) and the 3×3 cluster of irradiated crystals in the 2012 matrix 3 ( $\mu_{ind}^{3\times 3} = 7.7 \text{ m}^{-1}$ ) centered on crystal 11135 (right). A beam spot selection of  $4 \times 4 \text{ mm}^2$  has been applied to reduce shower containment effects.

The second method calculates the  $\sigma_{eff}$ , defined as half of the minimum interval containing 68% of the  $E_{3\times 3}$  distribution, and uses it for the estimation of energy resolution

$$\frac{\sigma(E)}{E} = \frac{\sigma_{eff}(E)}{E} \quad (3.13)$$

where  $E$  is the value obtained from a Crystal Ball fit corresponding to the most probable value of the  $E_{3\times 3}$  distribution. The second method, which uses the  $\sigma_{eff}$ , gives, as expected, a worse resolution than the first one. A comparison between the two methods applied to

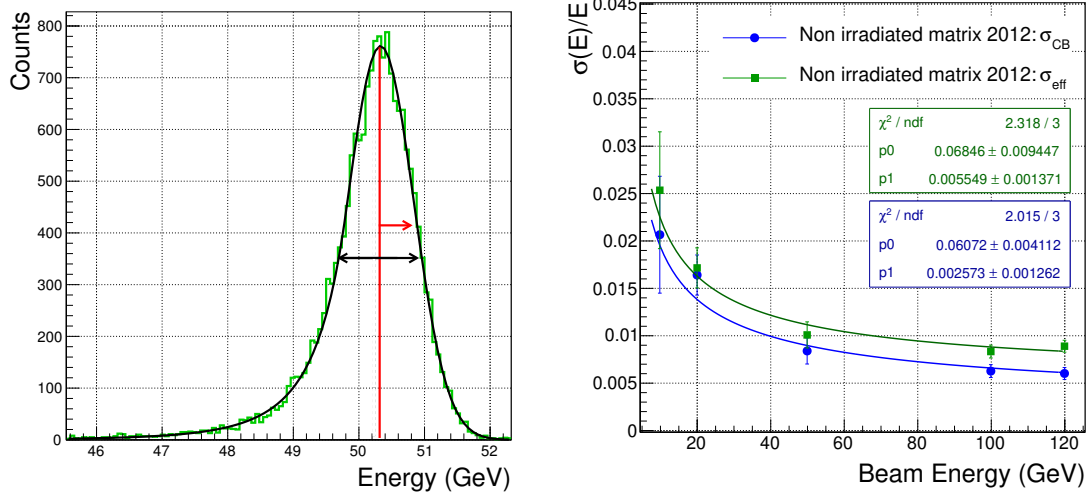


**Figure 3.21:** Left: amplitude distribution for a cluster of non-irradiated crystals using a 50 GeV electron beam. The red vertical line shows the position of the peak estimated using a Crystal Ball fit and the red arrow represents the value  $\sigma_{CB}$ . The black arrow represents the smallest interval containing 68% of the distribution equivalent to  $2\sigma_{eff}$ . Right: a comparison of the energy resolution estimated using the two different methods is shown for the non-irradiated matrix.

a matrix of non-irradiated crystals is shown in Fig. 3.21. The constant terms extracted from the fit using  $\sigma_{eff}$  and  $\sigma_{CB}$  are respectively 0.55% and 0.26%. In the following, only the results obtained using  $\sigma_{eff}$  are shown.

## 3.6 Test Beam Results

Results obtained during the test beam periods of 2011 and 2012 are summarized in this section. The analysis of scintillation pulses and the light output loss of damaged crystals is presented and a comparison of the energy resolution and linearity of  $3 \times 3$  crystal clusters belonging to different matrices is performed.

### 3.6.1 Scintillation Pulse Shapes

During the November 2011 test beam period, the measurement of the waveform of the pulse generated by a 50 GeV electron shower inside  $\text{PbWO}_4$  crystals was performed. For this measurement, PMT outputs were connected to an Agilent DSO90254A 2.5 GHz oscilloscope using 20 m high bandwidth coaxial cables and 1000 pulse waveforms were recorded for each crystal.

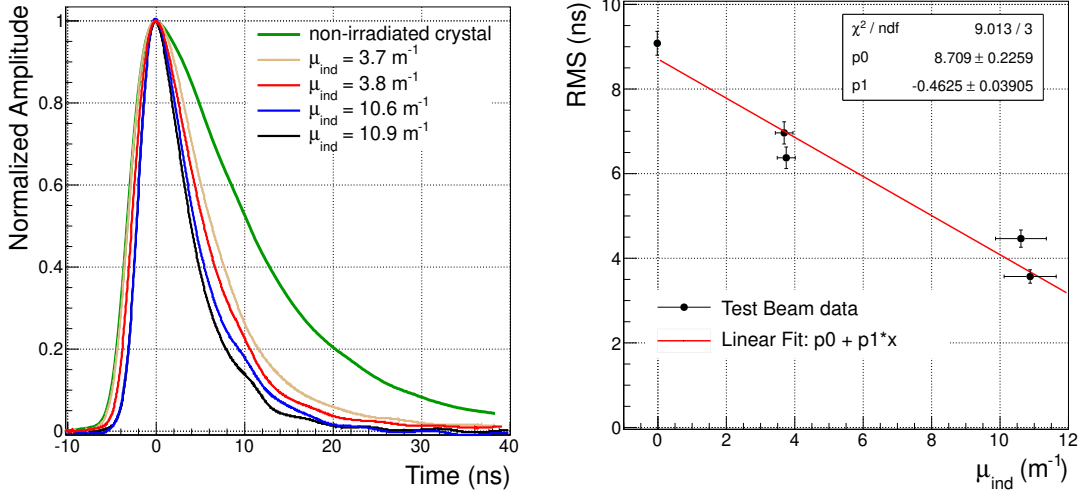


**Figure 3.22:** Left: Waveforms of a non-irradiated crystal and four proton-irradiated crystals are shown. The  $\mu_{ind}$  of the irradiated crystals is shown in the legend. Right: Correlation between  $\mu_{ind}$  and RMS of the average pulse fitted with a linear function (red).

The average waveforms, normalized to the amplitude, of a non-irradiated crystal and four proton-irradiated crystals are presented in Fig. 3.22. The pulse widths of the damaged crystals are almost twice shorter, which can be explained by the shorter average path of the scintillation photons due to the lower light transmission of the damaged crystals. A correlation between the  $\mu_{ind}$  of a given crystal and the RMS of its average waveform is shown in the right plot of Fig. 3.22.

### 3.6.2 Single Crystal Light Output

To estimate the Light Output (LO) loss of the proton-irradiated crystals, we compare the 50 GeV electron peak position of the irradiated and non-irradiated crystals, coupled to the same PMT with the same HV settings. The comparison was made using different crystals in June 2012 and using the same crystals in October 2012. The results are shown in Fig. 3.23.

A comparison between the peak position, obtained from a Crystal Ball fit of two different amplitude distributions, allows the LO loss to be obtained

$$LO_{loss} = \frac{Peak_{non-irr}^i - Peak_{irr}^i \cdot \frac{LY_1}{LY_2}}{Peak_{non-irr}^i}$$

The calculation of the LO loss has been performed by comparing crystals that have differences of 5-8% in their initial light yield (LY).  $LY_1$  is the LY of the reference non-irradiated

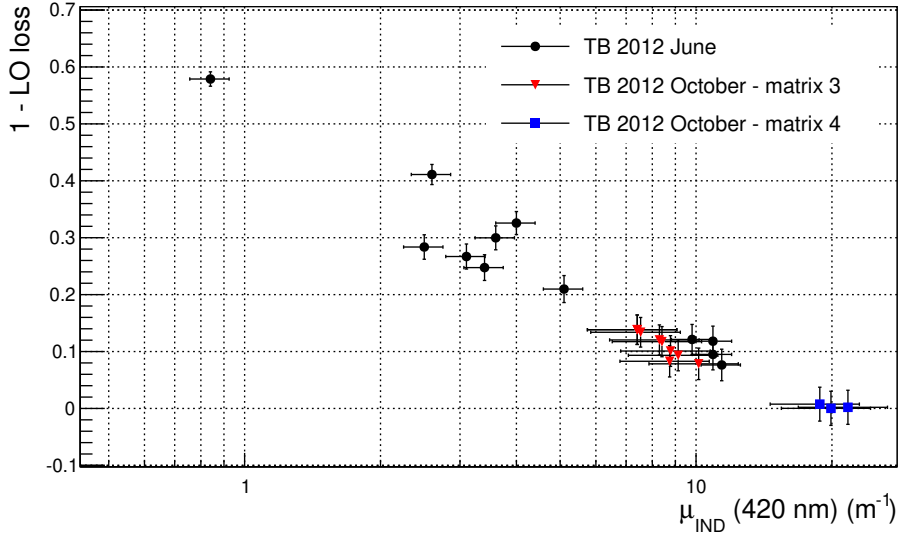


**Figure 3.23:** 1-LO<sub>loss</sub> corresponding to different values of  $\mu_{ind}$  is plotted on a logarithmic scale for 2012 June crystals (black circle), 2012 matrix 3 (red triangle) and 2012 matrix 4 (blue square).

crystal and  $LY_2$  is the LY of the irradiated crystal before being irradiated. A correction  $LY_1/LY_2$  was applied to take this difference into account. This correction will contribute to the systematic uncertainties due to the 5% precision of the light yield measurement. In October 2012, the LO loss was obtained comparing the same crystals before and after irradiation. In this case no correction for initial LY was needed. The average  $\mu_{ind}$  calculated for 2012 crystals, represents a lower limit to the effective  $\mu_{ind}$  which can affect the propagation of scintillation photons. This is due to the fact that the electron showers which start in  $10 \times 10 \text{ mm}^2$  around the crystal axis will produce the highest number of photons in the central region of the crystal where the damage is higher. However this effect is assumed negligible since the optical photons, being emitted isotropically, will travel along the whole crystal volume attenuated by an average value of  $\mu_{ind}$ . A detailed investigation of this effect will be discussed in Sec. 4.1.3.

The systematic error of this measurement has been estimated by comparing the light output of crystals which have not been irradiated and which should therefore have a LO loss equal to zero. The spread of the values around 0 is about 3% and we assumed this to be the systematic error affecting these measurements and dominating the statistical error due to the fitting procedure ( $\sim 0.1\%$ ). Estimation of LO loss for highly irradiated crystals ( $\mu_{ind} \approx 20 \text{ m}^{-1}$ ) is less precise since the contribution of the pedestal noise to the signal is stronger and the measured signal is very close to zero, as shown in Fig. 3.24.

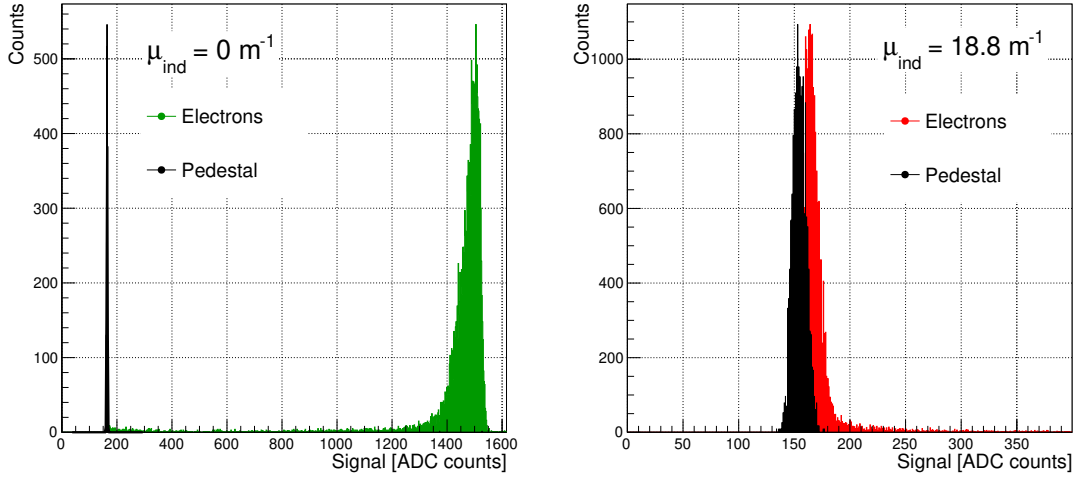


**Figure 3.24:** Left: ADC spectrum of a 50 GeV electron beam for crystal 11861 before irradiation. Right: ADC spectrum obtained for the same crystal after proton irradiation  $\mu_{ind} = 18.8 \text{ m}^{-1}$ . In both cases the black peak at low ADC values represents the pedestal.

### 3.6.3 Non-irradiated Matrix Performance

During May 2012 test beams, a  $5 \times 5$  matrix of non-irradiated crystals has been characterized with electrons to evaluate energy linearity and resolution. To estimate the systematic error of these measurements we computed the linearity and the resolution of all nine  $3 \times 3$  clusters centered around the nine central crystals. The average value of these curves was used as the best estimation for non-irradiated crystal linearity and resolution and the envelope was used to estimate the respective uncertainties.

A stochastic term of  $6.8 \pm 0.9\%$  and a constant term of  $0.55 \pm 0.13\%$  are obtained from the fit of the energy resolution curve in Figure 3.25. These values are consistent with results obtained in previous beam tests [44]. The response of the non-irradiated clusters to electrons of 10-120 GeV energy is linear within the experimental uncertainty of  $\sim 1\%$ .

### 3.6.4 Irradiated Matrices Performance

During the 2011 test beam period a matrix of proton-irradiated crystals with different  $\mu_{ind}$  in the range from 0 to  $11 \text{ m}^{-1}$  was tested. Some of the crystals were partially annealed by heating them to  $300^\circ\text{C}$  for several hours after irradiation, and the values of  $\mu_{ind}$  shown in Fig. 3.11 correspond to the induced absorption measured just before the beam test. The responses of two clusters centered around crystals 11 and 12 have been analyzed, and the average  $\mu_{ind}^{3 \times 3}$  of these highly non-uniform clusters is  $10.1 \text{ m}^{-1}$  and  $3.5 \text{ m}^{-1}$  respectively.

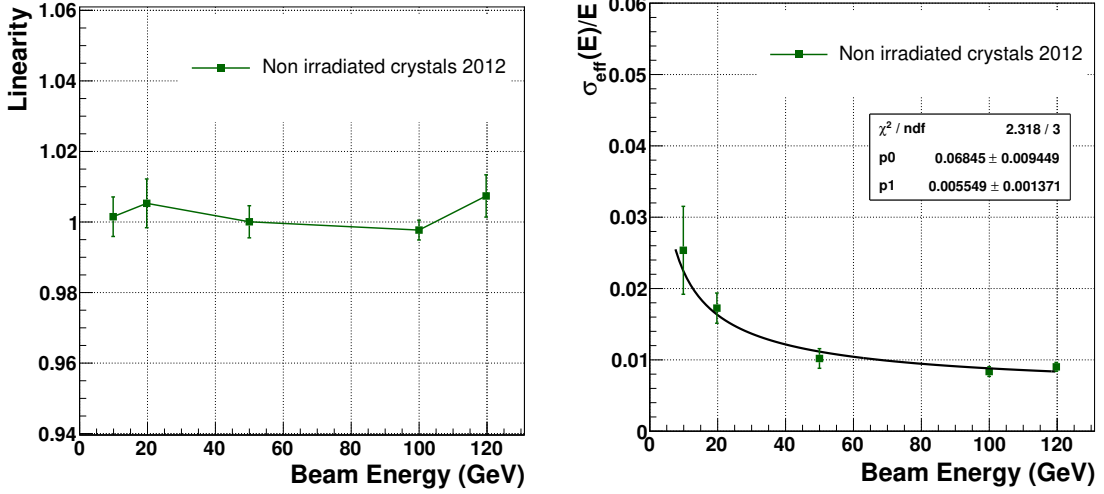


**Figure 3.25:** Average linearity (left) and energy resolution (right) for the  $3 \times 3$  clusters of non-irradiated crystals centered on the nine central crystals of 2012 matrix 1.

During the 2012 test beam period, three matrices of proton-irradiated crystals have been tested. Matrix 2 was made of crystals which were damaged and partially recovered during 2011, matrices 3 and 4 were made of the crystals from 2012 matrix 1 which had been irradiated at the CERN PS in July 2012 to fluences between  $5.3 \times 10^{13}$  p/cm<sup>2</sup> and  $1.3 \times 10^{14}$  p/cm<sup>2</sup>. The values of  $\mu_{ind}$  for the crystals used in the matrices studied during 2012 cover the whole range from 0 to  $20 \text{ m}^{-1}$ .

A comparison between the available matrix configurations has been performed to study the non-linearity as a function of  $\mu_{ind}^{3 \times 3}$  and the degradation of resolution due to the change of transparency of damaged crystals.

### Non Linearity of the Response

The matrices of non-irradiated crystals show a good energy linearity in the range 10-120 GeV whereas the irradiated matrices show an increasing non-linearity (see the left plot in Fig. 3.26).

The increase of non-linearity corresponding to higher values of  $\mu_{ind}$  can be interpreted as the effect of transparency loss on the uniformity of light collection efficiency  $\varepsilon_{LC}$  along the crystal length. A photon produced far from the photodetector will have a lower average probability to be detected which can be approximated by an exponential curve

$$\varepsilon_{LC} \approx K \cdot e^{-\nu(\mu_{ind}) \cdot D} \quad (3.14)$$

### 3.6. Test Beam Results

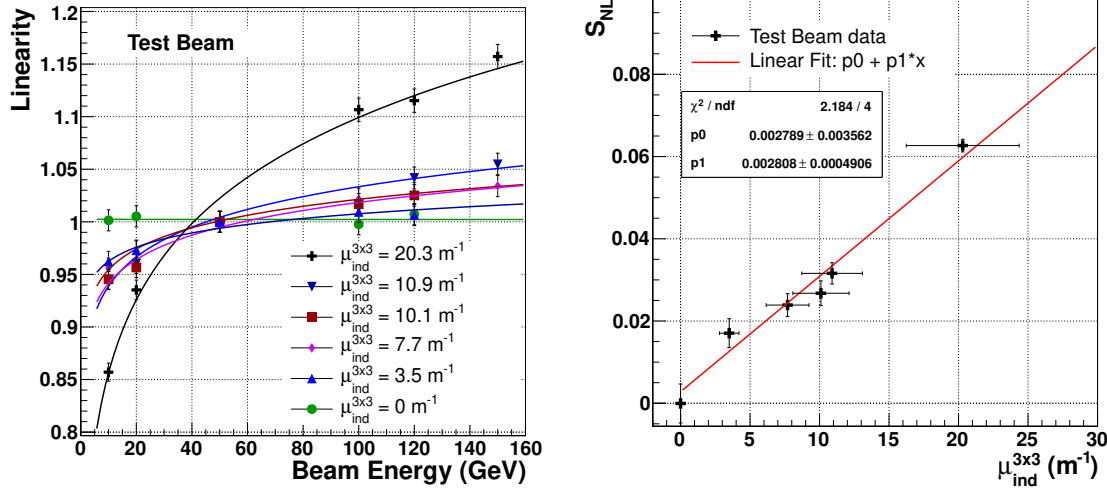


**Figure 3.26:** Left: Fit of linearity curves using the parametrization of Eq. 3.16. Right: Comparison between the non-linearity parameter  $S_{NL}$  obtained from the fit for different values of  $\mu_{ind}^{3\times 3}$ . Red line shows a linear fit of the data with no constraints on the parameters.

where  $K$  is the average probability for a photon produced at the distance  $D$  from the photodetector to be detected and  $\nu(\mu_{ind})$  is a positive attenuation coefficient which increases with larger  $\mu_{ind}$ . From Eq. 3.14 it can be seen that higher values of  $\mu_{ind}$ , i.e. higher values of  $\nu(\mu_{ind})$ , result in a larger non uniformity because the exponential curves become steeper.

Since the position  $t_{max}$  of shower maximum moves toward the rear face of the crystal with higher energy according to

$$t_{max} \propto \ln \left( \frac{E}{E_c} \right) \quad (3.15)$$

(with critical energy  $E_c = 7.94$  MeV for PbWO<sub>4</sub>), the light produced by low energy showers is more suppressed by the transparency loss since the average path to reach the photodetector is longer. The light attenuation along the crystal introduces a non-linear effect on the energy reconstruction. For each energy  $E_{beam}$  of the incoming electron, the exact effect of the  $\mu_{ind}$  on the non-linearity of the measured signal can be estimated by convoluting the longitudinal profile of shower development with the light collection efficiency curve  $\varepsilon_{LC}$ . In a first approximation, Eq. 3.14 and 3.15 suggest a parameterization of the linearity  $L$  as follows

$$L(E) = L_0 + \exp \left[ S_{NL} \cdot \ln \left( \frac{E}{E_c} \right) \right] \quad (3.16)$$

where  $S_{NL}$  is a non linearity parameter related to  $\mu_{ind}$  and  $L_0$  is an offset which takes into account the arbitrary normalization at 50 GeV. Using Eq. 3.16, in which  $L_0$  and  $S_{NL}$  are

Matrix ID	$\mu_{ind}^{central}$ [m <sup>-1</sup> ]	$\mu_{ind}^{3\times 3}$ [m <sup>-1</sup> ]	A [% GeV <sup>1/2</sup> ]	C [%]
2012 - matrix 1	0.0	0.0	$6.8 \pm 0.9$	$0.5 \pm 0.1$
2011 - cluster 12	3.4	3.5	$8.9 \pm 0.6$	$2.3 \pm 0.2$
2012 - matrix 3	7.4	7.7	$12.7 \pm 1.0$	$3.1 \pm 0.2$
2011 - cluster 11	10.9	10.1	$11.8 \pm 0.8$	$3.7 \pm 0.2$
2012 - matrix 2	11.4	10.9	$12.5 \pm 1.4$	$4.9 \pm 0.3$
2012 - matrix 4	21.7	20.3	$24.5 \pm 3.0$	$10.3 \pm 0.5$

**Table 3.3:** Stochastic and constant terms affecting the energy resolution as extracted from the fit are shown together with the central and average  $\mu_{ind}$  of the corresponding matrix.

free parameters, the linearity curves obtained from irradiated matrices have been fitted and the values of  $S_{NL}$  have been estimated. A good correlation between the value of  $S_{NL}$  and the  $\mu_{ind}^{3\times 3}$  of the corresponding matrix is observed as shown in the right plot of Fig. 3.26.

### Degradation of Energy Resolution

The curves of the energy resolution of each matrix have been compared in the left plot of Fig. 3.27 and a fit was performed in order to estimate the stochastic and constant terms. The values obtained from the fit using Eq. 3.12 are shown in Table 3.3.

The constant term degrades with increasing average  $\mu_{ind}$  of the crystals. In this test, several contributions affect the constant term: the different  $\mu_{ind}$  of the crystals within a  $3\times 3$  cluster, the partial containment of the shower inside the limited size of the matrix and the non-uniformity of light collection efficiency along a single crystal. The plots of Fig. 3.27 show that the constant term evolves from 0.55% for non-irradiated matrices to 10.3% for the most damaged matrix tested in 2012. To estimate the change in the constant term  $\Delta C$  induced by the damage and hence related to an increase of  $\varepsilon_{LC}$  non-uniformity, we subtracted the constant term of a non-irradiated matrix  $C_{ni}$  from the values of irradiated matrices  $C_i$  according to

$$\Delta C = \sqrt{C_i^2 - C_{ni}^2} \quad (3.17)$$

and compared this value with the  $\mu_{ind}^{3\times 3}$  of the corresponding cluster. A good correlation is observed between the increase of the constant term and the value of  $\mu_{ind}^{3\times 3}$ . The linear fit shown in the right plot of Fig. 3.27 provides a parametrization of this effect within the range of the measurements ( $\mu_{ind} = 0 - 20$  m<sup>-1</sup>).

The stochastic term obtained from the fit has been plotted as a function of the LO loss (Sec. 3.6.2) for the central crystal of the corresponding cluster. The evolution of stochastic

### 3.6. Test Beam Results

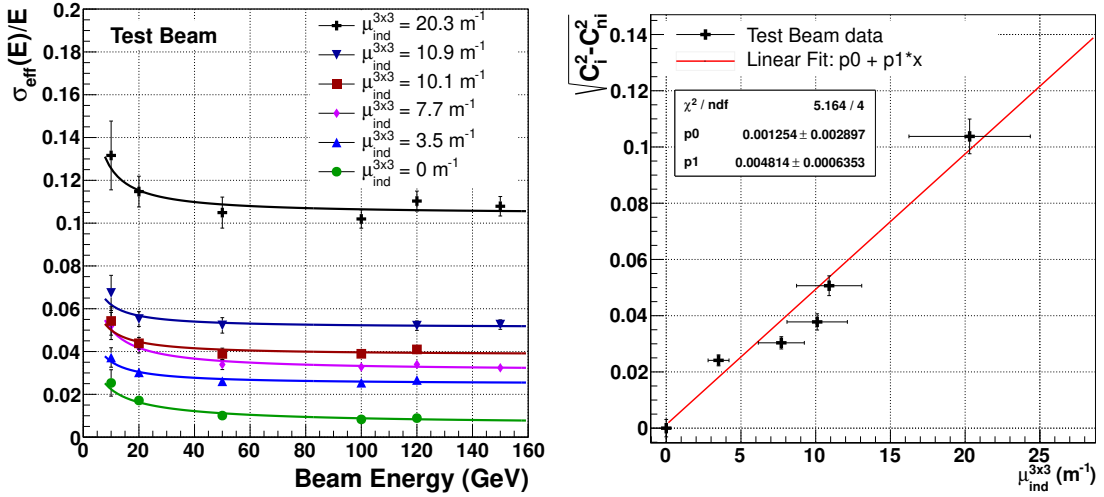


**Figure 3.27:** Left: the resolution at different energies is compared for different matrices. Right: correlation between the constant term degradation due to non-uniformity of light collection and the corresponding  $\mu_{\text{ind}}^{3\times 3}$ .

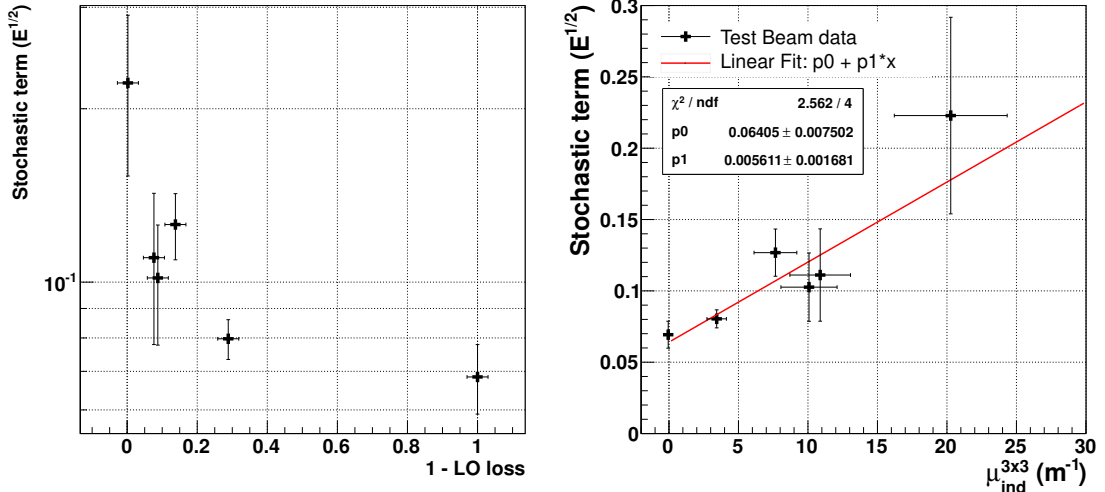


**Figure 3.28:** Left: Evolution of stochastic term extracted from the fit of energy resolution as a function of the LO loss of the central crystal in the  $3\times 3$  cluster. Right: correlation between the stochastic term and the corresponding induced absorption  $\mu_{\text{ind}}^{3\times 3}$ .

term is also shown as a function of the  $\mu_{\text{ind}}^{3\times 3}$  in the right plot of Fig. 3.28 and shows a consistent degradation. The estimation of the stochastic term obtained from the fit in Fig. 3.27 strongly relies on the low energy measurements (10-20 GeV). Due to the very few points available in this energy range it is subject to large fluctuations and can only be used as a qualitative indication.

### 3.7 Conclusions

This chapter provides important informations on the performance degradation expected for CMS ECAL endcap supercrystals in terms of light output loss, response linearity and energy resolution. The beam test was performed on calorimetric modules, constructed from  $5 \times 5$  proton-irradiated PbWO<sub>4</sub> crystals identical to those of ECAL endcaps. The tested modules were made of PbWO<sub>4</sub> crystals with different levels of proton induced damage up to an induced absorption coefficient  $\mu_{ind}$  of  $21 \text{ m}^{-1}$  for a fluence of  $1.3 \times 10^{14} \text{ p/cm}^2$ . Assuming no dose rate dependency and no annealing of the hadron damage, such induced absorption coefficients are expected to represent the effect of the charged hadron fluences predicted for the ECAL Endcaps (at  $|\eta| = 2.6$ ) up to an integrated luminosity of  $\sim 3000 \text{ fb}^{-1}$ .

The data collected during several test beam periods performed at the H4 facility at CERN have been analyzed and compared. Several important effects have been observed and understood. The light output significantly decreases due to transparency loss of the irradiated crystals. In addition, the detected scintillating pulses of crystals become faster as  $\mu_{ind}$  increases.

Using electrons in the 10-150 GeV energy range, the response of  $3 \times 3$  matrices of crystals has been investigated. A non-linearity of the energy reconstructed using irradiated matrices has been observed. We parameterized this effect as a function of  $\mu_{ind}$  using the experimental data. In addition, we observed that the constant term of the energy resolution increases from  $\sim 0.55\%$  to  $\sim 10.3\%$ . Other effects, such as variation in the shape of the amplitude distribution, have also been observed.

These results suggest that the main effects of the proton radiation damage in PbWO<sub>4</sub> crystals can be understood and described, to a first approximation, in terms of the light transmission loss inside the crystal. A simulation model was built to confirm this interpretation and to reproduce the degradation of crystal performance. The details of the simulation and the comparison with experimental results are presented in Chap. 4.

# Extrapolation of EE Crystals Performance Until the End of HL-LHC

---

The test beam results presented in Chap. 3 confirm that major effects of radiation damage in PbWO<sub>4</sub> crystals, i.e. resolution degradation, non linearity, light output loss and change in the pulse shape, are proportional to the  $\mu_{ind}$  of the crystal. To confirm and further improve the understanding of the mechanisms involved in the degradation of crystal performance, a simulation model was built (Sec. 4.1). It was demonstrated that reducing crystal transparency, i.e. increasing the probability that an optical photon is absorbed along its path, all the damage effects experimentally observed can be reproduced. The simulation was then validated through a detailed comparison with test beam data and allowed to extrapolate the ECAL performance throughout the whole operation of LHC and HL-LHC (Sec. 4.2).

## 4.1 Comparison of Test Beam Data with Simulation

Comparison of test beam data with simulation is a not straightforward task. Experimental measurements are affected by several systematics which are difficult to precisely reproduce in the simulation. Some of them are: limited precision on crystal intercalibration, non-uniform  $\mu_{ind}$  inside the crystals and between different crystals of a given matrix, beam profile, beam angular divergence, etc. In order to minimize these systematics, the comparison between data and simulation has been performed using the response of individual crystals instead of the 3×3 cluster reconstruction. In this case, transverse containment effects become more relevant and thus a beam spot selection of 4×4 mm<sup>2</sup> has been applied

on the events. The effects of this selection have been discussed in Sec. 3.5.5. The same beam spot selection has been applied also in the simulation, thus the influence of shower leakage on the energy resolution and linearity is supposed to be the same.

#### 4.1.1 Simulation Setup

The Geant4 toolkit [86] was used to simulate the setup geometry and all the physical processes from energy deposition to ray-tracing. The tapered geometry of EE crystals and the alveolar structures are reproduced as described in [44]. Two decay time constants of 5 ns and 15 ns with relative intensity of 40% and 60% respectively have been used. The emission spectrum and the intrinsic absorption length are obtained from laboratory measurements of non-irradiated EE crystals and are shown in Fig. 4.1.

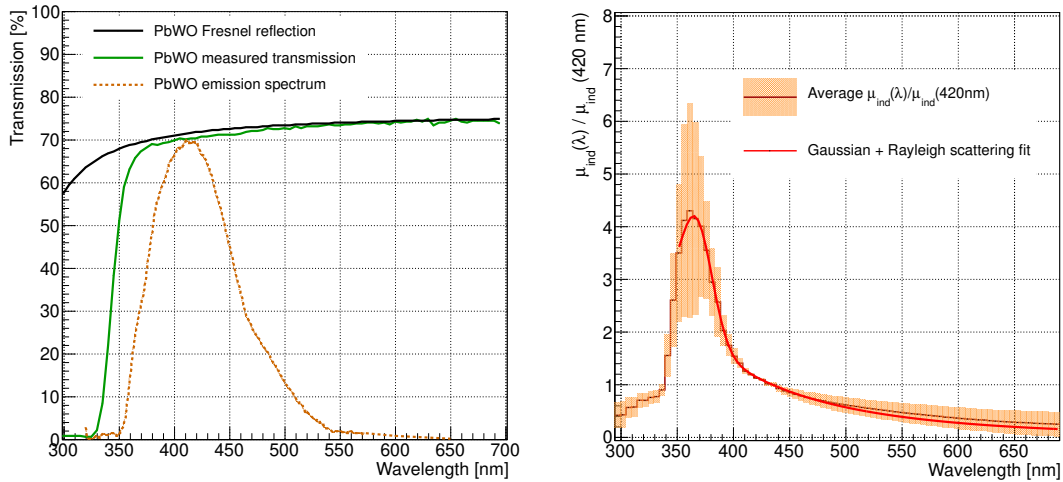


**Figure 4.1:** Left: maximum theoretical transmission of  $\text{PbWO}_4$  crystals compare with real transmission curve and emission spectrum measured on a non-irradiated EE-type crystal. Right: measurement of proton-induced absorption as a function of  $\lambda$  (normalized at 420 nm). Orange envelope represents the spread of measurements on different crystals.

The wavelength dependence of transmission loss due to hadron damage is obtained from experimental data as well. As shown in Fig. 4.1, regardless of the absolute value of  $\mu_{ind}$ , the  $\lambda$ -dependance has the same behavior and can be parameterized as

$$\mu_{ind}(\lambda) = A \cdot \lambda^{-4} + B \cdot e^{-\frac{(x-C)^2}{D^2}} \quad (4.1)$$

where the first term proportional to  $\lambda^{-4}$  represents the Rayleigh scattering and the gaussian component corresponds to an absorption band induced by radiation. The values of parameters obtained from the fit of experimental data are  $A = 3.11 \times 10^{10}$ ,  $B = 4.33$ ,  $C = 362.61$  and  $D = 14.99$ . A photodetector with size and refractive index as those used

in the test beam and coupled with grease to the rear face of the crystal has been simulated. As a first approximation, a uniform  $\mu_{ind}$  inside the crystal volume has been used. Effects of non-uniform  $\mu_{ind}$  are studied separately in Sec. 4.1.3 and are found to be negligible.

### 4.1.2 “Fast” and “Full” Simulations

Each simulated event consists of the following steps:

1. An electron with a given momentum is generated within a beamspot of  $4 \times 4 \text{ mm}^2$
2. Shower development is simulated and energy is deposited inside the crystal
3. Scintillation light is produced according to the scintillating properties of PbWO<sub>4</sub>
4. Optical photons are traced through the crystal until they reach the photodetector

Two different approaches are used to simulate the events: a “full” simulation and a “fast” simulation. The former uses Geant4 for the whole chain of processes whereas the latter makes use of a parameterization of the light collection efficiency along the crystal which allows to avoid the time-consuming simulation of steps 3 and 4.

#### Fast Simulation

To reduce the computation time of the simulation, it is more convenient not to trace every single photon generated during the shower development of each event. A possible solution which was adopted is to split the simulation into two separate steps: estimation of light collection efficiency inside the crystal and shower development.

When ionization energy is deposited in a point of the crystal volume it is converted into optical photons via the scintillation process described in Sec. 1.2. The probability for an isotropic photon produced at a position  $(x, y, z)$  inside the crystal will have an average probability  $\varepsilon_{LC}$  to be detected. By producing a large number of isotropic photons in each point of the crystal volume and measuring the fraction of detected photons as a function of position, 3D maps of light collection efficiency,  $\varepsilon_{LC}$ , can be obtained. For different values of  $\mu_{ind}$  this efficiency will be different as shown in Fig. 4.2 since the probability of photon absorption increases with  $\mu_{ind}$ .

Probability of light collection is approximately flat along the  $x$  and  $y$  coordinates of the crystal whereas it becomes strongly non uniform along the longitudinal axis  $z$ .

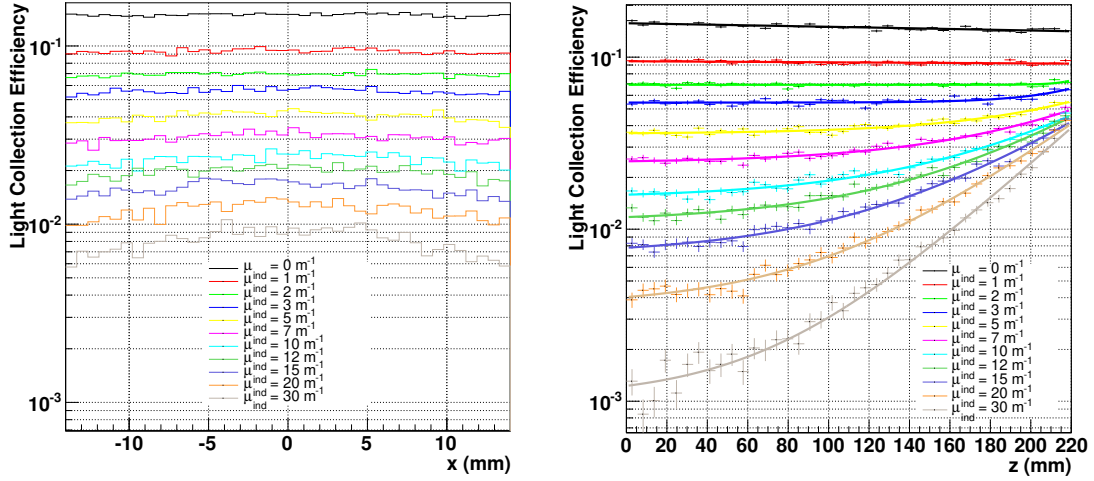


**Figure 4.2:** Top: schematic view of PbWO<sub>4</sub> simulated crystal. The photodetector is located at  $z = 220$  mm. Bottom: Light collection efficiency curves  $\varepsilon_{LC}$  across  $x$  (left) and along crystal length  $z$  (right) for different values of  $\mu_{ind}$ .  $x = 0$  corresponds to the central crystal axis and  $z = 0$  to the front face of the crystal.

Similar to Eq. 3.14, curves along  $z$  can be more generally parameterized by

$$\varepsilon_{LC}(z, \mu_{ind}) = \varepsilon_0(\mu_{ind}) \cdot \exp\left[\frac{z - 220}{\xi(\mu_{ind})}\right] + K(\mu_{ind}) \quad (4.2)$$

where  $\varepsilon_0$  is the light collection efficiency of photons produced at the rear face of the crystal (close to the photodetector at  $z = 220$  mm) and  $z$  is the distance along the crystal axis from the crystal front face expressed in mm.  $\xi(\mu_{ind})$  and  $K(\mu_{ind})$  are general free parameters which depend on  $\mu_{ind}$  and allow to take into account the non-exponential behavior of light propagation (e.g. reflection on the alveolar structure).

The optical signal detected for a given energy deposit is given by the combination of the energy deposited, directly proportional to the number of scintillation photons produced, with light collection efficiency. The contribution of the energy deposit  $E_i$  at position  $(x, y, z)$  to the total signal  $S_{tot}$  is given by

$$S_i = E_i(x, y, z) \cdot \varepsilon_{LC}(x, y, z) \quad (4.3)$$

Assuming a flat probability of light collection across  $x$  and  $y$  and integrating all the energy deposits weighted with the respective  $\varepsilon_{LC}(z)$  over the whole crystal length, the total signal is obtained

$$S_{tot}(\mu) = C_0 \int_{z=0}^L E(z) \cdot \varepsilon_{LC}(z, \mu) dz \quad (4.4)$$

in which the length of the EE crystals is  $L = 220$  mm and  $C_0$  represents an overall

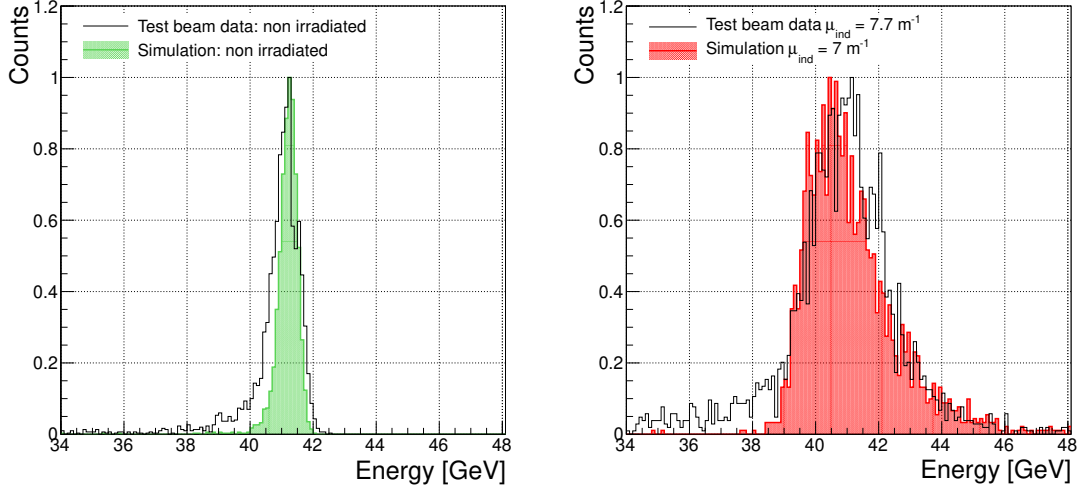


**Figure 4.3:** Comparison of energy distributions for a non-irradiated crystal (left) and a crystal with  $\mu_{ind} = 7.7 \text{ m}^{-1}$  (right). A beam spot selection of  $4 \times 4 \text{ mm}^2$  on 50 GeV electrons is used.

calibration constant (including intrinsic light yield of PbWO<sub>4</sub> and photodetector quantum efficiency).

Eq. 4.4 describes the principle of the fast simulation approach. Electron events are simulated and the shower is developed inside the crystal. Instead of tracing each single photon, the detected signal is estimated from energy deposits convoluted with pre-calculated curves of  $\varepsilon_{LC}$ . Event-by-event fluctuations of the longitudinal shower development will produce a smearing of the measured energy which is responsible for the increase of the constant term discussed in Sec. 3.6.4. The comparison of simulated energy distributions for different  $\mu_{ind}$  is shown in Fig. 4.3. The results demonstrate that simulation is able to properly describe the change in the tail asymmetry due to an increase of the  $\mu_{ind}$ , as observed in test beam data. Experimental distributions, especially for non irradiated crystals, show a larger low-energy tail which can be attributed to electron energy losses due to bremsstrahlung radiation along the H4 beam line. The limited precision of the beam spot selection in data due to the finite-position resolution of the wire chambers (about 0.5 mm) can also play a role.

The increase of constant term due to radiation damage,  $\sqrt{C_{irr}^2 - C_{nonirr}^2}$ , predicted by simulation shows a good agreement with test beam data as shown in the left plot of Fig. 4.4. At the same time, Eq. 4.4 can explain the non linear behavior presented in Sec. 3.6.4. As shower maximum moves towards the photodetector for higher energies, the scintillation light is less affected by induced absorption. This is confirmed by non-linearity curves obtained in the test beam which are well reproduced by the simulation as shown in the right plot of Fig. 4.4.

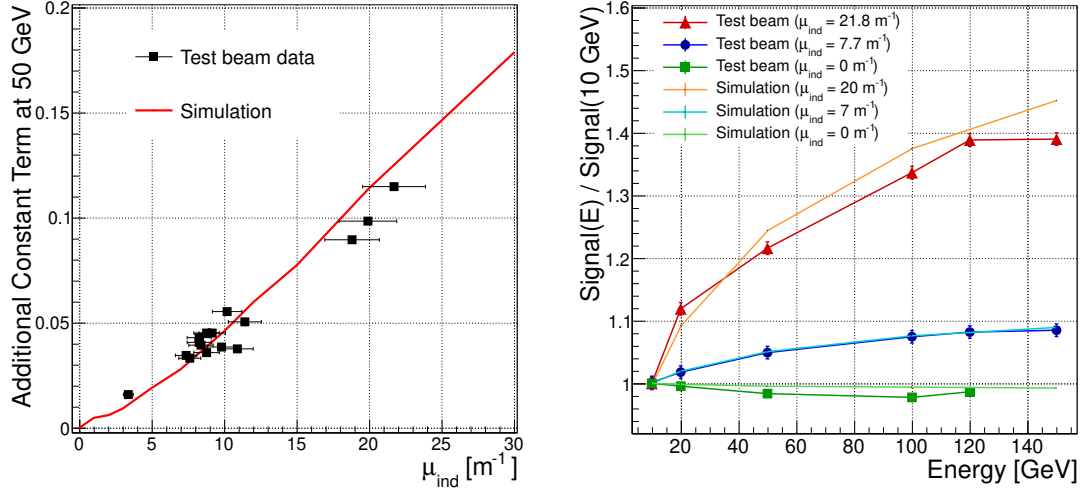


**Figure 4.4:** Left: degradation of constant term due radiation damage is well reproduced by simulation. Right: non linearity curves predicted by simulation matches well the test beam data.

## Full Simulation

Although the fast simulation is able to reproduce the degradation of constant term and response non-linearity, it cannot take into account other effects which require the full simulation approach. One of these effects is the change of the signal pulse shape presented in Sec. 3.6.1. Another effect that the fast simulation approach does not take into account is the contribution of Cherenkov light to the total signal. This is due to the fact that Cherenkov light is not proportional to the energy deposited via ionization but it is an additional process accompanying the shower development.

In the full simulation, all the processes introduced at the beginning of Sec. 4.1.2 are entirely simulated. Each photon, either it comes from scintillation or Cherenkov effect, is produced and traced inside the crystal. This is necessary since the  $\varepsilon_{LC}$  maps are valid only for isotropic light whereas Cherenkov light is strongly non-isotropic.

In the simulation, the intrinsic light yield of PbWO<sub>4</sub> was set in order to have a contribution of Cherenkov light to the total detected signal of 10% for non irradiated crystals, as experimentally measured in test beam [87]. For this purpose the quantum efficiency of the photodetector was taken into account as shown in Fig. 4.5. It is worth to notice that, since scintillation and Cherenkov light have different  $\lambda$ -dependence, the transmission loss affects these two light components in a different way. The results obtained with the full simulation demonstrate that Cherenkov light contribution to the total signal increases with  $\mu_{\text{ind}}$  as shown in the right plot of Fig. 4.5. This plays a role both on the estimation of light output and on the time response of the signal since an enhancement of Cherenkov

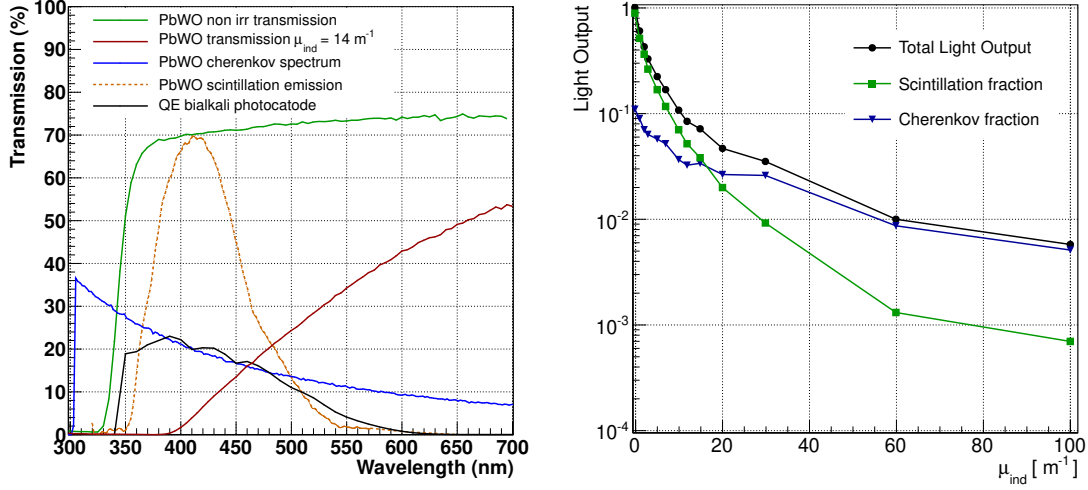


**Figure 4.5:** Left: wavelength dependence of Cherenkov and scintillation light compared with the transmission of hadron damaged crystals and the quantum efficiency (QE) of the photodetector. Right: contribution of scintillation and Cherenkov signal to the total light output at different  $\mu_{ind}$ .

light fraction produces on average faster pulses.

The change in the pulse shape observed in the data has been compared with simulation. The time of arrival of photons obtained from the simulation was convoluted with the time response of the PMT which introduces a smearing of  $\sigma_t(PMT) = 1\text{ ns}$ . Simulation results confirm that the shortening of the pulse shapes occurs because mostly the direct light is detected and the fraction of cherenkov light increases. A comparison between data and simulation is shown in Fig. 4.6 for a non-irradiated crystal and a crystal with  $\mu_{ind} \approx 10\text{ m}^{-1}$ . For the irradiated crystal test beam data are in perfect agreement with simulation whereas a slightly slower decay time is observed in data for non-irradiated crystal. This can be attributed to small differences in the initial transparency  $\mu_0$  which varies from crystal to crystal.

A comparison of resolution and linearity degradation obtained with full simulation was also compared and found consistent with the parameterized approach of the fast simulation. This mean that change of the Cherenkov light fraction does not play a relevant role on these two aspects and that the fast simulation is a good approximation in this case.

#### 4.1.3 Effect of a Non-Uniform $\mu_{ind}$ inside the Crystal

An overall good agreement is observed between data and simulation. However, an additional study was performed to investigate the possible effects of a non-uniform  $\mu_{ind}$  inside the crystal both along the transverse and longitudinal axis.

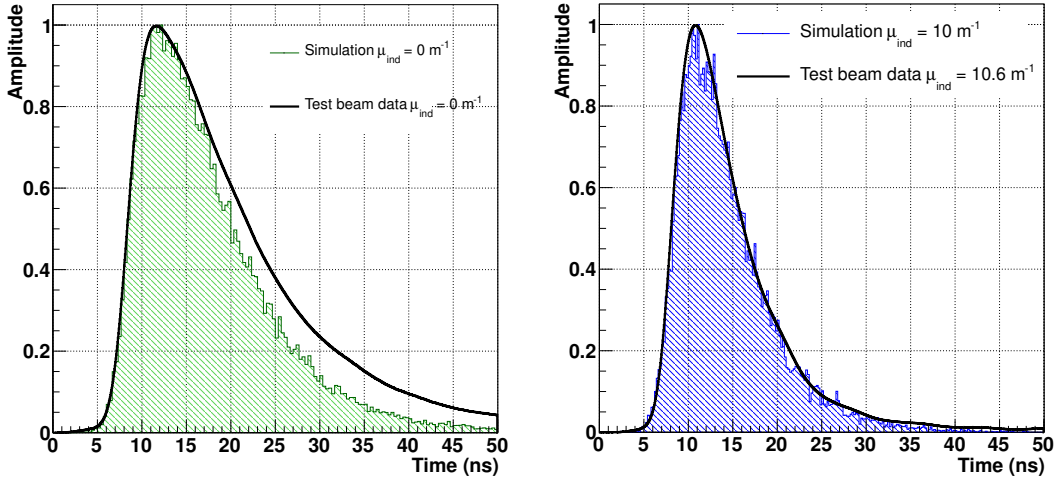


**Figure 4.6:** Comparison of pulse shapes predicted by simulation with test beam data for a non-irradiated crystal (left) and a crystal with  $\mu_{ind} \approx 10 \text{ m}^{-1}$ .

This study is of particular importance because the damage profiles of crystals irradiated with 24 GeV protons might differ significantly from those which will occur in the real CMS calorimeter. This is due to the fact that proton beam profile and energy used at the PS irradiation facility are far from representing the real mixture of particles (pions, protons, neutrons, mesons, ...) which are produced in the detector during LHC collisions. As confirmed by experimental measurements of PS irradiated crystals, 24 GeV protons deposit the maximum of their energy after  $\approx 7 \text{ cm}$  from the crystal front face as visible in Fig. 3.8.

To collect information about the real radiation environment inside CMS, four PbWO<sub>4</sub> crystals were positioned in a forward region of the detector close to CASTOR ( $z \approx 1460 \text{ cm}$  from interaction point, and  $R = 8-10 \text{ cm}$  distance from the beam pipe). Crystals were left in this position during the 2012 operation of LHC and were removed in January 2013. With FLUKA simulation [75, 76] the doses and hadron fluences expected have been calculated (see Table 4.1). Two months after removal, the crystal transmission was measured and the correspondin  $\mu_{ind}$  was calculated.

The damage profiles along crystal axis was also measured and small and smooth variations of  $\mu_{ind}$  along the  $x$  and  $y$  axis were observed (see Fig. 4.7). This small non-uniformity can be attributed to the hadron fluence gradient along  $\eta$  which indeed is stronger for crystal 11950 positioned closer to the beam pipe. Longitudinal profiles of damage (along crystal axis  $z$ ) are also shown on the right plot of Fig. 4.7 and show a behavior similar to those of PS irradiation. This non-uniformity can be interpreted as the combination of charged hadrons, charged pions and neutrons which is not flat along  $z$  as shown in Fig. 3.4.

#### 4.1. Comparison of Test Beam Data with Simulation

Crystal ID	$R$ [cm]	Protons	Neutrons	Pions	Total	$\mu_{ind}$ [ $\text{m}^{-1}$ ]
11950	8	$0.66 \times 10^{13}$	$0.25 \times 10^{14}$	$0.32 \times 10^{14}$	$0.64 \times 10^{14}$	8.8
11928	10	$0.41 \times 10^{13}$	$0.18 \times 10^{14}$	$0.18 \times 10^{14}$	$0.4 \times 10^{14}$	3.9

**Table 4.1:** Energy threshold on hadrons is  $E > 14.5$  MeV Contribution of the noise term to the energy resolution for each configuration of the matrices used during test beam running.

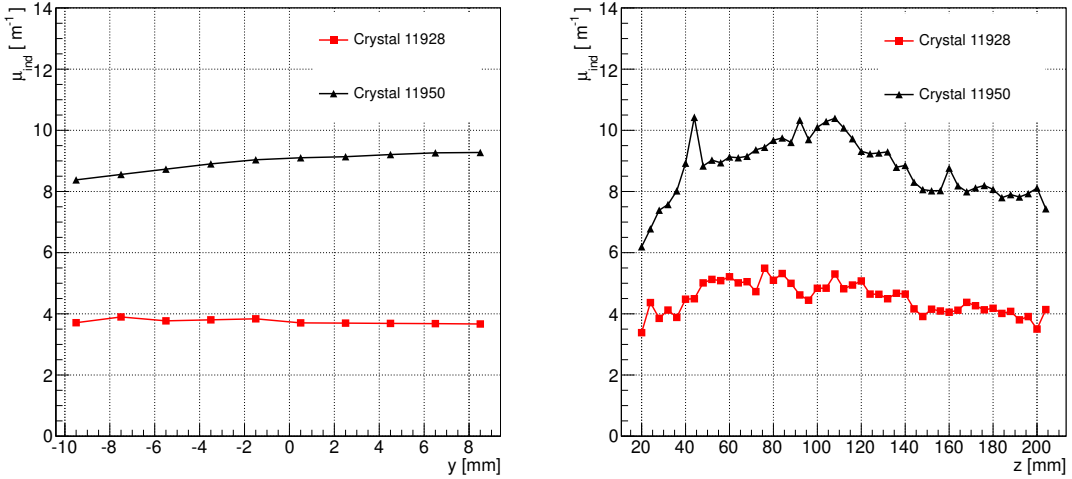


**Figure 4.7:** Damage profile across  $y$  (left) and along  $z$  (right) for two crystals irradiated in P5, at different  $\eta$  positions.

Given the difference in damage profiles between P5 and PS irradiations, a simulation was performed to evaluate the effect of non uniform  $\mu_{ind}$  along  $x, y$  and  $z$ . Damage profiles as the one in Fig. 3.7 for transverse axis and the one of Fig. 3.8 for longitudinal axis were simulated. Results were compared with the case of a flat  $\mu_{ind}$  equivalent to the average  $\mu_{ind}$  of the non uniform profile.

Negligible differences were observed in the  $\varepsilon_{LC}(z)$  curves as shown in Fig. 4.8 confirming that no significant effect on the energy resolution or linearity is expected. The light output corresponding to 50 GeV electrons was simulated in the three factorized scenarios of a flat  $\mu_{ind}$ , a non uniform damage across  $x, y$  axis and a non uniform damage along  $z$  axis. Comparison of these scenarios with the test beam data is reported in Fig. 4.9. The influence of non uniform  $\mu_{ind}$  on the light output is negligible with respect to experimental uncertainties. Small differences at the 2-3% level appear for high values of  $\mu_{ind}$ , as shown in the right plot of Fig. 4.9. However, these variations do not improve the agreement with data for high  $\mu_{ind}$ .

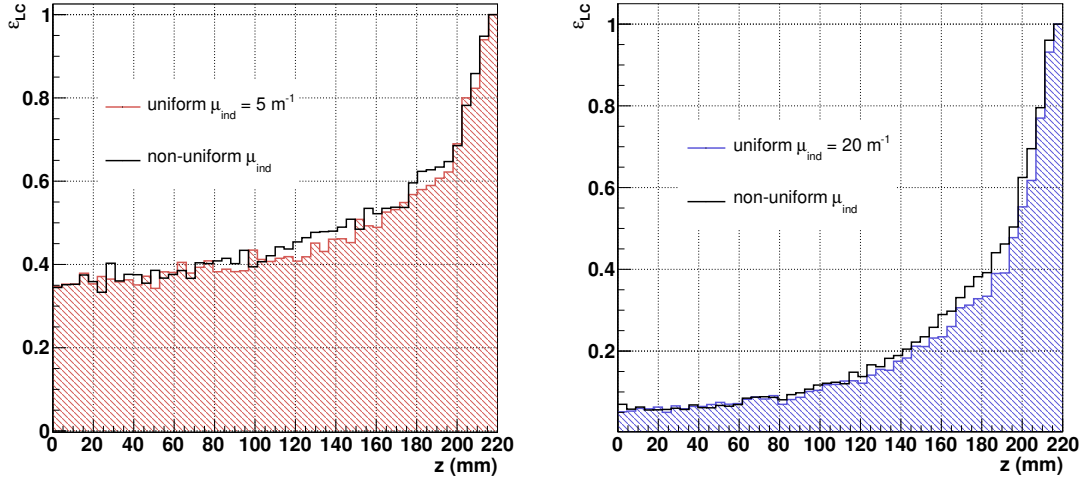


**Figure 4.8:** No significant difference is observed between  $\varepsilon_{LC}$  curves for crystal with uniform or non-uniform  $\mu_{ind}$ . Example of  $\varepsilon_{LC}$  curves for a crystal with  $\mu_{ind} = 5 \text{ m}^{-1}$  (left) and  $\mu_{ind} = 20 \text{ m}^{-1}$  (right).

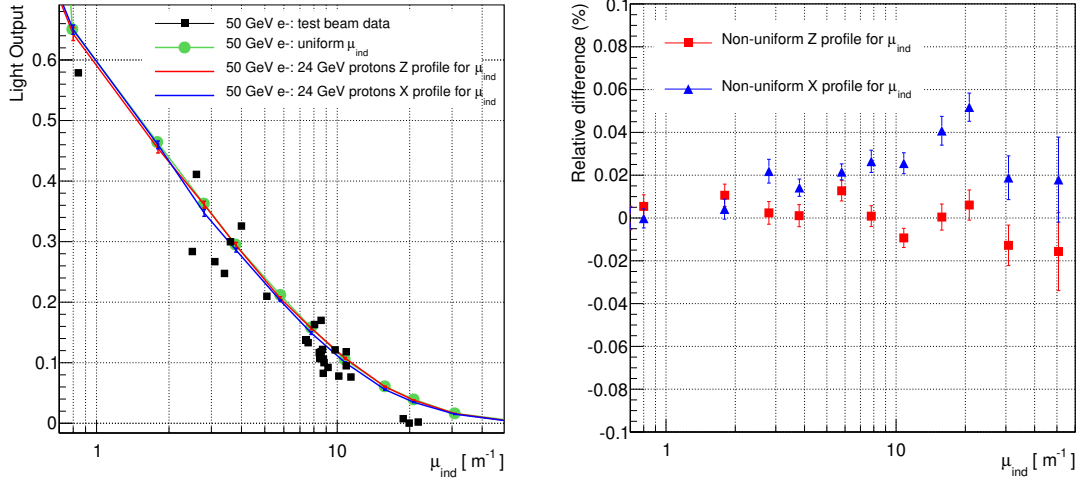


**Figure 4.9:** Right: influence of non-uniform  $\mu_{ind}$  on the simulated light output and comparison with test beam data (black dots). Left: relative difference of light output for uniform  $\mu_{ind}$  with respect to a non uniform one is within 2-3%. At high  $\mu_{ind}$ , a non uniform profile across crystal face  $x, y$ , can slightly worsen the loss of light.

For values of  $\mu_{ind}$  up to  $\approx 10 \text{ m}^{-1}$  simulation is in good agreement with observed light output. On the contrary, the highly irradiated crystals ( $\mu_{ind} \approx 20 \text{ m}^{-1}$ ) present a significantly lower light output with respect to simulation predictions. This was attributed to the precision of the experimental measurement for these crystals which was limited by the low gain of the PMT which lead to signal distributions very close to the pedestal as mentioned in Sec. 3.6.2.

The simulation developed in this section, showing a good agreement with test beam data, presents a powerful tool to extrapolate the effect of radiation damage at any  $\mu_{ind}$  in the range of experimental data ( $\mu_{ind} \leq 20 \text{ m}^{-1}$ ). It is therefore of fundamental importance to predict the performance of ECAL crystals throughout the whole operation of LHC and HL-LHC.

## 4.2 Extrapolation of Future ECAL Performance

The performance of ECAL will change in time during the next phases of LHC operation and even more quickly during the HL-LHC phase. The major aspects which will affect the evolution of calorimeter response are the following:

1. The dark current of barrel APDs will increase due to hadron-induced damage [45, 88] and will significantly affect the signal over noise ratio for the EB.
2. Response loss of the VPTs used in the EE [46] will arise due to the VPT conditioning and faceplate transparency loss.
3. The increase of collision rate will result in a much higher pileup affecting calorimeter performance under several aspects [89].
4. The radiation damage and transparency loss of PbWO<sub>4</sub> crystals will affect both EE and EB as discussed in Sec. 4.1.

The details of photodetectors ageing and pileup effects will not be discussed in this thesis, although they are being extensively studied by the CMS ECAL collaboration [89]. In the following, attention will be focused on the extrapolation of crystals performance.

### 4.2.1 Extrapolation of Crystal Ageing Effects on ECAL Performance

The results and the simulation presented in Sec. 4.1, provide a reliable starting point for the extrapolation of radiation damage effects at fluences and doses even higher than those experimentally measured. In particular, it is of crucial importance to understand whether the CMS ECAL calorimeter will be able to maintain a good performance until the of HL-LHC.

The conceptual steps required for the extrapolation of future ECAL performance are illustrated in Fig. 4.10. Based on the current program of LHC and HL-LHC operations in the next years (Sec. 3.2), it is possible to estimate the electromagnetic doses and hadron fluences as a function of time. Their values depend on the instantaneous and integrated

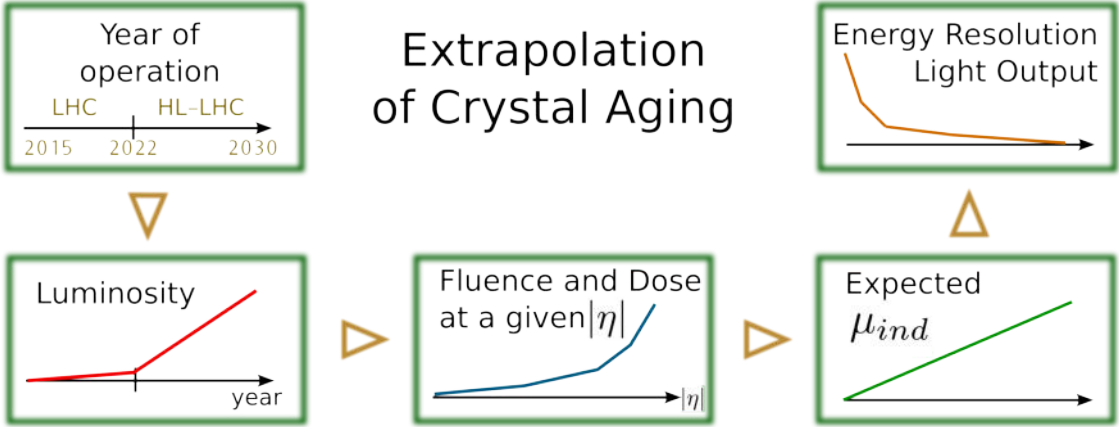


**Figure 4.10:** Conceptual steps to estimate the long term performance of ECAL crystals throughout the whole operations of LHC and HL-LHC.

luminosity at a given position of the detector  $(\eta, z)$ , according to Fig. 4.11, and can be expressed as

$$R(\eta) = 1.8 \times 10^{-6} \cdot e^{\eta/0.37} + 8.4 \times 10^{-5} \quad (4.5)$$

$$\Phi_h(\eta) = 4.5 \times 10^9 \cdot e^{\eta/0.75} - 2.6 \times 10^{10} \quad (4.6)$$

where  $R$  is the dose rate in [Gy/s] at the nominal instantaneous luminosity of LHC ( $\mathcal{L} = 10^{34} \text{ cm}^{-2}\text{s}^{-1}$ ) and  $\Phi_h$  is the charged hadron fluence corresponding to  $1 \text{ fb}^{-1}$ .

The total  $\mu_{ind}$  of a crystal is given by the combined effects of ionizing dose and hadron fluence. Extensive studies were made on the dose rate dependent damage due to ionizing radiation. The experimental dose rates studied in [68] covered the full range expected until the end of HL-LHC (from 0.00004 to 0.1 Gy/s) and suggest the following parameterization

$$\mu_{ind}^\gamma = 0.12 \cdot \log[R(\eta)] + 1.4 \quad (4.7)$$

where the dose rate  $R$  is expressed in Gy/s and the  $\mu_{ind}$  in  $\text{m}^{-1}$ . The correlation between hadron fluence and  $\mu_{ind}^{had}$  is the one obtained from the fit of experimental data in Eq. 3.4

$$\mu_{ind}^{had} = 1.49 \times 10^{-13} \cdot \Phi_h \quad (4.8)$$

Combining Eq. 4.7 with Eq. 4.8, crystal transparency losses are then defined as a function of  $\eta$  for the whole time of operations until the end of HL-LHC phase as a function of the total induced absorption

$$\mu_{ind}^{tot} = \mu_{ind}^\gamma + \mu_{ind}^{had} \quad (4.9)$$

As demonstrated with test beam and simulation studies, the effects of radiation damage can be understood and parameterized as a function of  $\mu_{ind}^{tot}$ . This allows to evaluate the

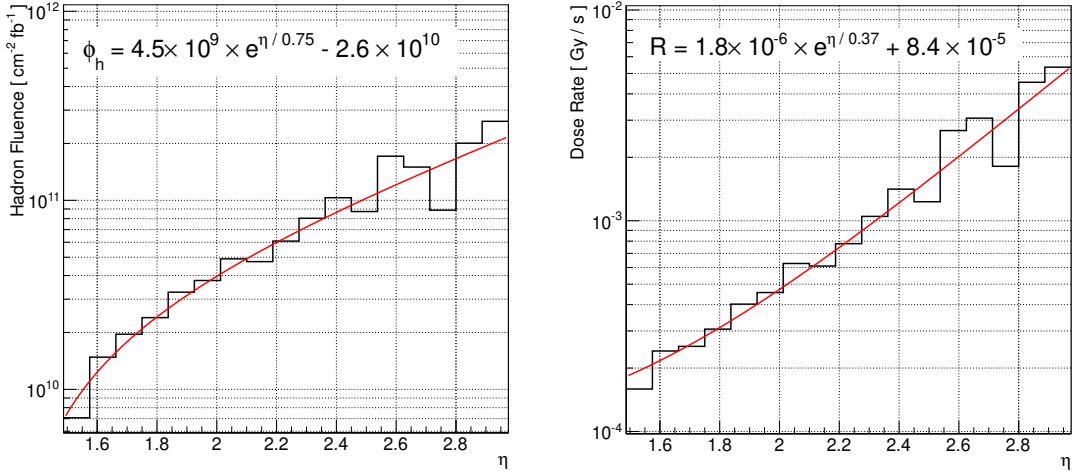


**Figure 4.11:** Charged hadron fluence and dose rate in the endcap region  $1.47 < |\eta| < 3.0$  at different  $|\eta|$  values. Dose rate corresponds to the LHC nominal instantaneous luminosity of  $\mathcal{L} = 10^{34} \text{ cm}^{-2}\text{s}^{-1}$ . Red line correspond to the fit the parameterization of Eq. 4.5.

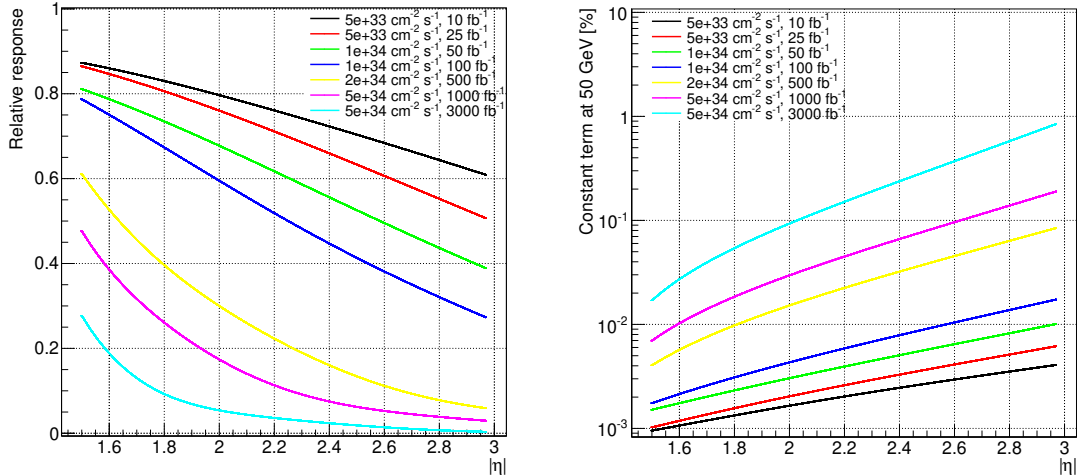


**Figure 4.12:** Left: response evolution of CMS EE PbWO<sub>4</sub> crystals at different periods of LHC and HL-LHC operation as a function of  $\eta$ . Right: degradation of constant term of energy resolution due to increase of  $\mu_{ind}$ .

intensity of observed effects (light output loss, increase in constant term, loss of linearity and change of pulse shapes) for different periods of LHC operation as shown in Fig. 4.12. Due to the very low dose rate and fluences, in the EB the  $\mu_{ind}$  will stay below  $2 \text{ m}^{-1}$  and the light output loss will be less than a factor 2 whereas in the EE the effects of radiation damage will become crucial. The response loss of EE crystals and the degradation of energy resolution due to the increase of the constant term are shown in Fig. 4.12 as a function of  $\eta$  for different phases of LHC and HL-LHC.

Given the relatively low light yield of  $\text{PbWO}_4$ , the signal collected by the photodetectors both in EB and EE, for non-damaged crystals, is about 4.5 photoelectrons per MeV of deposited energy [44]. Since the average noise of a single-channel is about 40 MeV [48], the light output loss due to radiation damage will significantly degrade the signal over noise ratio as well as the photostatistic term in Eq. 2.5. In addition to this, the contribution to the constant term due to the increase of longitudinal non-uniformity of light collection efficiency will become a dominant factor. In particular, during HL-LHC ( $1000 - 3000 \text{ fb}^{-1}$ ) the constant term at  $|\eta| = 2.2$  will contribute respectively up to 5 – 11% to the energy resolution.

#### 4.2.2 Conclusions

Through a detailed study of proton damaged crystals during the test beam campaign presented in Chap. 3 it was possible to build and validate a simulation model which is able to describe the observed effects. Such a model allows to estimate the consequences of crystal ageing on future ECAL performance.

The impact of energy resolution degradation on the physics analysis is being estimated using a model similar to the parameterized approach of Sec. 4.1.2. The light collection efficiency curves for different  $\mu_{ind}$  have been implemented in the CMSSW Software [90] and physics samples used for different analysis have been simulated for benchmark scenarios of integrated luminosity corresponding to 500, 1000 and  $3000 \text{ fb}^{-1}$ .

In addition to crystal transparency loss, the APDs and VPTs ageing and pileup effects have been implemented in the CMSSW simulation. The results of these studies demonstrate that ECAL will maintain a reasonable performance throughout the whole operation of the LHC as it was designed for.

However, during HL-LHC, the level of radiation damage will become too high and the performance of ECAL will be significantly degraded. Because of the strong  $\eta$  dependence the degradation of energy resolution will affect mostly the forward region of the detector ( $|\eta| > 2.2$ ). In the EE, the increase of constant term due to crystal ageing will dominate the energy resolution whereas in the EB, where crystal darkening is much lower, the APD noise current will become the limiting factor. Concerning the EB, strategies for APD noise mitigation are being investigated. A possibility could be to decrease the operating temperature from  $18^\circ\text{C}$  to  $10^\circ\text{C}$  which would significantly reduce the dark current. This option however, presents practical complications (e.g. modification of  $\text{PbWO}_4$  scintillation properties) which have to be taken into account. Concerning the EE, several attempts have been made to find feasible techniques for crystal recovery (thermal and optical annealing) which could be implemented in situ inside CMS. However, the practical limitations anticipated in Sec. 3.1.3, would not allow to sufficiently recover the crystal transparency.

With the current detector, the energy resolution in the endcap region during HL-LHC will be too low to maintain a reasonable performance. Such a loss of resolution would strongly affect the reconstruction of missing transverse energy (MET) limiting the studies of physics beyond the Standard Model. Furthermore it is particularly important, for the endcap calorimeters, to guarantee good reconstruction of jets. Jets resolution is crucial for many physics analysis which make use of jet-tagging and involves Higgs production through Vector Boson Fusion (VBF).

For this reason the high  $\eta$  regions of ECAL have to be replaced with a more radiation tolerant device in order to maintain and possibly improve the EE performance during HL-LHC. A cheap and simple solution to mitigate aging effects in the EE is presented in Appendix A. Preliminary studies shows that it would be possible to reduce the damage effects due to crystal darkening by adding a photodetector on the front face of PbWO<sub>4</sub> crystals. However, aiming to improve the granularity and the timing capabilities of the current detector, in addition to its radiation hardness, a set of new calorimeter options are being studied to replace the current ECAL endcaps as discussed in Chap. 5.



# Study of Radiation Hardness on Scintillator Candidates for Calorimetry at HL-LHC

---

Studies of radiation damage effects, similar to Chap. 3, have been performed for all the subdetectors of CMS (calorimeters, tracker, muon system). In particular, as the ECAL endcaps (EE) also the performance of the hadronic calorimeter in the forward region (HE) will be degraded by radiation. The loss of transparency of the plastic scintillator tiles and the wavelength-shifting (WLS) fibers used to collect the light to the photodetector will become the main source of signal loss. According to extrapolation of current data, the HE will not be able to operate during HL-LHC phase. Given the overall degradation of the CMS endcap calorimeters, an upgrade of the detector will be required during LS3 to maintain an adequate performance until the end of HL-LHC operation.

Within this framework, several R&D studies have started to investigate possible solutions for the development of more radiation hard devices to replace current endcap calorimeters. Common to all proposals, is the necessity to identify active materials which are able to withstand radiation doses and fluences up to the levels predicted for HL-LHC (Sec. 3.2).

In the following, new scintillating materials which represent potential candidates for calorimetry applications are discussed. A detailed investigation of damage effects induced by different type of radiation ( $\gamma$  and protons) is presented. Attention is focused on inorganic scintillators (e.g. LSO, YSO, LuAG, YAG) doped with rare earth ions such as  $\text{Ce}^{3+}$  and  $\text{Pr}^{3+}$ . The properties of doped quartz ( $\text{SiO}_2:\text{Ce}$ ) and Barium disilicate doped with Cerium (DSB:Ce) samples are also discussed.

## 5.1 Options for the CMS Endcap Calorimeters Upgrade

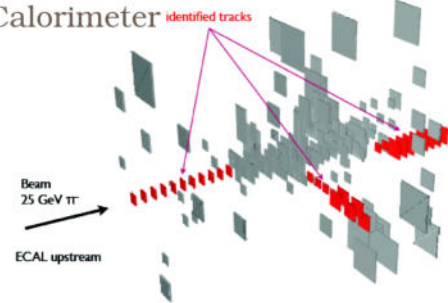
For the upgrade of the CMS calorimeters, several options are currently being considered [74] as shown in Fig. 5.1. One of the possibilities is to replace the current endcap calorimeters with a High Granularity Calorimeter (HGC) based on a dense absorber (e.g. lead or tungsten) interleaved with active layers of silicon devices. Recent progress in silicon detectors in terms of cost per unit area and radiation tolerance, might allow to use this technology to instrument large volumes such as those of hadronic calorimeters. The HGC detector would allow to apply the methods of particle flow to optimize the jet energy resolution as widely investigated by the CALICE collaboration in the context of future ILC/CLIC detectors [21].

Other proposals for the calorimeter upgrade are considering a different approach based on scintillator devices. In particular, a set of more radiation hard active materials is being considered to replace the plastic scintillator tiles + WLS fibers system used in the current hadronic calorimeter. Some of the options are:

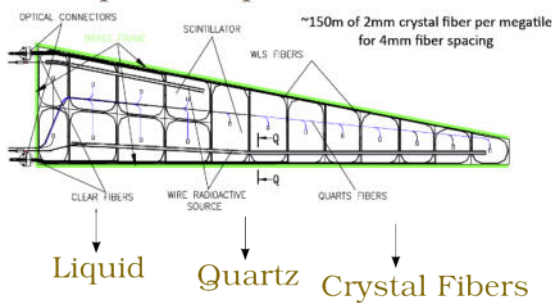
- use of a liquid scintillator (such as EJ-309 [91]) as active material;
- implementation of quartz plates painted with a radiation hard wavelength shifter dye (e.g. doped zinc oxide);
- substitution of current scintillator with a new one emitting in the green range of wavelength which is less sensitive to radiation damage;
- use of crystal fibers like as LuAG or YAG doped with rare earth ions ( $\text{Ce}^{3+}$  or  $\text{Pr}^{3+}$ ) arranged in a layer structure.

Concerning the electromagnetic calorimeter, the implementation of a “shashlik” sampling calorimeter similar to the one used in the LHCb experiment [38] is being considered. It would consist of absorber plates (e.g. tungsten) alternated with layers of active material (LSO:Ce or  $\text{CeF}_3$  currently considered) which are readout using a WLS embedded into a quartz capillary (QC). Such option would reduce the optical path of light inside the active material by extracting it with the WLS + QC system. Assuming that WLS and QC are more radiation hard than the active scintillator, this technique would improve the resistance of the device to radiation damage eliminating the main source of constant term degradation which would affect the current EE. A similar alternative design under consideration is a “sandwich” module in which the WLS fibers would run parallel to the edges of the plates saving costs and time required to drill and polish holes inside the crystals.

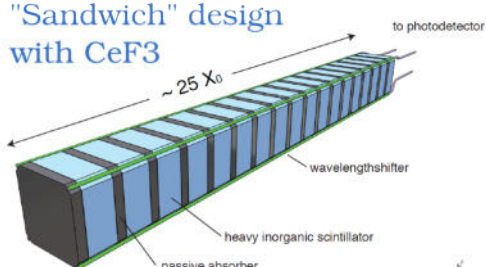
1. Digital Silicon Calorimeter



3. Replace HE plastic scintillator



2. Re-design a more radiation hard scintillating ECAL



"Shashlik" design with LYSO

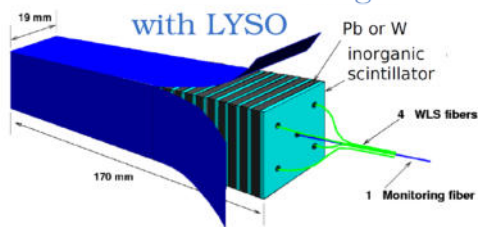


**Figure 5.1:** Top Left: schematic view of track identification and reconstruction in a digital high granularity calorimeter (HGCAL). Top Right: “sandwich” design for a sampling calorimetric module with WLS fibers positioned at the edges of crystal plates. Bottom Left: current structure of HE megatiles made of plastic scintillator readout through a wavelength shifter plus optical fiber system. Bottom Right: “shashlik” design for a sampling calorimeter with WLS fibers inserted into holes drilled in the center of the module.

In general, it is of common interest the research and development of wavelength shifters (e.g. shaped into fiber geometry) to collect the light from the scintillator and transport it to the photodetector. The majority of WLS used so far is not radiation hard and thus represents the weak point of several calorimeter device options. Crystal fibers, which are known to be more radiation hard with respect to standard plastic WLS, can provide an effective solution. For instance LuAG:Ce, which absorbs light around 350 and 450 nm re-emitting it in the green (around 520 nm), would allow to shift the light originating from LSO:Ce or CeF<sub>3</sub> scintillators (with emission peaks respectively at 420 and 340 nm). Similarly, quartz doped (SiO<sub>2</sub>:Ce) and heavy glass (DSB:Ce) fibers might provide a radiation hard solution either as scintillators or as wavelength shifters.

## 5.2 Requirements for Scintillator Candidates

The properties of scintillator candidates have to be carefully considered under several aspects in order to evaluate their real potential for calorimetry applications in HL-LHC. As anticipated in Sec. 1.1, for the design of a calorimeter it is crucial to consider that:

- High density ( $\rho$ ) improves the sampling fraction reducing stochastic fluctuations.
- Short radiation and interaction lengths ( $X_0, \lambda_I$ ) allow for more compact devices which can longitudinally contain the shower.
- A small Molière radius ( $R_M$ ) leads to a better transverse containment which, especially in high pile up conditions, can help to disentangle spatially overlapping events.

The scintillator properties are also of major importance for light-based calorimeters as discussed in Sec. 1.2.2. In particular:

- A high light yield ( $LY$ ) improves photostatics and S/N ratio.
- Fast response, i.e. short decay time ( $\tau_d$ ), is required to operate at high rate and pile up conditions.
- The wavelength of the emission spectrum has to be considered for optimal coupling with photodetectors quantum efficiency.
- Phosphorescence and long decay time components can limit the calorimeter performance at high rate, introducing an additional noise component to the signal.
- Stability of scintillation properties with temperature (light yield, decay kinetics, ...) is important to reduce fluctuations in the response.
- High refractive index ( $n$ ) enhances the amount of Cherenkov light produced and can improve light collection efficiency for specific geometries (e.g. fiber shape).

Considering the applications for calorimetry at HL-LHC, where big volumes have to be instrumented, the feasibility of large mass production at relatively low cost is an additional requirement which favors light and cheap elements like fused silica ( $\text{SiO}_2$ ) and glasses (DSB). However, such materials have a low stopping power and can only be used in sampling calorimeters in which a dense absorber could enhance the effective  $X_0$  and  $R_M$ . Heavy crystals, on the other hand, are particularly suitable to build homogenous calorimeters or to increase the sampling fraction in sampling calorimeters.

A large number of scintillators was discovered in the past decades [92], spanning almost the full range of the properties discussed above. However, the harsh radiation environment in which detectors at HL-LHC will have to operate adds stringent requirements on the radiation hardness of the materials. A set of scintillators, which are potential candidates for calorimetry at HL-LHC are listed in Table 5.1. Their basic properties are summarized although variation of dopant concentration and co-dopants can make a substantial difference on the scintillating properties. A campaign of irradiation studies on these materials has been carried out at CERN and it is still ongoing. The results achieved so far will be discussed in the next sections.

	$\rho$ [g/cm <sup>3</sup> ]	$X_0$ [cm]	$n$	LY [ph/MeV]	Decay time [ns]	Emission peak [nm]
LSO:Ce	7.4	1.14	1.82	high	40	420
YSO:Ce	4.4	3.4	1.82	high	40	420
LuAG:Ce	6.7	1.41	1.84	high	55	520
YAG:Ce	4.6	3.5	1.83	high	70	550
LuAG:Pr	6.7	1.41	1.84	high	20	350
YAG:Pr	4.6	3.5	1.84	high	24	310
DSB:Ce	4.0	3.3	1.73	medium	55	430
SiO <sub>2</sub> :Ce	2.6	12.3	1.55	medium	55	430
PbWO <sub>4</sub>	8.3	0.89	2.20	low	15	420
CeF <sub>3</sub>	6.2	1.70	1.62	medium	30	300-340

**Table 5.1:** Overview of scintillator candidates properties compared with well known PbWO<sub>4</sub> and CeF<sub>3</sub> crystals. Index of refraction is given at the wavelength emission maximum.

### 5.3 Lu<sub>2</sub>SiO<sub>5</sub> and Y<sub>2</sub>SiO<sub>5</sub> Crystals

Lutetium and Yttrium oxy-orthosilicate scintillating crystals doped with Ce<sup>3+</sup> ions, namely Lu<sub>2</sub>SiO<sub>5</sub>:Ce and Y<sub>2</sub>SiO<sub>5</sub>:Ce, are promising candidates for calorimetry applications. Their optical properties have been widely studied in [93, 94, 95]. As reported in Table 5.1, they are characterized by a relatively fast decay time ( $\sim 40$  ns) high light yield (up to 30000 ph/MeV depending on Cerium concentration). They have excitation peaks at 250–350 nm and emit light with a broad spectrum around 430 nm. A detailed study of radiation hardness on these inorganic crystals have been carried out with particular attention on the effects of the damage close to the band edge which have consequences on the intensity of crystal phosphorescence [96, 97, 98]. The experimental procedure and the results obtained are presented in this section.

### 5.3.1 Samples and Experimental Procedure

A set of LSO:Ce crystals doped with different concentration of  $\text{Ce}^{3+}$  and few YSO:Ce samples have been irradiated with  $\gamma$  and proton sources as summarized in Table 5.2. Cerium concentration varied from very low values to the standard concentration of commercially produced crystals (from 0.1 to 0.5 at%). This allowed to study the induced absorption at wavelengths below 400 nm, which are usually not accessible in standard LSO:Ce crystals due to the high concentration of Cerium. All crystals were grown by the Czochralski method [99] in inductively heated iridium crucibles in an atmosphere containing a small fraction of a percent of oxygen in bulk nitrogen. An additional sample of commercial LSO:Ce, produced by Siemens, was used as reference for this study and was not irradiated.

Samples have been first irradiated using a  ${}^{60}\text{Co}$  source (1.22 MeV  $\gamma$ -rays, 2 kGy absorbed dose, 1 kGy/h dose rate) at RINP Irradiation Facilities, in Minsk. The transmission of the samples was measured before and 30 minutes after irradiation in the 200-900 nm range to calculate the induced absorption. The samples were then annealed at three gradually increasing temperatures of 100°C, 200°C and 300°C in order to fully recover the  $\gamma$ -induced damage [96].

In a second step, crystals have been irradiated at the CERN PS facility with 24 GeV protons at a flux of about  $10^9 \text{ cm}^{-2}s^{-1}$  to an integrated fluence of  $3.6 \times 10^{13} \text{ cm}^{-2}$ .

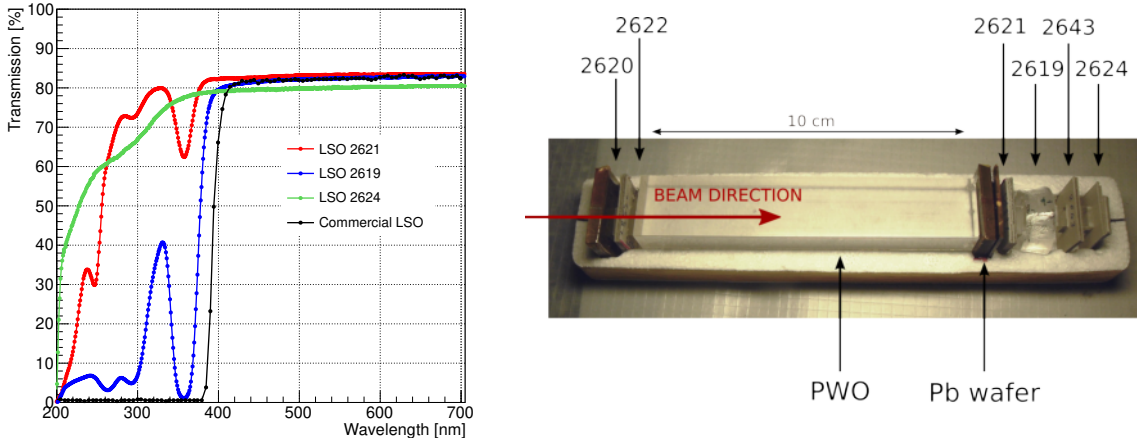


**Figure 5.2:** Left: transmission curves for LSO samples with different Cerium concentration before irradiation (2619 low doped, 2621 very low doped, 2624 undoped). Right: configuration of samples during proton irradiation at PS.

For proton irradiation, crystals were positioned as in the right picture of Fig. 5.2. Samples 2620 and 2622 were put in the front of a 10 cm long  $\text{PbWO}_4$  crystal whereas crystal 2621, 2624 and 2619 after the crystal which acted as a preshower. This allowed to check for

Sample	Crystal dimension along beam direction	Comment
LSO:Ce 2620	1.29 cm	Very low doped
LSO:Ce 2621	1.28 cm	Very low doped
LSO:Ce 2622	0.67 cm	Undoped
LSO:Ce 2624	0.98 cm	Undoped
LSO:Ce 2619	1.29 cm	Low doped
LSO:Ce Ref	1.00 cm	Standard doping
YSO:Ce 2643	2.00 cm	Standard doping
YSO:Ce 2668	2.00 cm	Standard doping

**Table 5.2:** Set of LSO:Ce and YSO:Ce samples used for radiation damage studies. Crystal length along the direction of proton beam which corresponds to the one used for  $\mu_{ind}$  calculation is also reported.

differences in the effect of direct proton damage with respect to the secondary particles originating from the cascade inside PbWO<sub>4</sub>. Measurements of transmission were then made 30 days after proton-irradiation, when the level of crystal activation was below the level for safe handling by the personnel.

### 5.3.2 Induced Absorption

Transmission curves measured before  $\gamma$ -irradiation are shown in Fig. 5.2 and compared with the transmission of a standard commercial LSO:Ce crystal. In the commercial sample, being highly doped, no light is transmitted below 400 nm because it is self absorbed by the Ce<sup>3+</sup> excitation levels. In this case the study of radiation damage in the UV range is not possible. On the contrary, in the other samples, having lower Cerium concentrations, it is possible to study the intrinsic transmission spectrum of the crystal at wavelengths below 400 nm.

### Gamma Irradiation

After  $\gamma$ -irradiation to a total dose of 2 kGy, all the samples showed a loss in transmission, especially at low wavelengths as shown in Fig. 5.3 for crystal 2621. A detailed study of the induced absorption revealed that several common color centers can be identified. A fit of the  $\mu_{ind}$  with a 5-gaussians model was performed, as shown for sample 2621 in Fig. 5.3, suggesting the presence of five  $\gamma$ -induced color centers around 240, 300, 340, 380 and 415 nm. An additional broad band at larger wavelengths ( $\approx$  550 nm) could probably exist although no fit was attempted due to the low resolution of such curve. The samples revealed a spontaneous recovery at room temperature (see Fig. 5.3) which was also monitored at higher temperatures (100, 200, 300 °C) as reported in [96].

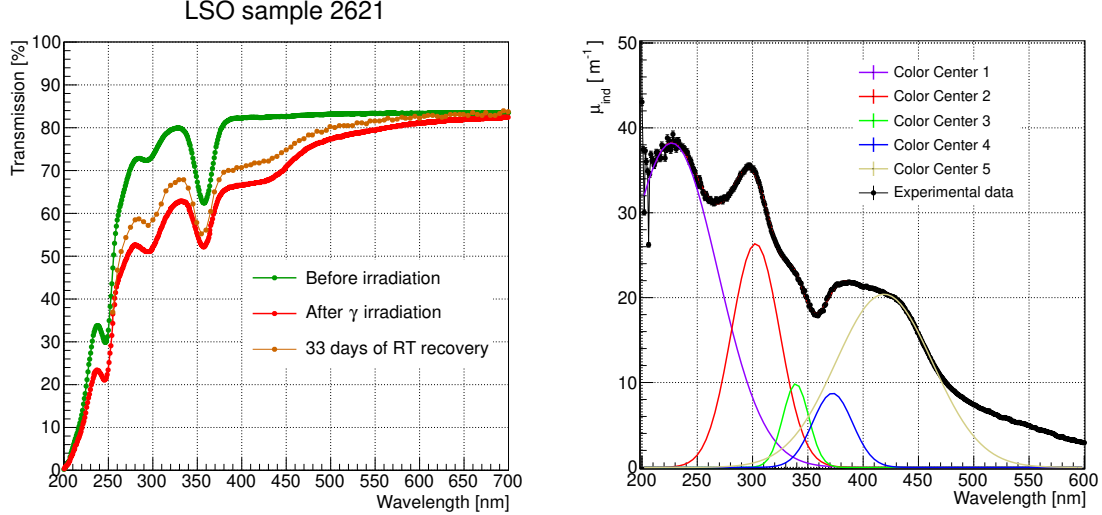


**Figure 5.3:** Left: transmission curves for crystal 2621, before and after  $\gamma$ -irradiation and after 33 of recovery at room temperature. Right: fit of induced absorption spectrum for sample 2621 indicating the presence of five color centers.

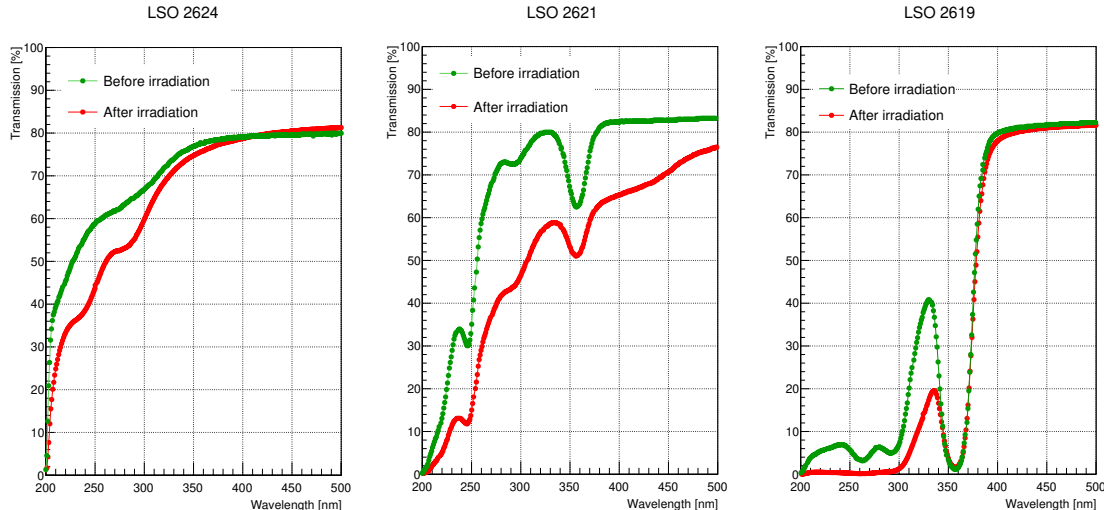


**Figure 5.4:** Transmission curves before and after proton irradiation for undoped (2624), very low doped (2621) and low LSO samples (2619).

## Proton Irradiation

All crystals have been annealed at 300°C for several hours recovering their initial transmission and then re-irradiated with protons. After proton irradiation, transmission curves reveal color centers similar to  $\gamma$ -irradiation but with a stronger absorption in the UV region which can be explained as additional damage modeled with a  $1/\lambda^4$  curve. Results are shown in Fig. 5.4.

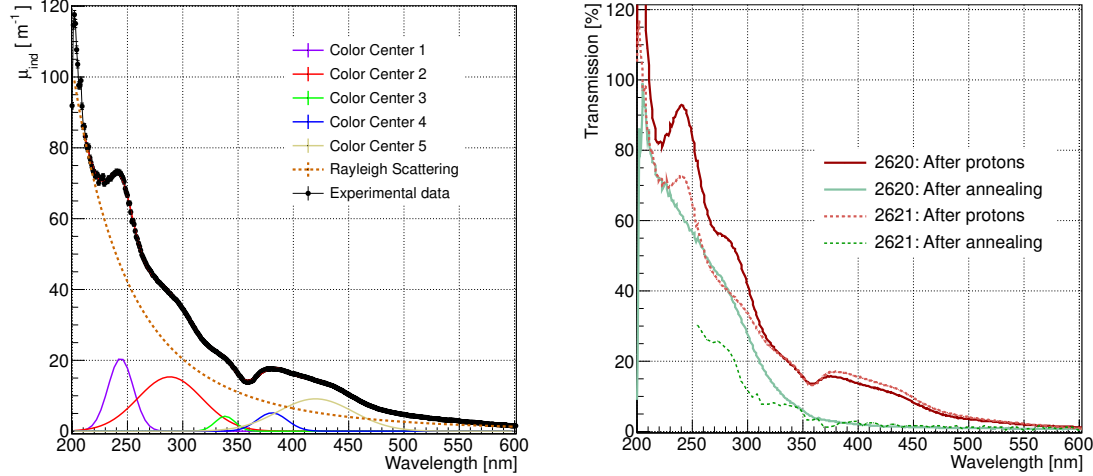


**Figure 5.5:** Left: induced absorption spectrum for crystal 2621 after proton irradiation. A fit with five color center and Rayleigh scattering curve is performed. Right: Comparison of  $\mu_{ind}$  for sample 2621 and 2620 after proton irradiation and after annealing at 300°.

To study the recovery dynamics, after proton irradiation, samples were put in a oven for several hours at 300°C and then measured again. Contrary to what previously observed with  $\gamma$ -damaged crystals, the transmission of the samples at low wavelengths does not completely recover. The intensity of color centers is significantly reduced but the low wavelength component almost remains unchanged (see the right plot in Fig. 5.5). This means that color centers below 360 nm are clusterized and their annealing requires more energy or longer treatments.

On the other hand, it has to be noticed that loss of transmission at the emission peak ( $\sim 420$  nm) is very different between samples. In particular, crystal 2619 shows almost no damage in that region if compared with sample 2621. This supports the idea that optimization of raw material quality, cerium concentration and growing parameters can improve the radiation hardness of LSO:Ce crystals in this range wavelengths.

Also the YSO:Ce samples showed a good radiation hardness above 400 nm both after  $\gamma$  and proton irradiation (see Fig. 5.6). Due to the high Cerium concentration, for these crystals, it was not possible to study induced absorption below the band edge. However, due to their similar crystalline structure LSO and YSO are expected to show similar color centers. This hypothesis is strongly supported by Thermo Stimulated Luminescence (TSL) studies carried out in [100, 101].

As argumented in [96], the nature of radiation damage in LSO, whose color centers are based on  $V_K$ -type traps, has peculiar differences with respect to PbWO<sub>4</sub> and requires additional considerations. In PbWO<sub>4</sub> crystals, having energy gap of  $E_g = 4.28$  eV, F-centers (anion vacancies) are also shallow, have a thermalization energy of 0.07 eV and

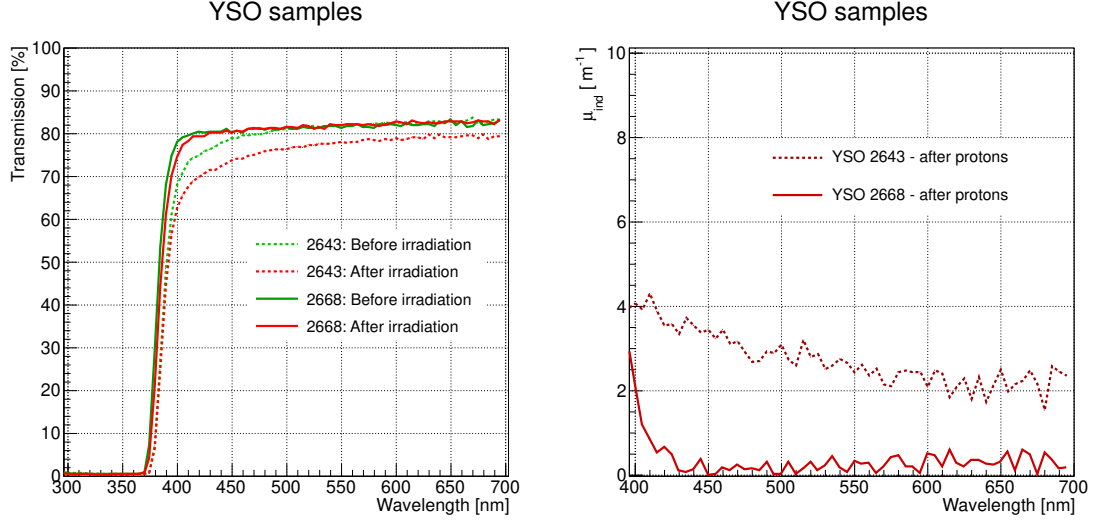


**Figure 5.6:** Left: Transmission curves before and after proton irradiation for YSO crystals 2643 and 2668. Right: Comparison of  $\mu_{ind}$  for sample 2643 and 2668 after proton irradiation.

decay rapidly at room temperature. For this reason, the recapture to deep centers is strongly favorized. The deepest electron trap center in  $\text{PbWO}_4$  is the Frenkel Type Defect (FTD), already existing at a moderate concentration in non-irradiated  $\text{PbWO}_4$  crystals. Defects concentration then increases after proton irradiation. Contrary to lead tungstate, LSO crystals have a larger band gap ( $E_g \approx 6$  eV) and thus the  $V_K$  centers create deep and stable F-centers. Oxygen vacancies also compete with the FTD in recapturing free carriers, making F-centers the dominating color centers in irradiated crystals.

### 5.3.3 Induced Phosphorescence

Measurements of induced absorption have shown that protons produce a significant number of additional  $V_K$ -type traps in LSO crystals which create stable color centers. As shown in Fig. 5.7, the  $d$ -level of  $\text{Ce}^{3+}$  is 0.5 eV below the bottom of the conduction band and F-centers have even larger thermalization energy ( $E_{th} \geq 1$  eV). In such configuration, F-centers weakly interact with unexcited ions in the matrix since their ground states are about 0.5 eV below the  $\text{Ce}^{3+}$  ion  $d$ -level state in the band gap.

The tunneling effect of the trapped electrons to  $\text{Ce}^{3+}$  ions leads to the creation of  $\text{Ce}^{2+}$  divalent ions, which have electronic states in the conduction band [102]. Delocalized electrons will be immediately recaptured by another trap. This process prevents spontaneous relaxation of F-centers in irradiated crystals. The situation completely changes when crystals with traps and color centers created by proton irradiation are used as scintillators in an environment exposed to high radiation levels.

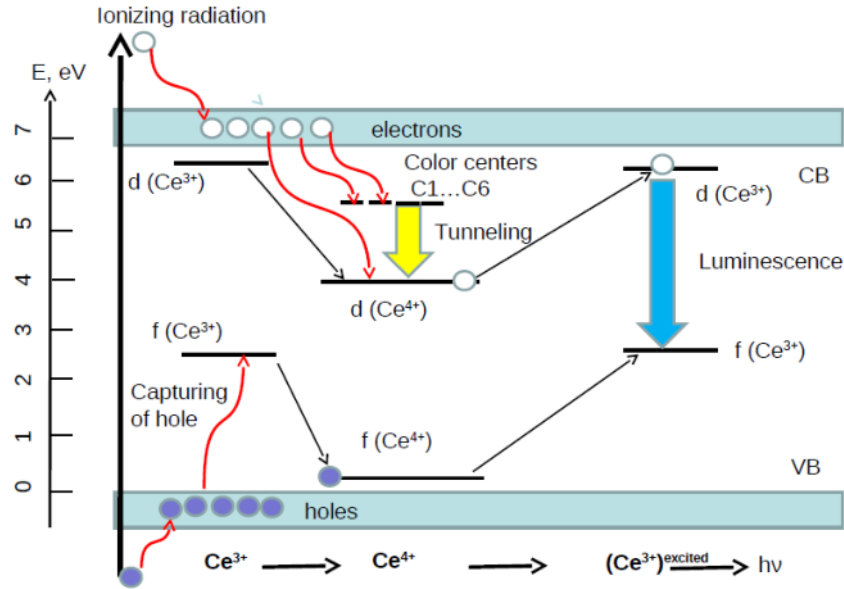
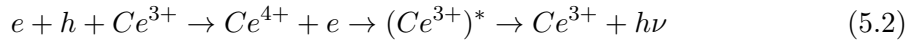
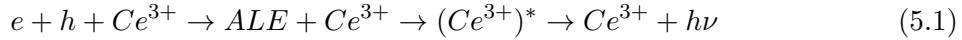


**Figure 5.7:** Schematic representation of band structure and phosphorescence mechanism in LSO crystals doped with Ce<sup>3+</sup> ions.

The scintillation in Ce-doped oxy-orthosilicates is in general driven by two processes [103]:



In oxides, luminescence occurs due to interaction with Self-Trapped Excitons (STE). The competing process with the formation of excitons is the direct capture of free thermalized carriers holes (h) and electrons (e) by Ce<sup>3+</sup> ions leading to the formation of the (Ce<sup>3+</sup>)<sup>\*</sup> excited state. While the Ce<sup>3+</sup> ion captures a hole, the short-term creation of a Ce<sup>4+</sup> ion occurs.

The unfilled *d*-level of Ce<sup>4+</sup> becomes lower than Ce<sup>3+</sup> *d*-level as well as the ground states of F-centers. In case of a high concentration of F-centers, they become effective donors of electrons through tunneling in the final stage of the process. Contrary to heavy LSO, where the density of holes in the valence band is very high, in light YSO the creation of excitons is fast and it is therefore the dominant process for scintillation [104].

Because of these mechanisms, represented in Fig. 5.7, a higher level of induced phosphorescence is expected in proton-damaged samples especially for LSO. To verify this expectation, proton-damaged crystals (after thermal annealing at 300°C) were irradiated with a 6 GBq <sup>60</sup>Co source for 24 hours at a dose rate of 0.15 Gy/h.

About 1 minute after irradiation their phosphorescence was measured with the setup shown in Fig. 5.8. Each crystal was positioned at 4 cm from a XP-2020Q PMT window

and two diaphragms were used to “probe” only a fraction of the crystal volume. An oscilloscope was then used to display the single electron pulses from phosphorescence in a given time window (in the range 0.1-10 ms). The average number of photoelectrons within this time window was used to calculate the phosphorescence rate for each crystal after normalization to the effective crystal volume ( $\text{kHz}/\text{cm}^3$ ). The PMT noise ( $\approx 0.95 \text{ kHz}$ ) has been estimated with the same procedure and subtracted from the signal.

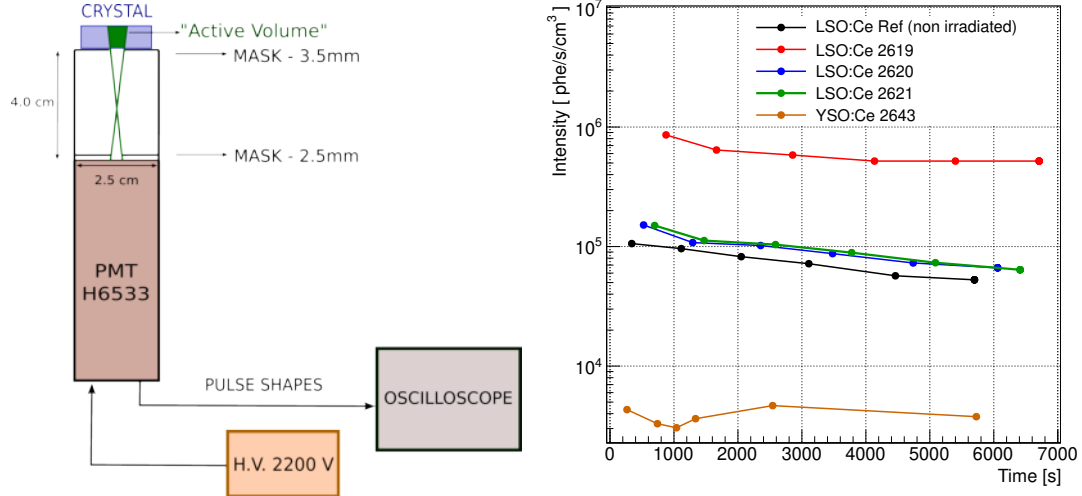


**Figure 5.8:** Left: schematic view of experimental setup used for phosphorescence measurement. Right: time dependence of phosphorescence intensity after  $\gamma$ -irradiation for different samples. YSO sample show negligible phosphorescence with respect to LSO crystals.

Results are reported in Fig. 5.8. As expected, the phosphorescence level of the irradiated YSO:Ce sample is comparable with the PMT thermal noise. Non-irradiated reference crystal showed the lowest phosphorescence with respect to the LSO:Ce samples. Proton-irradiated LSO crystal, doped with high concentration of Cerium (2619), shows about ten times higher phosphorescence level with an approximate decay time constant of about 900 s. On the contrary, irradiated LSO samples (2620, 2621) with a very low Cerium concentration show a much smaller level of phosphorescence. This effect can be explained by the decrease of the tunneling probability (from F-centers to luminescence centers) in the crystal with low  $\text{Ce}^{3+}$  concentration. In the case of high cerium concentration (sample 2619), the phosphorescence photon flux reaches  $5 \text{ MHz}/\text{cm}^3$  immediately after irradiation with dose rate of  $0.15 \text{ Gy/h}$ , but it could be dramatically larger at higher dose rates.

The phosphorescence leads to a redistribution of the scintillation light from the fast component to a very slow component. Therefore it would cause a strong noise count rate in LSO:Ce-based detectors operating in radiation environments with high hadron fluences. Implications of phosphorescence for calorimetry application, in particular for a Shashlik-type device, have been investigated in [98].

## 5.4 Lu<sub>3</sub>Al<sub>5</sub>O<sub>12</sub> and Y<sub>3</sub>Al<sub>5</sub>O<sub>12</sub> Crystals

The interest for Lutetium and Yttrium Aluminum garnet crystals, respectively Lu<sub>3</sub>Al<sub>5</sub>O<sub>12</sub> (LuAG) [105, 106] and Y<sub>3</sub>Al<sub>5</sub>O<sub>12</sub> (YAG) [107], has recently increased due to their excellent scintillating properties. Using Ce<sup>3+</sup> or Pr<sup>3+</sup> doping ions both high light yield (up to 25000 and 20000 photons/MeV resp.) and fast scintillation can be obtained ( $\tau_d = 55$  and 20 ns resp.) [108, 107]. Density and other properties are similar to LSO and YSO crystals, as reported in Table 5.1. However, for LuAG:Ce crystals the emission spectrum is shifted towards the green (with a maximum around 520 nm).

### 5.4.1 Induced Absorption

Radiation hardness of LuAG:Ce and LuAG:Pr crystals has been studied in detail in [109] by irradiating samples with a <sup>60</sup>Co  $\gamma$ -source up to 100 kGy of integrated dose. In particular, the occurrence of two color centers at 370 nm and 600 nm was observed and attributed to a contamination of Yb in the raw material. Such contamination is often present in Lu<sub>2</sub>O<sub>5</sub> raw materials whereas it is not mentioned for Y<sub>2</sub>O<sub>3</sub>, indicating that in the latter case the contamination of raw material is negligible. Additional irradiation studies have been performed at CERN, with both  $\gamma$ -rays and proton sources, on a set of crystals reported in Table 5.3 and shown in Fig. 5.10. The results confirmed the importance of raw material purity for radiation hardness as visible from the induced absorption spectra of several LuAG and YAG samples in Fig. 5.9.

Sample	Crystal dimensions [cm]	Type of irradiation
LuAG:Ce 2687	$0.3 \times 0.3 \times \mathbf{3.0}$	<sup>60</sup> Co $\gamma$ - 1 kGy
LuAG:Ce 2686	$0.5 \times \mathbf{0.5} \times 3.0$	protons - $3.5 \cdot 10^{13} \text{ cm}^{-2}$
LuAG:Ce 2055	$0.8 \times 0.8 \times \mathbf{4.2}$	1, 100 kGy $\gamma$ and protons
YAG:Ce 2671	$0.3 \times 0.3 \times \mathbf{4.5}$	<sup>60</sup> Co $\gamma$ - 1 kGy
YAG:Ce 2670	$0.5 \times \mathbf{0.5} \times 4.5$	protons - $3.5 \cdot 10^{13} \text{ cm}^{-2}$

**Table 5.3:** Set of LSO:Ce and YSO:Ce samples used for radiation damage studies. Crystal dimension along which the transmission was measured is highlighted with bold character.

For both crystals a loss of transmission is observed but for the YAG sample no clear absorption band is resolved above 500 nm. From the right plot of Fig. 5.9, it can be seen that the same band at 600 nm is observed in LuAG samples both after  $\gamma$  and proton irradiation whereas no particular structure can be identified for YAG. Observed damage effects, including a higher loss of transmission at low wavelengths after protons irradiation, can be interpreted similarly to what was previously discussed for oxy-orthosilicates (LSO and YSO) samples in Sec. 5.3.

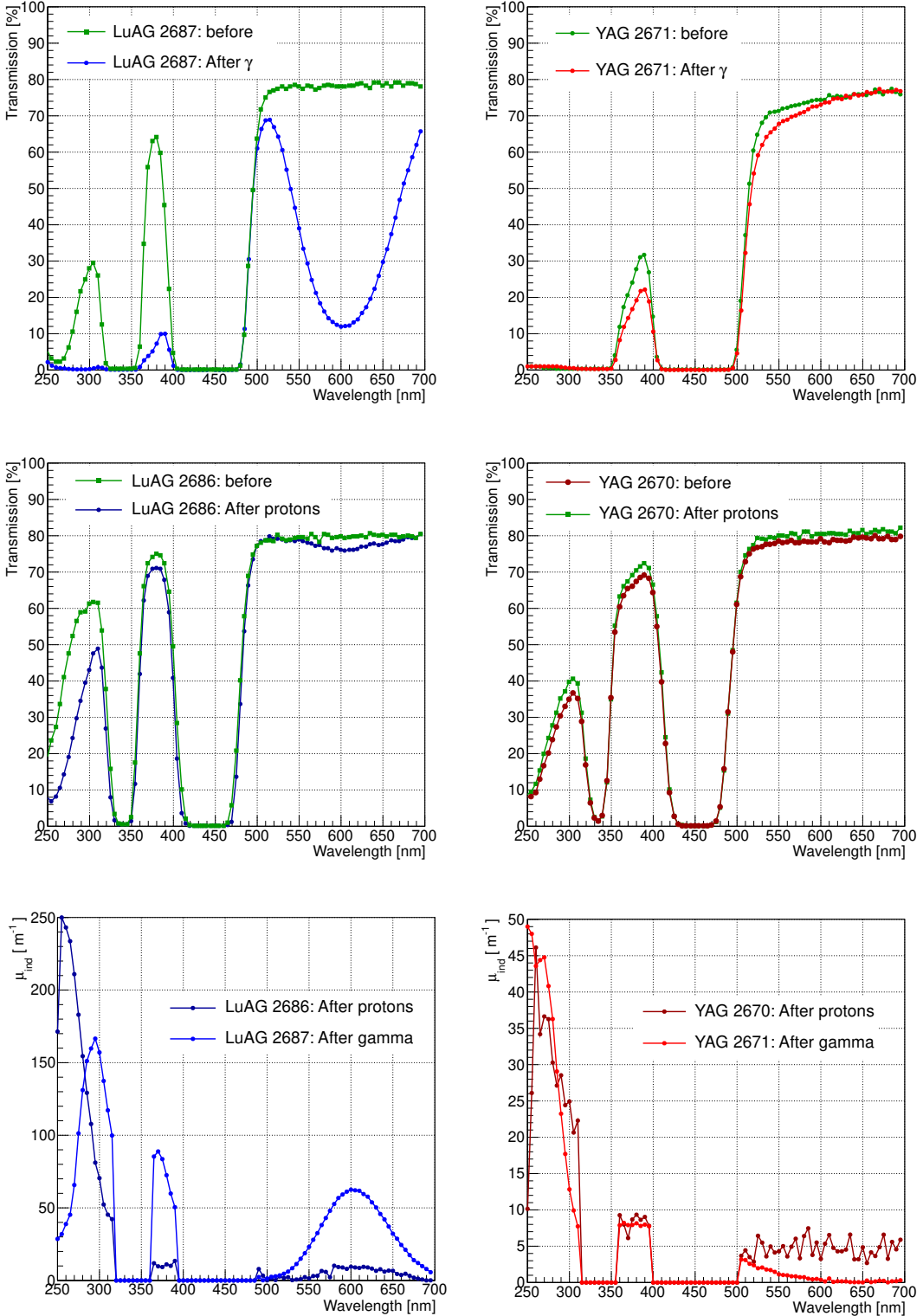


**Figure 5.9:** LuAG:Ce (left) and YAG:Ce (right) irradiation results using proton and  $\gamma$  sources.  $\mu_{ind}$  is set to zero when transmission is below 5% due to Cerium self absorption.

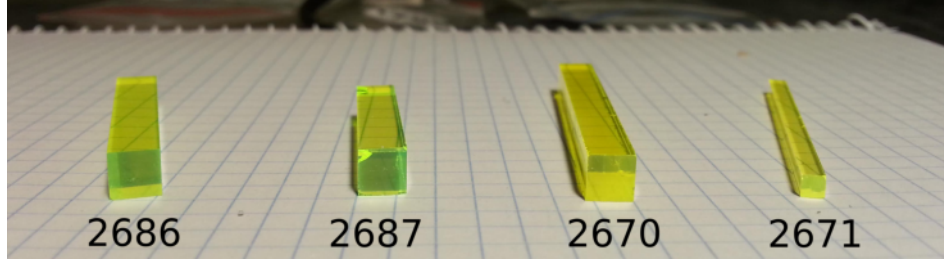


**Figure 5.10:** Picture of some LuAG:Ce (left) and YAG:Ce (right) samples used for irradiation test. The former being more greenish with respect to YAG:Ce which appears more yellowish.

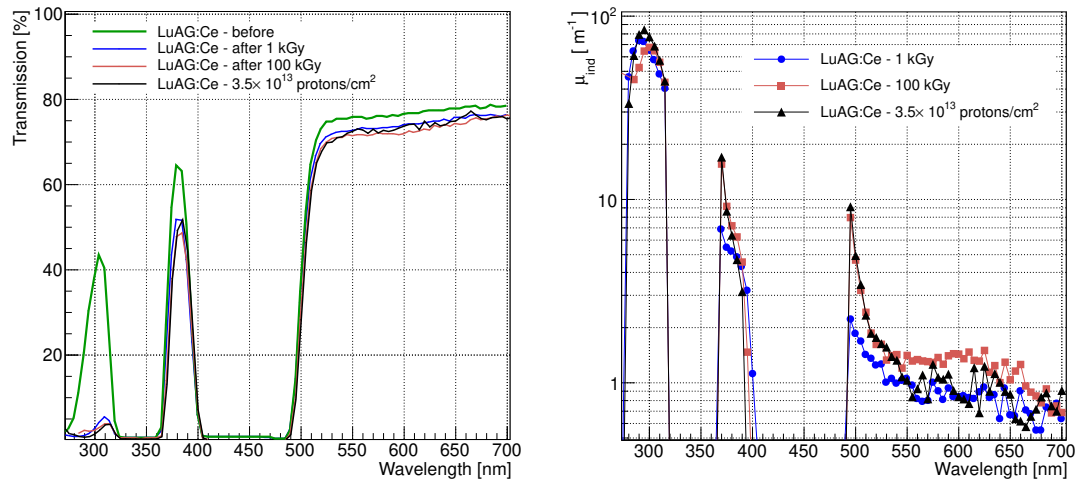


**Figure 5.11:** Left: Transmission curves before and after irradiation with different sources for LuAG:Ce crystal 2055. Right: Comparison of  $\mu_{ind}$  for sample 2055 after  $\gamma$ -irradiation up to 1 kGy (blue circles) and 100 kGy (red squares) and proton irradiation to fluence of  $3.5 \times 10^{13} \text{ cmm}^{-2}$ . Induced absorption was set to zero if transmission was below 5%.

The LuAG:Ce sample 2055, was grown with Bridgman technique [110] and studied under  $\gamma$  and proton irradiation at CERN. Proton irradiation was performed at PS to a cumulated fluence of  $3.5 \times 10^{13} \text{ p/cm}^2$  and two separate  $\gamma$  irradiation to doses of 1 and 100 kGy were performed. Before each irradiation the sample was thermally annealed at 300°C for several days and recovered completely its transparency.

The results obtained, in Fig. 5.11, show an excellent radiation hardness for this sample with no occurrence of absorption band at 600 nm. This confirms that particular attention to the quality of the raw material and to the growing process can significantly improve the radiation hardness of LuAG:Ce crystals. Induced absorption at the emission peak (520 nm) after each irradiation is always about  $\approx 1.5 \text{ m}^{-1}$  suggesting a saturation of the damage after high doses.

## 5.5 DSB:Ce Glass

Beside inorganic crystals, heavy scintillating glasses represent a suitable alternative option for calorimetry applications due to their relatively simple and low cost production. A new type of inorganic scintillating glass, named DSB, has been recently developed by “Radiation Instruments and New Components LLC” in Minsk for oil logging industry applications.

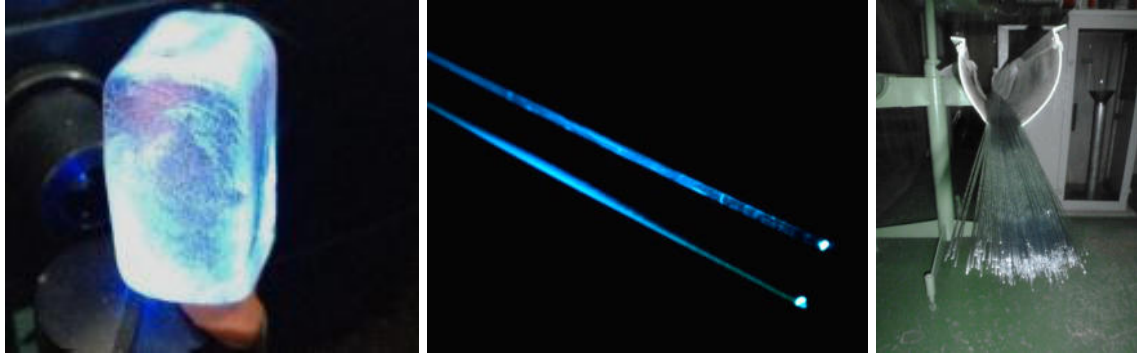


**Figure 5.12:** Picture of a DSB:Ce bulk sample (left) and fibers (center, right). Emission peak is in the blue range ( $\approx 420$  nm).

Sample	Dimensions [cm]	Ce Content [at %]	Raw material	Comment
DSB:Ce 2743	$1.5 \times 1.5 \times \mathbf{0.45}$	0.3	1	–
DSB:Ce 2744	$1.0 \times 1.0 \times \mathbf{0.45}$	1.2	1	Deficiency of SiO <sub>2</sub>
DSB:Ce 2745	$1.2 \times 1.2 \times \mathbf{0.45}$	1.6	1	Deficiency of SiO <sub>2</sub>
DSB:Ce 2746	$1.2 \times 1.2 \times \mathbf{0.45}$	1.2	1	Excess of SiO <sub>2</sub>
DSB:Ce 2747	$1.5 \times 1.5 \times \mathbf{0.45}$	0.4	2	–

**Table 5.4:** Set of DSB:Ce samples used for radiation damage studies. Crystal dimension along which the transmission was measured is highlighted with bold character.

The DSB is a disilicate of Barium, based on a mixture of BaO<sub>2</sub> and SiO<sub>2</sub>, produced by standard glass production technology at the temperature of 1400°C. The glass is then submitted to successive thermal annealing treatments at relatively low temperature below 1000°C to achieve its nano-structure. This material can be produced either in form of bulk or fiber shape with diameter of 0.3-2 mm and length up to 2 m (see Fig. 5.12).

The production of large quantities is relatively easy and the costs are significantly lower compared to crystal fibers, mostly due to the lower temperature required to melt the material (2060°C for LuAG). Optical properties of several DSB samples have been studied at CERN and results are summarized in Table. 5.1. Details on the characterization of the samples can be found in [111]. Five bulk DSB glass samples with different Cerium concentration as reported in Table 5.4 were investigated. Sample 2748 was produced from a different type of raw material purity with respect to other samples.

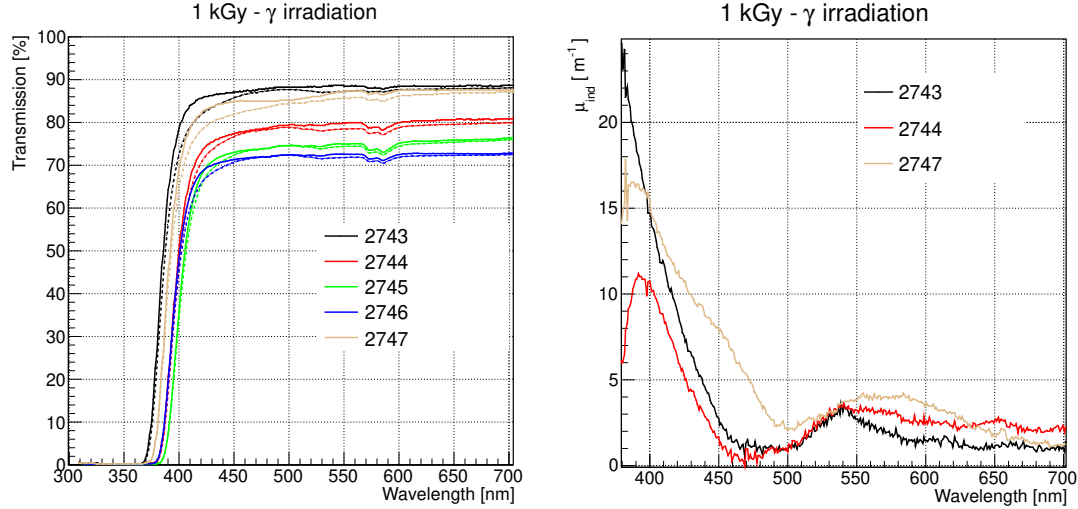


**Figure 5.13:** Left: Transmission curves before (straight line) and after 1 kGy of  $\gamma$  irradiation (dotted line) for DSB:Ce samples. Right: Comparison of  $\mu_{ind}$  for best samples (2743, 2744, 2747) after irradiation to 1 kGy.

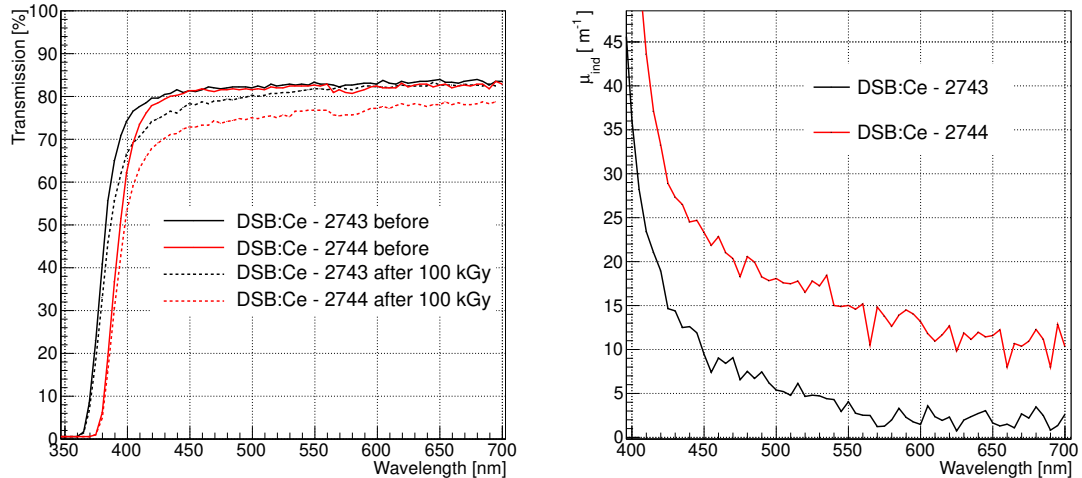


**Figure 5.14:** Left: Transmission curves before (straight line) and after 100 kGy of  $\gamma$  irradiation (dotted line) for DSB:Ce samples 2743 and 2744. Right: Comparison of  $\mu_{ind}$  for samples 2743 and 2744 after irradiation to 100 kGy.

Variations of  $\text{SiO}_2$  were also tested. Some of the samples showed a bad initial transmission. In particular it was noticed that high Cerium concentration lead to the creation of bubbles in the samples causing diffusion of light and hence a loss of transmission as shown in Fig. 5.13.

First irradiation tests were performed on DSB samples with gamma irradiation at a dose rate of 500 Gy/h to a total dose of 1 kGy. The  $\mu_{ind}$  for the samples with a good initial

transmission ( $> 75\%$ ) was calculated and is reported in the right plot of Fig. 5.13. In general, a better radiation hardness was observed for samples from raw material 1 yielding a  $\mu_{ind} \approx 5 \text{ m}^{-1}$  at 430 nm instead of  $10 \text{ m}^{-1}$  (as in the case of sample 2747). From this batch, the best samples 2743 and 2744 have been selected for a second  $\gamma$ -irradiation up to 100 kGy of integrated dose. The results obtained are shown in Fig. 5.14. The induced absorption measured at the emission peak (430 nm) was about  $15 - 20 \text{ m}^{-1}$ .

The radiation hardness of the tested samples is not yet at the level required for HL-LHC application. However, these preliminary results indicate that optimizing raw material purity and production parameters, radiation hardness of the DSB glasses can be improved. Further optimization of raw material and production conditions are currently being investigated.

## 5.6 SiO<sub>2</sub>:Ce Doped Quartz

Quartz compounds have been measured to be especially radiation hard due to the high content of OH<sup>-</sup> [112, 113]. For this reason they are widely used in very forward cherenkov calorimeters (Sec. 1.3). The possibility to dope this material with rare earth Ce<sup>3+</sup> ions, has been investigated in [114]. Fibers of SiO<sub>2</sub>:Ce have also been successfully grown by the “Dipartimento di Scienza dei Materiali” at the University of Milano-Bicocca [115]. Fibers were developed for dosimetry application and a R&D project has recently started to investigate the performance in high energy physics conditions. Dedicated irradiation studies and test beams are planned in the early future to assess their potential for calorimetry options.

## 5.7 Conclusions

Radiation hardness studies performed on a set of new scintillators suitable for calorimetry applications have been performed. Dedicated irradiation tests with  $\gamma$  and proton sources allowed to identify the best samples and to optimize the growth parameters. Good results have been obtained especially for heavy scintillating crystals (LSO, YSO, LuAG, YAG) whereas the development of radiation hard SiO<sub>2</sub>:Ce and DSB:Ce samples will require further optimization. In particular, the purity of the raw material has been identified as a fundamental requirement to avoid the formation of radiation-induced color centers inside the crystals. It was also demonstrated that Yttrium-based garnets and oxy-orthosilicates are not affected by induced-phosphorescence as in the case of Lutetium-based crystals (e.g. LSO).

## 5.7. Conclusions

---

The work on the optimization of these scintillators is still ongoing and further irradiation tests to higher doses and fluences are foreseen in the early future. At the meantime, the role of codopants such as Ca and Mg is being studied for LuAG:Ce crystals. It was already demonstrated that such codopants reduce the decay time making scintillation pulses faster and more suitable for HL-LHC conditions (25 ns bunch crossing rate). The effects of Ca and Mg codoping on the radiation hardness of the scintillator is also under investigation. As argued in the next chapter, several R&D studies aiming at the optimization of fiber shaped scintillators has started to provide a flexible tool for CMS calorimeter upgrade options. In Chap. 6, test beam results obtained with LuAG fibers are also presented.



# Test Beam Results on Crystal Fibers for Calorimetry Applications

---

The micro-pulling-down technique allows to grow single crystalline structures directly in a fiber shape. In this way, an extremely granular and high aspect ratio geometry can be obtained with a substantial saving of costs and time which would be required by properly cutting and polishing such crystal shape from a raw ingot. As discussed in Sec. 6.1, particular efforts were spent in the past years to improve and optimize this technique. The combined efforts of the Institute of Light and Matter (ILM, Lyon, France) and Fibercryst company allowed to obtain good quality fibers of both undoped and Cerium-doped LuAG crystals.

Given the wide range of applications of crystal fibers in calorimetry, as illustrated in Sec. 6.2, a set of tests with high energy beam were made to investigate the performance of this technology for high energy physics applications.

Studies were performed at CERN and Fermilab test beam facilities. The results obtained with calorimetric modules made of LuAG fibers inserted into a brass absorber, confirm the potential of this technology for applications in high energy physics detectors. The details of the calorimeter prototypes which have been tested are presented in Sec. 6.3 and Sec. 6.4. The experimental procedure as well as the results achieved are accurately discussed.

Several R&D efforts are still ongoing to further optimize the crystal fiber properties. Particular attention is focused on the improvement of radiation tolerance and time response of these scintillators. The status-of-art of this R&D is discussed in Sec. 6.5.

## 6.1 Crystal LuAG Fibers Grown with Micro-Pulling-Down Technique

The micro-pulling down process starts when a crystal seed is put in contact with the melt of the raw material. By pulling down the seed at a regular speed ( $\approx 0.2 - 1$  mm/min) the melt solidifies in a crystalline fiber-shaped structure, as shown in Fig. 6.1. The main advantage of the micro-pulling-down technique ( $\mu$ PD) is the possibility to grow crystals directly shaped into peculiar geometries (e.g. circular, hexagonal, square) avoiding the expensive need of cutting and polishing.

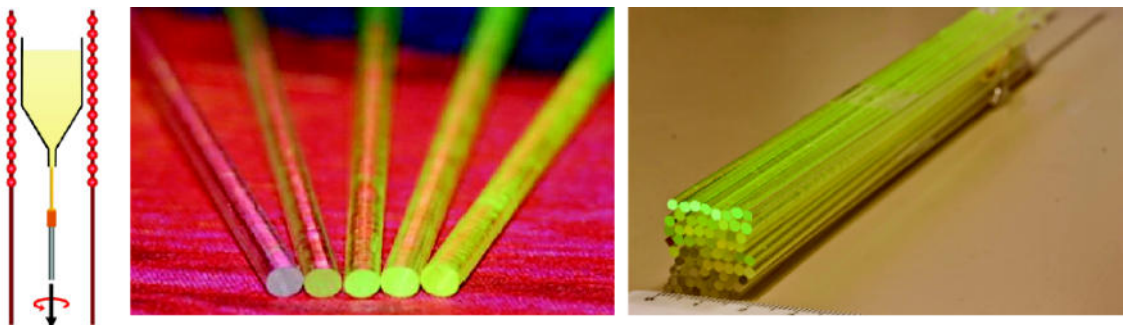


**Figure 6.1:** Schematic view of micro-pulling-down technique to grow crystal fibers (left) and pictures of LuAG crystal fibers with different Cerium concentrations (right).

If compared with standard Bridgman or Czochralski techniques, the  $\mu$ PD growing process is particularly important since the whole crystal (surfaces included) is required to have an optimal quality. For this reason it is fundamental to identify key parameters which influence the growth process. Some of these are:

- the crystal seed orientation;
- the growth atmosphere  
(to avoid creation of structural defects such as oxygen vacancies);
- the design of the thermal insulation and melt temperature  
(to avoid non-uniformities along the growth process);
- the pulling rate and the absence of parasitic vibrations  
(to obtain a smooth surface state);
- the quality of the raw material  
(since impurities may lead to creation of color centers).

In the past years, attention was focused on the optimization of LuAG:Ce and LuAG undoped cylindrical fibers of 2 mm diameter. The improvements on the quality of fibers

obtained in the past years through a dedicated process of growth parameters optimization are documented in [116]. It was found that, to maintain a good surface state, a slow pulling rate around 0.5 mm/min or below is required. This allowed to largely improve optical properties such as light propagation inside the fiber.

A detailed characterization of the optical properties of recently grown LuAG fibers is presented in [117]. Measurements of light yield and attenuation length were made, leading to the identification of best samples and improving our understanding of light propagation processes in crystals with a high aspect ratio [118]. In the last months attention was focused on establishing reference growth parameters to allow a good reproducibility of the samples (see the right picture in Fig. 6.1). The large number of fibers (more than 100 samples) grown by Fibercrust and ILM was then used to build calorimetric prototypes as presented in the following sections.

## 6.2 Motivations for Crystal Fibers Calorimetry

Beside the set of options which are currently considered for the CMS calorimeters upgrade in view of the HL-LHC phase, crystal fibers technology has a large potential for high energy physics experiments at future colliders. The extreme flexibility given by the fiber geometry allows for multiple implementations of this technology in calorimeter designs as illustrated in Fig. 6.2.

In addition to excellent timing properties, the next generation of detectors will require a significantly better jet energy resolution. To face such requirements, it was proposed earlier an approach based on meta-crystals [119, 120, 121]. In this concept, trunks of *cables* constructed from heavy inorganic single crystalline fibers are assembled to form the detector modules as reported in the top left drawing of Fig. 6.2. This solution provides an excellent granularity, is dense enough to avoid the necessity of an absorber (hence excluding sampling fluctuations) and uses the dual-readout technique to improve energy resolution of hadrons and jets. The dual readout capability can be obtained with a uniform combination of doped and undoped fibers which are designed to measure respectively the scintillation and Cherenkov signals.

In particular, LuAG crystals have been identified as promising candidates for such application due to the high refractive index ranging from 2.14 at 190 nm to 1.85 at 520 nm [122, 123] and thus the low Cherenkov threshold (97 keV for electrons). In addition to the high density ( $\rho = 6.73 \text{ g/cm}^3$ ) and relatively short radiation and interaction lengths:  $X_0 = 1.41 \text{ cm}$  and  $\lambda_I = 23.3 \text{ cm}$ , LuAG is an efficient Cherenkov radiator. For these reasons, dedicated studies have been made to confirm and directly test with high energy beams the performance of LuAG fibers. Preliminary tests were already made during short periods in 2009 and 2010 [124] but recent progress in fibers quality [116] and the necessity

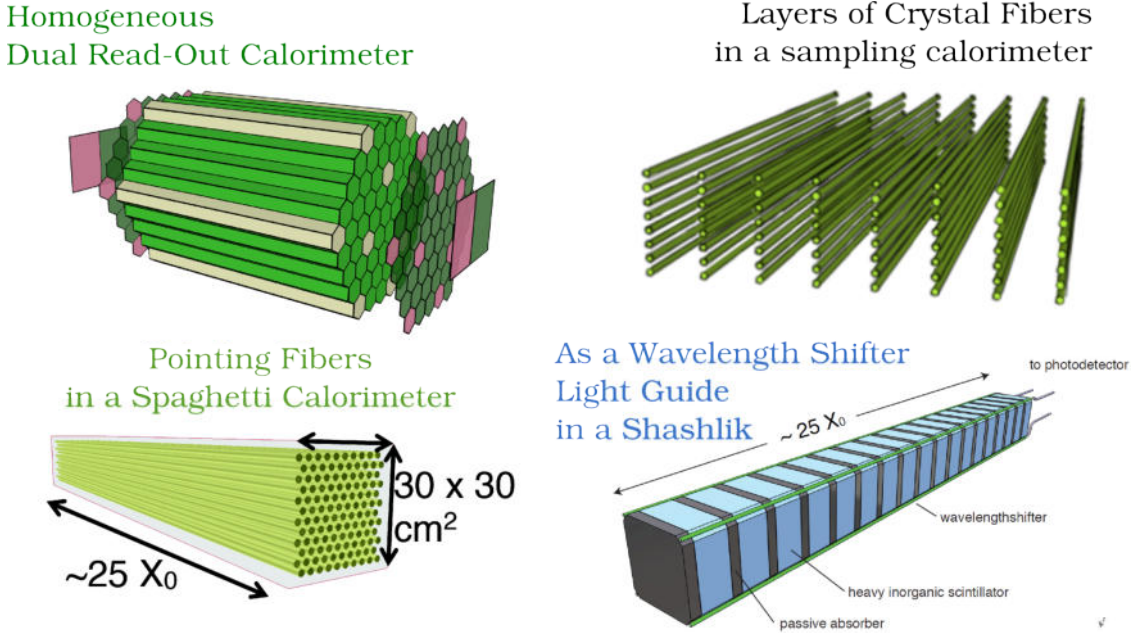


**Figure 6.2:** Top Left: simplified drawing of a homogeneous calorimeter providing a high granularity and dual readout capabilities due to the combination of Cherenkov (white) and scintillating (green) fibers as presented in [119]. Top right: schematic view of crystal fibers planes which can be inserted into an absorber structure as the one of current CMS hadronic calorimeter (Sec. 2.2.4). Bottom left: example of a SpaCal sampling calorimeter module consisting of a dense absorber filled with crystal fibers with longitudinal axis oriented along beam direction. Bottom right: crystal fibers used as a radiation hard wavelength shifter to readout the light of a “Shashlik” calorimeter as anticipated in Chap. 5.

to study different calorimeter designs (as those in Fig. 6.2) required new dedicated test beams.

Two separate calorimetric modules, with different configurations of crystal fibers and different readout techniques have been tested. A first test was performed at CERN H2 facility in 2012 [125]. Nine LuAG fibers were inserted into a brass module of  $3 \times 3 \times 22 \text{ cm}^3$  and oriented with fiber axis along beam direction (referred as *pointing configuration*). The obtained results allowed to characterize individual fiber response in terms of light output and time profile, encouraging the production of more fibers to be used in a larger calorimetric module. In 2014, a new sampling calorimeter prototype was tested at the Fermilab National Laboratories (FNAL). A set of 56 LuAG:Ce fibers and 8 LuAG undoped fibers was used to fill a brass module of  $4 \times 25 \times 16 \text{ cm}^3$ . The device was positioned with fiber axis perpendicular to beam direction (referred as *transverse configuration*) and each fiber was directly readout using Silicon Photomultipliers (SiPMs). Although both calorimetric modules suffers from sampling fluctuations and energy leakage due to the limited size, the test beam allowed to study the fiber response to high energy electrons and pions. Different readout options, such as direct coupling to SiPMs, optical clear fibers and WLS + QC system, have also been tested.

## 6.3 Preliminary Test Beam in Pointing Configuration

As anticipated, the flexibility of fiber geometry allows to design a large number of calorimeters. One of the simplest design is a calorimeter consisting in modules where fiber axis is oriented along beam direction. Submodules, made of bunch of fibers inserted into an absorber structure can then be arranged to more complex geometries depending on the detector requirements. The idea of using scintillating fibers in similar configuration was largely studied and used for the H1 experiment at Hera (Desy) [126]. A Spaghetti Calorimeter (SpaCal) prototype made of lead and plastic scintillating fibers was tested in [127] and energy resolution of  $\sigma_E/E = 7.1\%/\sqrt{E} \pm 0.6\%$  was achieved for electrons during test beams. This type of calorimeter also provides an extremely high transverse segmentation which is simply limited by the number of photodetectors and electronic channels used to read out the signal. High granularity can significantly improve particle identification as preliminary investigated in [128] and can help to mitigate pileup effects.

The SpaCal detector discussed above could not be used in HL-LHC due to the extremely high radiation levels which would rapidly deteriorate the plastic fiber transparency and thus the calorimeter response. However, it could be interesting to consider a SpaCal design which makes use of radiation tolerant active materials such as scintillating crystals. In addition to radiation hardness, the overall containment capability of the calorimeter would be improved, due to the small radiation length and Molière radius of heavy crystals. For this new design, several aspects like the geometry (fiber to absorber ratio) and the readout (crystal to photodetector optical coupling) should be investigated in detail to optimize the detector performance. In this section, a preliminary study performed on a small calorimetric module made of brass and LuAG crystal fibers is presented. The work is based on tests performed at CERN SPS and documented in our earlier publication [125].

### 6.3.1 LuAG Fibers and Calorimetric Module

During 2012 and 2013, single crystalline fibers of LuAG:Ce of 2 mm diameter have been grown at the ILM by the  $\mu$ PD technique along the  $\langle 111 \rangle$  crystallographic axis with an accurate control of the pulling rate and of the applied heating power. To initiate the growth process, an oriented seed crystal is put in direct contact with the melt at the bottom of the iridium crucible. Pulling rates used were ranging from 0.25 to 0.32 mm/min. More details on the growing process parameters optimized for a best fiber quality can be found in [129]. The obtained LuAG fibers were then cut to a length of 22 cm.

A selection of 7 LuAG:Ce and 2 undoped LuAG fibers was used for the assembly of a small calorimetric module consisting of a brass volume, shaped with the tapered geometry (approximately  $3 \times 3 \times 22$  cm $^3$ ) of a EE PbWO<sub>4</sub> crystal. The fibers were wrapped with

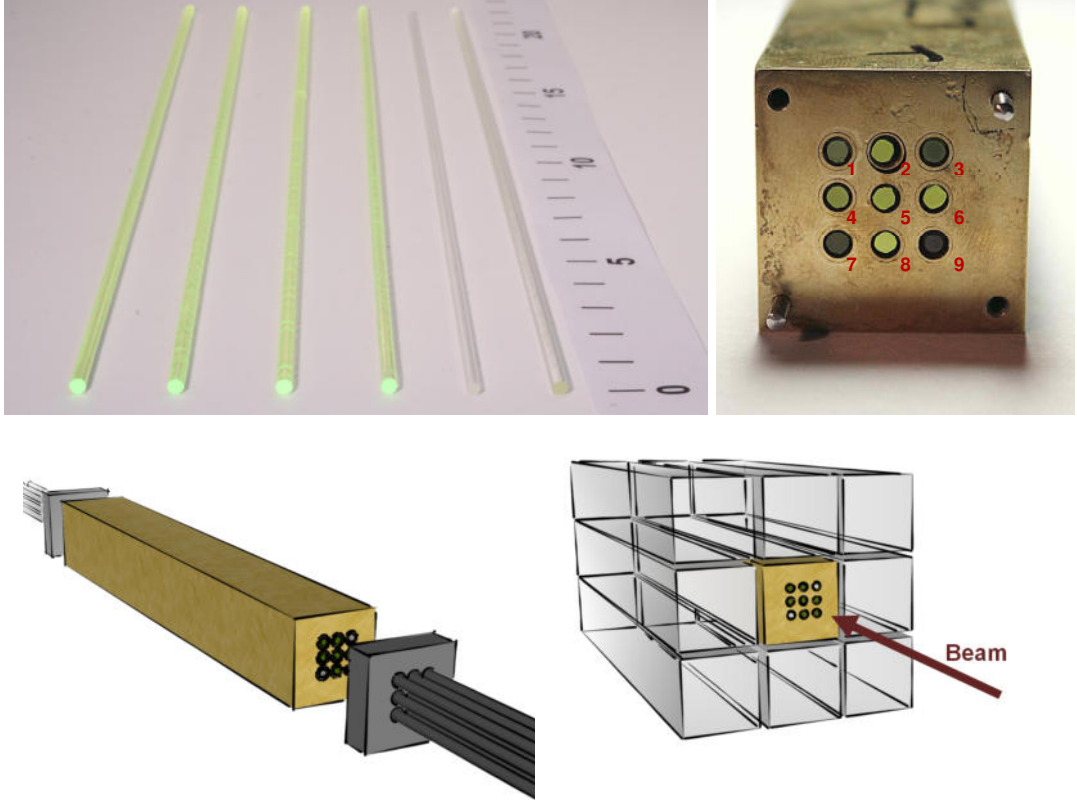


**Figure 6.3:** (Top) Pictures of a set of Cerium-doped (green color) and undoped (transparent) LuAG fibers and the brass absorber containing 9 LuAG fibers. (Bottom) The mini-CFCAL (brass absorber with 9 LuAG fibers) is connected to optical fibers for light extraction and inserted in a matrix of PbWO<sub>4</sub> crystals.

Teflon and inserted in holes of 3 mm diameter (see Fig. 6.3). The Teflon wrapping was not supposed to enhance the light output or the light propagation inside the fibers [116]. It was mostly used to protect the fibers when handling the brass element. Undoped fibers were put at the top left (number 1) and the bottom right (number 9) holes of the absorber as shown in Fig. 6.3 and the remaining holes (number 2,3,4,5,6,7,8) were filled with LuAG fibers doped with similar Cerium concentrations. In the following, we will refer to this module (brass absorber containing 9 LuAG fibers) as mini-CFCAL (miniaturized version of a crystal fiber calorimeter).

### 6.3.2 H2 Beam Line and Test Beam Setup

The mini-CFCAL has been tested in the H2 test beam line at the Super Proton Synchrotron (SPS) at CERN. A 400 GeV/c primary proton beam extracted from the SPS towards the North Areas splits into three beams one of which is then directed onto the T2 primary target. The proton beam intensity incident on this target is several 10<sup>12</sup> protons

### 6.3. Preliminary Test Beam in Pointing Configuration

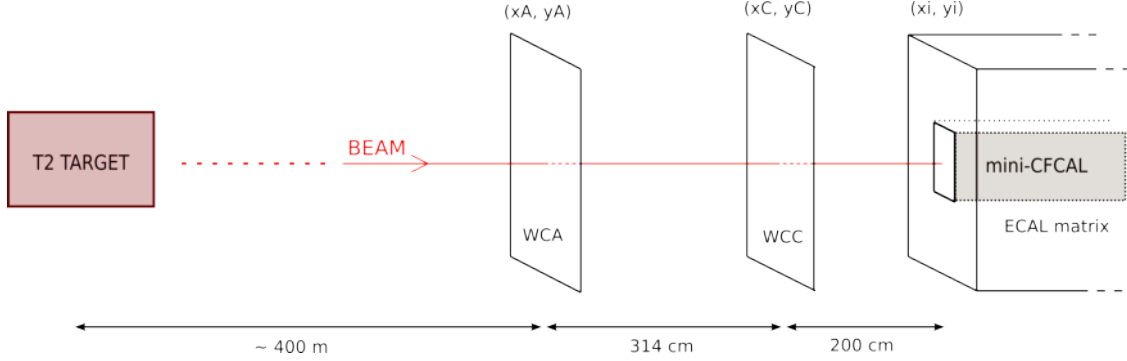


**Figure 6.4:** Sketch of the last stage of the H2 beam line at CERN, SPS. The ECAL matrix containing the mini-CFCAL is shown as well as the wire chambers WCA and WCC used in this analysis. The red arrow indicates the electrons beam direction.

per bunch. The H2 beam line picks up particles emerging from the primary target, makes a selection in terms of momentum and angle and transports them to the user areas. A detailed description of the beam line is available in [130].

A set of detectors located along the beam line allows to measure intensity and size of the beam. In this way the beam steering and focusing can be optimized. Scintillating counters located upstream from the tested prototype were used to trigger the events. Multiwire proportional chambers (WCA and WCC) shown in Fig. 6.4 provide detailed beam profiles and individual particles tracking information. The impact point on the mini-CFCAL ( $x_i, y_i$ ) was calculated by extrapolating the particle trajectory according to

$$x_i = x_{wca} + (x_{wcc} - x_{wca}) \cdot \frac{z_{wca}}{z_{wca} - z_{wcc}} \quad (6.1)$$

where  $z_{wca}$  is the distance of WCA from the absorber,  $z_{wca} - z_{wcc}$  is the distance between the two wire chambers and  $x_{wca}, x_{wcc}$  are the horizontal coordinates measured by wire chambers WCA and WCC respectively. The information on the particle position allows to study the crystal fibers response as a function of the impact point. The angular spread of the incoming particles was estimated both on  $x$  and  $y$  axis. The average angle of incoming particles was below 0.1 degrees with small fluctuations,  $\sim 0.02$  degrees, corresponding to  $\sim 1$  mm spatial resolution at the target location [125].

For the present study, a beam of electrons with energies of 50, 80, 100, 120 and 150 GeV and intensity around 2000 triggers per spill has been used. The beam size on the target was around  $40 \times 40$  mm $^2$  in order to uniformly cover the whole mini-CFCAL front face.

The mini-CFCAL was inserted in the center of eight neighboring PbWO<sub>4</sub> crystals which allowed to estimate the fraction of shower leakage and the position of the module with respect to the wire chambers reference frame. The electron beam was set parallel to the fibers

axis as shown in Fig. 6.3. For the light extraction, each extremity of the mini-CFCAL was coupled with Silicon grease (Rhodorsil Paste 7) to nine Teflon cladded plastic fibers which optically transport the analog signal from the fibers ends to the silicon photomultipliers (SiPM).

The SiPMs used are KETEK 20  $\mu\text{m}$  green-sensitive devices [131] with photon detection efficiency (PDE) of  $\sim 21\%$  at 520 nm and active area of  $2.2 \times 2.2 \text{ mm}^2$ , the gain of which was tuned to be  $\sim 1$  count per photo-electron by AC-coupling. The charge signal is measured and encoded into a non-linear digital scale by the Charge Integrator IC (QIE) [50]. The QIE uses the LHC clock to divide time into regular bins and measure the accumulated charge in each 25 ns time bin. Internally, the QIE uses capacitors to accumulate the charge and measure the voltage. There are four such capacitors on each QIE, and the QIE uses each capacitor in turn, discharging it for two clocks before using it again. Thus, each subsequent time sample comes from a different capacitor. The outputs of three QIE channels are digitally combined onto a high-speed optical link and sent to the HCAL Trigger/Readout (HTR) board. The HTR board buffers the incoming digital data and transfers it to the Data Concentrator Card which in turn transfers data to the central DAQ [132].

### 6.3.3 Test Beam Results

#### Response of Ce-doped and Undoped LuAG Fibers

Two different types of LuAG fibers have been used as active material inside the absorber: Ce-doped fibers to produce scintillation and undoped fibers as Cherenkov radiator. Their response to electrons, with energy between 50 and 150 GeV, has been studied in terms of light output and pulse shape.

Using the wire chambers informations a selection of electrons having their impact point within 2 mm radius from the center of a given fiber was done and the average pulse shape recorded from the two types of fibers was calculated. Results corresponding to 80 GeV electrons are shown in the left plot of Fig. 6.5.

A clear difference is visible between the Cherenkov pulse (measured with undoped fibers) having a fast decay time  $< 10$  ns and the scintillation pulse (given by Ce-doped fibers) which shows a longer decay time of  $\approx 60\text{-}100$  ns. The extra slower component in the undoped fiber was attributed to a Cerium contamination of the Lutetium oxyde. The experimental setup only allowed a 25 ns sampling rate which limits a detailed study of the pulse shape, a more precise measurement of the pulses performed in previous test beams [124] is shown on the right plot of Fig. 6.5 for comparison.

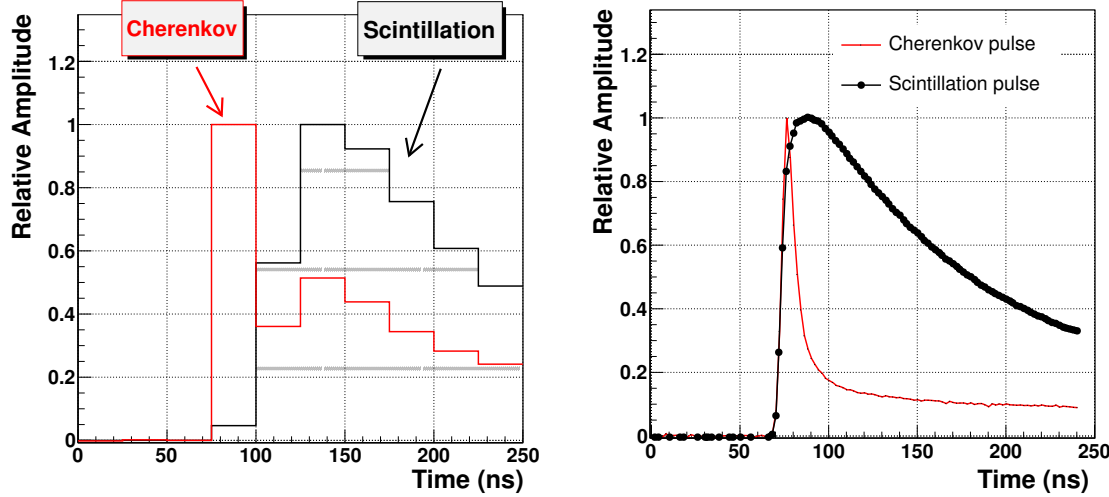


**Figure 6.5:** Left: Comparison between the average pulse shape of a Ce-doped fiber (black) and an undoped fiber (red) using 80 GeV electrons. Right: average pulse shapes with better time granularity for Ce-doped fibers (black dots) and undoped fibers (red) obtained in previous test beam using photomultiplier tubes readout with an oscilloscope [124].

Applying the same beam spot selection, the distributions of signal induced by 80 GeV electrons in the two types of fibers were obtained. The signal of each SiPM was converted in number of photoelectrons using conversion factors  $C^i$  obtained by calibrating each SiPM channel with LED signals. Ce-doped fibers, as expected, show a much higher signal ( $\sim 1800$  photoelectrons) with respect to the undoped fibers ( $\sim 80$  photoelectrons), see Fig. 6.6. These values correspond to photoelectrons measured from the back end of a given fiber, hence this number will increase for scintillating fibers, by a factor  $\sim 2$ , if also the front end signal of each fiber is considered. Furthermore, a fraction of the photons ( $\approx 60\%$ ) is lost in the optical chain which transports the light from fiber end to SiPM because of coupling inefficiencies and absorption inside the optical fiber.

### Transverse Granularity

To investigate the response of fibers as a function of the electrons impact point we made use of the wire chambers information to scan along  $x$  and  $y$  axis the whole mini-CFCAL. After a selection of events within  $\pm 5$  mm on the  $y$  axis, the average response of a given fiber while changing the impact point on the  $x$  axis was calculated. The same procedure was performed for the  $y$  axis. The maximum values  $IC_x$  and  $IC_y$  of these transverse profiles correspond to the average response of the fiber when the impact point is equivalent to the fiber position, on the  $x$  and  $y$  axis respectively.

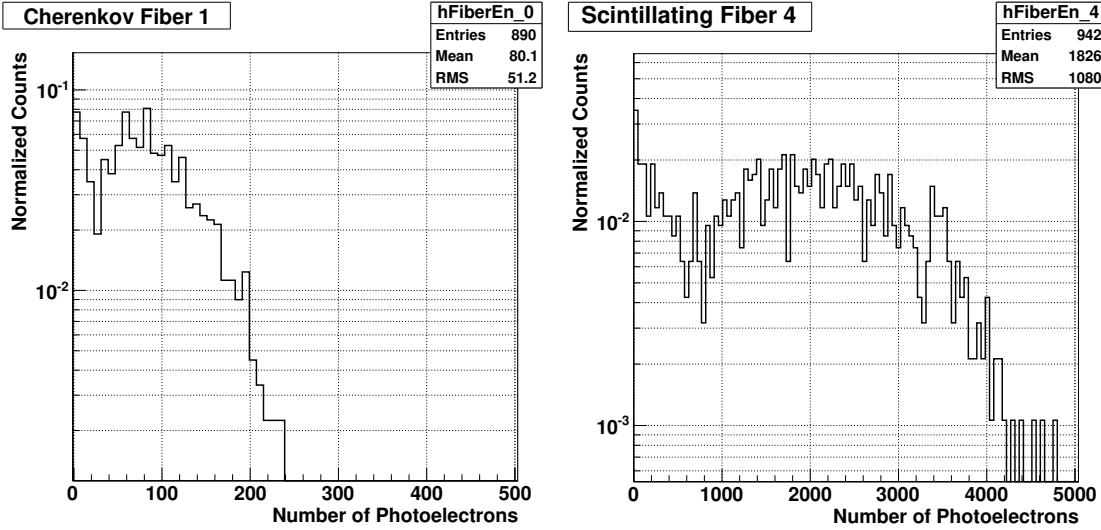


**Figure 6.6:** Distribution of photoelectrons measured from one end of a Cherenkov fiber (left) and a scintillating fiber (right) using 80 GeV electrons within a  $2 \times 2 \text{ mm}^2$  beam spot around the center of the selected fiber.

These coefficients are proportional to the light output of each fiber. Therefore, we can define intercalibration coefficients between fibers as

$$IC^i = \frac{IC_x^i + IC_y^i}{2} \quad (6.2)$$

This intercalibration procedure is necessary to normalize the signal from different fibers in order to take into account their different light output which is related to the Cerium concentration, the fiber quality and the optical coupling between crystal fibers, optical fibers and SiPMs. The normalized distributions for the central row and central line fibers are shown in Fig. 6.7. Transverse profiles on the  $y$  axis show narrower peaks around the fiber positions reflecting the higher quality of the beam profile on the  $y$  axis with respect to the  $x$  axis.

### Energy Reconstruction

Once intercalibration coefficients are applied, the particle energy can be reconstructed summing up the contribution from different fibers in order to collect the maximum fraction of energy deposited by the shower in the mini-CFCAL. Events within a beam spot of 5 mm radius around the central fiber have been selected in order to consider only electrons which starts the shower inside the array of fibers.

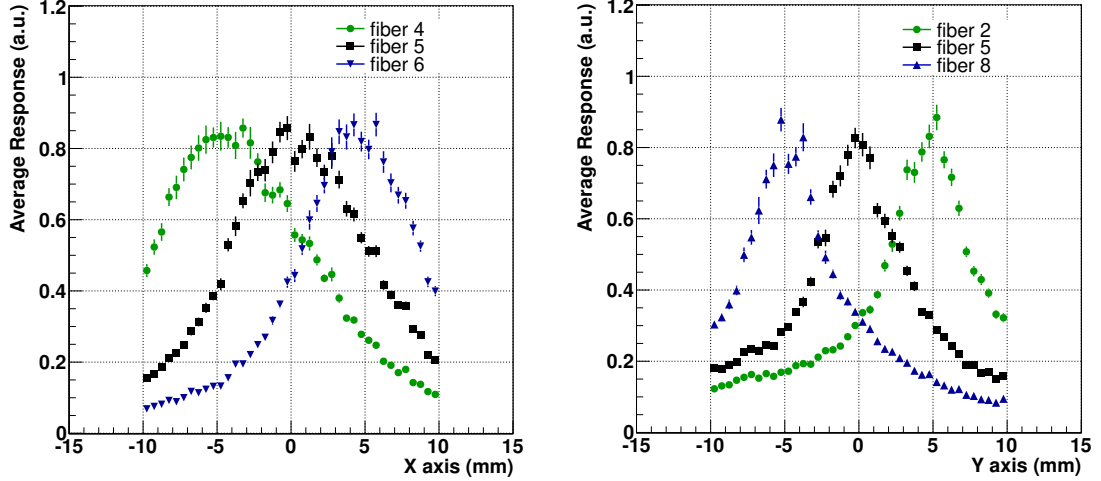


**Figure 6.7:** Left: Average response of the fibers of the central row as a function impact point along the x axis: fiber 4 (green), fiber 5 (black), fiber 6 (blue). Right: Average response of the fibers of the central line as a function impact point along the y axis: fiber 2 (blue), fiber 5 (black), fiber 8 (green).

The contribution of each fiber, after intercalibration, has been summed up event by event to reconstruct the total signal

$$E_{reco} = \sum_{i=1}^9 S_{front}^i \cdot C^i \cdot IC^i \quad (6.3)$$

where  $S_{front}^i$  is the signal measured from the front end of each fiber  $i$ ,  $C^i$  are calibration factors to convert the SiPM channel into photoelectrons, obtained using a LED signal as reference, and  $IC^i$  are the intercalibration coefficients.

For the energy reconstruction, only signals from the front end of the fibers have been used, since for two fibers (namely fiber 3 and fiber 5) the back signal was not available because of a wrong tuning of the corresponding SiPM voltages. If all back readouts were available, reconstructing the signal using both front and back signals could slightly increase the resolution because of the higher photostatistics. Using electrons at different energies between 50 and 150 GeV, we studied the evolution of the fibers array response. The distributions of the reconstructed amplitude,  $E_{reco}$ , are then fitted with a Gaussian function to estimate the peak position. The module response shows a good correlation with the beam energy as shown in the right plot of Fig. 6.8. The energy resolution of the reconstructed amplitude varies from 15% to 20%, being dominated by a constant term due to the transverse non-uniformity of the response and several experimental systematics discussed in Sec. 6.3.4.

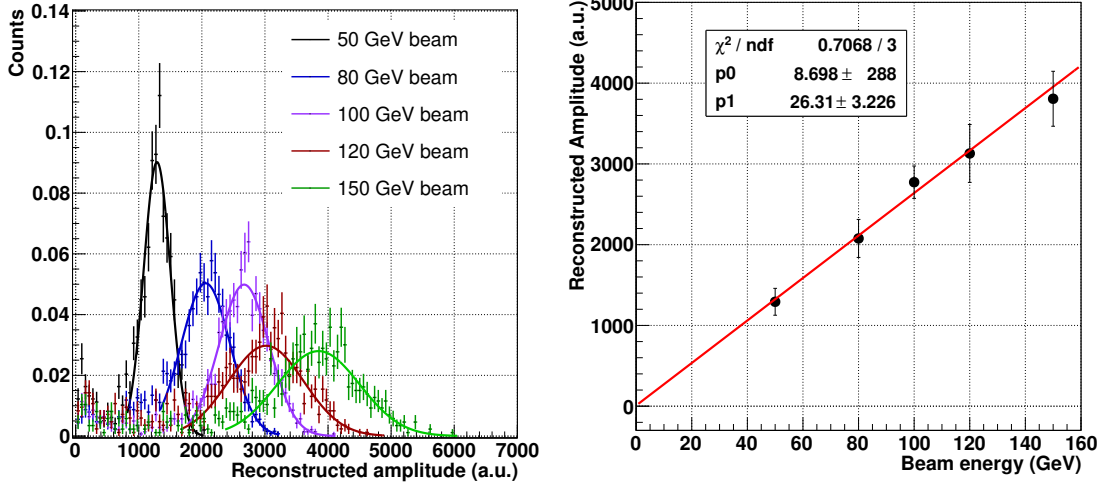


**Figure 6.8:** Left: distributions of reconstructed amplitude  $E_{reco}$  at different beam energy. Right: correlation between the peak value of  $E_{reco}$  distributions and the beam energy with a linear fit (red line). Error bars represent the statistical error on the estimation of peak position.

### Longitudinal Shower Profile

While increasing the energy  $E$  of incoming electrons, the position of the shower maximum  $t_{max}$  moves towards the back of the absorber according to

$$t_{max} \propto \ln(E) \quad (6.4)$$

This change in the shower profile along the longitudinal axis  $z$  is expected to produce a different ratio of the front and back signals. We can define a dimensionless estimator of the shower maximum position as

$$R_{BF} = \ln \left( \frac{S_{back}}{S_{front}} \right) \quad (6.5)$$

where  $S_{front}$  and  $S_{back}$  are respectively the signals measured at the front and back end of a fiber. The value of  $R_{BF}$  was estimated for both Cherenkov and scintillating fibers using different beam energy in the range from 50 to 150 GeV. A beam spot selection of 5 mm around the selected fiber was applied in order to reduce the noise background. In Fig. 6.9, results obtained with the Cherenkov fiber number 1 are shown. We observed a clear correlation between the value of  $R_{BF}$  and the beam energy which demonstrates the feasibility of longitudinal shower profile studies using a double readout technique. Similar results are obtained using the scintillating fiber number 4 as shown in Fig. 6.10.

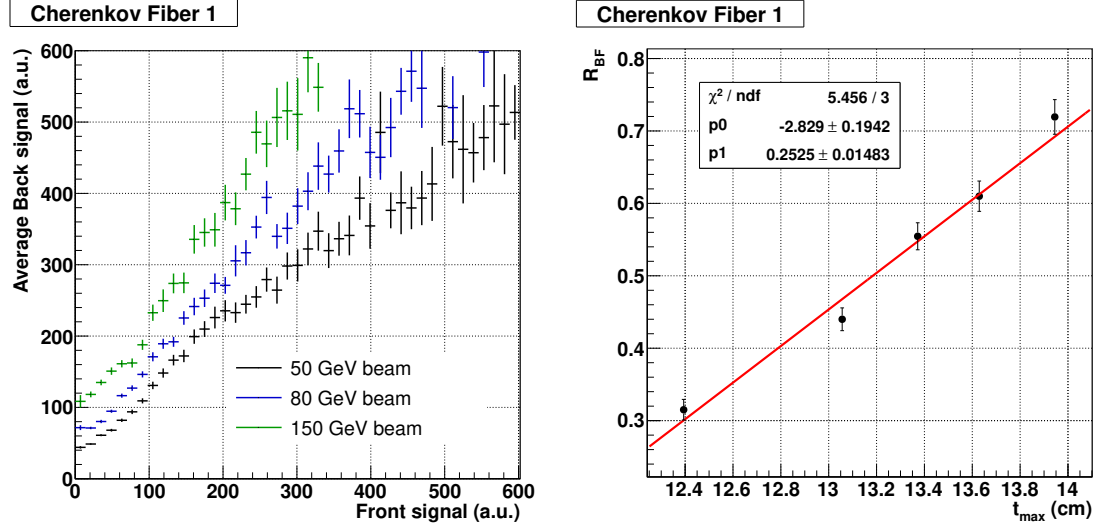


**Figure 6.9:** Left: the correlation between front  $F$  and back  $B$  signals of Cherenkov fiber number 1 is shown at different beam energy. Right: correlation between  $R_{BF}$  and the theoretical  $t_{max}$  position for a given beam energy with a linear fit (red). Error bars represent the statistical uncertainty on the points.

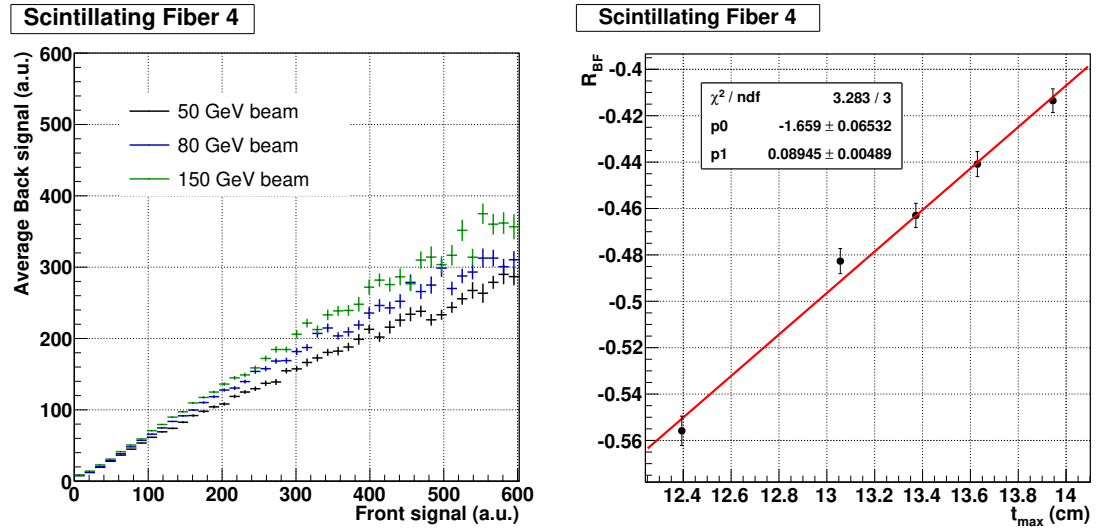


**Figure 6.10:** Left: the correlation between front  $F$  and back  $B$  signals of scintillating fiber number 4 is shown at different beam energy. Right: correlation between  $R_{BF}$  and the theoretical  $t_{max}$  position for a given beam energy with a linear fit (red). Error bars represent the statistical uncertainty on the points.

The different nature of scintillation and Cherenkov light, the former being emitted isotropically whereas the latter has a favorite direction, can explain the difference between the two type of correlations. As expected, the Cherenkov fiber shows a much higher signal at the rear end with respect to the front one.

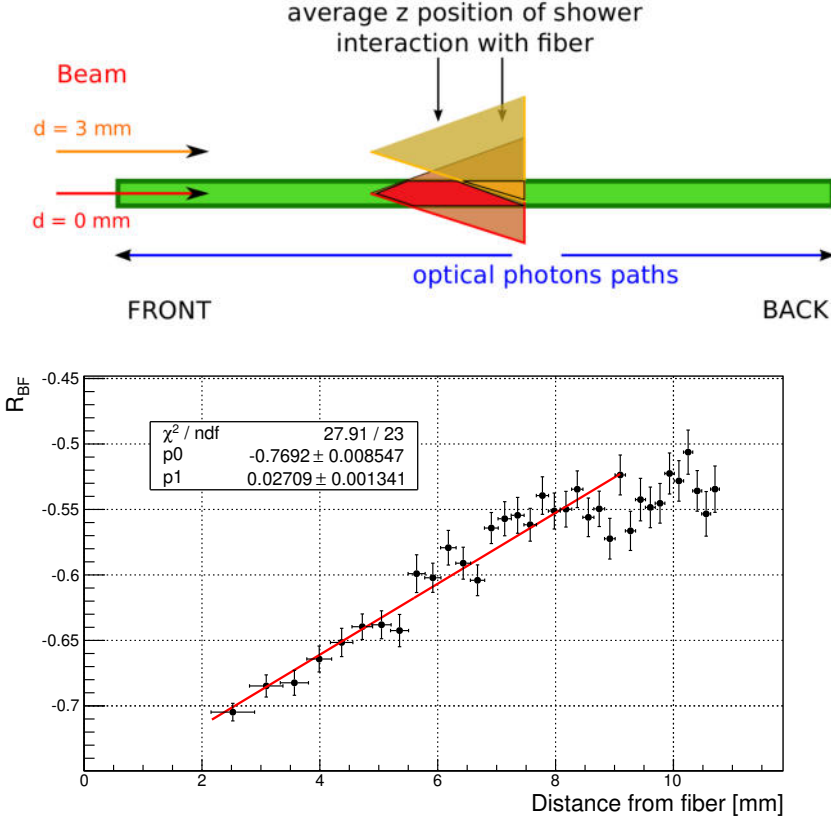


**Figure 6.11:** Top: A sketch to naively represent the drift of the average interaction point of the shower with a given a fiber when the electron impact point move away from the fiber center. Bottom: correlation between the value of  $R_{BF}$  and the position the distance of electrons from the fiber. A linear fit is performed in the range (2-9) mm distance (red line). Error bars represent the statistical uncertainty on the points.

The value of  $R_{BF}$  is also expected to show a correlation with the impact point of electrons (along the  $x$  and the  $y$  axis) since the fraction of the electromagnetic shower which interacts with a fiber will move towards the back end when the shower develops far from the fiber position, as represented in the naive sketch of Fig. 6.11. To study the effect of the impact point on the value of  $R_{BF}$ , we selected events within concentric rings at a given distance from the selected fiber and calculated the average value of  $R_{BF}$  for each ring. Results are shown in the right plot of Fig. 6.11. As expected, we observe a significant correlation between the distance of the electron impact point from a fiber and the value of  $R_{BF}$ . The back signal proportionally increases with respect to the front signal when electrons are generating the shower further from the fiber. In such conditions, only a small fraction of the shower interacts with the fiber reducing the scintillation signal which, in turn, increases the sampling fluctuations.

### 6.3.4 Discussion

These first test beam results confirm the potential of LuAG fibers for high energy physics applications. A significant amount of light was extracted from both the Cherenkov and the scintillating fibers. The response of single fibers to electrons depends on the impact point of the particle and thus it can be used to study the transverse profile of the shower. Combination of the signals from clusters of adjacent fibers can be used to build algorithms which allow an estimation of the particles impact point and angle.

The feasibility of using double readout (i.e. make use of signal from both front and rear ends of each fiber) to increase the knowledge on the shower profile along the fiber axis has been investigated. Good correlations of the back and front signals ratio  $R_{BF}$  with the shower maximum position (along  $z$  axis) and with the impact point of electron on the mini-CFCAL front face ( $x, y$  axis) were found. The optimization of the double readout can provide even more informations on the longitudinal shower profile without the necessity to increase the longitudinal segmentation and hence the number of channels.

More issues related to the real potential of such calorimeter in the context of particle flow algorithms or dual readout corrections (i.e. reading out the scintillation and Cherenkov light separately on a event by event basis to correct for hadronic shower fluctuations) are not addressed in this test beam study because of the limited size of the module. Nevertheless, current data can be used to validate simulation tools in order to investigate new geometries and configurations. A Geant4 simulation was performed to allow a first comparison with data and to investigate the potential of a larger array of fibers in terms of energy resolution.

The same geometry of the mini-CFCAL, in terms of fiber packing, was simulated extending the array of fibers to a  $40 \times 40$  matrix inserted in a brass absorber with transverse dimensions of  $22 \times 22$  cm $^2$ . Such geometry, shown in Fig. 6.12, will be referred as *Geometry A*. A different geometry (*Geometry B*) was also simulated, in which the gap between the fibers and the absorber (resulting from the 0.5 mm layer of Teflon) was reduced to 0.1 mm. An hexagonal packing was chosen here so that the spacing between fibers centers is reduced to 3 mm (see Fig. 6.12). In this case, a  $123 \times 123$  matrix of 22 cm long fibers is needed to fill a brass block of  $\sim 33 \times 33 \times 22$  cm $^3$ .

Electrons of energy between 1 and 150 GeV, uniformly spread on a  $10 \times 10$  mm $^2$  area and with a small angular spread of 5 mrad, which aims to reproduce the experimental conditions of the test beam, were simulated. For *Geometry A*, the electrons direction was oriented in the same configuration as in the test beam whereas for *Geometry B* the electrons beam direction was set perpendicular with respect to the fiber axis in order to reduce the spatial non-uniformity of the response. The energy deposited by the electromagnetic shower inside the active volume of LuAG fibers was measured and allowed to study the

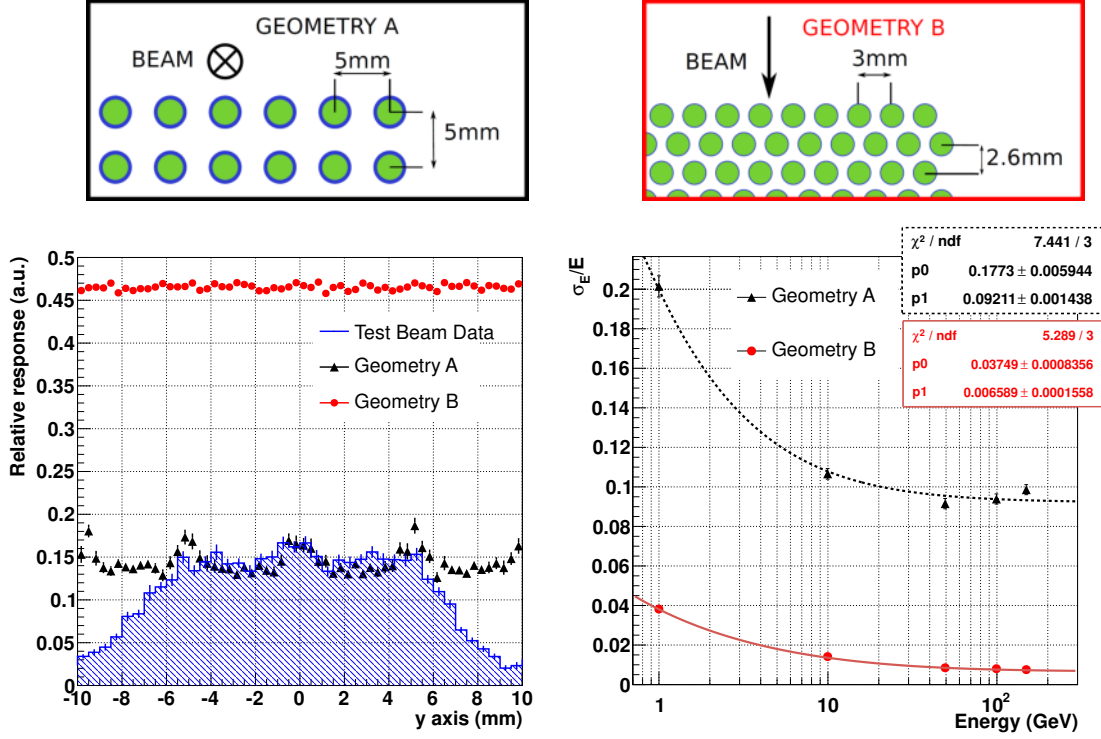


**Figure 6.12:** Top: a sketch of *Geometry A* (left) and *Geometry B* (right). The blue gaps between fibers (green) and the absorber (white) represent the Teflon layers. The beam direction is also illustrated for the two configurations. Bottom left: fraction of electron energy deposited in the array of fibers as a function of a 50 GeV electron impact point along y axis for *Geometry A* (black) and *Geometry B* (red). Experimental data points are shown with a blue line. Bottom right: Energy resolution curves for *Geometry A* (black) and *Geometry B* (red) at different beam energies fitted using  $\sigma_E/E = \sqrt{p_0^2/E + p_1^2}$  where  $p_0$  and  $p_1$  represent the stochastic and the constant term respectively.

transverse non-uniformity of the response as shown in Fig. 6.12. We can observe that the response of the mini-CFCAL decreases when the impact point of electrons is out of the fiber array of  $\pm 5$  mm. In both data and simulation of *Geometry A* the response fluctuates periodically when the impact point moves from the center of the fibers to the brass between adjacent fibers. When the granularity and the packing configuration are improved (as in *Geometry B*), the fraction of the shower sampled by the active volume is increased by a factor  $\sim 3$  and the non-uniformity of the response is reduced.

The evolution of energy resolution with respect to the electron energies is shown in the right plot of Fig. 6.12. The resolution predicted for *Geometry A* ( $\sim 10\%$ ) is better than the experimental resolution of the distributions in Fig. 6.8 which is  $\sim 15 - 20\%$ . The difference was attributed to several factors: a poorer transverse containment of the shower due to the smaller array of fibers in the mini-CFCAL, the contribution of the electronic noise, the limited precision of intercalibration coefficients between fibers and other systematics related to the experimental setup and beam quality.

### 6.3. Preliminary Test Beam in Pointing Configuration

---

The resolution that can be achieved with the granularity of *Geometry B* in a non-pointing fibers configuration, having a stochastic term of  $\sim 3.7\%$  and a constant term of  $\sim 0.7\%$  is very promising. Such a good resolution is achieved by means of tilting the detector of  $90^\circ$  which results in a better transverse uniformity of the response which was one of the main limitation to the energy resolution of *Geometry A*.

Driven by these considerations and by the availability of a larger number of fibers, a new test beam was setup during 2013-2014 as discussed in the following section.

## 6.4 FNAL Test Beam in Transverse Configuration

The potential of crystal fiber technology for calorimetry applications was confirmed with the test beam presented in Sec. 6.3. In the meantime, the quality of crystal fibers further improved and the know-how was transferred from the ILM to the Fibercryst company [133] in order to increase the production capability. During early 2014, new batches of LuAG:Ce and LuAG undoped fibers were grown by ILM and Fibercryst and successively characterized at CERN.

Given the considerations of Sec. 6.3.4 and the larger number of fibers available, we decided to investigate a calorimetric module performance in which the fiber axis is transverse with respect to beam direction. Such configuration is of particular interest because it could be used to replace the current plastic scintillator in the HE megatile. The use of crystal fibers layers would improve the HE resolution due to the higher sampling fraction resulting from a denser active material and would yield a radiation hard calorimeter able to withstand HL-LHC conditions.

A test beam was performed at the Fermilab Test Beam Facility (FTBF), during March and August 2014, using a calorimetric module with 64 LuAG fibers arranged in a 8-layers configuration. As discussed in Sec. 6.4.3, it might be convenient to extract the signal from several fibers by mean of a common optical guide to reduce the number of readout channels. For this reason, the feasibility to read out multiple fibers with a WLS + Quartz Capillary (QC) system was also investigated. The results achieved, confirming the potential of crystal fiber technology for calorimetry applications, are presented in the following.

### 6.4.1 Experimental Setup

#### MT6 Beam Line at FTBF

The test beam was performed at the Fermilab Test Beam Facility (FTBF) [134]. The beam originates from the Booster which accelerates protons from 400 MeV to 8 GeV and injects them into the Main Injector. At this step, the beam is accelerated up to 120 GeV at a frequency of 53 MHz and extracted using a QXR quadrupole circuit. Along the MTest beam line a set of magnets and collimators are used to deliver the beam to the experimental area MT6. About 134 m upstream, a 30 cm Aluminum target (MT4) can be moved in the beam line to obtain secondary electrons and pions in the 1-32 GeV energy range.

The MT6 experimental area, see Fig. 6.13, provides a scintillator counter which can be used to select electrons over the pions background. A set of multiwire proportional chambers

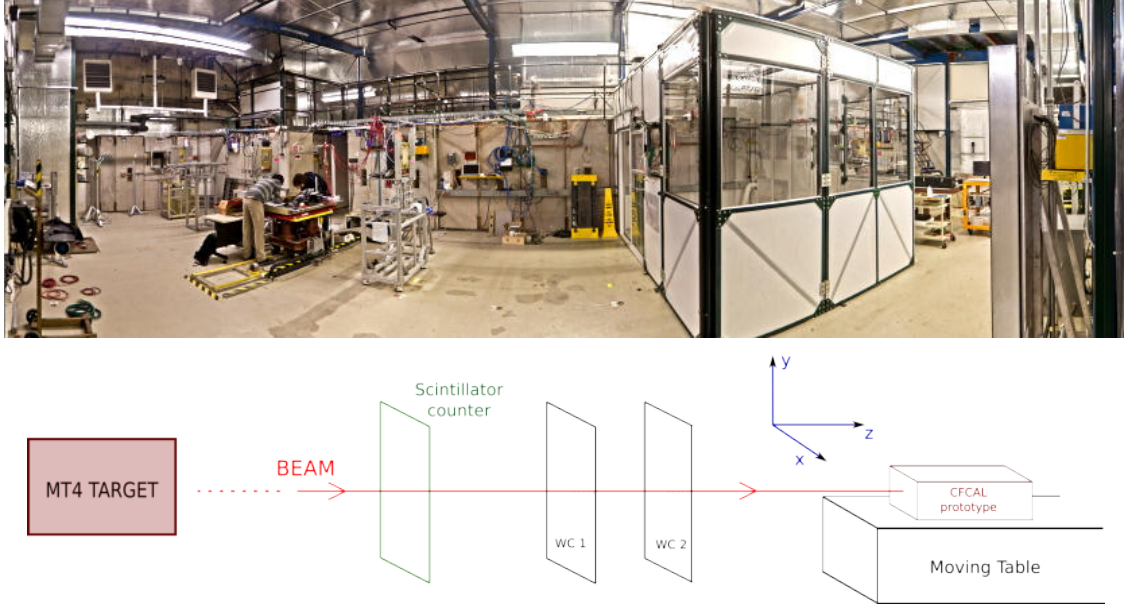


**Figure 6.13:** Top: picture of the experimental hall MT6.2 at the FTBF facility. Bottom: schematic view of main components along the beam line used for the test beam study.

(MWPC) with  $\approx 1$  mm spatial resolution are available to monitor the beam profile along the line [134]. A movable table with remote control is situated after the first two wire chambers (WC1 and WC2) and was used to position the calorimetric module described in the following.

### The Calorimetric Module

The calorimetric module ( $25 \times 17 \times 7$  cm $^3$ ) was made of a brass groove filled with 56 LuAG:Ce scintillating fibers and 8 undoped LuAG fibers as shown in Fig. 6.14. Vertical spacing (along  $y$ ) between the center of adjacent holes was 4 mm. Fibers were arranged in 8 layers of 8 fibers each, interleaved by 16 mm of brass along the beam direction ( $z$  axis). The fourth layer, corresponding to the shower maximum of 16 GeV electrons, was filled with undoped fibers whereas the remaining holes harbored LuAG doped fibers with different concentration of Cerium. Fibers were wrapped with a thin layer of Teflon at the two ends in order to maintain about 0.2 mm air layer between the fiber lateral surface and the brass absorber.

One end of each fiber was coupled to a KETEK Silicon Photo Multiplier (SiPM) using standard optical grease. The SiPMs consist of 12100 cells of 20  $\mu\text{m}$  width with an active area of  $2.2 \times 2.2$  mm $^2$ . Recovery time of SiPMs was measured in laboratory to be around 30 ns with break down voltage of  $25.4 \pm 0.2$  V. The photon detection efficiency (PDE) is about 20% at LuAG:Ce emission peak (520 nm) with a maximum of 33% at 420 nm. The

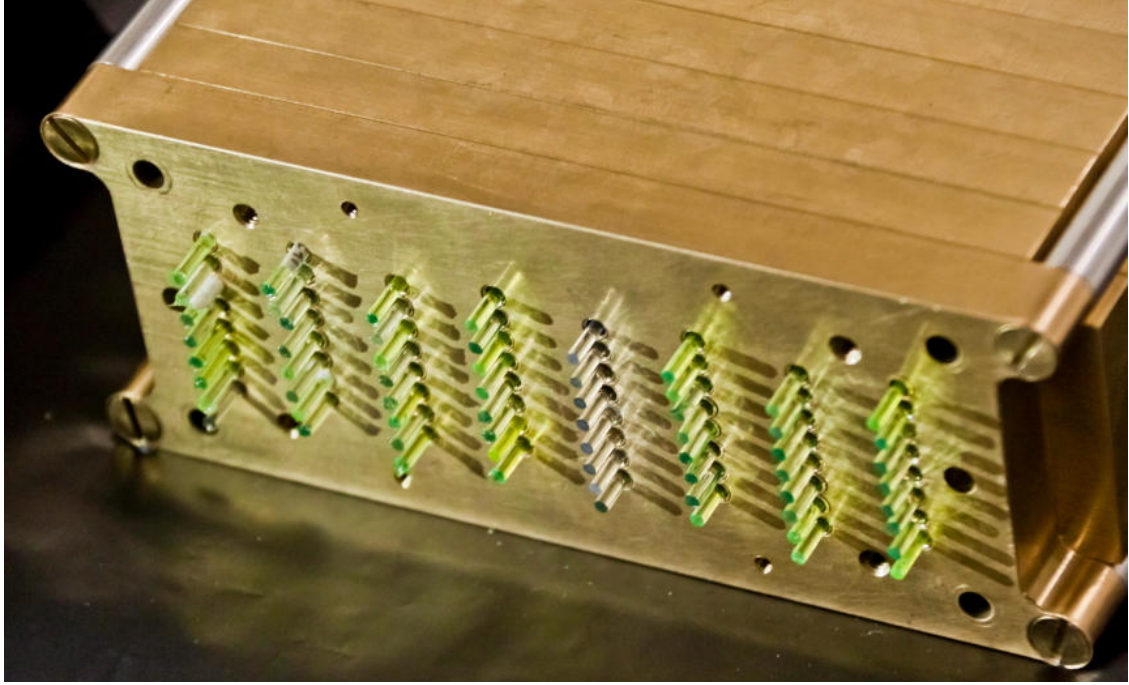


**Figure 6.14:** Picture of the calorimetric module consisting of a brass absorber groove with 8 layers of 8 crystal fibers each. The fourth layer from the right contains the undoped LuAG fibers as visible from the color of the fibers which does not show the typical greenish color of Cerium emission.

choice of this particular type of SiPM was driven by their particularly high PDE in the UV region (18% at 350 nm) which maximizes the detection of Cherenkov photons from undoped fibers.

The signals generated from the  $8 \times 8$  array of SiPMs were readout with two PADE boards of 32 channels each, allowing for a on-line data monitoring using a standard PC. The PADE system was built for Proton Computed Tomography and used in previous test beam at Fermilab [135]. Although it has a 20 MHz analog bandwith with AC coupling, which makes the pulse shaping slow and bipolar, it was suitable for this test because of its capability to readout multiple SiPMs simultaneously. The pulse shapes are slowed also by the readout system which samples at a frequency of about 78 MHz.

The temperature of the electronic board and SiPM was also monitored using a sensor connected to the PADE and was kept stable around  $20 \pm 1^\circ\text{C}$ . A LED system was used to inject pulsed light into the rear side of brass holes. The light passing through the fibers was then used to calibrate the SiPM response. The LED driver was positioned on the top of the absorber and optical clear fibers were used to split the light into 64 channels as shown in Fig. 6.15. The trigger signal was given by the scintillator counter and linked to the PADE system which synchronized the data acquisition with the beam spill.

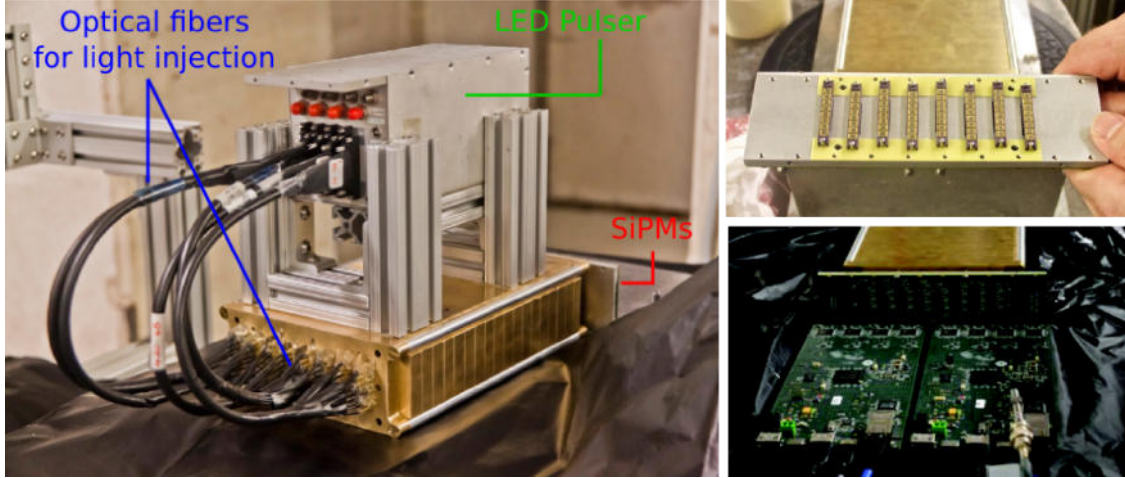


**Figure 6.15:** Left: LED system to inject the light into the 64 channels of fibers. Right: array of  $8 \times 8$  SiPMs (top) and the two PADE boards used for the readout through a standard ethernet cable connected to a PC (bottom).

#### 6.4.2 Analysis Procedure

In this section, the procedure used for the analysis of the test beam data is presented. The response of individual fibers was studied to characterize their performance and optimize the operation of the full calorimetric module. A first part of the test beam was performed in a pointing configuration, similarly to what previously tested at CERN. The study of fiber response as a function of beam position allowed to intercalibrate the fibers. In a second moment, the module was rotated in a transverse configuration as shown in Fig. 6.16 and tested with electrons of different energy. In this configuration, the fiber attenuation lengths were measured and the response of the full module to electrons and pions was studied. Each fiber, connected to a SiPM and the corresponding readout channel, was identified by a numerical index as reported in Fig. 6.16.

#### Signal Reconstruction

The pulse of the signal is a combination of the scintillation/Cherenkov light, the SiPM response and the electronic chain used to amplify and measure the signal. A typical pulse is shown in Fig. 6.17 and consisted of  $N$  time samples of 13 ns each. The average of the first 4 samples was used to calculate the pedestal value and the subtracted from each time sample event-by-event. All the SiPMs showed a similar pedestal value around 100 ADC count with a  $\sigma_{ped}$  of 1 ADC count.

Given the peculiar bipolar shape of the pulse, which is not entirely positive and often saturates in its negative part (see right plot of Fig. 6.17), the full integral of the time samples is not a good estimator of the number of photoelectrons. Therefore, it was decided

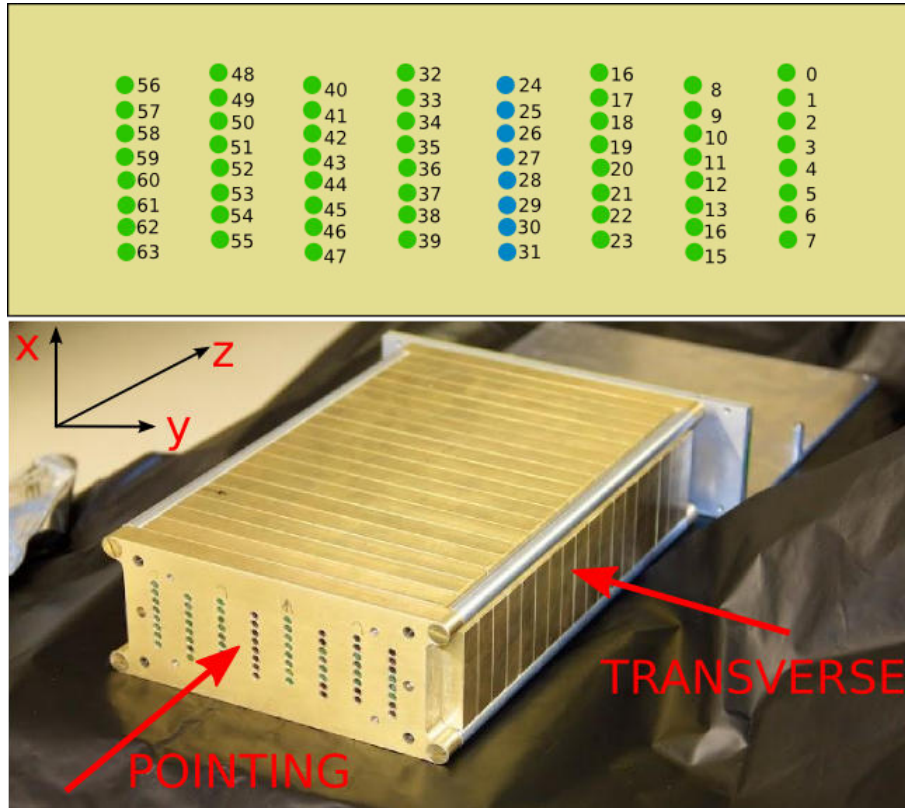


**Figure 6.16:** Top: schematic view of fiber positioning with numerical index, the fourth layer from the right contains the undoped LuAG fibers. Bottom: picture of the calorimetric module. The beam direction with respect to module axis is shown for both *pointing* and *transverse* configuration.

to use the integration of the signal in the first 27 samples, corresponding to the positive area of the pulse, as an estimator of the light intensity.

### LED Calibration

In order to calibrate SiPM response, pulses of blue and green light were flashed into the 64 fibers. The light distribution were then used to estimate the number of photoelectrons per ADC channel according to

$$n_{phe} = \frac{(peak_{led} - peak_{ped})^2}{\sigma_{led}^2 - \sigma_{ped}^2} \quad (6.6)$$

The green LED produced the larger signal due to the better transmission of the LuAG:Ce crystals at high wavelengths and was then used for calibration. Fig. 6.18 shows the signal distribution obtained with the green LED flashing in fiber number 4 compared to the

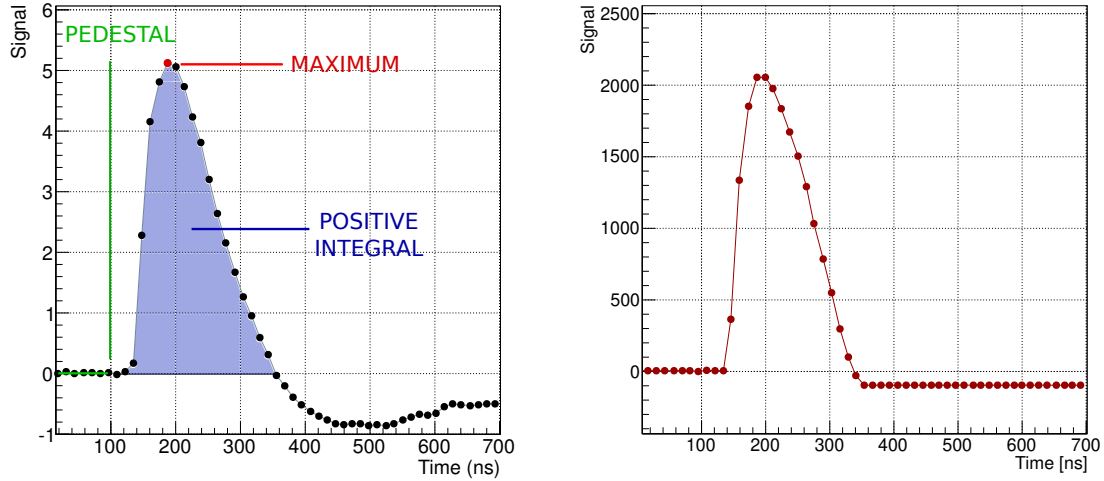


**Figure 6.17:** Left: average pulse shape from a scintillating fiber corresponding to 16 GeV electrons. Right: scintillation pulse showing a saturation in the negative part.

corresponding pedestal. However, for some channels, the LED signal was too low (below 5 photoelectrons) and could not provide a proper calibration. This occurred for the fibers having a very poor transmission of light as demonstrated by the clear correlation observed between the LED signal and the fiber attenuation lengths. Since all the SiPMs are supposed to be identical and they were operated at the same bias voltage and temperature their gain is expected to be identical. For this reason, when the LED signal was too low, the average ADC-to-phe coefficient calculated above the 5 photoelectrons threshold, indicated by the green line in Fig. 6.18, was used. On average, 10 photoelectrons corresponded to a pulse with an amplitude maximum of  $\approx 55$  ADC counts and a positive integral of  $\approx 300$  ADC counts.

### Intercalibration Procedure

In order to investigate the performance of the calorimetric module and to reconstruct the energy of incoming particle using the signal from several fibers, the intercalibration of all the 64 channels is required. Variation of Cerium concentration (from  $\approx 0$  for undoped fibers, up to  $\approx 600$  ppm for highly doped ones), results in variation of intrinsic light yield (LY) which gives different intensity of fiber response to electron beam. The different quality of the fiber surface state and internal defects also affects the light transmission introducing fiber-to-fiber variation of the response. Systematics due to the coupling efficiency between the fiber and the SiPM are an additional source of channel-by-channel fluctuations. The intercalibration procedure described in the following aims to take into account all these effects and to correct for them.

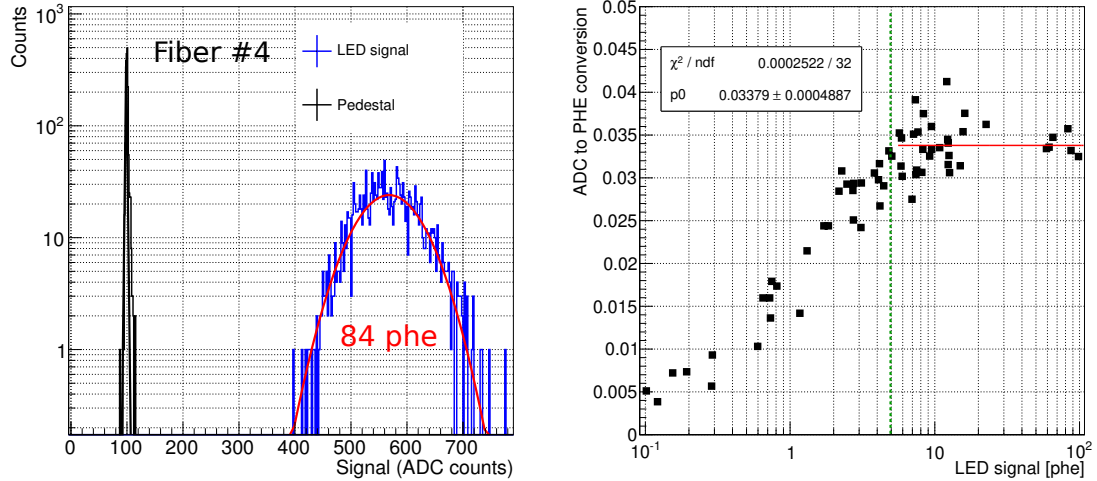


**Figure 6.18:** Left: example of LED distribution compared with pedestal for a good fiber. Right: ADC-to-phe conversion coefficients as a function of signal from LED. A fit (red line) was performed on the conversion coefficients obtained from SiPMs which measured more than 5 photoelectrons (green dotted line) to get their average value.

Beside the purpose of intercalibration, a precise characterization of fibers response, in terms of light output and attenuation length, represents a powerful tool to confirm laboratory measurements and to identify the fibers which are more suitable for calorimetry applications. In particular, it is desirable to have high light yield and large attenuation length to guarantee good signal and spatially uniform response.

To obtain intercalibration coefficients, the absorber was rotated to have fiber axis orientated along the beam direction. Using 16 GeV electrons, a full scan of the module surface was made. Similar to the procedure described in Sec. 6.3.3, the wire chamber informations allowed to extract the profile of fiber response as a function of electron impact point. A fit of the energy distributions with symmetric Crystal Ball function was made, as shown in Fig. 6.19. The fit allowed to calculate the position of each fiber with respect to wire chambers coordinate frame and to obtain intercalibration coefficients according to Eq. 6.2.

A fit of the  $(x, y)$  coordinates obtained for all the fibers was made to estimate the effective distance between holes (along  $x$ ) and layers (along  $y$ ). We obtained an average distance between holes of  $\Delta x = 3.993$  mm and  $\Delta y = 16.226$  mm between adjacent layers. The results are in perfect agreement with the geometrical design and demonstrates that a good alignment of the beam with respect to the absorber was made.

The intercalibration coefficients obtained with this procedure represent a convolution of the longitudinal shower profile with the non-uniformity of fiber response along its axis.

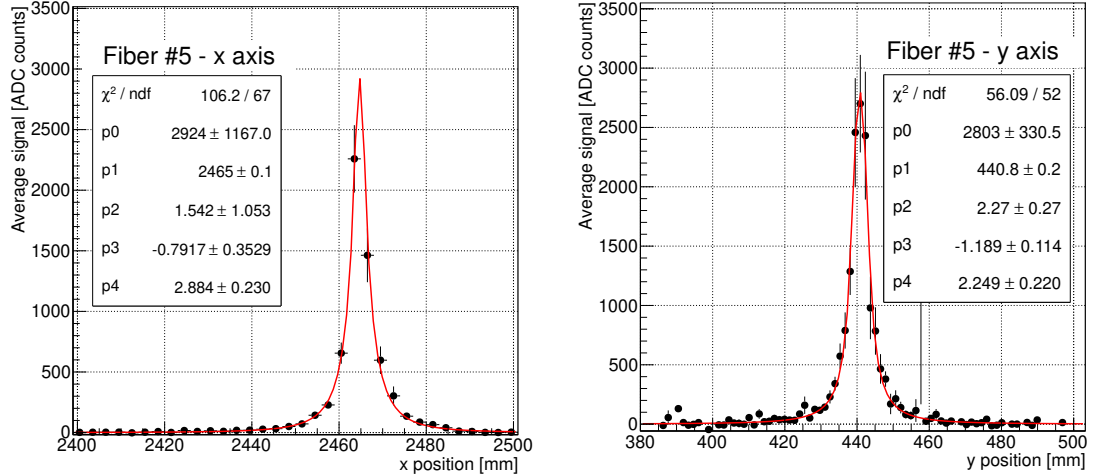


**Figure 6.19:** Average response of scintillating fiber #5 as a function of impact point along the  $x$  (left) and  $y$  (right) axis. Electron of 16 GeV have been used in pointing configuration. A fit with a Crystal Ball function is performed to obtain the coordinates of fiber centers ( $p_1$ ) and maximum average response ( $p_0$ ).

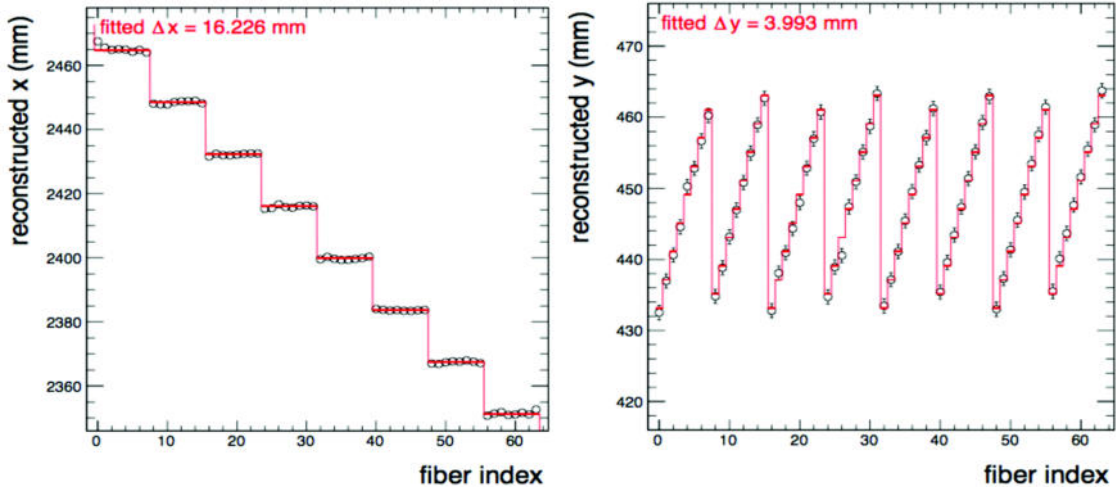


**Figure 6.20:** Coordinates of fiber centers both on  $x$  (left) and  $y$  axis (right) as a function of fiber index, as obtained from a fit response profiles of Fig. 6.19.

The light extracted from a given fiber can be parameterized as

$$R = S_{cint} + C_{cher} \approx \left[ LY \int E_{dep}(z) \varepsilon_{LC}(z) dz \right] + C_{her} \quad (6.7)$$

where the light collection efficiency can be approximated by

$$\varepsilon_{LC}(z) = \varepsilon_0 \cdot \exp \left[ -\frac{z}{L_{att}} \right] \quad (6.8)$$

where  $\varepsilon_0$  includes SiPM-to-fiber coupling inefficiencies and Fresnel losses,  $z$  is the distance of energy deposit from photodetector and  $L_{att}$  the attenuation length. According to Eq. 6.7 and Eq. 6.8, the intercalibration coefficients ( $IC^i$ ) are not directly proportional to the intrinsic  $LY$  of the fiber since they are affected by the fiber attenuation length.

In first approximation, the Cherenkov light contribution in Ce-doped fibers can be neglected. This is well motivated by the much larger number of scintillation photons produced and because Cherenkov photons, emitted mostly in the UV region, are strongly absorbed by the Cerium absorption bands at 330 and 450 nm.

It can also be assumed that Cherenkov light, although non-isotropic, is affected by attenuation length in a similar way than scintillation photons. As addressed in Sec. 6.4.3, the non-isotropic emission of Cherenkov light produces a non negligible effect on light output which will require an additional correction factor for the calibration of undoped fibers.

Under these assumptions, according to Eq. 6.7, it is possible to disentangle the effect of attenuation length from the light yield of the fiber  $LY$  and its coupling efficiency  $\varepsilon_0$ . This requires the measurement of  $L_{att}$  for each fiber, as described in the next section.

### 6.4.3 Results

#### Attenuation Lengths

All the fibers were fully characterized at CERN laboratories. Attenuation lengths were measured using both radioactive  $\text{Na}^{22}$  source and a LED pulser using a dedicated bench set up by *Kristof Pauwels* and described in detail in [116]. However, it is important to measure how the non-uniformity of light collection affects the fibers response to electromagnetic shower. This is because the excitation volume in which scintillation occurs in case of electromagnetic showers is rather different with respect to low energy  $\gamma$ -rays excitation.

For this purpose, the absorber was positioned in transverse configuration with fiber axis perpendicular to the beam. A 16 GeV electron beam was moved along crystal length to measure the variation of fiber response. A beam spot of 4 mm around the fibers axis was used to calculate the average signal as a function of distance from the photodetector. The test beam measurements of attenuation lengths have been compared with laboratory data. A good agreement was found as reported in Fig. 6.21 confirming that the two type of measurements, at a first approximation, can be considered equivalent and equally reliable.

Fit of attenuation curves for fibers 7, 13 and 40 are shown in Fig. 6.22. Fiber response was parameterized with an exponential curve according to Eq. 6.8. Estimation of attenuation length for all the 64 fibers is shown on the right plot of Fig. 6.22. Most of the fibers have attenuation higher than 10 cm and best samples reaches up to  $\approx 100$  cm.

#### 6.4. FNAL Test Beam in Transverse Configuration

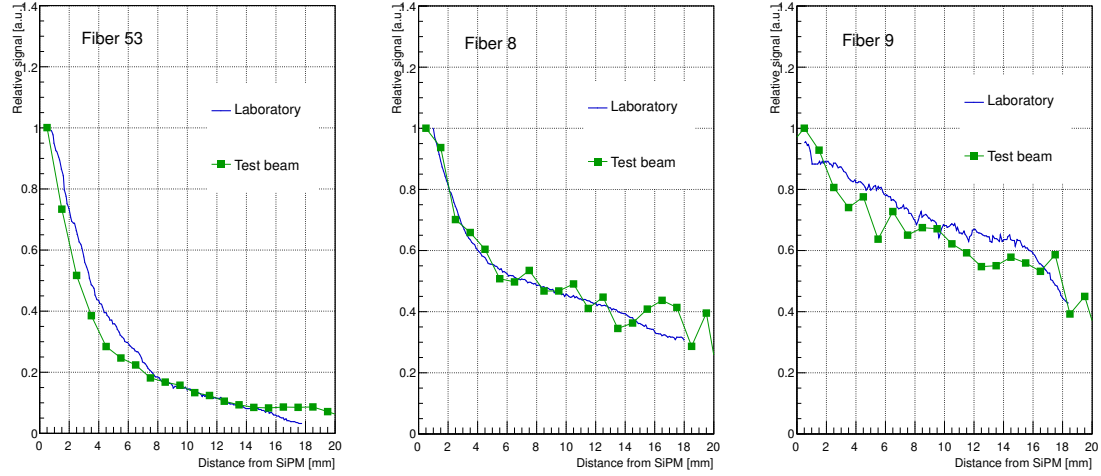


**Figure 6.21:** Comparison of attenuation length curves as measured with LED pulser in laboratory (blue) and as obtained from test beam data (green) for fibers 53, 8 and 9.

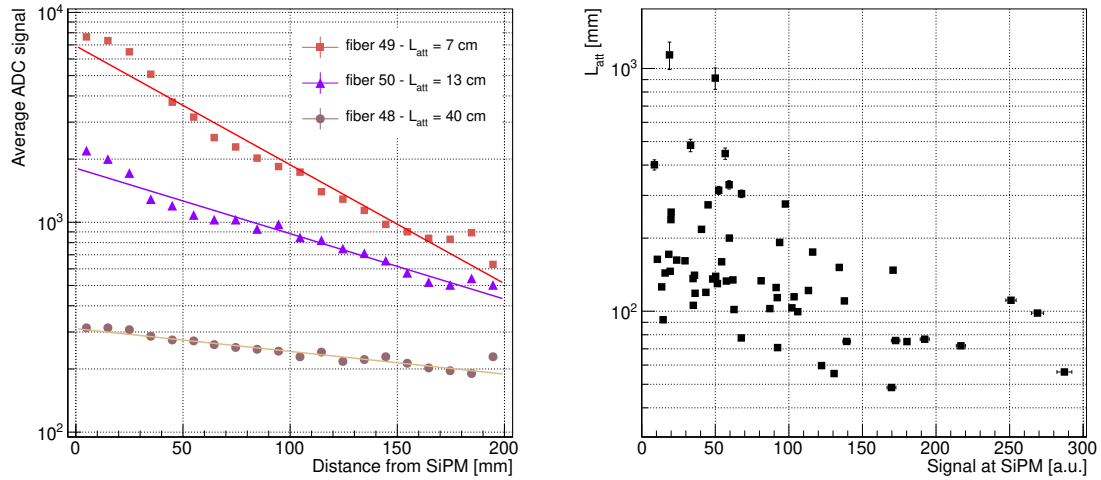


**Figure 6.22:** Left: curves of attenuation length for fiber 48, 49 and 50 showing different values of  $L_{att}$ . Right: attenuation lengths obtained for all the 64 fibers are plotted with the corresponding signal measured close to the SiPM ( $x = 0$ ) where light attenuation is negligible.

Attenuation length represents an important parameter for the identification of best fiber samples. The values obtained in this test demonstrate that growing uniform fibers is possible by properly tuning the growth parameters, such as pulling rate, crucible temperature and Cerium concentration. In particular, it can be observed that high light output (i.e. large signal from the fiber when beam is close to the SiPM) is usually correlated with a poor attenuation length as shown in Fig. 6.21. A possible interpretation is that higher Cerium concentration, yielding larger light yield, also enhance the probability of light self

absorption. At the meantime, there could be some Cerium-related defects which arise during the growing process and which is correlated to the dopant concentration.

As illustrated in Eq. 6.7, the fiber response strongly depend on the  $L_{att}$  which makes more difficult the correlation of light signal with the energy deposit  $E_{dep}$ . To disentangle the fiber-to-fiber variations of response due to intrinsic light yield  $LY$  and coupling inefficiencies  $\varepsilon_0$  from the attenuation length we had to rely on simulation.

To this extent, the curves of attenuation lengths obtained have been inserted into a Geant4 simulation which reproduced in details the experimental calorimetric module. A beam of 16 GeV electrons in pointing configuration was simulated. A beam spot of 4 mm diameter around each fiber was used to select events and measure the distribution of energy deposited in the fiber ( $E_{dep}$ ). In a second step, the energy deposits were convoluted with the fiber attenuation length event-by-event. Comparing these two distributions it is possible to obtain coefficients which correct for the signal loss due to  $L_{att}$

$$MC_{PTT} = \frac{\left( \int E_{dep}(z) \exp(-\frac{z}{L_{att}}) dz \right)_{pointing}}{\int E_{dep}(z) dz} \quad (6.9)$$

These coefficients allow to *convert* intercalibrations constants from pointing-to-transverse configuration. Assuming that channel-to-channel fluctuations of coupling inefficiencies ( $\varepsilon_0^i$ ) are small, Eq. 6.10 can be used as an indication of the intrinsic light yield of a given fiber

$$LY^i \cdot \varepsilon_0^i = \frac{R_{pointing}^i}{MC_{PTT}^i} \quad (6.10)$$

The light yield, usually defined as the number of photons *produced* per MeV of energy deposited, is an intrinsic properties of the material as defined in Sec. 1.2.2. On the contrary, the light output, which is the amount of light *measured* at the photodetector, strongly depends on the crystal geometry and light propagation processes occurring inside the material (diffusion, absorption, reflections). By correcting the light output for the attenuation length, according to Eq. 6.10, we expect to obtain a number which is proportional to the intrinsic light yield of the fiber. This number can be compared with the light output measured when electron shower is developed very close to the photodetector (and thus light propagation effects are negligible).

Simulating the average energy deposited in the fiber volume in a given module configuration we can then compare the light yield estimation obtained from pointing and transverse configuration. Results are shown in the following section.

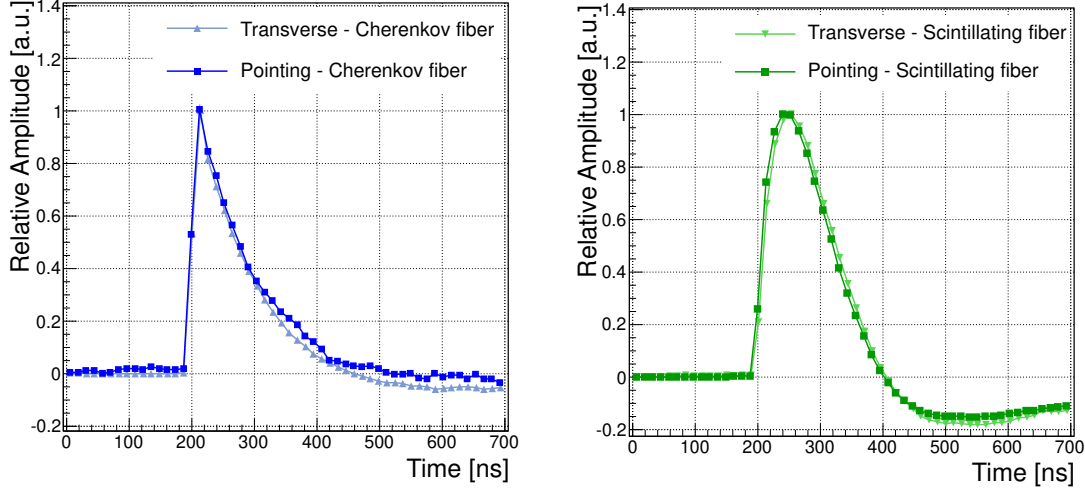


**Figure 6.23:** Left: average normalized pulse shapes of an undoped LuAG fiber measured in transverse and pointing configuration. Right: average normalized pulse shapes of a Ce-doped LuAG fiber measured in transverse and pointing configuration.

### Pulse Shapes and Light Output

All the channels showed a good response to electrons. The pulses extracted from different fibers, convoluted with the system response, were averaged and compared. The slow shaping time of the PADE system [135] limited a precise study of the pulse shapes. Nevertheless, we clearly observed the undoped fibers having a faster and narrower pulse with respect to the scintillating ones, thus demonstrating the different origin of the light signal (see Fig.6.23).

Estimation of the light output per MeV of deposited energy was also made for both transverse and pointing configuration of the absorber. To take into account the different amount of energy deposited in the fibers in these two orientations of the module we relied on a Geant4 simulation of the full setup performed by our colleague *Andrea Benaglia*. As shown in the left plot of Fig. 6.24, the average energy deposited in each fiber in pointing configuration by 16 GeV electrons of 4 mm diameter beam spot around the fiber center, was about 284 MeV. In the right plot of Fig. 6.24 the energy deposited in a fiber of a given layer for transverse configuration is also shown and varies between 15 and 55 MeV.

Selecting 16 GeV electrons hitting the calorimeter in pointing configuration within a 4 mm diameter beam spot around the fiber the light output was estimated. As shown in Fig. 6.25, scintillating fibers yield about 5.4 phe/MeV in both pointing and transverse configuration. Few fibers yield a very low signal probably related to bad coupling with SiPM and some other fibers produce up to 14-20 photoelectrons due to the higher concentration of Cerium. To estimate intrinsic light yield of the fiber is not straighforward since many factors have

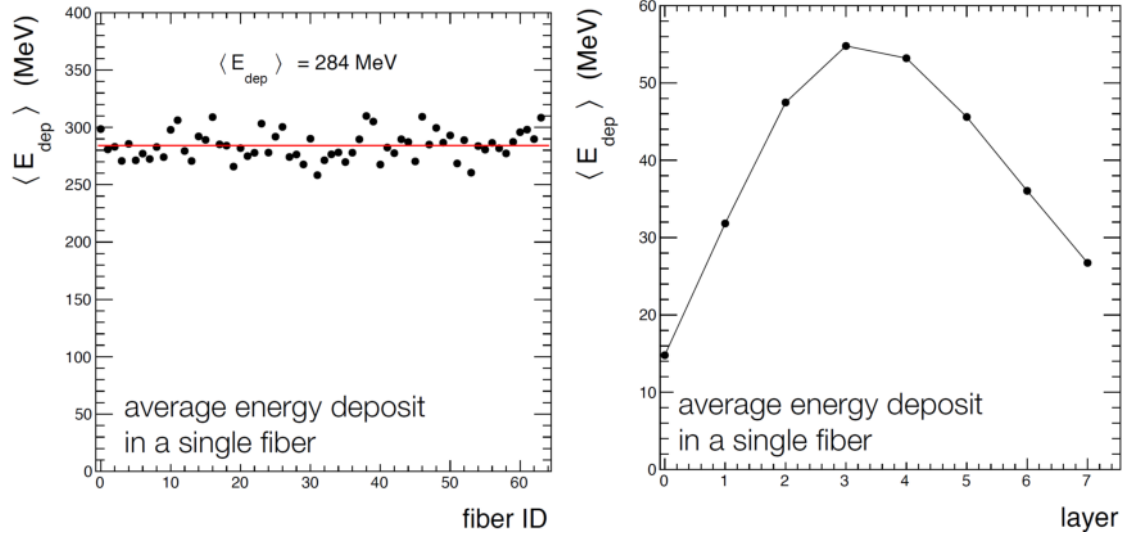


**Figure 6.24:** Left: average energy deposited in a single fiber by 16 GeV electrons. A 4 mm diameter beam spot around fiber center is used. Right: energy deposited in a single fiber of a given layer (by 16 GeV electrons in transverse configuration) with a beam spot of 4 mm around fiber longitudinal axis. These values are obtained with a precise simulation of the full experimental setup using the Geant4 toolkit.

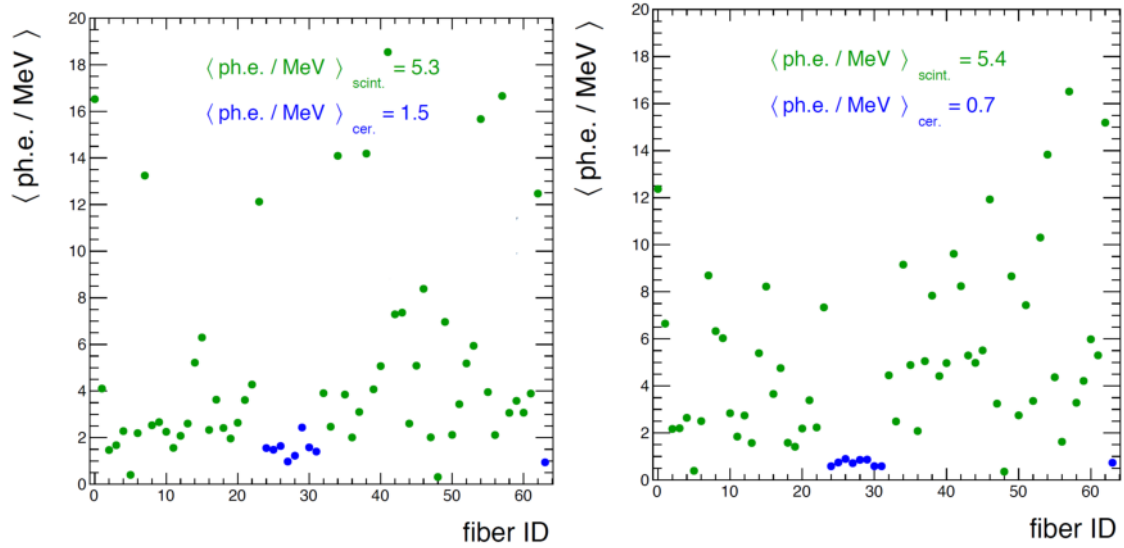


**Figure 6.25:** Estimation of fiber light output per MeV of deposited energy in pointing (left) and transverse (right) configuration. Undoped LuAG fibers are represented by blue dots whereas Ce-doped ones are the green dots.

to be taken into account: photon losses due to the bad optical coupling; 20% PDE of the SiPMs at 520 nm and limited time integration gate due to the slow shaping time of the readout system.

The cherenkov fibers yield on average 1.5 phe/MeV in pointing configuration and 0.7 phe/MeV in transverse configuration. This is attributed to the anisotropic emission of Cherenkov light which favors light extraction in pointing configuration. The ratio of the cherenkov light output between the two configurations is

$$Asymmetry_{ch} = \frac{LO_{ch}^{pointing}}{LO_{ch}^{transverse}} \approx 2.14 \quad (6.11)$$

This coefficient can be used to apply an additional correction to the intercalibration constants of undoped fibers obtained in pointing configuration.

### Particle Identification and Event Selection

As anticipated in Sec. 6.4.1, the beam provided by the FTBF facility is a mixture of pions and electrons in the 2-32 GeV energy range. The relative fraction of the two type of particles depends on beam energy and was measured by previous CALICE experiments and is reported in [134]. The pions do not start a shower inside our calorimetric module due to the relatively small  $\lambda_{int}$ . They behave mostly like minimum ionizing particles (MIP), and thus produce a signal in only few fibers ( $\sim 8$ ) depositing a small amount of energy ( $\approx 2$  MeV). Therefore, they can be identified in the left-bottom region of the scatter plot in Fig. 6.26. On the contrary, electrons will trigger an electromagnetic cascade having its maximum around the 3rd and 4th layer of fibers in the module (depending on beam energy). In this case, a higher fraction of energy (15-55 MeV) will be deposited in a larger number of fibers ( $\geq 40$ ). We define a fiber as *active*, if the signal it yields for a given event is higher than 10 times the sigma of the pedestal

$$R_{fib} > E_{th} = 10\sigma_{ped} \approx 15 \text{ADC counts} \quad (6.12)$$

The left plot in Fig. 6.26 clearly shows how it is possible to exploit the high granularity of the module and identify the nature of impinging particle based on the multiplicity of active fibers. We demonstrated that requiring a minimum of active fibers per event according to

$$N_{active\ fibers} > 15 + 5 \times \log_2(E_{beam}) \quad (6.13)$$

it is possible to reject the pion background and to reproduce the electron fraction expected for a given beam energy as shown in Fig. 6.26. If the requirement of Eq. 6.13 is satisfied the energy distributions for electron become gaussian and the low energy tails disappear as shown in the left plot of Fig. 6.27.

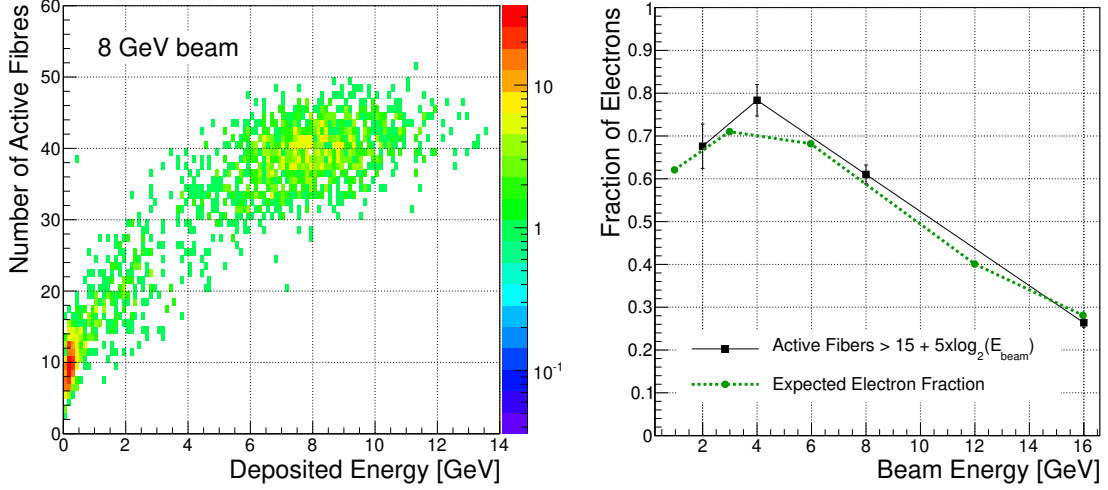


**Figure 6.26:** Left: scatter plot showing the different signatures of electrons and pions in the calorimetric module. Electrons are in the top right side of the plot since they deposit a higher amount of energy producing signals in a larger number of fibers due to the spread of the EM shower. Right: Efficiency of the multiplicity cut to select events originated from electrons (black dots) with respect to nominal e- fraction (dotted line).

### Energy Resolution and Linearity

To measure the response of the calorimetric module to a wide range of energies, we used electron beams between 2 and 16 GeV. At these energies the electromagnetic shower is reasonably contained ( $\geq 85\%$ ) in the module with maximum signal around the 4th and the 5th layer of fibers. For 32 GeV energy the shower leakage becomes larger and the fraction of electron events over the pion background decreases significantly (around 10% of electrons).

The energy deposited in the active part of the module was reconstructed by summing up the signals  $R_i$  of all the fibers after intercalibration

$$E_{reco} = G \cdot \sum_i R_i \quad (6.14)$$

where  $G$  is an overall calibration constant defined to match the module response with the signal of 4 GeV electrons. As shown in Fig. 6.27, energy distributions show a good linear behavior in the 2-8 GeV energy range with small deviations at 16 GeV due to increased shower leakage.

As expected, we observed a beam spot dependence of the energy resolution. As confirmed by the simulation, the attenuation lengths of the fibers introduce a smearing on the reconstructed energy which depends on the impact point of the electron. Reducing the size of

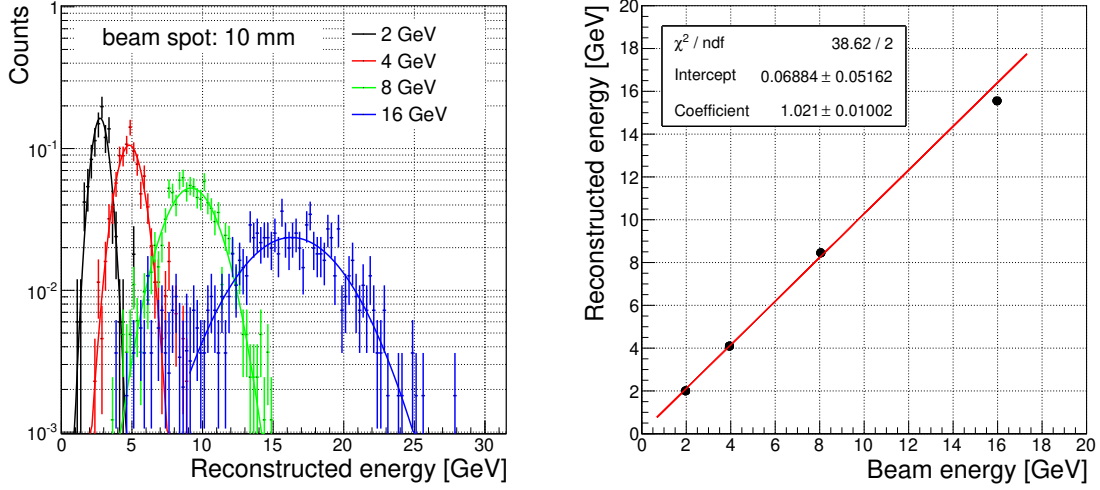


**Figure 6.27:** Position of electron peak reconstructed by summing up the signal of all the fibers as a function of beam energy. Deviation from linearity at high energies are due to the higher longitudinal shower leakage.

the beam spot along the axis of the fibers, this effect is reduced and the energy resolution improves approaching the ideal limit in which no attenuation occurs along the fiber. This is shown in Fig. 6.28, where experimental curves of energy resolution are compared with simulation predictions with and without the fiber attenuation length effect.

As expected by simulation, the energy resolution is this calorimeter prototype is limited by the longitudinal shower leakage and by the attenuation length of the fibers. Additional contribution to the constant term arises in the experimental data due to the limited precision of the intercalibration coefficients as discussed in Sec. 6.4.2.

### Shower Profile

The high granularity of this calorimeter prototype provides useful informations on the shower profile on event-by-event basis. The potential of this information was already shown and used in Sec. 6.4.3 to efficiently indentify electron events over the pion contamination.

Using electron events at different energies, the longitudinal profile of the shower was also studied. For each event, the signal from the fibers belonging to the same vertical layer was summed up. This allowed to obtain the profiles of deposited energy shown in the left plot of Fig. 6.29. A fit of the shower shape was performed according to Eq. 1.4 to obtain an estimation of the shower maximum position. The results are reported in the right plot of Fig. 6.29 and confirm the shift of the shower maximum towards the back of the absorber proportional to  $\ln(E_{beam})$  as expected from Eq. 1.5.

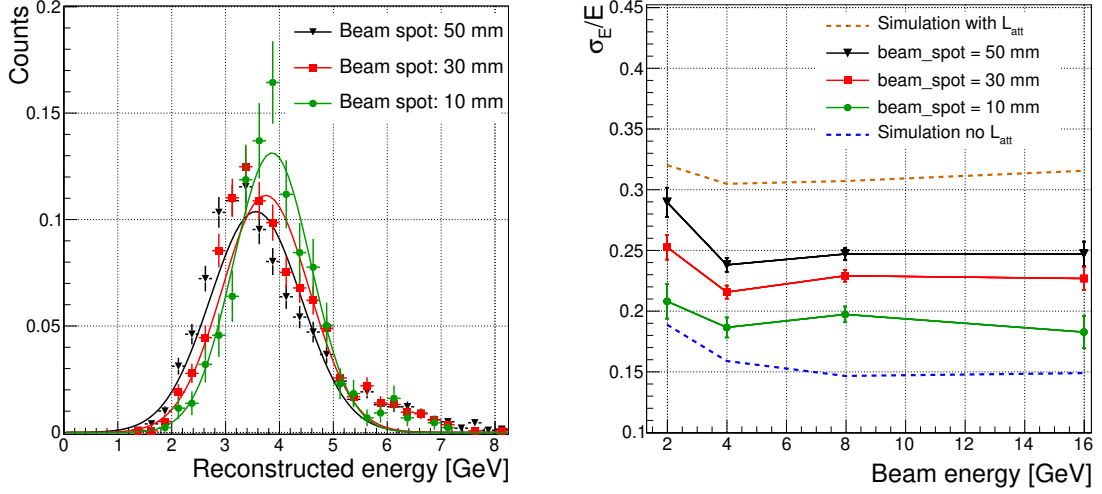


**Figure 6.28:** Left: energy distributions for 4 GeV electrons using different beam spot selections. Right: experimental curves of energy resolution for different beam spots compared with expectation from simulation with and without the effects of fibers  $L_{att}$ .

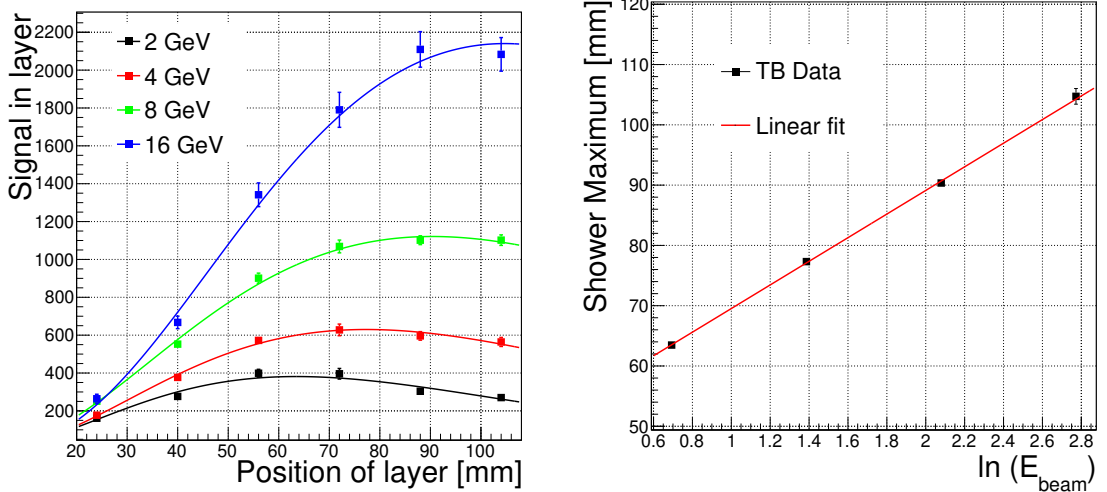


**Figure 6.29:** Profile of longitudinal shower development at different beam energies. The fraction of detected signal in each layer of fibers is shown.

Unfortunately, during these runs of the data acquisition, the SiPMs of the last two layers were not operational due to a malfunction of the voltage supplier. This limited the measurement of shower profiles to the first six layers.

### Test of WLS + Quartz Capillary Readout System

A different technique for the readout of the fibers was also investigated: the signal extracted from several fibers was been optically summed by coupling them to a wavelength-shifter (WLS) inserted into a quartz capillary (QC). The QC is then used as a radiation hard optical guide to transport the signal from a layer of fibers to a common photodetector.

The implementation of this readout technique in a real calorimeter would allow to reduce the number of readout channels providing a radiation tolerant system for light collection. Two different WLS fibers matching the emission spectrum of LuAG:Ce have been tested: a green-to-orange WLS (Kuraray-O<sub>2</sub>) and a green-to-red WLS (EJ-284). The emission and excitation spectra of these fibers are shown in Fig. 6.30.

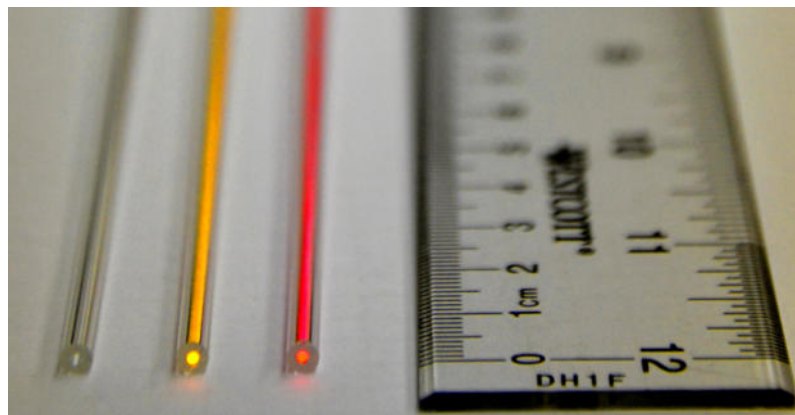
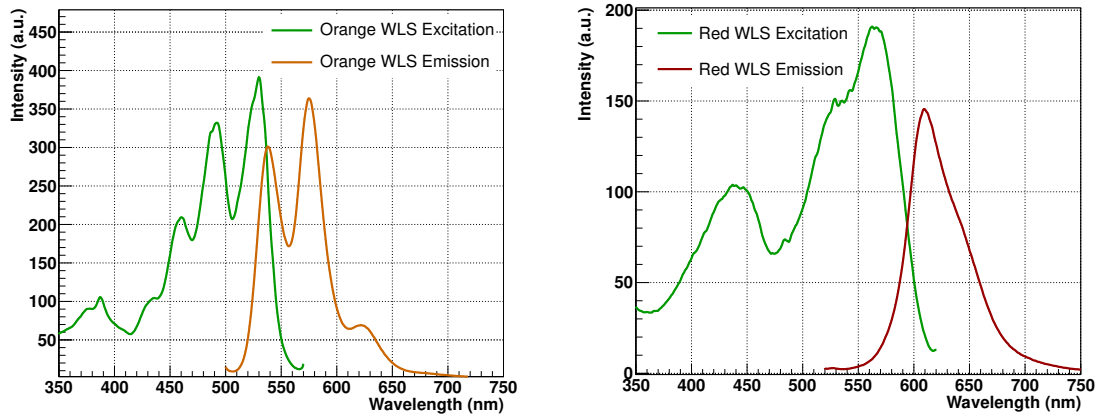


**Figure 6.30:** Top: excitation and emission spectra of the orange green-to-orange WLS (Kuraray-O<sub>2</sub>), left, and green-to-red WLS (EJ-284), right, wavelength shifter fibers used in this test and matching to the LuAG:Ce emission peak. Bottom: a picture of the WLS fiber inserted into a quartz capillary of 1 mm (2 mm) inner (outer) radius is shown.

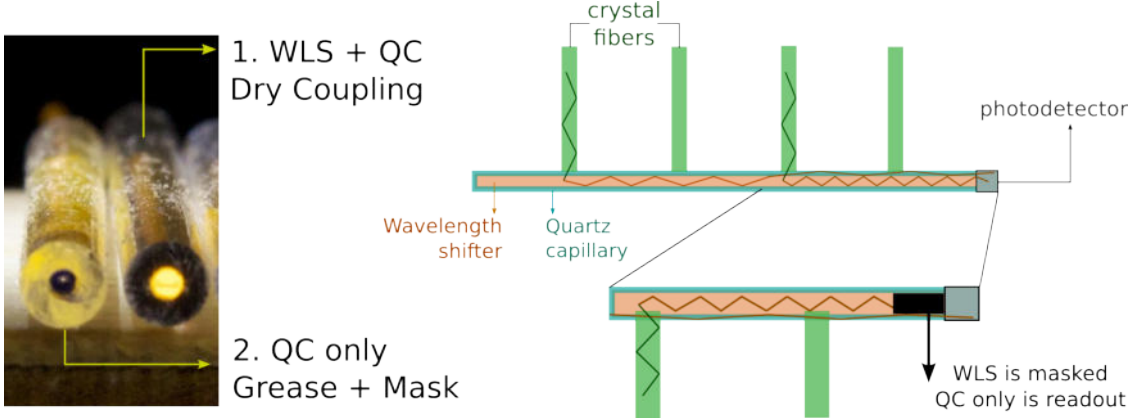


**Figure 6.31:** Picture of the WLS+QC light guide system in the two different configurations: (1) WLS+QC is used and light propagates mostly in the WLS fiber, (2) QC only is readout by masking the end of the WLS fiber.

Two configurations of the WLS+QC system have been tested as shown in Fig. 6.31:

1. DRY-COUPLING: wavelength-shifter fibers are inserted into the quartz capillary and both WLS and QC are readout with the SiPM;
2. GREASE+MASK: optical grease is inserted in between the WLS and QC to reduce air gap and to enhance the light extraction from the WLS to the QC. A light stopper as shown in Fig. 6.31 is also used to mask the light propagating inside the WLS fiber. In this configuration only the light transmitted through the QC is measured at the SiPM.

As clearly visible from the picture in Fig. 6.31, in configuration 1 the light propagates mostly through the WLS fiber. When grease is inserted in between the WLS and QC for configuration 2, the light can more easily propagate into the QC reach the photodetector. Since a “light stopper” was used to mask the end of the WLS in this second configuration, the light could only be collected from the external ring of the quartz capillary. Since standard WLS fibers are not sufficiently radiation hard, the second configuration is the one which should be considered as a candidate option to readout the signal from a detector operating in a high radiation environment.

A mechanical support with 4 layers of holes matching the geometry of the brass module was used to couple 8 WLS+QC light guides to the end of the crystal fibers as shown in Fig. 6.32. In this way, each WLS+QC tube receives the light produced from 4 different fibers. The upstream end of the capillary was masked whereas the rear end was coupled to an array of 8 SiPMs. The module was positioned in transverse configuration and 16 GeV electron beam was positioned at about 5 cm distance from the WLS to avoid direct excitation of WLS fiber.

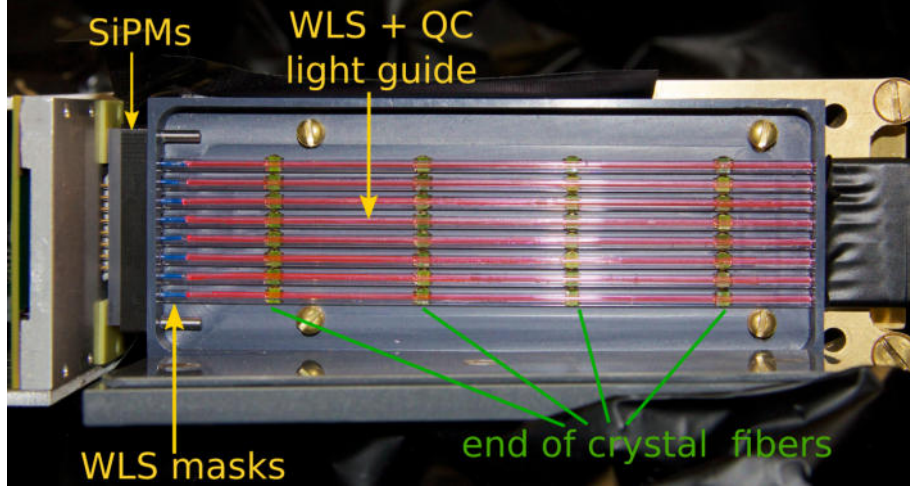


**Figure 6.32:** Side view of the calorimetric module with 8 red WLS inside quartz capillaries coupled to the 8 lines of 4 LuAG:Ce fibers each. The light propagating inside the WLS is shielded and only the signal from the quartz capillary is readout on the left side using SiPMs.

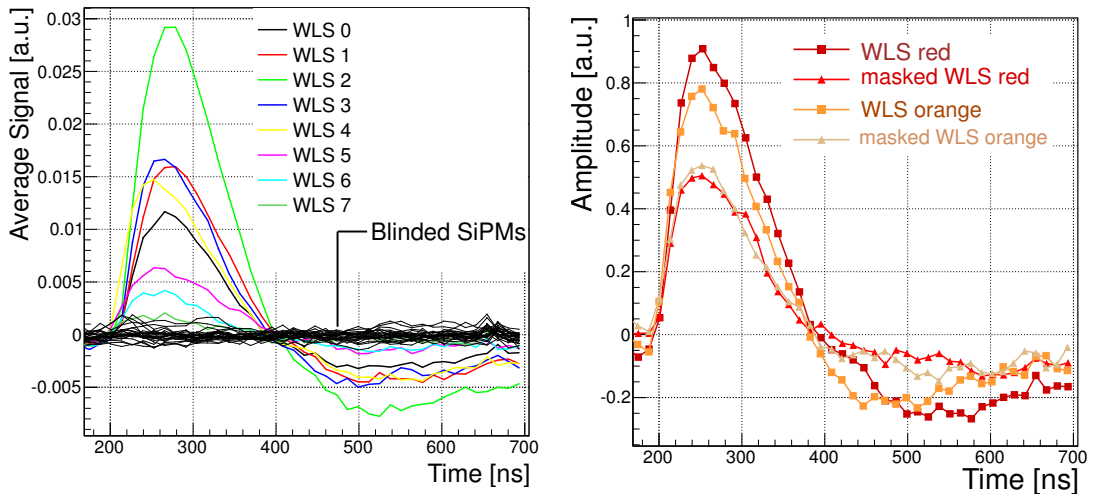


**Figure 6.33:** Left: average pulse shapes from the SiPMs during “WLS runs” with red wavelength shifter in configuration 1. Black lines show the signals from blinded photodetectors which were not connected to the WLS+QC. The colored lines correspond to the 8 channels coupled to the WLS+QC light guides. Right: comparison of the average pulses of WLS line number 2 for different configurations.

Despite the relatively low amount of energy deposited in the four sampled layers ( $\approx 160$  MeV), a signal was observed from all the capillaries as shown in the left plot of Fig. 6.33. This test was performed using both orange and red WLS in the two different configurations discussed earlier. Average pulse shapes reported in Fig. 6.33 show that this readout technique does not introduce a significant deviation from pure scintillation pulses and that configuration 1, as expected, yields a slightly larger signal.

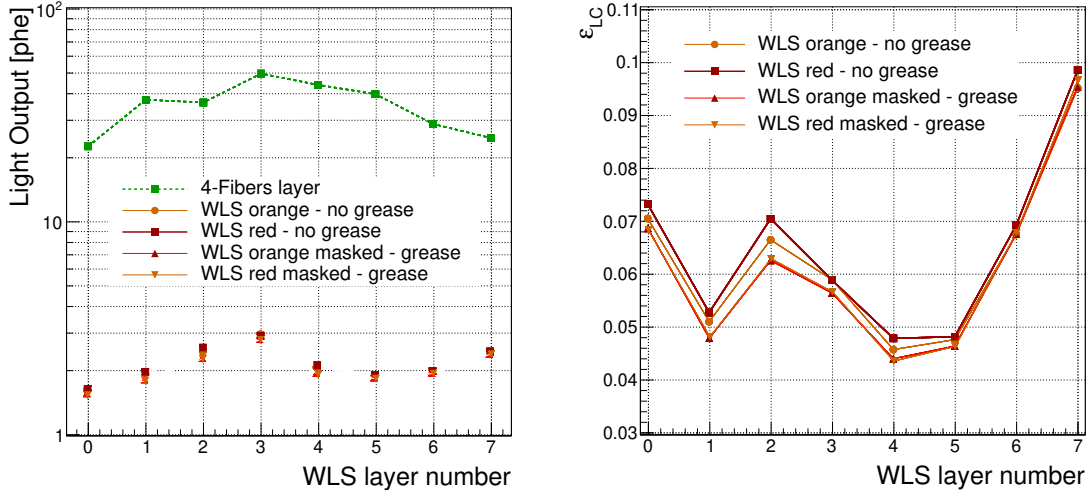


**Figure 6.34:** Left: comparison of the light output corresponding to a line of 4 LuAG:Ce fibers compared with the signal observed using the WLS+QC light collection system. Right: light collection efficiency estimated as the ratio of Eq. 6.15 for different configurations.

An exact estimation of the light collection efficiency with this kind of readout system is not a trivial task. First of all, the signal measured from the WLS was very small introducing large photostatistic fluctuations. In addition, to allow for mechanical installation of the WLS, the module position was changed during this test with respect to the previous runs in transverse configuration. Thus, it is not possible to directly compare light output of the fibers in transverse configuration with the one of the corresponding WLS+QC tube. For this reason, a simulation-based correction ( $E_i^{WLS+QC}/E_i^{transv}$ ) which accounts for the difference in deposited energy between the two configurations was used.

The total light output given by the sum of 4 fiber in a row ( $\sum_i^4 R_i$ ) was estimated from the measurements made in transverse configuration with direct coupling to the SiPMs as shown in Fig. 6.34.

This number, ranging from 20 to 50 photoelectrons, varies from line to line due to the different light yield of the fibers presented in Sec. 6.4.3. This number was compared with the light output from the corresponding WLS+QC tube ( $S_i^{WLS+QC}$ ) and the light collection efficiency was estimated according to

$$\varepsilon_i^{LC} = \frac{\sum_i^4 R_i}{S_i^{WLS+QC}} \cdot \frac{E_i^{WLS+QC}}{E_i^{transv}} \quad (6.15)$$

The results obtained for all the 8 WLS fibers in the four different configurations are reported in Fig. 6.34. We obtained an average light collection efficiency around  $6 \pm 3\%$ . This calculation includes the effect of the PDE of the SiPM which is about 20% at 520 nm

(LuAG:Ce emission peak) whereas it drops to about 10% at 625 nm (red WLS emission peak), and thus is responsible for the 50% of the photoelectron signal loss.

These results represent a proof of concept for a radiation tolerant light guide system which would be able to reduce the number of readout channels. Further tests are being performed in laboratory to confirm the estimation of light collection efficiency and optimize the optical coupling to enhance the light extraction.

## 6.5 Discussion and Conclusions

The potential of crystal fibers for calorimetry application was proved and confirmed with several test beam periods in which sampling calorimeter modules, consisting of LuAG fibers embedded into a brass structure, were tested.

In particular, the larger Crystal Fiber Calorimeter (CFCAL) prototype tested at FNAL demonstrated the capability of similar devices to efficiently separate electron from pion events. This was possible because of the high granularity of the calorimeter module. The electromagnetic shower profile for electrons of different energies (between 2 and 16 GeV) was also accurately measured. The intercalibration of all the channels in a similar device was successfully obtained, although it presents non-trivial challenges due to the non-uniformity of light yield and attenuation length of different fibers.

However, this first prototype was built with crystal fibers grown from different producers and including different batches of fibers grown with different parameters. The characterization of fiber response obtained with this test beam allowed to identify the best fibers for calorimetry applications, i.e. good attenuation lengths (above 20 cm) and high light yield. This will allow the producers to fix a set of optimized growth parameters to achieve a good reproducibility of fibers quality.

Further properties of the crystal fibers can be optimized to enhance their potential for calorimetry applications at HL-LHC. These are mostly a good tolerance to  $\gamma$ - and hadron-irradiation, and a fast scintillation response.

To this extent, GDMS (Glow Discharge Mass Spectrometry) [136] measurements are being performed on raw materials in order to identify and remove impurities which can cause the creation of color centers as discussed in Chap. 5. In parallel, several fibers are being irradiated with gamma and proton sources at CERN to compare the effect of radiation on the fibers attenuation length and light output.

The effect of balanced Calcium-codoping on radiation hardness of LuAG:Ce crystals is also being investigated and shows promising results. At the same time, codopants can also quench the slow component of LuAG:Ce scintillation leading to a faster response.

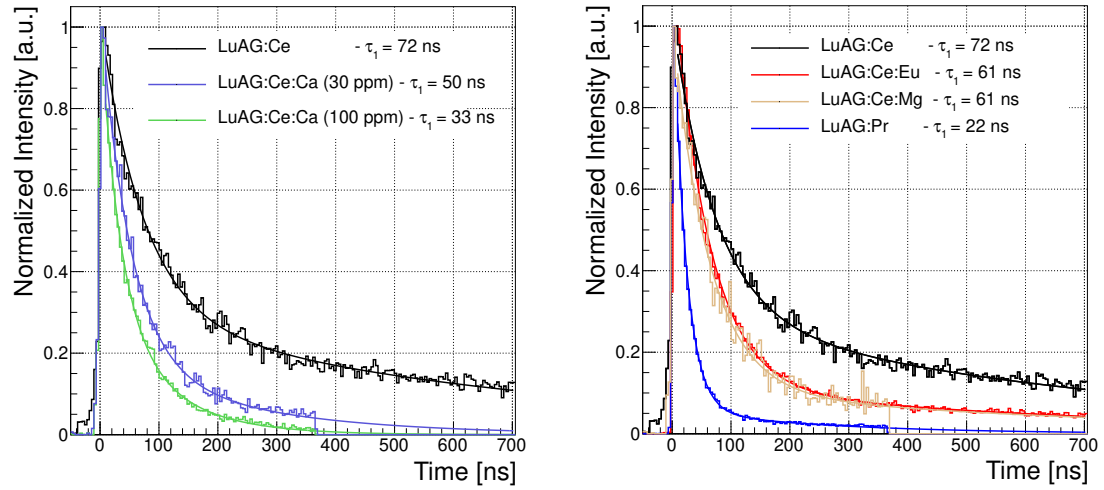


**Figure 6.35:** Left: comparison of LuAG:Ce scintillation pulse (black) with samples codoped with 30 and 100 ppm of Calcium. Right: comparison of LuAG:Ce scintillation pulse (black) with samples codoped using Eu and Mg (red, yellow) and with a LuAG:Pr crystal (blue).

This is being studied at CERN on dedicated samples as reported in Fig. 6.35. Also doping with Praseodymium ions or codoping with Europium and Magnesium are a viable options to obtain faster pulses as discussed in [137].

# Conclusions and Outlook

---

A coherent model to describe the PbWO<sub>4</sub> crystals aging due to radiation damage has been obtained and presented in this thesis. This was achieved by mean of dedicated irradiation studies and beam tests performed at CERN during 2011 and 2012. A simulation model was built to extrapolate the future performance of the CMS electromagnetic calorimeter throughout the whole LHC and High Luminosity LHC phase.

The understanding of radiation damage effects on the detector performance is of fundamental importance to evaluate whether the CMS calorimeter will be able to operate under the harsh radiation environment of HL-LHC. The present study demonstrated that the forward region of the CMS calorimeter, closer to the beam pipe, will not maintain a sufficient performance due to a strong loss of light output with a consequent degradation of the energy resolution.

In this framework, several R&D studies have started to investigate viable options for a radiation tolerant upgrade of the CMS forward calorimeters (ECAL and HCAL). The characterization of several scintillator candidates which can be used in scintillator-based detectors has been presented. First results of irradiation with protons and  $\gamma$ -rays on Cerium-based inorganic crystals and barium disilicate scintillator (DSB:Ce) confirm their potential as radiation tolerant active materials for calorimetry applications in HL-LHC.

Particular efforts have been spent to optimize the quality and the scintillation properties of LuAG:Ce crystalline fibers grown with the micro-pulling-down technique. This technology provides a powerful and flexible tool for the design of several calorimeters. A set of sampling calorimeter prototypes, made of LuAG fibers inserted into a brass absorber, have been tested both at CERN and Fermilab test beam facilities. The results presented in this thesis confirm the potential of crystal fiber technology for calorimetry applications.

These years represent an exciting period for detectors in high energy physics. While LHC has just decided to exploit its full potential, extending the program until the end of High Luminosity phase around 2030, new collider experiments are being discussed such as ILC and CLIC. As a consequence, it is a unique moment for particle detector science to research and develop new technologies which might significantly improve the performance of detectors.

Important challenges, as the possibility to operate at extremely high collision rates and in extremely high radiation environments need to be faced. High precision energy measurements must be achieved in calorimeters which are required, at the same time, to provide a fast and precise time response. These two properties will have to be combined coherently into a sort of “4-Dimensions”. High granularity and fast timing detectors can be used to mitigate pile up effects and to improve the overall calorimeter resolution and vertexing capability especially to photons, jets and neutral hadrons.

The limitations of the current CMS calorimeter and the challenging environment it will have to face during HL-LHC have been presented in this thesis. The status of the art of current R&D on new scintillating materials and calorimeter designs has also been introduced.

This thesis thus represents a starting point of several R&D studies for future calorimeters in high energy physics. Future irradiation tests are planned to further optimize the radiation hardness of candidate materials. New calorimeter prototypes will also be tested looking towards a real implementation into the CMS detector during the upgrade foreseen around 2022. In addition, particular efforts will be spent to improve the calorimeter time response. Faster scintillation processes can be achieved with a balanced choice of dopants and codopants in the crystal host matrix as discussed in this thesis. The use of fast photodetectors, such as Multi Channel Plates (MCP), will also be investigated as a viable way to improve timing precision of the detector.

## Double Readout Option to Mitigate ECAL Endcaps Aging

---

As introduced at the end of Chap. 4, it is possible to reduce the effects of radiation damage on PbWO<sub>4</sub> crystals performance by adding a photodetector coupled to the front face of the crystal as shown in Fig. A.1. Since electromagnetic particles (up to 100-200 GeV) develop the shower maximum in the first part of the crystal volume, the light will be mainly produced in this region. As a consequence, the front photodetector will strongly enhance the overall probability of light collection. As discussed in the following, this will play a role on the crystal performance especially in case of high induced absorption.

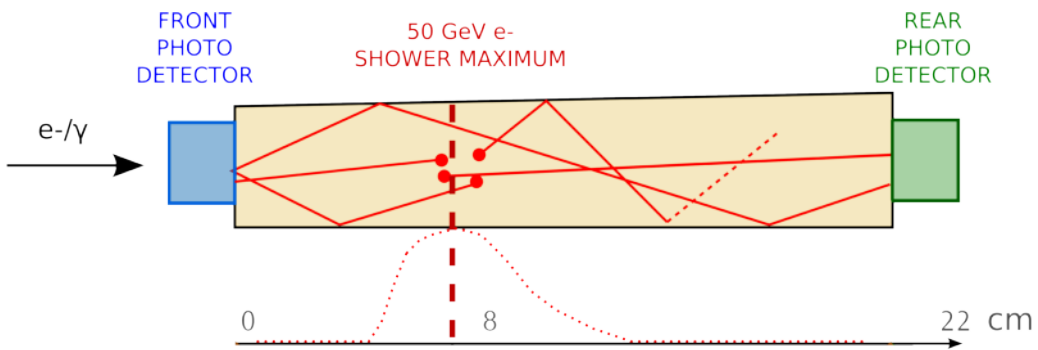


**Figure A.1:** Schematic view of a ECAL endcap crystal, couple to a standard VPT (rear photodetector) and an additional photodetector placed in the front face (front photodetector). This configuration enhance the probability of light collection and mitigate damage effects.

## A.1 Implications on Light Collection Efficiency

A simulation was performed to study the performance of a EE crystal in a *double readout* configuration. The reflecting layer on the front face of the PbWO<sub>4</sub> crystal has been replaced with a photodetector identical to the current ECAL VPTs (same dimensions and quantum efficiency). The transparency of the crystal was changed in the range between  $\mu_{ind} = 0$  and  $\mu_{ind} = 25 \text{ m}^{-1}$ . The photons collected at the front (rear) generate a signal  $F$  ( $R$ ) which takes into account the quantum efficiency of the VPT as in previous simulation

$$F = \int \int N_{ph}(\lambda, z) QE(\lambda) \varepsilon_{LC}(\lambda, z) d\lambda dz \quad (\text{A.1})$$

The two signals can then be combined together to yield the total response of the *double readout EE*

$$S = F + R \quad (\text{A.2})$$

In this case the effective light collection efficiency  $\varepsilon_{LC}$  along the crystal length changes and the curves become more flat. This is shown for different values of  $\mu_{ind}$  (0, 5 and 15 m<sup>-1</sup>) in Fig. A.2.

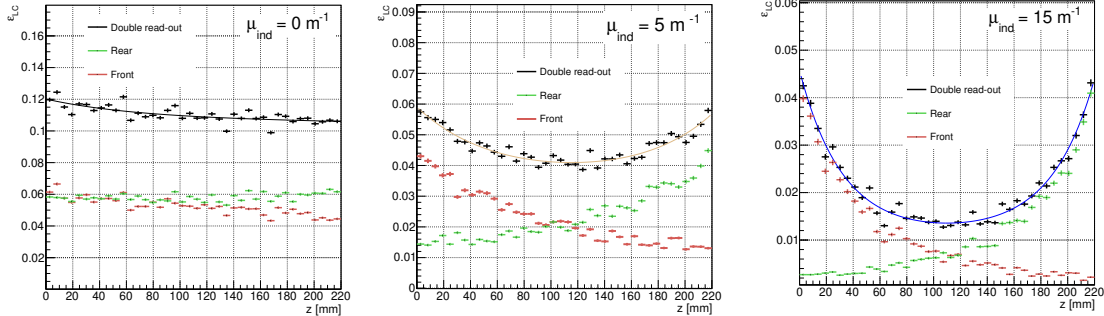


**Figure A.2:** Light collection efficiency curves for double readout EE crystals having different  $\mu_{ind}$ . Red and green curves correspond respectively to front and rear photodetectors whereas the black curve corresponds to the sum of both signals  $S$ . A fit with a sum of two exponential curves is performed and well reproduces the simulated efficiency.

Due to the removal of the reflector, the amount of light collected by the rear detector decreases because it is partially extracted and measured from the front face. However, the overall light output ( $S$ ) given by the sum of front and back signals is higher with respect to that of current ECAL crystals. In particular, the gain of light output becomes larger for higher  $\mu_{ind}$  as shown in Fig. A.3 and especially for low energy particles which develop the shower in the early part of the crystal, closer to the front photodetector.

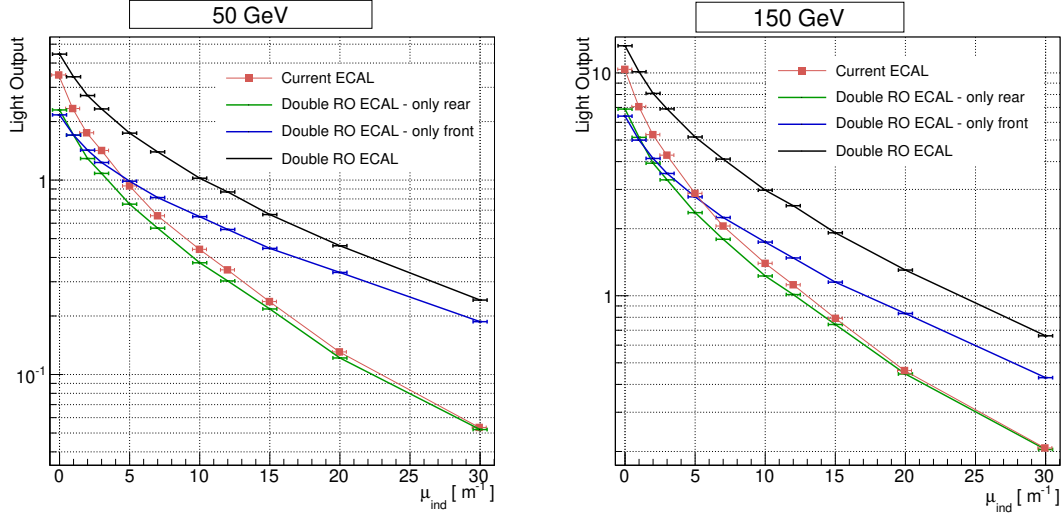


**Figure A.3:** Evolution of relative light output corresponding to 50 GeV (left) and 150 GeV (right) electron showers for different  $\mu_{ind}$ . A comparison between the current EE readout configuration (red square dots) and the double readout (black line) is shown.

## A.2 Improvements of Energy Resolution

As a consequence of the enhanced light output, the photostatistic term in the energy resolution will improve according to Eq. A.3

$$A \propto \frac{1}{\sqrt{LO}} \quad (\text{A.3})$$

Simulation predictions are shown in the left plot of Fig. A.4. The improvement in photostatistics is higher for larger  $\mu_{ind}$  and for low energies particles which are those more affected by the stochastic term of energy resolution ( $\sigma_E/E \propto A/\sqrt{E}$ ). Assuming a photodetector identical to current VPT, the noise term  $B$  of Eq. 3.11 will degrade because the new photodetector will contribute with additional electronic noise according to

$$\left(\frac{B}{S}\right)_{double} = \sqrt{\left(\frac{B_1}{S_1}\right)^2 + \left(\frac{B_2}{S_2}\right)^2} \quad (\text{A.4})$$

The additional noise would affect mostly non-irradiated crystals, with low  $\mu_{ind}$  and for which the gain in the light output is lower. For large values of  $\mu_{ind} > 15 \text{ m}^{-1}$  the additional noise becomes negligible (< 20%).

More relevant to the mitigation of aging effects is the influence of new light collection efficiency curves to the degradation of the constant term. As shown in Fig. A.2 the profile of  $\varepsilon_{LC}$  along crystal axis become more flat. According to Eq. 4.4 this is translated into a reduced degradation of the scintillation signal which quench the darkening effects on

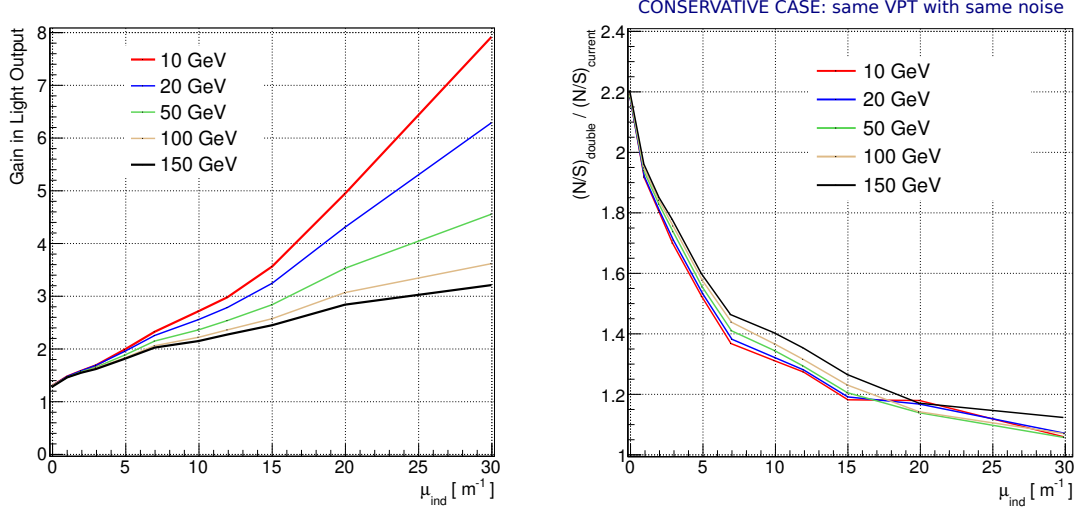


**Figure A.4:** Left: gain in light output, defined as the ratio of light output of a double readout EE and a standard EE, is shown as function of  $\mu_{ind}$  for different energies of electrons. Right: increase in noise term of Eq. A.4, assuming an identical VPT as front photodetector, is shown for different  $\mu_{ind}$  and electron energies.

energy resolution and linearity. The energy distributions are back to a symmetric shape, as shown in Fig. A.5, and degradation of constant term and linearity are strongly mitigated in the double readout configuration as shown in Fig. A.6.

Further improvements can be obtained with a smarter combination of the signals from the front and rear photodetectors. Approximating the  $\varepsilon_{LC}$  curves with symmetric exponential curves, Eq. A.1 can be written, for a given  $\lambda$ , as

$$F = \int_0^{22} N_{ph}(z) \varepsilon_{LC}^F(z) dz \propto \int_0^{22} N_{ph}(z) \cdot e^{-\frac{z}{L_{att}(\mu_{ind})}} \quad (\text{A.5})$$

$$R = \int_0^{22} N_{ph}(z) \varepsilon_{LC}^R(z) dz \propto \int_0^{22} N_{ph}(z) \cdot e^{-\frac{22-z}{L_{att}(\mu_{ind})}} \quad (\text{A.6})$$

in which  $z$  is the distance in cm from the front face of the crystal and  $L_{att}$  the attenuation coefficient which approximates the exponential behavior of  $\varepsilon_{LC}$  for a given  $\mu_{ind}$ .

In a first approximation, we can assume that each shower produces the photons at the average position  $z_{ave}$  along the crystal depending on the energy of the primary particle

$$z_{ave} = K(\lambda) \ln \left[ \frac{F(z_{ave})}{R(z_{ave})} \right] \quad (\text{A.7})$$

where  $K(\lambda)$  is a constant which depends on  $L_{att}(\mu_{ind})$ .

## A.2. Improvements of Energy Resolution

---

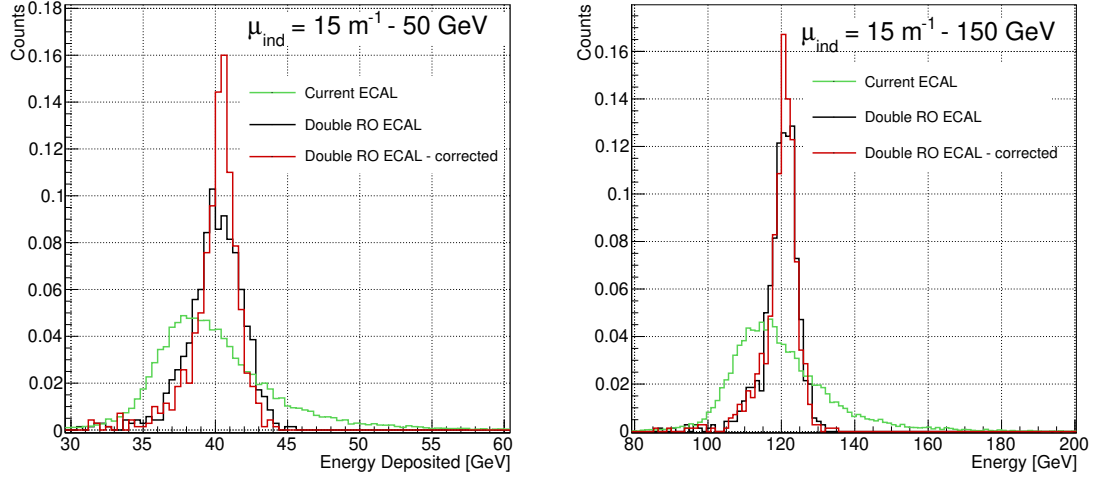


**Figure A.5:** Energy distributions for 50 GeV (left) and 150 GeV (right) electrons in different readout configurations for EE. Correction based on double readout (red curve) allow to restore the symmetric shape of the distribution and to improve its resolution.

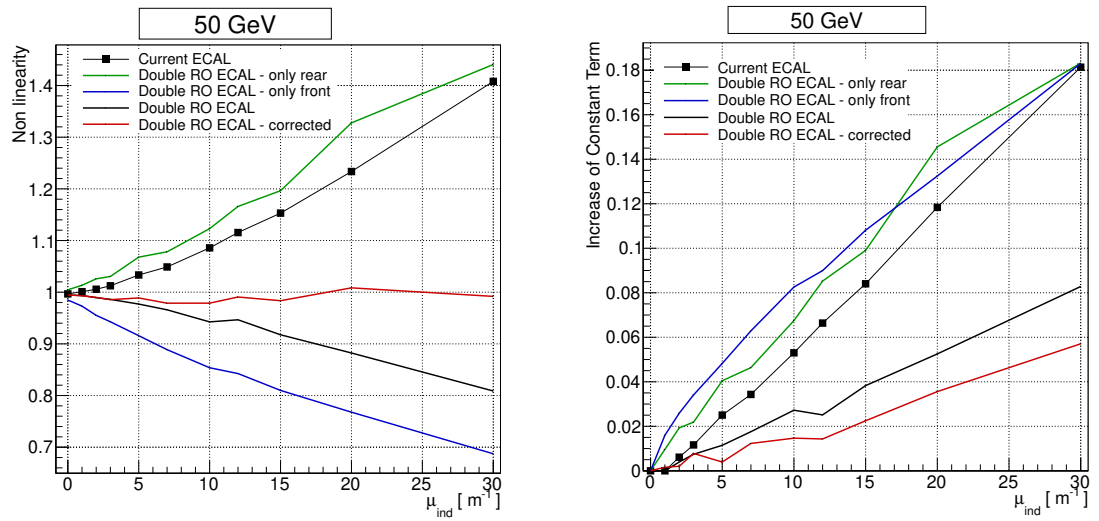


**Figure A.6:** Left: improvements in response linearity of damaged crystals for a double readout configuration with and without corrections, compared with current ECAL endcaps. Right: evolution of constant term for different  $\mu_{ind}$  and different EE readout options.

	Stochastic	Noise	Constant	Total
Current ECAL (10 GeV)	3.5%	20%	8%	20%
Double RO ECAL (10 GeV)	1.9%	24%	2%	24%
Current ECAL (50 GeV)	1.8%	4%	8%	10%
Double RO ECAL (50 GeV)	1.1%	4.8%	2%	5.3%
Current ECAL (150 GeV)	0.9%	1.2%	8%	8%
Double RO ECAL (150 GeV)	0.6%	1.5%	2%	2.6%

**Table A.1:** Comparison of different contributions to EE energy resolution for the double readout option after correction of Eq. A.8 and the current EE configuration.

Assuming that  $L_{att}(\mu_{ind})$  is unknown it is still possible to combine the two signals of Eq. A.5 and Eq. A.6 to correct for the average light attenuation

$$S_{corr} = F(z_{ave}) \cdot e^{\frac{z_{ave}}{L_{att}}} + S(z_{ave}) \cdot e^{\frac{22-z_{ave}}{L_{att}}} \quad (\text{A.8})$$

$$= 2F(z_{ave}) \cdot \sqrt{\frac{R(z_{ave})}{F(z_{ave})}} \quad (\text{A.9})$$

This correction allows to further improve the energy resolution of damaged crystals, by taking into account the event-by-event fluctuations of longitudinal shower development. In addition, the linearity of the crystal response is fully restored as shown in Fig. A.6.

It is also important to notice that more precise corrections can be implemented in the real ECAL detector. Since the loss of transparency of the crystals is monitored with a laser, the in-situ monitoring can be used to define crystal-by-crystal correction coefficients based on the exact profile of  $\varepsilon_{LC}(\mu_{ind})$ . Combining the different contributions of stochastic, noise and constant term, the overall energy resolution of a double readout EE can be obtained and compared with the current configuration. Results are summarized in Table. A.1 for 10, 50 and 150 GeV.

### A.3 Practical Considerations

At high energies ( $> 100$  GeV), being more relevant for the ECAL endcaps where detected particles have larger momenta, the degradation of the constant term would be strongly mitigated by a double readout EE. Assuming a  $\mu_{ind}$  of  $15 \text{ m}^{-1}$ , as predicted for  $|\eta| = 2.2$  after  $3000 \text{ fb}^{-1}$ , the constant term of 150 GeV electrons energy resolution would decrease to  $\approx 2\%$  instead of the  $\approx 8\%$  predicted for the current calorimeter.

At low energies ( $\approx 10$  GeV), the additional noise term dominates the energy resolution. Therefore, in an upgrade scenario of the ECAL endcaps, efforts should be spent to identify photodetectors with a tunable gain and thus with a lower noise with respect to current

VPTs. Radiation hard SiPMs can already represent a viable option for the front photodetector. A double readout configuration for EE might also improve the timing capability and particle identification of the current ECAL, exploiting the information given by the separate front and back signals. Further simulation studies will be performed and laboratory and test beams are planned to confirm experimentally the results of this preliminary study.



# Bibliography

---

- [1] C. Fabjan and R. Wigmans, *Energy measurement of elementary particles*, Report on Progress in Physics **52** (1989) 1519.
- [2] V. S. Murzin, *Progress in elementary particle and cosmic-ray physics*, J. G. Wilson and I. A. Wouthuysen eds., North Holland Publ. Co. **9** (1967) 247.
- [3] G. B. Kim et al., *Thermal Model and Optimization of a Large Crystal Detector using a Metallic Magnetic Calorimeter*, [arXiv:1402.2334](https://arxiv.org/abs/1402.2334).
- [4] T. Bowen et al., *A Detector development study of acoustic calorimetry at Fermilab energies*, Fermilab Proposal 0528 (1977) .
- [5] G. Mavromanolakis, *Quartz fiber calorimetry and calorimeters*, [arXiv:physics/0412123](https://arxiv.org/abs/physics/0412123).
- [6] M. Lundin, *On the electromagnetic energy resolution of Cherenkov-fiber calorimeter*, Nucl. Instr. Meth. A **372** (1996) 359.
- [7] O. Ganel and R. Wigmans, *Quartz fiber calorimetry for LHC experiments*, Nucl. Instr. Meth. A **365** (1995) 360.
- [8] R. Wigmans, *Calorimetry, Energy Measurement in Particle Physics*, Internal Series of Monographs on Physics **107** (2000) .
- [9] P. B. Cushman, *Electromagnetic and hadronic calorimeters*, Instrumentation in High Energy Physics, ed. F.Sauli, World Scientific 1992, Advanced Series on Directions in High Energy Physics **9** (1992) 281.
- [10] Particle Data Group Collaboration, J. Beringer et al., *Review of Particle Physics*, Phys. Rev. **D86** (2012) 010001.

- 
- [11] R. Wigmans, *On the energy resolution of uranium and other hadron calorimeters*, Nucl. Instr. Meth. A **259** (1987) 389.
  - [12] R. Wigmans, *Advances in hadron calorimetry*, Annual Review of Nuclear and Particle Science **41** (1991) 133.
  - [13] S. Lee and R. Wigmans, *On the Energy Measurement of Jets in High-Energy Physics Experiments*, Nucl. Instr. Meth. A **316** (1992) 184.
  - [14] N. Akchurin et al., *Beam test results from a fine-sampling quartz fiber calorimeter for electron, photon and hadron detection*, Nucl. Instr. Meth. A **399** (1997) 202.
  - [15] U. Amaldi, *Fluctuations in calorimetry measurements*, Physica Scripta **23** (1981) 409.
  - [16] N. Akchurin et al., *Hadron and jet detection with a dual-readout calorimeter*, Nucl. Instr. Meth. A **537** (2005) 537–561.
  - [17] CMS Collaboration, S. Chatrchyan et al., *Determination of jet energy calibration and transverse momentum resolution in CMS*, JINST **6** (2011) P11002.
  - [18] CMS Collaboration, M. Thomson, *Particle Flow Calorimetry*, J. Phys.: Conf. Ser. **110** (2008) 092032.
  - [19] M. Thomson Proc. of EPS-HEP 2003, Aachen. Topical Vol. of Eur. Phys. J. C Direct (2004) .
  - [20] CMS Collaboration, *Particle-flow event reconstruction in CMS and performance for jets, taus, and  $\cancel{E}_T$* , CMS Physics Analysis Summary CMS-PAS-PFT-09-001 (2011) . <http://cdsweb.cern.ch/record/1194487>.
  - [21] The CALICE Collaboration, C. Adloff et al., *Particle Flow Calorimetry*, JINST **6** (2011) P07005.
  - [22] S. Seifert et al., *Accurate measurement of the rise and decay times of fast scintillators with solid state photon counters*, JINST **7** (2012) P09004.
  - [23] P. A. Rodnyi, *Physical processes in inorganic scintillators*, Nucl. Instr. Meth. A **490** (1997) 30–50.
  - [24] A. N. Annekov et al., *Lead tungstate scintillation material*, Nucl. Instr. Meth. A **490** (2002) 30–50.
  - [25] F. P. Bowden and L. T. Chadderton, *Fission fragment damage to crystal lattices: dislocation formation*, Proc. R. Soc. Lond **A269** (1962) .
  - [26] P. Bagnaia et al.  
<http://user.web.cern.ch/public/en/About/History-en.html>.

- [27] F. J. Hasert et al, *Search for elastic muon neutrino electron scattering*, Phys. Lett. B **46** (1973) 121–124.
- [28] Gargamelle Neutrino Collaboration, *Observation of neutrino-like interactions without muon or electron in the Gargamelle neutrino experiment*, Phys. Lett. B **46** (1973) 138–140.
- [29] UA1 Collaboration, *Experimental Observation of Isolated Large Transverse Energy Electrons with Associated Missing Energy at  $\sqrt{s} = 540 \text{ GeV}$* , Phys. Lett. B **122** (1973) 103–116.
- [30] UA2 Collaboration, *Evidence for  $Z_0 \rightarrow e^+ e^-$  at the CERN anti-p-p Collider*, Phys. Lett. B **129** (1973) 130–140.
- [31] CMS Collaboration, S. Chatrchyan et al., *Observation of a new boson at a mass of 125 GeV with the CMS experiment at the LHC*, Phys.Lett. B **716** (2012) 30–61, [arXiv:1207.7235](https://arxiv.org/abs/1207.7235).
- [32] CMS Collaboration, S. Chatrchyan et al., *Observation of a new boson with mass near 125 GeV in pp collisions at  $\sqrt{s} = 7$  and 8 TeV*, JHEP **1306** (2013) 081, [arXiv:1303.4571](https://arxiv.org/abs/1303.4571).
- [33] ATLAS Collaboration, G. Aad et al., *Observation of a new particle in the search for the Standard Model Higgs boson with the ATLAS detector at the LHC*, Phys.Lett. B **716** (2012) 1–29, [arXiv:1207.7214](https://arxiv.org/abs/1207.7214).
- [34] L. Evans and P. Bryant, *LHC Machine*, JINST **3** (2008) S08001.
- [35] ALICE Collaboration, K. Aamodt et al., *The ALICE experiment at the CERN LHC*, JINST **3** (2008) S08002.
- [36] ATLAS Collaboration, *The ATLAS Experiment at the CERN Large Hadron Collider*, JINST **3** (2008) S08003.
- [37] CMS Collaboration, S. Chatrchyan et al., *The CMS experiment at the CERN LHC*, JINST **3** (2008) S08004.
- [38] LHCb Collaboration, J. Alves, A. Augusto et al., *The LHCb Detector at the LHC*, JINST **3** (2008) S08005.
- [39] CMS Collaboration, S. Chatrchyan et al., *Search for Physics Beyond the Standard Model Using Multilepton Signatures in pp Collisions at  $\sqrt{s} = 7 \text{ TeV}$* , Phys. Lett. B **704** (2011) 411–433.
- [40] OPERA Collaboration, M. Guler et al., *OPERA: An appearance experiment to search for  $\nu_\mu \leftrightarrow \nu_\tau$  oscillations in the CNGS beam. Experimental proposal*, Technical Design Report .

- 
- [41] OPERA Collaboration, T. Adam et al., *Measurement of the neutrino velocity with the OPERA detector in the CNGS beam*, [arXiv:1109.4897](https://arxiv.org/abs/1109.4897).
  - [42] D. Kotlinski et al., *The design of the CMS pixel detector system*, Nucl. Instr. Meth. A **447** (2002) 446–50.
  - [43] CMS Collaboration, *The Tracker Project Technical Design Report*, CERN/LHCC 98-6, CMS TDR 5 (1998) .
  - [44] CMS Collaboration, *The Electromagnetic Calorimeter Project: Technical Design Report*, Technical Report CERN-LHCC-97-33 **CMS-TDR-4** (1997) S08004.
  - [45] Z. Antunovic et al., *Radiation hard avalanche photodiodes for the CMS detector*, Nucl. Instr. Meth. A **537** (2005) 379.
  - [46] Y. Gusev et al., *Super radiation hard vacuum phototriodes for the CMS endcap ECAL*, Nucl. Instr. Meth. A **535** (2004) 511–516.
  - [47] P. Adzic et al., *Energy resolution of the barrel of the CMS electromagnetic calorimeter*, JINST **2** (2007) P04004.
  - [48] CMS Collaboration, S. Chatrchyan et al., *Energy calibration and resolution of the CMS electromagnetic calorimeter in pp collisions at  $\sqrt{s} = 7$  TeV*, JINST **8** (2013) P09009.
  - [49] M. Anfreville et al., *Laser monitoring system for the CMS lead tungstate crystal calorimeter*, Nucl. Instr. Meth. A **594** (2008) 292.
  - [50] CMS Collaboration, C. S et al., *The CMS Hadron Calorimeter Project*, Technical Design Report CMS, CERN (1997) .
  - [51] CMS Collaboration, G. Bayatian et al., *CMS physics*, Technical Design Report CMS, CERN (2006) .
  - [52] CMS Collaboration, C. S et al., *Performance of the CMS Hadron Calorimeter with Cosmic Ray Muons and LHC Beam Data*, JINST **5** T03012.
  - [53] ECAL/HCALs Collaboration, E. Yazgan, *The CMS barrel calorimeter response to particle beams from 2-GeV/c to 350-GeV/c*, J. Phys. Conf. Ser. **160** (2009) 012056.
  - [54] G. Bayatian et al., *Design, performance and calibration of the CMS forward calorimeter wedges*, Eur. Phys. J. **C53** (2008) 139–166.
  - [55] CMS Collaboration, G. Acquistapace et al., *CMS, the magnet project: Technical design report*, Technical Design Report CMS, CERN (1997) .
  - [56] CMS Collaboration, *The CMS muon project: Technical Design Report*, Technical Design Report CMS, CERN (1997) .

- [57] CMS Collaboration, P. Gunnellini, *The CASTOR calorimeter at the CMS experiment*, [arXiv:1304.2943](https://arxiv.org/abs/1304.2943).
- [58] X. Aslanoglou et al., *First performance studies of a prototype for the CASTOR forward calorimeter at the CMS experiment*, [arXiv:0706.2576v3](https://arxiv.org/abs/0706.2576v3).
- [59] CMS Collaboration, O. Grachov et al., *Status of zero degree calorimeter for CMS experiment*, AIP Conf. Proc. **867** (2006) 258–265.
- [60] O. Grachov et al., *Measuring photons and neutrons at zero degrees in CMS*, Technical Design Report CMS, CERN .
- [61] CMS Collaboration, P. Sphicas et al., *CMS: The TriDAS project. Technical design report, Vol.2: Data acquisition and high-level trigger* , .
- [62] CMS Electromagnetic Calorimeter Collaboration, P. Adzic et al., *Radiation hardness qualification of PbWO<sub>4</sub> scintillation crystals for the CMS Electromagnetic Calorimeter*, JINST **5** (2009) P03010, [arXiv:0912.4300](https://arxiv.org/abs/0912.4300).
- [63] M. Kobayashi et al., *Improvement in radiation hardness of PbWO<sub>4</sub> scintillating crystals by La doping*, Nucl. Instr. Meth. A **404** (1998) 149.
- [64] A. Annenkov et al., *Suppression of the radiation damage in lead tungstate scintillation crystal*, Nucl. Instr. Meth. A **426** (1999) 486.
- [65] A. Annenkov et al., *Lead tungstate scintillation material*, Nucl. Instr. Meth. A **490** (2002) 30.
- [66] M. Nikl et al., *Radiation induced formation of color centers in PbWO<sub>4</sub> single crystals*, J. Appl. Phys. **82** (1997) 5758.
- [67] A. Annenkov et al., *On the Mechanism of Radiation Damage of Optical Transmission in Lead Tungstate Crystal*, Phys. Status Solidi (a) **191** (2002) 277.
- [68] Z. Liyuan et al., *Performance of the monitoring light source for the CMS lead tungstate crystal calorimeter*, IEEE Trans. Nucl. Sci. **52** (2005) 1123.
- [69] P. Lecomte et al., *High-energy proton induced damage in PbWO<sub>4</sub> calorimeter crystals*, Nucl. Instr. Meth. A **545** (2005) 63.
- [70] P. Lecomte et al., *High-energy proton induced damage study of scintillation light output from PbWO-4 calorimeter crystals*, Nucl. Instr. Meth. A **564** (2006) 164.
- [71] P. Lecomte et al., *Comparison between high-energy proton and charged pion induced damage in PbWO<sub>4</sub> calorimeter crystals*, Nucl. Instr. Meth. A **587** (2008) 266.
- [72] G. Pazzi et al., *Delayed recombination luminescence in lead tungstate (PWO) scintillating crystals*, Journal of Luminescence **102–103** (2004) 791–796.

- [73] E. Auffray et al., *Experimental Study of Lead Tungstate Scintillator Proton-Induced Damage and Recovery*, Proceedings for the Scint 2011 Conference (2011) . [http://cds.cern.ch/record/1406800/files/CR2011\\_257.pdf](http://cds.cern.ch/record/1406800/files/CR2011_257.pdf).
- [74] CMS Collaboration, *Technical Proposal for the Upgrade of the CMS detector through 2020*, CERN-LHCC-2011-006 **3** (2012) S08004.
- [75] G. Battistoni et al., *The FLUKA code: Description and benchmarking*, AIP Conference Proceeding (2007) 31–49. <http://www.fluka.org/fluka.php>.
- [76] A. Ferrari et al., *FLUKA: a multi-particle transport code*, 2005. <http://www.fluka.org/fluka.php>.
- [77] M. Glaser et al., *Dosimetry Assessments in the Irradiation Facilities at the CERN-PS Accelerator*, IEEE Trans. Nucl. Sci. (2006) 2016–2022.
- [78] C. Furetta et al., *Fluence and dosimetric measurements for a  $\pi^\pm$  irradiation facility*, Nucl. Phys B Proc. Suppl. 44 (1995) 503–509.
- [79] E. Auffray et al., *Performance of ACCOS, an Automatic Crystal quality Control System for the PWO crystals of the CMS calorimeter*, Nucl. Instr. Meth. A **456** (2001) 325.
- [80] Hamamatsu and Photonics, *Photomultiplier tubes and assemblies for scintillating counters and high energy physics*, [http://neutron.physics.ucsb.edu/docs/High\\_energy\\_PMT TPM00007E01.pdf](http://neutron.physics.ucsb.edu/docs/High_energy_PMT TPM00007E01.pdf).
- [81] Hamamatsu and Photonics, *Datasheet of Hamamatsu R8619 PMTs*, <http://www.hamamatsu.com/resources/pdf/etd/R8619 TPMH1331E03.pdf>.
- [82] Y. Pishchalnikov et al., *Performance of Hamamatsu R5380: Low gain PMT*, <http://inspirehep.net/record/367901?ln=it>.
- [83] *Charge Analog-to-Digital Converter*, <http://teledynelecroy.com/lrs/dsheets/1182.htm>.
- [84] N. I. Corp., *LabVIEW System Design Software*, <http://www.ni.com/labview/>.
- [85] *ROOT Analysis Framework*, <http://root.cern.ch/drupal/content/rootfit>.
- [86] S. Agostinelli et al., *Geant4: a simulation toolkit*, Nucl. Instr. Meth. A **506** (2003) 250.
- [87] N. Ackurin et al., *Cherenkov light contribution in lead tungstate crystals*, J. Phys.: Conf. Ser. **110** (2008) 092034.
- [88] S. Baccaro et al., *Radiation damage effect on avalanche photodiodes*, Nucl. Instr. Meth. A **426** (1999) 206–211.

- [89] CMS Collaboration, *Technical Proposal for the Phase II Upgrade of the Compact Muon Solenoid*, CERN-LHCC-2014-XXX **X** (2014) XXXX.
- [90] CMS Collaboration, *The CMS Software Framework*,  
<http://cms-sw.github.io/cmssw/index.html>.
- [91] Eljen Technology. "<http://www.eljentechnology.com/index.php/products/liquid-scintillators/73-ej-309>".
- [92] S. Derenzo et al., *The quest for the ideal inorganic scintillator*, Nucl. Instr. Meth. A **505** (2003) 111–117.
- [93] J. Chen et al., *Large size LSO and LYSO crystal scintillators for future high-energy physics and nuclear physics experiments*, Nucl. Instr. Meth. A **572** (2007) 218–224.
- [94] H. Feng et al., *Temperature dependence of luminescence characteristics of LSO:Ce scintillator grown by the Czochralski method*, J. Appl. Phys. **108** (2010) 218–224.
- [95] P. C. Ricci et al., *Ce<sup>3+</sup>-doped lutetium yttrium orthosilicate crystals: Structural characterization*, Material Science and Engineering B **146** (2008) 2–6.
- [96] E. Auffray et al., *Radiation damage of LSO crystals under  $\gamma$  and 24 GeV protons irradiation*, Nucl. Instr. Meth. A **721** (2013) 76–82.
- [97] E. Auffray et al., *Radiation Damage of Oxy-Orthosilicate Scintillation Crystals Under Gamma and High Energy Proton Irradiation*, IEEE Trans. Nucl. Sci. **61** (2014) .
- [98] E. Auffray et al., *The impact of proton induced radioactivity on the LSO:Ce, YSO:Ce detectors*, IEEE Trans. Nucl. Sci. (2013) 1–5.
- [99] J. Derby et al., *An integrated process model for the growth of oxide crystals by the Czochralski method*, Journal of Crystal Growth **97** (1989) 792–826.
- [100] P. Dorenbos et al., *Afterglow and thermoluminescence properties of scintillation crystals*, J. Phys: Condens. Matter **6** (1994) 4167–4180.
- [101] S. Blahuta et al., *Defects identification and effects of annealing on Lu<sub>2(1-x)</sub>Y<sub>2x</sub>SiO<sub>5</sub> (LYSO) single crystals for scintillation application*, Materials **4** (2011) 1224–1237.
- [102] T. Enquist et al., *Isotopic yields and kinetic energies of primary residues in 1 A GeV <sup>208</sup>Pb+p reactions*, Nucl. Phys. A **686** (2001) 481.
- [103] D. J. Morrisey et al., *Systematics of momentum distributions from reactions with relativistic ions*, Phys. Rev. C **39** (1989) 460.
- [104] A. J. Van Lint et al., *The physics of radiation damage in particle detectors*, Nucl. Instr. Meth. A **253** (1987) 453–459.

- [105] H. Ogino et al., *Scintillation characteristics of Pr-doped Lu<sub>3</sub>Al<sub>5</sub>O<sub>12</sub> single crystals*, *Journal of Crystal Growth* **292** (2006) 239–242.
- [106] H. Ogino et al., *Growth and scintillation properties of Pr-doped Lu<sub>3</sub>Al<sub>5</sub>O<sub>12</sub> crystals*, *Journal of Crystal Growth* **287** (2006) 335–3382.
- [107] J. Mares et al., *Scintillation properties of Ce<sup>3+</sup> - and Pr<sup>3+</sup> -doped LuAG, YAG and mixed Lu<sub>x</sub>Y<sub>1-x</sub>AG Garnet Crystals*, *IEEE Trans. Nucl. Sci.* **59** (2012) 2120–2125.
- [108] C. Dujardin and other, *LuAG:Ce fibers for high energy calorimetry*, *Journal of Applied Physics* **108** (2010) 13510.
- [109] M. V. Derdzyan et al., *Radiation hardness of LuAG:Ce and LuAG:Pr scintillator crystals*, *Journal of Crystal Growth* **361** (2012) 212–216.
- [110] A. Petrosyan et al., *Bridgman growth and site occupation in LuAG:Ce scintillator crystals*, *Journal of Crystal Growth* **312** (2010) 3136–3142.
- [111] E. Auffray et al., *DSB:Ce<sup>3+</sup> scintillation glass ceramics for future calorimetry*, to be published .
- [112] I. Dumanoglu et al., *Radiation-hardness studies of high OH<sup>-</sup> content quartz fibres irradiated with electrons*, *Nucl. Instr. Meth. A* **490** (2002) 444–455.
- [113] K. Cankoçak et al., *Radiation-hardness measurements of high OH<sup>-</sup> content quartz fibres irradiated with 24 GeV protons up to 1.25 Grad*, *Nucl. Instr. Meth. A* **585** (2008) 20–27.
- [114] M. Carrara et al., *Characterization of a Ce<sup>3+</sup> doped SiO<sub>2</sub> optical dosimeter for dose measurements in HDR brachytherapy*, *Rad. Meas.* **56** (2013) 312–315.
- [115] N. Chiodini et al., *Ce-doped SiO<sub>2</sub> optical fibers for remote radiation sensing and measurement*, *Proc. SPIE 7316, Fiber Optic Sensors and Applications VI* (2009) .
- [116] K. Pauwels et al., *Single crystalline LuAG fibers for homogeneous dual-readout calorimeters*, **8** (2013) 09019.
- [117] K. Pauwels, *Inorganic single crystalline fibers for dual-readout calorimetry*, <http://cds.cern.ch/record/1522569/files/CERN-THESIS-2013-013.pdf>.
- [118] K. Pauwels et al., *Effect of aspect ratio on the light output of scintillators*, *IEEE Trans. Nucl. Sci.* **59(5)** (2012) 2340–2345.
- [119] P. Lecoq, *Metamaterials for novel X- or γ-ray detector designs*, *IEEE Nucl. Sci. Symp. Conf. Record* (2008) 1405–1409.

## Bibliography

---

- [120] P. Lecoq, *New crystal technologies for novel calorimeter concepts*, Journal of Physics: Conference Series **160** (2009) 12016.  
<http://stacks.iop.org/1742-6596/160/i=1/a=012016>.
- [121] E. Auffray et al., *Dual readout calorimeter with heavy scintillating crystal fibers*, IEEE Nucl. Sci. Symp. Conf. Record (2008) 3262–3265.
- [122] M. Letz et al., *Temperature-dependent Urbach tail measurements of Lutetium Aluminum garnet single crystals*, Physical Review B **81** (2010) 155109.
- [123] Y. Kuwano et al., *Crystal growth and properties of  $(Lu, Y)_3Al_5O_{12}$* , Journal of Crystal Growth **260** (2004) 159–165.
- [124] G. Mavromanolakis et al., *Studies on sampling and homogeneous dual readout calorimetry with meta-crystals*, Journal of Instrumentation **6** (2011) 10012.
- [125] M. Lucchini et al., *Test beam results with LuAG fibers for next-generation calorimeters*, JINST **8** (2013) P10017.
- [126] H1 SpaCal Collaboration, *Performance of an Electromagnetic Lead/Scintillating-Fibre Calorimeter for the H1 Detector*, Nucl. Instr. Meth. A **374** (1996) 149–156.
- [127] H1 SpaCal Collaboration, *The H1 Lead/Scintillating-Fibre Calorimeter*, Nucl. Instr. Meth. A **386** (1997) 397–408.
- [128] H1 SpaCal Collaboration, *Hadronic response and e/pi-Separation with the H1 lead/fiber Calorimeter*, DESY Red Report (1997) 95–250.
- [129] X. Xu et al., *Ce-doped LuAG single-crystal fibers grown from the melt for high-energy physics*, Acta Materialia **67** (2014) 232–238.
- [130] T. Medvedeva, *The Frontier of Modern Calorimetry: Hardware advances and Application in Particle Physics Analysis*, 2014.  
[http://www.princeton.edu/physics/graduate-program/theses/theses-from-2014/thesis\\_medvedeva.pdf](http://www.princeton.edu/physics/graduate-program/theses/theses-from-2014/thesis_medvedeva.pdf).
- [131] Y. Musienko et al., *Radiation Damage Studies of Silicon Photomultipliers for the CMS HCAL Phase I Upgrade*, [http://ndip.in2p3.fr/ndip14/AGENDA/AGENDA-by-DAY/Presentations/5Friday/PM/ID37166\\_Musienko.pdf](http://ndip.in2p3.fr/ndip14/AGENDA/AGENDA-by-DAY/Presentations/5Friday/PM/ID37166_Musienko.pdf).
- [132] E. Hazen et al., *The CMS HCAL data concentrator: A modular, standards-based implementation*, 7th Workshop on Electronics for LHC Experiments, Proceedings (2001) 347–350.
- [133] Fibercryst Company, <http://www.fibercryst.com>.

- [134] *FTBF Fermilab Test Beam Facilities*,  
<http://www-ppd.fnal.gov/ftbf/beam/delivery.html#mtest>.
- [135] *Technical scope of work for the 2013 Fermilab Test Beam Facility program*,  
[http://www-ppd.fnal.gov/ftbf/TSW/PDF/T1043\\_tsw\\_signed.pdf](http://www-ppd.fnal.gov/ftbf/TSW/PDF/T1043_tsw_signed.pdf).
- [136] T. Note, *Glow Discharge Mass Spectrometry (GDMS) Service*,  
<http://www.eag.com/documents/glow-discharge-mass-spectrometry-gdms-services-TN102.pdf>.
- [137] M. Nikl et al., *Defect Engineering in Ce-Doped Aluminum Garnet Single Crystal Scintillators*, *Crystal Growth and Design* **9** (2014) 4827–4833.